HZDR-044

POSITRON EMISSION TOMOGRAPHY FOR THE DOSE MONITORING OF INTRA-FRACTIONALLY MOVING TARGETS IN ION BEAM THERAPY

Kristin Stützer

Wissenschaftlich-Technische Berichte
HZDR-044 · ISSN 2191-8708

WISSENSCHAFTLICH-
TECHNISCHE BERICHTE

HZDR
HELMHOLTZ
ZENTRUM DRESDEN
ROSSENDORF

Wissenschaftlich-Technische Berichte
HZDR-044

Kristin Stützer

POSITRON EMISSION TOMOGRAPHY FOR THE DOSE MONITORING OF INFRA-FRACTIONALLY MOVING TARGETS IN ION BEAM THERAPY

HZDR

HELMHOLTZ
ZENTRUM DRESDEN
ROSSENDORF

Druckausgabe: ISSN 2191-8708

Elektronische Ausgabe: ISSN 2191-8716

Die vorliegende Arbeit wurde als Dissertation an der Medizinischen Fakultät Carl Gustav Carus der Technischen Universität Dresden sowie als Wissenschaftlich-Technischer Bericht des Helmholtz-Zentrum Dresden-Rossendorf mit der Berichtsnummer **HZDR-044** veröffentlicht.

Kontaktdaten des Autors:

OncoRay – National Center for Radiation Research in Oncology
Medizinische Fakultät Carl Gustav Carus
Technische Universität Dresden

Fetscherstr. 74, PF 41
01307 Dresden
Tel.: +49 351 458-4123
Fax: +49 351 458-7311
kristin.stuetzer@oncoray.de
http://www.oncoray.de

2014

Herausgegeben vom

Helmholtz-Zentrum Dresden - Rossendorf

Bautzner Landstr. 400

01328 Dresden

Germany

Aus dem National Center for Radiation Research in Oncology – OncoRay
Sprecher: Herr Prof. Dr. Michael Baumann

Positron emission tomography for the dose monitoring of intra-fractionally moving targets in ion beam therapy

Dissertationsschrift

zur Erlangung des akademischen Grades
Doktor der Medizintechnologie
Doctor rerum medicinalium (Dr. rer. medic.)
vorgelegt
der Medizinischen Fakultät Carl Gustav Carus
der Technischen Universität Dresden

von

Dipl.-Phys. Kristin Stützer

aus Erfurt

Dresden 2013

1. Gutachter: Prof. Dr. Wolfgang Enghardt

2. Gutachter: Prof. Dr. Gerhard Kraft

Tag der mündlichen Prüfung: 4. Dezember 2013

gez.: ....
Vorsitzender der Promotionskommission
(Prof. Dr. Jörg van den Hoff)

Abstract

Ion beam therapy (IBT) is a promising treatment option in radiotherapy. The characteristic physical and biological properties of light ion beams allow for the delivery of highly tumour conformal dose distributions. Related to the sparing of surrounding healthy tissue and nearby organs at risk, it is feasible to escalate the dose in the tumour volume to reach higher tumour control and survival rates. Remarkable clinical outcome was achieved with IBT for radio-resistant, deep-seated, static and well fixated tumour entities. Presumably, more patients could benefit from the advantages of IBT if it would be available for more frequent tumour sites. Those located in the thorax and upper abdominal region are commonly subjected to intra-fractional, respiration related motion. Different motion compensated dose delivery techniques have been developed for active field shaping with scanned pencil beams and are at least available under experimental conditions at the GSI Helmholtzzentrum für Schwerionenforschung (GSI) in Darmstadt, Germany.

High standards for quality assurance are required in IBT to ensure a safe and precise dose application. Both underdosage in the tumour and overdosage in the normal tissue might endanger the treatment success. Since minor unexpected anatomical changes e.g. related to patient mispositioning, tumour shrinkage or tissue swelling could already lead to remarkable deviations between planned and delivered dose distribution, a valuable dose monitoring system is desired for IBT. So far, positron emission tomography (PET) is the only *in vivo*, *in situ* and non-invasive qualitative dose monitoring method applied under clinical conditions. It makes use of the tissue autoactivation by nuclear fragmentation reactions occurring along the beam path. Among others, β^+-emitting nuclides are generated and decay according to their half-life under the emission of a positron. The subsequent positron-electron annihilation creates two 511 keV photons which are emitted in opposite direction and can be detected as coincidence event by a dedicated PET scanner. The induced three-dimensional (3D) β^+-activity distribution in the patient can be reconstructed from the measured coincidences. Conclusions about the delivered dose distribution can be drawn indirectly from a comparison between two β^+-activity distributions: the measured one and an expected one generated by a Monte-Carlo simulation. This workflow has been proven to be valuable for the dose monitoring in IBT when it was applied for about 440 patients, mainly suffering from deep-seated head and neck tumours that have been treated with ^{12}C ions at GSI.

In the presence of intra-fractional target motion, the conventional 3D PET data processing will result in an inaccurate representation of the β^+-activity distribution in the patient. Four-dimensional, time-resolved (4D) reconstruction algorithms adapted to the special geometry of in-beam PET scanners allow to compensate for the motion related blurring artefacts. Within this thesis, a 4D maximum likelihood expectation maximization (MLEM) reconstruction algorithm has been implemented for the double-head scanner Bastei installed at GSI. The proper functionality of the algorithm and its superior performance in terms of suppressing motion related blurring artefacts compared to an already applied co-registration approach has been demonstrated by a comparative simulation study and by dedicated measurements

with moving radioactive sources and irradiated targets. Dedicated phantoms mainly made up of polymethyl methacrylate (PMMA) and a motion table for regular one-dimensional (1D) motion patterns have been designed and manufactured for the experiments. Furthermore, the general applicability of the 4D MLEM algorithm for more complex motion patterns has been demonstrated by the successful reduction of motion artefacts from a measurement with rotating (two-dimensional moving) radioactive sources. For 1D $\cos^2$ and $\cos^4$ motion, it has been clearly illustrated by systematic point source measurements that the motion influence can be better compensated with the same number of motion phases if amplitude-sorted instead of time-sorted phases are utilized. In any case, with an appropriate parameter selection to obtain a mean residual motion per phase of about half of the size of a PET crystal size, acceptable results have been achieved. Additionally, it has been validated that the 4D MLEM algorithm allows to reliably access the relevant parameters (particle range and lateral field position and gradients) for a dose verification in intra-fractionally moving targets even from the intrinsically low counting statistics of IBT-PET data.

To evaluate the measured β^+-activity distribution, it should be compared to a simulated one that is expected from the moving target irradiation. Thus, a 4D version of the simulation software is required. It has to emulate the generation of β^+-emitters under consideration of the intra-fractional motion, their decay at motion state dependent coordinates and to create listmode data streams from the simulated coincidences. Such a revised and extended version that has been compiled for the special geometry of the BASTEI PET scanner is presented within this thesis. The therapy control system provides information about the exact progress of the motion compensated dose delivery. This information and the intra-fractional target motion needs to be taken into account for simulating realistic β^+-activity distributions. A dedicated preclinical phantom simulation study has been performed to demonstrate the correct functionality of the 4D simulation program and the necessity of the additional, motion-related input parameters.

Different to the data evaluation for static targets, additional effort is required to avoid a potential misleading interpretation of the 4D measured and simulated β^+-activity distributions in the presence of deficient motion mitigation or data processing. It is presented that in the presence of treatment errors the results from the simulation might be in accordance to the measurement although the planned and delivered dose distribution are different. In contrast to that, deviations may occur between both distributions which are not related to anatomical changes but to deficient 4D data processing. Recommendations are given in this thesis to optimize the 4D IBT-PET workflow and to prevent the observer from a mis-interpretation of the dose monitoring data. In summary, the thesis contributes on a large scale to a potential future application of the IBT-PET monitoring for intra-fractionally moving target volumes by providing the required reconstruction and simulation algorithms. Systematic examinations with more realistic, multi-directional and irregular motion patterns are required for further improvements. For a final rating of the expectable benefit from a 4D IBT-PET dose monitoring, future investigations should include real treatment plans, breathing curves and 4D patient CT images.

Zusammenfassung

Die Ionenstrahltherapie (englisch: ion beam therapy, IBT) ist eine vielversprechende Behandlungsoption im Bereich der Strahlentherapie. Die charakteristischen physikalischen und biologischen Eigenschaften der Ionenstrahlen werden genutzt, um tumorkonformale Dosisverteilungen zu erzeugen. Die verbesserte Schonung des an den Tumor angrenzenden Normalgewebes und eventuell naheliegender Risikoorgane ermöglicht eine Dosissteigerung im Zielgebiet und somit potentiell höhere Tumorkontroll- und Überlebensraten. Für tiefliegende, gegenüber konventioneller Strahlung resistente, statische und gut fixierte Tumore wurden bereits beachtliche klinische Resultate erzielt. Wahrscheinlich könnten noch mehr Patienten von den Vorteilen der IBT profitieren, wenn diese auch für häufiger auftretende und intrafraktionell bewegliche Tumore uneingeschränkt nutzbar wäre. Verschiedene bewegungskompensierte Bestrahlungsmethoden wurden entwickelt und stehen zumindest unter experimentellen Bedingungen für weitere Untersuchungen am GSI Helmholtzzentrum für Schwerionenforschung (GSI) in Darmstadt zur Verfügung.

Um eine sichere und präzise Dosisapplikation in der IBT zu ermöglichen, werden hohe Anforderungen an die Qualitätssicherung gesetzt. Sowohl auftretende Überdosierungen im Normalgewebe als auch Unterdosierungen im Tumor können den Therapieerfolg gefährden. Da bereits kleine, unerwartete anatomische Veränderungen, zum Beispiel durch Fehlpositionierung des Patienten, Schrumpfung des Tumors oder Schwellungen, zu erheblichen Abweichungen zwischen geplanter und applizierter Dosisverteilung führen können, gibt es Bestrebungen, die applizierte Dosis zumindest qualitativ zu verifizieren. Die Positronen-Emissions-Tomografie (PET) ist derzeit die einzige, bereits klinisch erprobte Methode für ein *in vivo*, *in situ* und nicht-invasives qualitatives Dosismonitoring. Diese Methode ist im Stande, die Autoaktivierung des bestrahlten Gewebes zu erfassen, welche aufgrund von Kernfragmentierungsprozessen entlang des Strahlweges erzeugt wird. Unter anderem werden in diesen Reaktionen instabile Nuklide erzeugt, die entsprechend ihrer Halbwertszeit unter Emission eines Positrons zerfallen. Bei der anschließenden Positron-Elektron-Annihilation werden zwei 511 keV Photonen in entgegengesetzter Richtung emittiert und können mittels eines geeigneten PET-Scanners als Koinzidenzereignis detektiert werden. Die im Patienten induzierte dreidimensionale (3D) β^+-Aktivitätsverteilung kann aus den gemessenen Koinzidenzen rekonstruiert werden. Ein Vergleich der gemessenen mit einer erwarteten, mittels Monte-Carlo Simulation erzeugten β^+-Aktivitätsverteilung erlaubt es, Schlussfolgerungen über die tatsächlich im Patienten deponierte 3D Dosisverteilung zu ziehen. Diese Art der Datenauswertung wurde erfolgreich für die qualitative Dosisverifikation von über 440 Patienten eingesetzt, deren Tumore (vorwiegend im Kopf- und Halsbereich) an der GSI mit ^{12}C-Ionen bestrahlt wurden.

Bei der konventionellen 3D IBT-PET-Datenverarbeitung wird eine mögliche intrafraktionelle Bewegung des Zielgebietes nicht berücksichtigt und fehlerhaft rekonstruierte β^+-Aktivitätsverteilungen sind die Folge. Daher werden vierdimensionale, zeitaufgelöste (4D) Rekonstruktionsalgorithmen benötigt, die für die spezielle Geometrie eines in-beam PET-

Scanner adaptiert wurden und eine Kompensation der bewegungsinduzierten Artefakte ermöglichen. Im Rahmen der vorliegenden Arbeit wurde für den an der GSI installierten Doppelkopf-PET-Scanner BASTEI ein 4D Maximum-Likelihood-Expectation-Maximization (MLEM) Algorithmus implementiert. Die Funktionsfähigkeit des Algorithmus sowie dessen verbesserte Reduktion von Bewegungsartefakten im Vergleich zu einem bereits vorhandenen Koregistrierungsansatz wurde anhand verschiedener Messungen mit bewegten radioaktiven Quellen und bestrahlten Phantomen sowie einer vergleichenden Simulationsstudie dargelegt. Für die Experimente wurden entsprechende Phantomgeometrien (zumeist aus Polymethylmethacrylat (PMMA)) sowie ein Bewegungstisch für reguläre eindimensionale (1D) Bewegungsmuster entworfen und gefertigt. Zudem wurde durch die erfolgreiche, quasi-statische und nahezu artefaktfreie Rekonstruktion einer rotierenden und sich damit zweidimensional bewegenden Aktivitätsverteilung die prinzipielle Anwendbarkeit des 4D MLEM Algorithmus für komplexere Bewegungsmuster gezeigt. Systematische Punktquellenmessungen mit 1D $\cos^2$- und $\cos^4$-förmigen Bewegungsmustern haben deutlich gemacht, dass der Bewegungseinfluss mit der gleichen Anzahl an Bewegungsphasen besser kompensiert werden kann, wenn die Bewegungsphasen entsprechend der Bewegungsamplitude anstelle der -phase unterteilt sind. In jedem Fall können aber zufriedenstellende Rekonstruktionsergebnisse erzielt werden, wenn durch geeignete Parameterwahl eine mittlere Restbewegung pro Bewegungsphase von maximal etwa der halben Größe eines Detektorkristalls eingestellt wird. Durch weitere Experimente konnte gezeigt werden, dass nach der Rekonstruktion mit dem 4D MLEM Algorithmus die relevanten Parameter für die qualitative Dosisverifikation (Teilchenreichweite, laterale Feldposition und -gradienten) zuverlässig erfasst werden können. Dies ist auch dann der Fall, wenn nur eine verminderte Anzahl an Koinzidenzereignissen, so wie sie unter klinischen Bedingungen zu erwarten ist, für die Auswertung verwendet wird.

Um die gemessene β^+-Aktivitätsverteilung besser zu beurteilen, sollte sie mit einer simulierten, für die bewegungskompensierte Bestrahlung erwarteten Verteilung verglichen werden und es bedarf deshalb einer 4D Version der Simulationssoftware. Diese muss die Erzeugung sowie den Zerfall der Positronenemitter unter Berücksichtigung der intrafraktionellen Bewegung simulieren und aus den gültigen Koinzidenzereignissen Listmode-Datensätze erstellen. Eine derart überarbeitet Version des Simulationsprogramms wurde für den BASTEI PET-Scanner erstellt und wird in dieser Arbeit vorgestellt. Informationen über den exakten Verlauf der bewegungskompensierten Bestrahlung werden durch das Therapiekontrollsystem geliefert. Diese Informationen sowie die intrafraktionelle Bewegung werden in die Simulation realistischer β^+-Aktivitätsverteilungen bzw. der zugehörigen Listmode-Datensätze einbezogen. Anhand einer präklinischen Phantom-Simulationsstudie wurde die korrekte Funktionsweise des Simulationsprogramms sowie die Notwendigkeit der zusätzlichen Parameter gezeigt.

Im Gegensatz zur Datenauswertung für statische Zielvolumina bedarf es bei intrafraktioneller Bewegung gegebenenfalls zusätzlichen Aufwand, um eine Fehlinterpretation aus dem Vergleich der gemessenen und simulierten β^+-Aktivitätsverteilung zu vermeiden. In der vorliegenden Arbeit wird beispielhaft gezeigt, dass sich bei fehlerhafter Bewegungskompensation die gemessene und simulierte β^+-Aktivitätsverteilung einander ähneln können, obwohl die applizierte Dosisverteilung deutlich von der geplanten abweicht. Im Gegensatz dazu können auch Abweichungen zwischen Messung und Simulation auftreten, die nicht auf anatomische Veränderungen, sondern auf eine ungenaue 4D Datenverarbeitung zurückzuführen sind. Es werden Vorschläge unterbreitet, um den Prozess der 4D IBT-PET Datenauswertung zu optimieren und somit Fehlinterpretationen zu vermeiden.

Die vorliegende Dissertationsschrift enthält durch die Bereitstellung der benötigten 4D Rekonstruktions- und Simulationsprogramme grundlegende Arbeiten für eine mögliche zukünftige Anwendung der 4D IBT-PET als qualitatives Dosismonitoring bei intrafraktionell bewegten Zielvolumina. Für weitere Verbesserungen des Verfahrens sind zusätzliche systematische Betrachtungen mit realistischeren, mehrdimensionalen und unregelmäßigen Bewegungsmustern notwendig. Zukünftige Untersuchungen sollten außerdem echte Bestrahlungspläne, Atemkurven sowie 4D Patienten-CT-Daten einschließen, um den erwartbaren Nutzen eines 4D IBT-PET Dosismonitorings besser abschätzen zu können.

Contents

List of Figures

List of Tables

List of abbreviations

1D	One-dimensional
2D	Two-dimensional
3D	Three-dimensional
4D	Four-dimensional, time-resolved
BASTEI	β^+-activity measurement at the therapy with energetic ions
BEV	Beam's eye view
BGO	Bismuth germanate
CT	X-ray computed tomography
DKFZ	German Cancer Research Center
DNA	Deoxyribonucleic acid
DOI	Depth of interaction
FFT	Fast Fourier transformation
FOV	Field of view
FWHM	Full width at half maximum
FWTM	Full width at tenth maximum
FZR	Forschungszentrum Rossendorf
GSI	GSI Helmholtzzentrum für Schwerionenforschung
HIMAC	Heavy-ion medical accelerator in Chiba
HIT	Heidelberg Ion-Beam Therapy Center
HU	Hounsfield unit
HZDR	Helmholtz-Zentrum Dresden-Rossendorf
IARC	International Agency for Research in Cancer
IBT	Ion beam therapy
IC	Ionization chamber
ICRU	International Commision on Radiation Units and Measurements
IMPT	Intensity modulated particle therapy
IMRT	Intensity modulated radiotherapy
LCR	Local contrast recovery
LET	Linear energy transfer
LOR	Line of response
LUT	Look-up table
MLEM	Maximum likelihood expectation maximization
MRI	Magnetic resonance imaging
MWPC	Multi-wire proportional chamber

NEMA	National Electrical Manufacturers Association
NRMSE	Normalized root mean square error
NSCLC	Non-small cell lung cancer
OAR	Organ at risk
PE	Polyethylene. $(C_2H_4)_n$
PET	Positron emission tomography
PMMA	Polymethyl methacrylate. $(C_5H_8O_2)_n$
PMT	Photomultiplier tube
PSI	Paul Scherrer Institute
RBE	Relative biological effectiveness
SNR	Signal-to-noise ratio
SOBP	Spread-out Bragg peak
TOF	Time-of-flight
UKL-HD	Heidelberg University Hospital
US	Ultrasound
WEPL	Water equivalent pathlength

Frustration, although quite painful at times,
is a very positive and essential part of success.
Bo Bennett

1 Motivation

Contents

1.1 Potential and obstacles of ion beam therapy

Cancer diseases are the leading cause of death worldwide. A total number of 7.6 million cancer related deaths in 2008 was estimated by the World Health Organization and its cancer research agency, the International Agency for Research in Cancer (IARC) (Ferlay *et al.* 2010a). Besides individual genetic factors and different physical, chemical and biological carcinogens, the age is a fundamental risk factor for cancer incidence. Due to population growth and ageing, a global burden of 22.3 million new cancer incidences in 2030 is predicted compared with 12.7 million incidences in 2008 (Bray *et al.* 2012). Figure 1.1 displays the absolute and percentage distribution of the most frequent cancer sites for incidence and mortality in 2008. Lung cancer is the most common cancer and has one of the highest case fatality rates (ratio of mortality to incidences) of about 86%. Only liver cancer has an even higher fatality rate of about 93%. Improving the treatment options for these frequently occurring cancers could prevent many deaths.

Conventional curative treatment strategies include surgery, radiotherapy and systemic therapy or combinations thereof and have to be selected individually. If possible, surgery is the

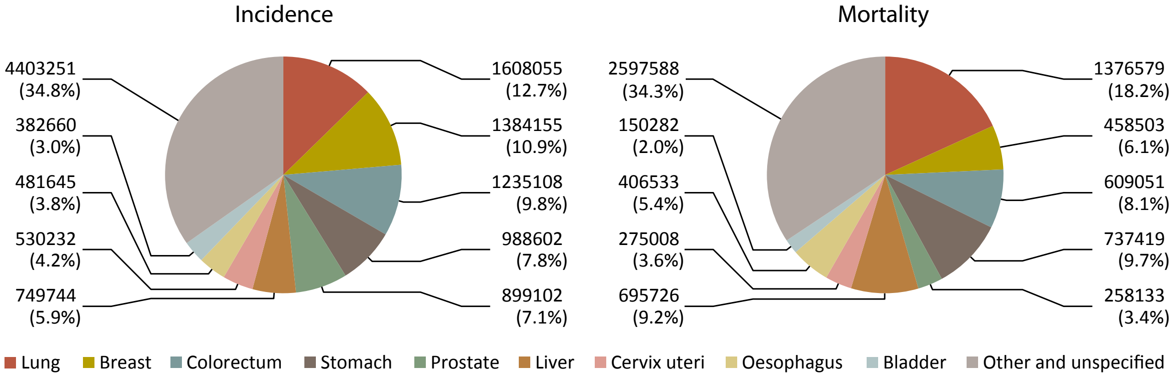

Figure 1.1: Estimated cancer incidence and mortality worldwide in 2008 from data provided by the GLOBOCAN databank of the IARC (Ferlay *et al.* 2010b). The pie charts show the absolute and percentage distribution of the most frequent cancers (exclusive non-melanoma skin cancer) summarized for both sexes.

method of choice for primary treatment of early stage localized cancer. For inoperable patients, radiotherapy may often be an alternative. Continuous improvements in radiotherapy result in better local tumour control and higher survival rates. Evidence for improved outcome by the application of e.g. new treatment planning algorithms and beam delivery techniques, the combination of radiotherapy with chemotherapeutic drugs or revised treatment schedules and prescribed doses is obtained by the evaluation of clinical trials. For non-small cell lung cancer (NSCLC) which accounts for the majority (about 80%) of all lung cancers, Partridge *et al.* (2011) reviewed 24 published clinical trials and found a clear tumour dose-response relation. Therefore, dose escalation studies are suggested for treating NSCLC. Also for liver metastasis, high-dose radiotherapy seems to be effective (Rusthoven *et al.* 2009).

To deliver higher doses, the treatment field should be limited to the tumour volume and the surrounding normal tissue, and nearby organs at risk (OARs) must be prevented from additional dose to avoid severe acute complications and late effects. Today, several external radiotherapy modalities are available beside the conventional three-dimensional (3D) conformal radiotherapy. For instance, in static and rotational intensity modulated radiotherapy (IMRT) the dose distribution is adjusted to the 3D tumour shape by modulating the beam intensity when irradiating from different directions. Stereotactic radiotherapy and radiosurgery use high doses delivered in one or only a few fractions for non-invasive tumour ablation and thus require improved delivery precision. Another approach is the ion beam therapy (IBT) utilizing proton beams or beams of other light ions like helium, carbon or oxygen. From a physical point of view, ion beams have the advantage to generate steep dose gradients, in particular in the beam direction as illustrated for ^{12}C ions in figure 1.2. The inverse depth-dose

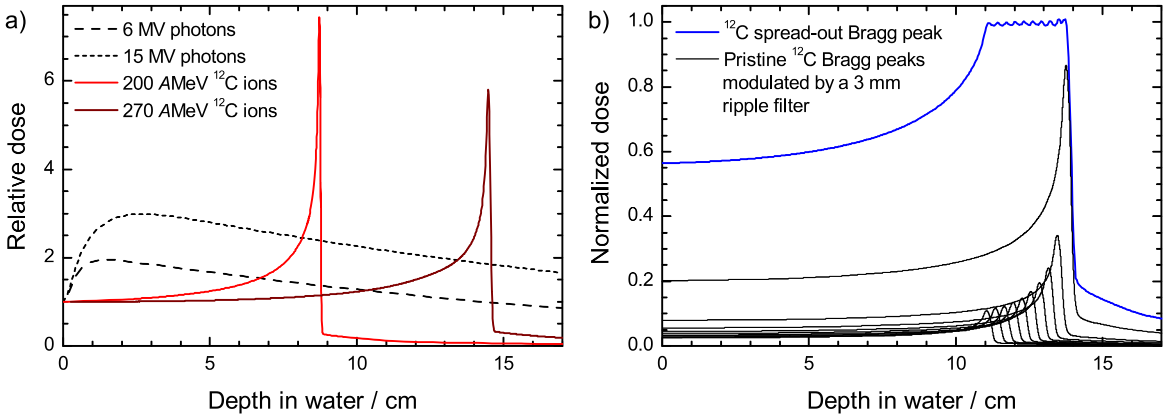

Figure 1.2: Comparison of depth-dose curves in water (a) for 6 MV and 15 MV photons provided by Hoinkis and Tillner (2013) and for pristine ^{12}C ions beams of 200 *A*MeV and 270 *A*MeV taken from Schardt *et al.* (2010), both with courtesy of the authors. The curves are scaled to the same dose in the entrance channel. The superposition of single Bragg peaks with suitable energies leads to the formation of a spread-out Bragg peak (SOBP) at a defined depth (b). The intensities of ten ^{12}C beams with energy differences of about 3.5 *A*MeV had been optimized by the treatment planning program TRiP (Krämer *et al.* 2000) to generate a deep-seated high dose plateau (the SOBP) of about 27 mm width (with courtesy of C. Bert).

profiles of mono-energetic ions possess a characteristic narrow high-dose region, the Bragg peak, and a rapid distal fall-off at the end of the ion range. Therefore, ion beam plans allow for same homogeneous dose coverage of the tumour volume as e.g. IMRT photon plans do, but they provide a better sparing of healthy tissue and nearby radiosensitive structures by utilizing only a few treatment fields. From a radiobiological point of view, the potential benefit from the increased relative biological effectiveness (RBE) is an additional argument for the application of ions, especially those heavier than protons. Their high linear energy transfer (LET) causes a more effective radiation damage to the tissue and helps to reduce radioresistance due to hypoxia or poor reoxygenation in some tumours.

Several studies and clinical trials (Schulz-Ertner and Tsujii 2007; Jensen *et al.* 2012; Ogino 2012) provide sound evidence that carbon ion and proton radiotherapy yield better outcome than photon radiotherapy for several tumour entities in terms of reaching higher local control and overall survival rates as well as inducing less side effects. Uveal melanomas, specific tumours of the skull base and pediatric tumours (Combs *et al.* 2009) are for instance considered as clear indications for IBT. Promising outcome has also been reported for early stage lung cancer (Miyamoto *et al.* 2003; Nihei *et al.* 2006) and hepatocellular carcinoma (Kato *et al.* 2004; Chiba *et al.* 2005). Although IBT might offer such a high clinical potential, only 37 IBT facilities were operating worldwide at the end of 2011 (PTCOG 2012) but with tendency to rise. The majority, namely 33 of the 37 facilities offered proton beams and only 6 of them were capable to treat patients with carbon ion beams.

Besides the clinical aspects, the benefit of IBT has to be validated taking also economical and safety issues into account. The ongoing discussion about the cost-effectiveness of particle therapy lacks in a general consensus (Lodge *et al.* 2007; Pijls-Johannesma *et al.* 2008). For lung tumours, Peeters *et al.* (2010) stated a relatively small cost difference between particle and photon therapies and predicted reduced costs for hypofractionated schedules for which excellent results have already been achieved with carbon ions (Miyamoto *et al.* 2007). Other obstacles for a better establishment of IBT are technical challenges related to ion range uncertainties. The depth of the the Bragg peak position in the patient is well tunable by the initial ion energy but is strongly affected by the composition of the traversed tissue. Thus, the patient-specific tissue densities must seriously be taken into account when selecting the required beam energies for creating a treatment plan where the spread-out Bragg peak (SOBP) position should match exactly with the tumour depth. Uncertainties in the finally administered dose distribution in the patient may originate systematically or coincidentally from imaging, dose calculation, patient setup, changed patient constitution and beam delivery. For instance, the final treatment plan is in some degree subjected to artefacts in the planning X-ray computed tomography (CT) image, the calibration between Hounsfield units (HUs) in the CT image and stopping power (Schaffner and Pedroni 1998; Rietzel *et al.* 2007), the treatment planning algorithm itself (Endo *et al.* 1996; Krämer *et al.* 2000; Paganetti *et al.* 2008) and the variability of its required input parameters. Additionally, the exact verification of treatment plans in water phantoms is limited by the accuracy of the dose measurement mostly performed with ionization chambers that quantify doses with an estimated standard uncertainty of about 2% for protons and about 3% for other ions (IAEA 2000). Commissioning errors as well as limited precision of patient positioning devices and of beam delivery components like energy degraders, patient-specific compensators or movable beam nozzles introduce further inaccuracy. Thus, high standards of quality assurance are exceedingly required in IBT. These include the compilation of robust treatment plans, the initial commissioning and daily, weekly or otherwise scheduled consistency checks of all hard- and software components (Jäkel *et al.* 2000; Karger *et al.* 2000).

Beside the technical issues, the influence of the patient itself has to be considered. Including the effects of non-tissue components like metal implants, prostheses or inserted fiducial markers for range calculations is quite difficult (Jäkel and Reiss 2007). Basically, variable tissue geometry between imaging for treatment planning and each fraction of radiotherapy application might induce density changes within the treatment field and thus lead to a range shifting in IBT. This inter-fraction variability is e.g. related to patient weight loss, tissue swelling and secretion formation due to inflammatory processes, different filling of the gastrointestinal tract for lesions in the abdominal region as well as tumour shrinkage as a direct treatment response. For fractionated photon radiotherapy of NSCLC, Fox *et al.* (2009) reported individual tumour shrinkage between 0.2% and 81.6% of the initially defined volume after the application of 50 Gy within 25 daily fractions.

All these circumstances justify the demand of *in situ* dose verification systems for IBT since severe overdosage in healthy tissue and underdosage in the tumour volume might already be caused by slight density deviations within the beam path. Contrary to photon radiotherapy, a portal imaging technique that utilizes the therapeutic ion beam is not feasible since the ions are absorbed in the patient. Ions with higher energy than used for the treatment itself might be used for radiography imaging if the tissue has a limited thickness and ions will therefore be transmitted (Rinaldi *et al.* 2013). At the Paul Scherrer Institute (PSI) in Villigen, Switzerland a new concept has been brought into experimental operation. A 150 kV X-ray fluoroscopy system mounted at Gantry 2 takes images in beam's eye view (BEV) direction, either prior to the treatment for position verification or synchronized with beam delivery to control the irradiation (Safai *et al.* 2012). Other monitoring techniques rely on secondary radiation emerging from the products of nuclear reactions between a fraction of the incident ions and tissue nuclei. Within a femto- to picosecond time frame after such reactions took place, prompt γ-rays are emitted from excited nuclei. Different detector concepts like slit (Testa *et al.* 2009; Smeets *et al.* 2012) or Compton (Kormoll *et al.* 2011; Roellinghoff *et al.* 2011; Kurosawa *et al.* 2012) cameras are still under investigation for the direct assessment of the ion range. An adequate handling, processing and evaluation of these data is pursued for a real-time monitoring. Nowadays, positron emission tomography (PET) is the only dose monitoring technique for IBT that has already been successfully applied under clinical conditions (Hishikawa *et al.* 2002; Enghardt *et al.* 2004b; Parodi *et al.* 2007c; Hsi *et al.* 2009; Nishio *et al.* 2010). Positron emitters are created by nuclear fragmentation reactions as a side effect during the irradiation with stable ion beams (Enghardt *et al.* 1992). Typically, the relevant radioactive nuclides decay according to their specific half-lives within seconds to tens of minutes into stable nuclides under the emission of a positron. Subsequently emitted annihilation photons can be detected as coincidence events by a dedicated PET scanner and thus allow for the reproduction of the induced β^+-activity in the body. However, the finite half-lives and the time-consuming reconstruction impede a real-time dose validation. Only relative changes of tumour and body shape during fractionated therapy can be identified by a simple comparison of β^+-activity distributions from different fractions (Nishio *et al.* 2010). A more extensive analysis includes the precalculation of an anticipated β^+-activity (Pönisch *et al.* 2004; Parodi *et al.* 2007a) and a comparison with the measurement. Consequently, conclusions can be drawn about potentially dislocated dose portions in the patient and an intervention before the next fraction is possible.

Between 1997 and 2008, a pilot project was carried out by the German Cancer Research Center (DKFZ), the Heidelberg University Hospital (UKL-HD), the GSI Helmholtzzentrum für Schwerionenforschung (GSI) and the Forschungszentrum Rossendorf (FZR) (today Helmholtz-Zentrum Dresden-Rossendorf (HZDR)). About 440 patients mainly suffering from head and neck cancer have been treated with ^{12}C ions at a medical beamline installed at GSI in Darmstadt (Eickhoff *et al.* 2009). The HZDR group monitored for all patients the dose delivery of each fraction by means of a double-head PET scanner which was directly integrated into the treatment site (Enghardt *et al.* 2004a). Dedicated algorithms for the reconstruction of β^+-activity distributions and the simulation of expected PET data sets had been developed and were successfully applied.

1.2 Objectives of the thesis

IBT has demonstrated promising clinical results due to its tumour conformal dose distribution. The treatment precision for tumour entities in the thoracic or upper abdominal region like lung, liver or pancreatic tumours suffers from intra-fractional motion, mainly related to respiration. The concept of traditional photon radiotherapy to add safety margins in the treatment plan to cover a predicted motion amplitude is inappropriate for IBT with actively scanned ion beams. Thus, four-dimensional, time-resolved (4D) treatment planning and new motion-mitigated beam delivery techniques involving real-time target localisation and adaptation of the irradiation have been developed. The complexity of these techniques and the large intra-fractional density fluctuations in particular within the thorax region increase the risk of a potentially inaccurate dose deposition and demands control.

The IBT-PET dose monitoring has shown benefit when it was applied for static and well-fixated tumour entities. It has not been employed for intra-fractionally moving targets yet, including the reconstruction and simulation of data sets. If it would be applied in its approved status for studying activated moving structures, precise conclusions about the delivered dose would be contradictable due to motion related blurring artefacts in the reconstructed PET images from measured data sets. The reason therefor is the transportation of generated β^+-emitters until their decay together with the moving anatomical structures. In general, although the β^+-emitters might be placed all the time at the position where they have been created within the moving target, they will decay at another coordinate relative to the fixed PET scanner coordinate system. Annihilation photons will accordingly be registered by other detector elements and thus distort the information in the measured data set. To compensate the induced artefacts, motion information has to be involved when reconstructing β^+-activity distributions. Furthermore, the motion and related beam adaptation has to be modelled when simulating IBT-PET data sets. Only then, simulated and measured data sets may contain comparable information.

Within this thesis, three main issues are addressed related to the revision of the IBT-PET dose monitoring for a potential application with moving targets. After some basics about particle therapy, moving targets and IBT-PET the following topics will be discussed:

- Reconstruction of IBT-PET data under consideration of target motion:
  An implemented time-resolved reconstruction algorithm is presented. Its performance is evaluated by means of a simulation study, systematic off-line experiments and dedicated phantom irradiation. The applicability of the reconstruction method for different motion mitigated beam deliveries is also demonstrated by phantom experiments.

- Simulation of IBT-PET data sets taking into account the target motion, adaptive beam delivery and variable decay positions of the β^+-emitters:
  The revised simulation software for generating expected IBT-PET data sets from moving target structures is explained in detail. The simulation result is utilized for the rating of the measured β^+-activity distribution and thus is an important part of the whole IBT-PET monitoring. The functionality of the 4D simulation is exemplified by means of a selected experiment scenario.

- Drawing conclusions from the comparison between measured and simulated 4D IBT-PET images in the presence of deficient motion mitigation or data synchronization:
  Beside the identification of usual properties like correct particle range, field position and local deviations, attention has to be turned to the availability of possible treatment errors related to breakdown or malfunction of the motion compensation. Systematic experiments are presented which demonstrate the limitation of the dose verification for moving targets utilizing the hitherto existing workflow. Related recommendations for a correct interpretation of the 4D IBT-PET data are given.

2 Ion beam therapy and moving targets

Contents

Robert Wilson raised the idea of using fast protons or heavier ions for radiotherapy in 1946 (Wilson 1946). The first medical application of proton beams succeeded 1954 at the Lawrence Berkeley Laboratories and 1957 in Uppsala. Others followed in Havard, Dubna, Moscow, Loma Linda, Massachusettes, Chiba, Tsukuba and Villigen, just to mention a few. Patient treatment with heavier ions started 1975 at the Lawrence Berkeley Laboratory using helium and neon beams. Finally, carbon ions prevailed and are now available for therapy in Chiba, Hyogo, Gumna (all in Japan), Lanzhou (China), Pavia (Italy) and Heidelberg (Germany) (PTCOG 2012). At the latter, IBT with oxygen is also planned for the future (Kurz *et al.* 2012). Moreover, even mixed beam irradiation scenarios had already been considered (Kanai *et al.* 1997).

Until today, almost 10^5 patients in total have been treated with ion beams worldwide, more than 80% of them with protons and nearly 10% with carbon ions (PTCOG 2012). A limited number of patients underwent a treatment of lesions in the lung or liver. Clinical studies at the facilities in Loma Linda (USA), Tsukuba, Kashiwa, Hyogo and Chiba (all in Japan) have reported promising outcome for these patients (Pijls-Johannesma *et al.* 2010; Skinner *et al.* 2011; Tsujii and Kamada 2012). However, the potential of ion beam therapy might not have been fully exploited for these patients, due to the passive beam shaping mostly in combination with limited motion compensation and missing dose monitoring.

2.1 Physical and biological properties of ion beams

Wilson's suggestion for applying ion beams in radiotherapy was based on the specific ionization of ion beams within tissue, their reduced straggling compared to electrons and the previously investigated dependency of biological damage from ionization density. Within this section, the physical and biological rationale will be presented that made IBT becoming a serious treatment modality in radiotherapy.

2.1.1 Dose deposition

When high energetic charged particles pass through matter, they are capable to produce ionization, i.e. to liberate bound electrons of the medium by inelastic collisions and thus to loose gradually their energy. When the particles have slowed down to an energy below a certain cutoff energy, ionization becomes impossible and the particles are considered as non-ionizing radiation. The remaining energy near the end of the particle range is spent to other processes like excitation and elastic scattering. The elastic collisions between the incident ions and the atoms of the material are mediated by their Coulomb interaction. A third process that might lead to energy loss is the emission of bremsstrahlung in the electric field of the atomic nuclei or electrons. For heavy, charged particles with a mass $M > m_e$ (heavier than electrons), this process can be neglected for therapy relevant energies in comparison to the ionization processes, since the intensity of the bremsstrahlung is in classical approximation proportional to the square of the acceleration in the electric field and therefore $\sim M^{-2}$.

Stopping power

The mean energy E that is lost within a distance l is described by the stopping power S. This quantity depends on the type of the charged particles, their energy and the material where the stopping takes place. To reduce the dependence on the density of the material the mass stopping power

$$\frac{S}{\rho} = \frac{1}{\rho}\frac{\mathrm{d}E}{\mathrm{d}l} \qquad \left[\frac{S}{\rho}\right] = \mathrm{J\,m^2\,kg^{-1}} \tag{2.1}$$

is considered (ICRU 2011). This total mass stopping power is composed by the different channels of energy loss between the charges of the projectiles and the target nuclei and can be expressed as

$$\frac{S}{\rho} = \frac{1}{\rho}S_{\mathrm{el}} + \frac{1}{\rho}S_{\mathrm{nuc}} + \frac{1}{\rho}S_{\mathrm{rad}}, \tag{2.2}$$

where S_{el} denotes the electronic stopping power related to inelastic interactions with the electrons in the material and resulting in ionization or excitation of the atoms, S_{nuc} the nuclear stopping power related to elastic Coulomb interaction and S_{rad} the radiative stopping power related to the emission of bremsstrahlung which is negligible in the following considerations.

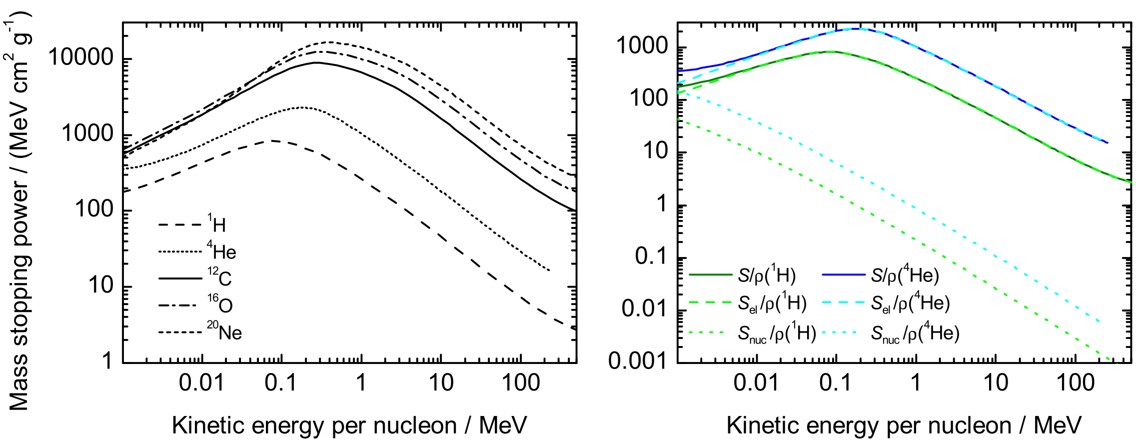

Figure 2.1: Total mass stopping power of liquid water in dependence of the kinetic energy per nucleon for ions already been used or planned to be used in IBT (left) and the electronic S_{el}/ρ and nuclear mass stopping ratio S_{nuc}/ρ exemplary shown for protons (^{1}H) an helium ions (^{4}He) (right). Data for protons and helium ions originate from the online database of the National Institute of Standards and Technology (NIST) (Berger *et al.* 2005) with values according to the International Commision on Radiation Units and Measurements (ICRU 1993a). Data for heavier ions (^{12}C, ^{16}O, ^{20}Ne) are taken from Paul and Schinner (2003).

Figure 2.1 shows the total mass stopping power of water for ions that had been (^{4}He, ^{20}Ne), are (^{1}H, ^{12}C) or will soon be (^{16}O) applied in IBT. From the detailed presentation for protons and helium ions, it is clearly visible that the total mass stopping power is dominated by the electronic stopping power in a wide energy range relevant for IBT.

Electronic energy loss

The energy loss in single collisions due to the electronic interaction was the first time described in a classical approximation by Bethe (1930). For moderately relativistic charged particles (except electrons) with mass M, velocity v and charge $Z_{\mathrm{eff}} \cdot e$, the mean energy loss in material is given by the Bethe formula (Beringer *et al.* 2012)

$$-\frac{\mathrm{d}E}{\mathrm{d}l} = 4\pi N_{\mathrm{A}} r_e^2 m_e c^2 Z_{\mathrm{eff}}^2 \frac{Z_{\mathrm{m}}}{A_{\mathrm{m}}} \frac{1}{\beta^2} \left[\frac{1}{2} \ln \frac{2 m_e c^2 \gamma^2 T_{\mathrm{max}}}{I^2} - \beta^2 - \frac{\delta(\beta\gamma)}{2} - \frac{C}{Z_{\mathrm{m}}} \right] \tag{2.3}$$

with variables as explained in table 2.1. Material related influence is considered by the term $Z_{\mathrm{m}}/A_{\mathrm{m}}$ which defines the electron density n_e of the material and by the mean excitation energy I which is e.g. given for different materials by the International Commision on Radiation Units and Measurements (ICRU) (ICRU 1984). Without the correction terms δ and C, (2.3) holds true in a wide range of particle velocity ($\beta \gtrsim 0.1$). The energy loss in a given material is mainly a function of the particle charge ($\sim Z_{\mathrm{eff}}^2$) and its velocity (β). An important relation is the increase of energy loss per unit length when the velocity and hence β decreases continuously as the particle passes through the medium. Only a minor dependence on the particle mass M is given by T_{max} which is the maximum kinetic energy transfer to a free electron within a single collision. This quantity is calculated and approximated for heavy

Table 2.1: Overview and definition of variables used in Bethe formula (2.3).

Symbol	Definition	Unit or Value
$m_e c^2$	Electron mass $\cdot c^2$	$0.510\,998\,918(44)$ MeV
N_A	Avogadro's number	$6.022\,1415(10) \times 10^{23}\,\mathrm{mol}^{-1}$
r_e	Classical electron radius	$2.817\,940\,325(28)$ fm
$Z_\mathrm{eff} \cdot e$	Effective charge of incident particle	
Z_m	Atomic number of stopping medium	
A_m	Atomic mass of stopping medium	$\mathrm{g\,mol}^{-1}$
β	v/c	
γ	Lorentz factor $1/\sqrt{1-\beta^2}$	
I	Mean excitation energy of stopping medium	eV
T_max	Maximum energy transfer in single collision	eV
$\delta(\beta\gamma)$	Density effect correction to ionization energy loss	
C	Shell correction for small energies	

particles with ($M \gg m_e$) as

$$T_\mathrm{max} = \frac{2m_e c^2 \beta^2 \gamma^2}{1 + 2\gamma m_e/M + (m_e/M)^2} \approx 2m_e c^2 \beta^2 \gamma^2. \tag{2.4}$$

For very high as well as low energies the correction terms must be considered. At high energies, the electric field of the particle gets deformed and extended. The density effect correction δ accounts for a limited field extension due to polarization effects of the medium which results in a shielding of distant electrons and consequently, a smaller energy loss by collisions with these electrons. The shielding due to polarization depends strongly on the density of the medium. δ is normally computed with the parametrization after Sternheimer and Peierls (1971). The fitting formula and fitted parameters for several media are for instance compiled by Sternheimer *et al.* (1984). For energy loss at low energies, the shell correction C/Z_m accounts for the atomic binding of electrons which cannot be considered as static anymore as it is done for higher energies. A discussion of low-energy corrections can be found in the ICRU report 49 (ICRU 1993a). With properly included corrections, (2.3) is accurate within 1% for $\beta \gtrsim 0.05$ or protons with energies about 1 MeV (Beringer *et al.* 2012).

Particle range and straggling

Ion beams possess a well-defined range in material. It is defined as the traversed distance until the total kinetic energy has been transferred to the medium and the particle is at rest. The mean particle range R is calculated by the integration of the reciprocal stopping power over energy (between initial kinetic energy $E_\mathrm{kin,0}$ and 0) or over the velocity (between the initial velocity v_0 and 0)

$$R = \int_0^{E_\mathrm{kin,0}} \frac{1}{\frac{\mathrm{d}E}{\mathrm{d}l}} \mathrm{d}E = \int_0^{v_0} \frac{\mathrm{d}l}{\mathrm{d}E} \frac{\mathrm{d}E}{\mathrm{d}v} \mathrm{d}v. \tag{2.5}$$

Considering the stopping power of electronic interactions described in (2.3) and identifying the energy E proportional to particle mass and thus proportional to the number of nucleons A in the particle ($E = A \cdot f(v)$), the following correlation is evident

$$R(E_{\mathrm{kin},0}) \sim \frac{A}{Z^2}. \tag{2.6}$$

Since the interactions are of statistical nature with a very high number of ion-electron collisions and since large angle scattering is unlikely for ions, only a slight straggling in range is observable between same particles with same initial kinetic energy $E_{\mathrm{kin},0}$. The angular spread of the Coulomb scattering, relevant near the end of the particle range, depends heavily on the mass of the projectiles. Consequently, lighter charged particles (protons) are more likely to undergo large-angle scattering and thus show a more pronounced straggling in lateral dimension and also in range than heavier ions like carbon. For particles with mass number A and charge number Z having a mean range R in water (given in cm), Tobias *et al.* (1980) parametrized the uncertainties considered as Gaussians by giving the standard deviation for range straggling σ_x and lateral straggling σ_y as

$$\sigma_x = 0.012\frac{R^{0.951}}{A^{0.5}} \qquad \sigma_y = 0.0294\frac{R^{0.896}}{Z^{0.207}A^{0.396}}. \tag{2.7}$$

To give a number, at a range of 20 cm in water which is in first order an acceptable approximation for tissue, one obtains $\sigma_x = 0.6\,\mathrm{mm}$ and $\sigma_y = 1.1\,\mathrm{mm}$ for carbon ions ($A = 12, Z = 6$) and $\sigma_x = 2.1\,\mathrm{mm}$ and $\sigma_y = 4.3\,\mathrm{mm}$ for protons ($A = Z = 1$), respectively.

Linear energy transfer (LET) and dose

Besides the stopping power and the finite range, the LET of ion beams is an often referred quantity. It defines for a certain material and a given type and energy of particle the mean energy loss by electronic stopping within a certain distance. Thus, it is (except the sign) equivalent to the mean energy loss described by (2.3). For dosimetric considerations the deposited energy near the particle track is relevant. The released secondary electrons themselves may transfer their kinetic energy by further ionisation of surrounding atoms. So-called Δ-electrons with higher kinetic energy may leave the considered volume. Therefore, the restricted linear energy transfer is defined as

$$LET_\Delta = S_{\mathrm{el}} - \frac{\mathrm{d}E_{\mathrm{ke},\Delta}}{\mathrm{d}l}, \tag{2.8}$$

where $E_{\mathrm{ke},\Delta}$ expresses the mean sum of kinetic energies greater than Δ from all released secondary electrons (ICRU 2011). According to the LET value, one differentiates between low LET radiation (LET $\lesssim 3.5\,\mathrm{keV}/\mu\mathrm{m}$) like electrons, γ- or X-rays and high LET radiation such as neutrons and low-energetic ions. The low LET radiation creates a diffuse and low dense pattern of ionization, but for high LET radiation a substantial number of ionization events occur within a short part of a particle track (cp. figure 2.2). The LET value has to

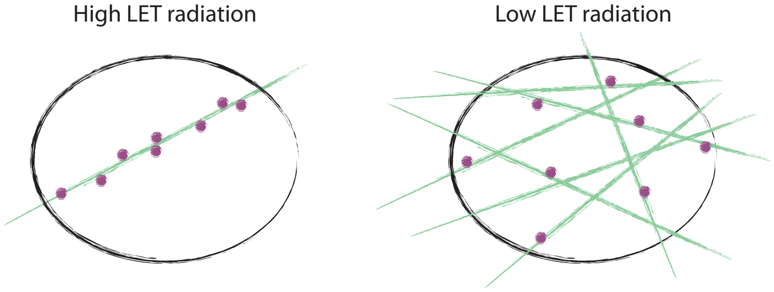

Figure 2.2: Schematic representation of ionization density in a restricted volume (black) for high and low LET radiation. In both examples the same number of ionization events (purple) are produced that illustrate the same amount of deposited dose. In contrast to the locally dense ionization along the particle track (green) of high LET radiation an equally distributed pattern of ionization is generated by the low LET radiation.

be clearly distinguished from the dose which is the clinically prescribed value that has to be matched when computing treatment plans in radiotherapy. The same amount of dose can be delivered with high or low LET radiation. The absorbed dose D is defined as the mean imparted energy to matter of mass m

$$D = \frac{\mathrm{d}E}{\mathrm{d}m} \qquad [D] = \mathrm{J\,kg^{-1}} = \mathrm{Gy}. \tag{2.9}$$

A combination of the information about energy dependent stopping power and dose for high LET ion beams results in the characteristic depth-dose profiles for homogeneous matter as already shown for ^{12}C ions impinging on water in figure 1.2. The often called inverse profiles of ion beams possess a flat plateau region in the entrance channel where only less dose is deposited due to low LET, if particles are not too heavy. When the projectiles have slowed down the LET increases and a sharp dose peak, the Bragg peak, is formed at the end of the finite range. Thus, ion beams are capable to constitute tumour conformal dose distributions with reduced entrance dose and almost completely missing exit dose.

Nuclear fragmentation

For the exact calculation of dose distributions, the influence of nuclear fragmentation reactions has also to be considered in IBT since beam fragmentation tend to deteriorate the sharp dose contours. A fraction of the incident ions undergoes these processes which are mainly peripheral collisions occurring primarily at higher energies. A two-step model of the fragmentation reactions was at first proposed by Serber (1947) and is today known as abrasion-ablation model (Gaimard and Schmidt 1991). The collision time between the incident particle and the nucleus is quite short (10^{-23} s) in comparison to the time scale of interaction between nucleons in the nucleus (10^{-21} s – 10^{-16} s). The composition of the reaction partners is modified during the collision step and a certain amount of excitation energy is transferred to the so-called prefragments. In the second step, the system reorganizes by thermalisation and deexcitation under evaporation of neutrons, protons and light nuclei as well as by fission and the emission of gamma rays. A detailed outline on heavy fragment production by nucleus-nucleus collisions is given by Hüfner (1985).

Consequences of nuclear fragmentations for IBT with ions heavier than protons can be summarized as follows (Kraft 2000). Since in peripheral collisions only a small amount of momentum is transferred to the target nuclei, the projectile fragments remain quite large and propagate with almost unchanged velocity. However, the emission angle of the fragments is larger than the lateral scattering by electronic interaction. This leads to a broadening of the beam profile. The projectile fragments can also undergo secondary fragmentation which might not be neglected. Due to the reduced mass and/or charge number of the projectile fragments, their lateral and range straggling changes a little according to (2.7), and in particular their mean range differs from that of the primary projectiles and scales according to (2.6). For instance for ^{12}C ion beams, the typical projectile fragment ^{11}C will be stopped proximal and others like ^{11}B in the fragment tail distal to the planned Bragg peak position. Hence, the Bragg peak becomes broadened which has to be considered for treatment planning. If treatment plans are created for passive beam delivery (cp. section 2.2.1), one has to keep in mind that material in the beam path used for beam modulation like range shifters or absorbers induces an additional amount of fragments which is avoidable when active delivery techniques (cp. section 2.2.1) are applied. Related to the intolerable amount of generated fragments from ion beams heavier than neon, these particles are not contemplated for radiotherapy. Cross sections for certain fragmentation reactions of lighter ion beams ($5 \leq Z \leq 10$) (Schall *et al.* 1996) reveal that carbon beams produce a quite small amount of low-Z fragments.

2.1.2 Biological effectivity

The absorbed dose is a well defined quantity. However, in several biological systems or under changed conditions same dose values can evoke varying biological reactions.

Cell death and survival curve

The mechanisms leading to radiation effects in biological systems can be classified in two groups. If the energy is absorbed in the critical target molecule itself, it is referred to as a direct effect. If radiation is absorbed by other structures and in a subsequent step transferred to the target molecule, it is called an indirect effect. A typical example for the latter one is the radiation induced hydrolysis of water accompanied with the formation of oxygen radicals which are likely to induce chemical reactions. The most important target molecule in radiotherapy is the deoxyribonucleic acid (DNA). The aim is to induce modifications in the double-stranded DNA molecule of the tumour cells. These modifications will result in mutations and in mitotic or clonogenic cell death[1] if repair mechanisms fail. Non-repaired double-strand breaks or incorrect reparation results are considered to be the main mechanism

---

[1] The cell looses its reproductive integrity and its ability to proliferate indefinitely. Such a cell is considered as dead although it might retain its ability to synthesize proteins and DNA and undergoes a small number of cell cycles.

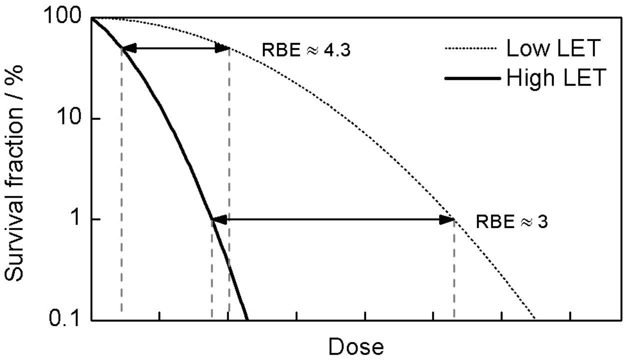

Figure 2.3: Schematic representation of cell survival curves for different LET radiation after Herrmann *et al.* (2006). Low LET radiation requires higher doses for inducing the same amount of cell death. The dose ratio (RBE) changes with considered value of survival fraction.

for biological effects. Hence, cell survival is an often investigated quantity to rate the effectivity of a particular dose. The cellular survival fraction s/s_0 of an initial cell population s_0 after the irradiation with a dose D is well described by the widely accepted linear quadratic (LQ) model (Kellerer and Brenot 1974)

$$\ln\left(\frac{s}{s_0}\right) = -\alpha D - \beta D^2 \qquad [\alpha] = \mathrm{Gy}^{-1} \qquad [\beta] = \mathrm{Gy}^{-2}. \tag{2.10}$$

α and β are cell and tissue specific constants that determine the initial slope and curvature of the survival curves. Influencing factors for cell survival are e.g. radioresistance, repair capacity, current cell cycle phase, fractionation schedule of the radiotherapy, duration of irradiation, oxygen supply, existence of biological or chemical modifications and the quality of radiation (Herrmann *et al.* 2006). Also the difference in ionization density of high and low LET radiation induce different responses in biological systems. Figure 2.3 shows the typical progression of cell survival curves for high and low LET radiation.

Relative biological effectiveness (RBE)

To quantify the influence of certain factors onto cell survival, the parameter RBE is used. It rates the biological response to a dose delivered with a specific type of radiation. In particular, the RBE for a certain test radiation that delivers a dose D_T is related to a dose of a reference radiation D_X (predominantly ^{60}Co γ-rays or 250 keV X-rays) that generates the same effect in a given biological system under identical conditions and is defined as (Herrmann *et al.* 2006)

$$\mathrm{RBE} = \left.\frac{D_X}{D_T}\right|_{\text{same endpoint}}, \tag{2.11}$$

where a biological endpoint could e.g. be a certain amount of cell survival as illustrated in figure 2.3 for the high LET test radiation. Detailed considerations and recommendations concerning the RBE in IBT are given by the IAEA (2008). The RBE value is rather complex.

In first approximation it increases with LET and as the LET increases along the path of slowing down ions the RBE rises in depth. The RBE of ion beams depends additionally on the particle type, even if they have the same LET (Goodhead *et al.* 1992). For proton beams a constant generic RBE value of 1.1 is recommended for clinical practice by the ICRU (2007), although experimental data give evidence that the RBE rises clearly at the distal end of the proton Bragg peak (Paganetti *et al.* 2002). For carbon ions a variety of RBE values have been reported, even RBE > 6 can be found in the literature. Ando and Kase (2009) reviewed the published RBE values for high LET radiation for different biological systems and endpoints. The higher RBE values with nonlinear dose dependence for carbon ion beams make carbon favourable in comparison to proton beams. However, the increased RBE values, either constant or variable, have to be taken into account during treatment planning. Treatment plan optimization is not restricted to the consideration of physical dose, but rather the isoeffective dose D_{isoE} (Wambersie *et al.* 2007; IAEA 2008) should form a homogeneous Bragg peak in the target volume.

2.2 Technical aspects of ion beam delivery

2.2.1 Active and passive beam delivery technique

Currently, there are two ion beam delivery techniques available for the administration of treatment fields to specific tumour locations. These are commonly referred to as scattered and scanned or passive and active beam delivery (Kraft 2000), but also as beam widening and conformal technique (Blattmann 1992), respectively. Both methods fit the treated volume in two dimensions in BEV to the shape of the target volume.

Passive beam delivery

Highly energetic, narrow ion beams with constant energy are provided by cyclotrons or synchrotrons. To realize a useful beam cross section covering the tumour size in BEV, the narrow beam is defocused and passively widened by double scattering techniques or semi-actively by wobbling magnets (Chu *et al.* 1993). Also a combination of both systems is feasible as it was installed at the heavy-ion medical accelerator in Chiba (HIMAC) (Kanai *et al.* 1999). To form a SOBP, the particle energy is modulated by moving or static ridge filters or rotating modulator wheels. The material of varying thickness generates a specific SOBP extension and conformation taking also the RBE dependence into account. The components are produced for individual tumour thicknesses. Additional homogeneous degraders or range shifters are brought into the beam path to reduce the remaining maximum energy according to the maximal required penetration depth for a specific patient. In lateral dimension the treatment field is confined by an individually fabricated collimator or a commercial multileaf collimator. The distal shape of the high dose volume is adapted to the distal tumour contour by an individually manufactured range compensator put directly at the skin of the patient. Components for passive beam delivery are summarized by Kraft (2000) and presented in more detail

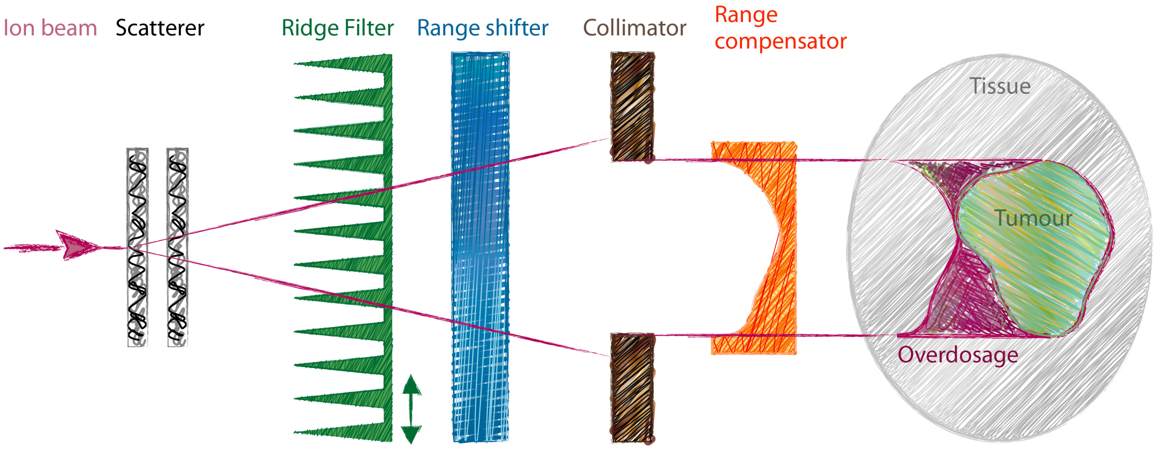

Figure 2.4: Outline of passive beam shaping with components as explained in the text using double scatter beam broadening and range modulation by a moving ridge filter. The volume treated by the SOBP covers the whole tumour volume and its distal shape is adapted to the distal target curvature by a patient specific range compensator. However, the proximal shape of the high dose region does obviously not reproduce the proximal target contour. Consequently, overdose regions upstream of the tumour have to be accepted.

by Chu *et al.* (1993). Figure 2.4 shows a scheme of the various components and illustrates the main disadvantage of this beam delivery technique. Since the longitudinal extension of the SOBP is constant for the whole lateral field cross section, the high dose volume overlaps unnecessarily with healthy tissue proximal to the target volume.

Active beam delivery

Active beam delivery was at first brought into operation using proton beams at PSI (Pedroni *et al.* 1995) and carbon ion beams at GSI (Haberer *et al.* 1993). The raster scanning with carbon ions is nowadays also available at the Heidelberg Ion-Beam Therapy Center (HIT) (Heeg *et al.* 2004) and at the HIMAC in Japan (Furukawa *et al.* 2010b). The concept of active beam delivery is rather simple as illustrated in figure 2.5. The target volume is divided into a grid of volume elements (voxels), and for each voxel a certain isoeffective dose is prescribed. Voxels that require same beam energy to match the Bragg peak depth with the voxel position (depending on proximal tissue density) are grouped together in iso-energy slices. Within each slice the thin pencil beam with a full width at half maximum (FWHM) of a few millimetres is scanned by means of dipole magnets in lateral direction (horizontally and vertically) from voxel to voxel. At each position a predefined amount of ions is deposited using raster scanning, where the scan velocity is modulated while the beam is sweeping from voxel to voxel, or spot scanning, where the beam is turned off when changing the magnetic field for the next position. Changes between energies are either realized by absorbers of different thickness at cyclotron accelerators, which are normally used in proton therapy, or by the accelerator itself. Synchrotrons allow for a pulse to pulse variation of the beam energy, intensity and FWHM. The layers are separated in depth by only a few millimetres to allow for overlapping of Bragg peaks. To minimize the number of required energies in the treatment

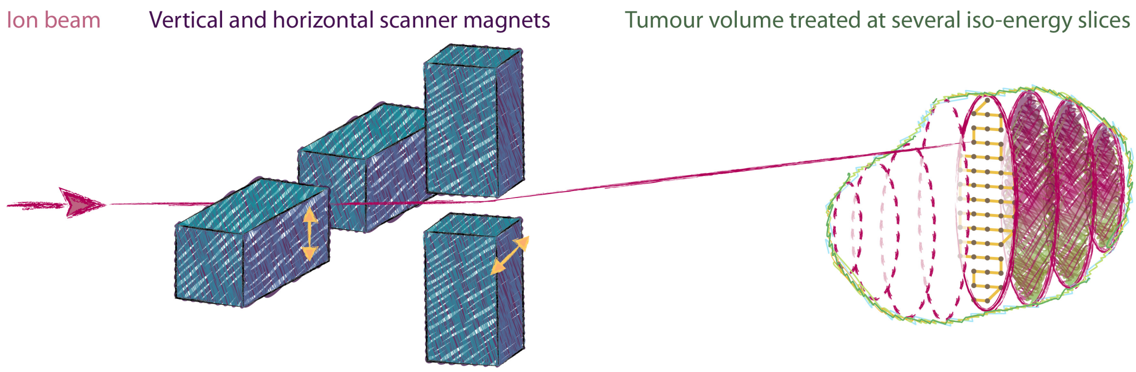

Figure 2.5: Illustration of active ion beam delivery using vertical and horizontal deflection magnets to direct a pencil beam to a certain lateral position in the planned treatment volume. The requested ion beam energy defines the depth of the Bragg peak in the target. In each iso-energy slice, the beam is scanned along a predefined path. Hence, the whole target volume is covered with an individual dose without using any patient specific components.

plan, ripple filters are used to broaden the Bragg peak (Weber and Kraft 1999).

In principle, arbitrary depth dose profiles are produced by this technique, but treatment planning is more complex (Krämer *et al.* 2000; Krämer and Scholz 2000). The dose deposited in a certain voxel is composed of the Bragg peak dose at the voxel depth and the dose deposited by ions of higher energy traversing that voxel to deeper seated voxels. Nevertheless, active beam delivery with raster scanning magnets is the favourable implementation in upcoming installations and is predicted to be the standard technique in the future of IBT (Jäkel *et al.* 2008). Active beam delivery of carbon ions at the GSI facility has been used for investigations within this thesis.

2.2.2 Beam monitoring for pencil beam scanning

Beam monitors are important components for the active beam delivery, since it demands the measurement and control of particle fluences and beam position with high precision and within a few microseconds. For this purpose, parallel-plate ionization chambers (ICs) are used to measure particle fluxes that range for carbon ions approximately from 2×10^6 to 1×10^9 ions per second (Voss *et al.* 1998; Furukawa *et al.* 2010b). Multi-wire proportional chambers (MWPCs) are employed for the monitoring of beam position and focus size. For safety reasons, the monitoring units are mounted at the last segment of the beamline, they might be installed as redundant systems and failures in their read-out electronic as well as the detection of unexpected beam properties have to cause interlocks (Badura *et al.* 1997). At GSI, a front-end therapy control system is responsible for the control of beam position and scanner magnets. Data of the MWPC are read and analysed during treatment and saved afterwards for documentation purpose (Brand *et al.* 1998).

If the required number of particles at a certain beam position has been detected by integrating the measured IC values, a co-called nextpoint signal initiates a change of beam direction (Badura *et al.* 2000). At GSI, these nextpoint signals are recordable and can be used in combination with the logged MWPC data for a retrospective analysis of the beam delivery.

2.2.3 Considerations in treatment planning related to patient CT image

For reaching a certain depth in inhomogeneous tissue, the energy selection of pencil beams has to be performed very carefully. As known from (2.3) and (2.5), the range of ions depends directly on the electron density of the penetrated material. Thus, diagnostic imaging for treatment planning in IBT has to provide information on that quantity. The absorption of X-ray photons in tissue is related to the tissue electron density, and therefore CT images are employed for treatment planning. Other imaging techniques like magnetic resonance imaging (MRI) may provide comparable spatial resolution and higher time contrast without radiation exposure and can be exploited for target delineation; but as long as the electron density is not reproducible from these techniques, CT imaging stays mandatory for treatment planning in IBT. The attenuation of the tissue is converted into the grey values of the Hounsfield scale and presented in a voxelized image. The Hounsfield unit (HU) of a certain tissue is calculated by its linear attenuation coefficients μ as

$$HU = 1000 \cdot \frac{\mu - \mu_{\mathrm{water}}}{\mu}. \tag{2.12}$$

By this definition, the HU of water is 0 and that of air is -1000. HUs in the voxels along the beam path are transformed into water equivalent pathlength (WEPL), and a corresponding energy is selected. Final treatment plans are verified with respect to range by measurements in water phantoms prior to the treatment. Even if differences between several CT scanners can be compensated, a lot of effort was necessary to reduce the uncertainty between ion range and HU by means of different calibration approaches (Schneider *et al.* 1996; Jäkel *et al.* 2001; Kanematsu *et al.* 2003). Finally, the accuracy of carbon ion range determination in soft tissue from CT images was reported to be within 1 mm for typical depths of head and neck cancer (Rietzel *et al.* 2007).

For further reduction of uncertainties, optimal beam angles have to be selected based on the planning CT image for creating robust treatment plans (Jäkel and Debus 2000; Cao *et al.* 2012). Besides the sparing of critical structures and OARs, tissue inhomogeneities within the irradiation field should be avoided as far as possible. Limited possibilities of settings at fixed beam nozzles promote the necessity of ion beam gantries when searching for optimal beam angles. Several gantry concepts are realized for proton beams. The first gantry for carbon beams went recently into operation in Heidelberg (MedicalPhysicsWeb 2012), and a superconducting rotating gantry is in the design phase at the National Institute of Radiological Sciences in Japan (Iwata *et al.* 2012).

If motion has to be considered during treatment planning, a 4D CT scan is required. The provided data set consists of a stack of 3D CT images, each representing a quasi-static motion phase of a periodic motion or of one specific motion cycle. If a conventional static CT image was acquired from a free-breathing patient, the CT image would result in a time-averaged, and thus blurred and inaccurate reproduction of anatomical structures within the thorax and abdomen (Shimizu *et al.* 2000; Rietzel *et al.* 2005).

2.3 Organ motion in ion beam therapy

The more precisely a dose distribution can be adapted to the tumour contour, the smaller are the safety margins, and consequently, the higher is the disturbing influence of target motion. Besides the dose errors emerging when the target is shifted laterally out of the treatment field, IBT is additionally prone to misdosage if the WEPL of the penetrated tissue proximal to the target changes during therapy. Especially the precise and favourable active beam delivery has a high tendency to fail if the patient is insufficiently immobilized and/or motion mitigation techniques are omitted.

2.3.1 Types of organ motion

Target motion can arise from several physiological processes and is hardly avoidable. The most severe influence of target motion is found for those entities located in the thoracic and abdominal region. Due to its origin, motion becomes relevant on different time scales. Three types of organ motion can be classified (Langen and Jones 2001).

1. Spontaneous and position-related patient motion
   Patient motion is most efficiently suppressed by well established immobilization techniques. Individual devices are mounted as tight as possible and tolerable. Additionally, the treatment and the imaging for treatment planning should be performed in same position and with same fixation devices. Since patient motion occurs on a time scale of several minutes and longer, it can be neglected after the patient has been precisely positioned, normally based on its bony anatomy.
2. Inter-fractional motion
   Slow physiological processes like digestion and peristalsis evoke changes in patient anatomy within a few minutes to hours and days. Within a fraction the influence can almost be ignored, and an intervention is only required at the beginning of a fraction. The inter-fractional motion extend of different tumour sites has been investigated in several studies (Langen and Jones 2001). Typical targets affected by inter-fractional motion are e.g. prostate, bladder, rectum and uterus, but also liver and pancreas might be involved. Changes in patient condition like weight loss might also be observable on a day-to-day level, and often tumour shrinkage starts already during the fractionated therapy as exemplarily shown for NSCLC by Britton *et al.* (2007) and Fox *et al.* (2009). Due to the related increase in contralateral lung dose in some cases an adaptive replanning is recommended by Hui *et al.* (2008).
3. Intra-fractional motion
   Targets changing their position on a time scale of seconds to minutes will definitely

affect the delivered dose distribution, although the patient has been positioned correctly. Intra-fractional motion can originate from slow progressive processes like peristalsis or muscle relaxation during prolonged treatment times. A more important influence in the thorax and upper abdomen arises from periodic motion due to heart beat (Mori *et al.* 2007) and breathing (Seppenwoolde *et al.* 2002; Liu *et al.* 2007). Respiration related changes in WEPL have been examined for pancreatic (Kumagai *et al.* 2009), liver (Minohara *et al.* 2003) and lung cancer (Mori *et al.* 2007, 2008), and local changes in WEPL of even more than 20 mm have been reported.

An increased impact of intra-fractional motion on the dose inhomogeneity is found for active beam delivery with scanned ion beams. In particular, this is the case for intensity modulated particle therapy (IMPT) where the total dose is optimized by means of multiple fields (Lomax 1999; Gemmel *et al.* 2008). An inter-field motion of 5 mm for an IMPT plan was found to generate local underdosage in the target volume of about 20% (Lomax 2008). A more general problem for active beam delivery is the unpredictable interference of pencil beam motion and target motion (Phillips *et al.* 1992). Generated interplay patterns with regions of over- and underdosage are strongly affected by several parameters like the scanning direction (Lambert *et al.* 2005) or the motion amplitude and start phase (Bert *et al.* 2008). Motion mitigation methods are required to avoid the occurrence of interplay patterns (Grözinger *et al.* 2006) and to exploit the full potential of IBT for the treatment of moving tumours in the lung or liver.

2.3.2 Detection of intra-fractional motion

A reliable detection of the target motion is a prerequisite for a successful motion compensation. Real-time information is needed for an instantaneous tuning of beam parameters. The available systems can be classified into systems for direct measurement of the tumour motion and those for measuring a motion surrogate signal. Modern radiotherapy facilities are sometimes equipped with kV X-ray imaging systems suitable for taking fluoroscopic sequences. In combination with fiducial markers implanted near or into the tumour (Shirato *et al.* 2003), the most precise measurement of tumour motion is feasible. However, the implantation bares additional risks and fiducial markers are not well suited for IBT because of their unknown influence in the CT images that are used for treatment planning and energy selection to meet certain ion ranges (Jäkel and Reiss 2007). Due to the radiation burden of fluoroscopy, it cannot be applied throughout the whole treatment delivery. A non-invasive but also direct imaging modality is ultrasound (US) that can be applied for monitoring abdominal organs or the diaphragm. 3D tracking accuracy below 2 mm has been reported for tracking the liver in volunteers (Harris *et al.* 2010). The feasibility of implementing US for target tracking in IBT is currently under investigation by means of phantom measurements at HIT (Schwaab *et al.* 2012).

Respiratory motion is mostly detected by means of surrogates. Spirometry might be used to detect surrogate signals like temperature, flow and volume (Hoisak *et al.* 2004) of inhaled air. It might also be used to control the breathing during treatment by means of deep-inspiration breath hold (Mah *et al.* 2000) or active breathing control (Wong *et al.* 1999). The stereoscopic observation of optical markers attached to the patient skin or the optical scanning of the body surface (Hughes *et al.* 2009) delivers alternative surrogates. Strain gauges or pressure belts clasped around the thorax (Li *et al.* 2006b) measure a one-dimensional (1D) motion signal allowing to detect defined states of a breathing cycle. However, the correlation between the motion signal and the internal target motion is always a critical issue of motion surrogates. For instance, Gierga *et al.* (2005) report a generally good correlation but also possible variation in tumour state for a certain external marker position. Hysteresis and time delay may vary with tumour size, its location and the considered motion direction. For motion consideration within this thesis, it may be assumed that the correct internal target motion is accessible.

Internal target trajectories have been investigated in detail e.g. for bronchial carcinoma by fluoroscopic imaging of implanted fiducial markers (Seppenwoolde *et al.* 2002) or by CT imaging (Liu *et al.* 2007). For anatomical structures that undergo a remarkable motion during a breathing cycle, a predominant motion amplitude in the cranio-caudal direction has been observed, for both tumours located in the thorax (Keall *et al.* 2006) and organs within the abdomen (Brandner *et al.* 2006). A simplified 1D approximation for the motion pattern over time t is given by Lujan *et al.* (1999) using the parametrization

$$y(t) = y_0 - a \cdot \cos^{2n}\left(\frac{\pi \cdot t}{\tau} - \Phi_0\right), \tag{2.13}$$

with y_0 indicating the elongation at exhalation, a the peak-to-peak amplitude, τ the period time of a breathing cycle and Φ_0 the phase at $t = 0$. Shirato *et al.* (2004) used this equation to fit tumour trajectories received from fluoroscopic marker tracking and revealed that the value of the parameter n is mostly equal to 1 (43%) or 2 (38%). Although real 3D motion patterns are more complex in terms of exhibiting irregular modulations of the amplitude and frequency as well as probable baseline shifts, the described motion pattern (2.13) with $n < 3$ is often used for systematic experimental investigations. The values of the other motion parameters show a quite large variability between several patients. For lung tumours, the value of the peak-to-peak amplitude a depends on the location of the tumour inside the lung (upper or lower lobe) and its possible attachment to a bronchus or the chest wall. Mean values are often reported to be below 10 mm (Keall *et al.* 2006). Especially the more seldom cases with higher values (also above 20 mm) require an adequate motion compensation during treatment because of their increased risk for inducing dose failures.

2.3.3 Motion compensated ion beam therapy

The critical influence of target motion on the homogeneity of the dose distribution in IBT demands a 4D treatment planning for active pencil beam scanning (Bert and Rietzel 2007; Knopf *et al.* 2010) and passive beam delivery (Engelsman *et al.* 2006) as well. Several solutions for motion mitigated beam delivery have been proposed. Most of them rely on the initially extracted motion information from a 4D planning CT image and the acquisition of motion parameters during treatment. For choosing a certain mitigation technique, patient-specific parameters like physiological condition, tumour size, location and motion pattern as well as accelerator parameters like dose rate, availability, restrictions in energy modulation, maximum scan speed for active beam delivery and the time latency of beam monitoring have to be considered.

The most relevant motion compensation techniques in IBT for free breathing patients are identified as follows (Rietzel and Bert 2010; Schardt *et al.* 2010; Knopf *et al.* 2010; Bert and Durante 2011).

1. Margin based approach
   Like in photon therapy, the planned target volume is expanded to cover the whole target at any time (ICRU 1993b, 1999), and the treatment plan is delivered like a static one. This method has already been successfully applied for lung cancer using passive beam delivery (Bush *et al.* 2004; Nihei *et al.* 2006), but for larger motion amplitudes the amount of involved normal tissue limits the dose given to the tumour. For scanned ion beams, a simple adding of safety margins is not sufficient because of interplay effects. Nevertheless, safety margins are also required for other motion mitigation techniques to overcome their limited precision.
2. Rescanning (or repainting)
   Raster scanning is applied for the multiple irradiation of the target volume with a correspondingly less amount of particles per scan (Phillips *et al.* 1992). Different repainting strategies are presented by Zenklusen *et al.* (2010). For non-synchronized target and beam motion, the compensation of interplay patterns improves with rising number of rescans. Uncorrelated target and beam motion can e.g. be established by a random delay between the rescans or a random order of energy slices (Seco *et al.* 2009). Rescanning has not been applied for patients yet, but simulation studies (Knopf *et al.* 2011) pronounce that the benefit of rescanning will be dependent on the geometry and number of treatment fields and on several motion and beam parameters. The major drawbacks of rescanning are the flattening of field gradients, high doses delivered to surrounding healthy tissue and the prolonged treatment time because of the reduced beam intensity.
3. Gating
   A real-time monitoring of the respiration cycle is used for temporal synchronization of the beam application within a predefined motion state (Minohara *et al.* 2000). The motion amplitude during the beam delivery, normally at end-expiration phase, is significantly reduced, and safety margins can be decreased. The residual motion within the gating window may still induce interplay patterns, but they are reducible by an enlarged pencil beam width (Bert *et al.* 2009). Gated irradiation with passive beam shaping is under investigation and in clinical use at several ion beam centres (Nihei *et al.* 2006;

Lu *et al.* 2007; Iwata *et al.* 2010). Evidently, gating increases irradiation time. This may become a critical issue at synchrotron-based facilities, since the restricted duty cycle of the accelerator may miss the gating window. Variable beam extraction phases can enlarge the synchrotron efficiency and thus reduce the treatment time (Tsunashima *et al.* 2008).

4. Tracking
   To compensate for target motion in all directions during the whole respiration cycle, the scanned particle beam has to be adapted in lateral position and energy. A future implementation of proton beam tracking is intended at Gantry 2 at PSI (Safai *et al.* 2012). Up to now, the only prototype for beam tracking (Bert *et al.* 2007; Grözinger *et al.* 2008) and promising results from phantom studies (Bert *et al.* 2010) are available at GSI. The raster scanning magnets are utilized to follow the detected lateral target motion in real time (within 1 ms with an accuracy below 0.16 mm). For energy adjustment, the therapy control system drives a double-wedge degrader that is placed proximal to the target (Weber *et al.* 2000). Bragg peak depth changes of 5 mm in water are achievable within 16 ms (Saito *et al.* 2009). An alternative wedge design integrated into the beamline has been proposed by Chaudhri *et al.* (2010). The obvious advantages of beam tracking are the precise dose distribution, the potentially reduced margins allowing for dose escalation in the tumour and the irradiation without prolongation of treatment time. However, a detailed investigation of robustness against uncertainties in motion monitoring and changes in patient geometry or motion patterns during the beam delivery is required prior to a clinical implementation of beam tracking.

A combined application of these approaches is feasible to overcome the remaining drawbacks of the individual methods. For instance, an additional rescanning during gated beam delivery may reduce residual interplay patterns (Furukawa *et al.* 2010a), or the delivery of a rescanned treatment plan while tracking the target may reduce the influence of temporarily imprecise motion signals. At GSI there is a unique availability of a motion mitigated ^{12}C pencil beam irradiation using rescanning, gating and/or tracking for experimental operation.

2.4 Dose monitoring by means of positron emission tomography

Quality management in IBT demands high effort during treatment planning, plan verification and beam delivery as it had e.g. been reported for the former German heavy ion therapy project at GSI (Karger *et al.* 2000). Furthermore, an *in vivo* verification of the actually delivered dose distribution is highly desired. Changes in tissue density within the treatment field can arise from

- anatomical changes due to tissue swelling, shrinkage or deformation,
- inaccurate positioning of the patient and
- patient motion,

and may cause serious deviations between planned and delivered dose distribution. The dose monitoring should discover these deviations. This requires a reliable verification and/or detection of

- lateral field position,
- ion beam range and
- local deviations proximal to the Bragg peak.

Currently, several approaches are under investigation concerning an *in vivo* and *in situ* dose verification. The delayed effect of fatty replacement in the vertebral bone marrow after proton therapy can be visualized by means of MRI but only post-treatment (Gensheimer *et al.* 2010). Retrospective, contrast-enhanced MRI seems to be feasible to verify the proton range in liver cancer patients (Yuan *et al.* 2013). The detection of emitted prompt γ-rays during the beam delivery promise a high count rate and valuable information about particle range, but detector design, data handling and reconstruction have to be improved further to reach clinical feasibility.

The only method of an *in vivo* dose monitoring that has already been successfully proven under clinical conditions in IBT is positron emission tomography (PET). Pioneering work started 1979 in Berkeley, USA (Llacer *et al.* 1979), where later a few patients had been irradiated with radioactive probing beams. Similar concepts were investigated at the HIMAC facility for delivering radioactive (^{11}C) beams with therapeutic (Urakabe *et al.* 2001) or probing (Iseki *et al.* 2004) purpose. The position where the beam has been stopped in the tissue can directly be visualized. Due to the high costs for the production of radioactive beams and safety concerns related to shielding of the beam, this method did not prevail. During the last two decades, promising experiences have been obtained with PET imaging in combination with IBT using stable carbon and proton beams. So far, several patients have been monitored after passive beam delivery in the USA (Parodi *et al.* 2007c; Hsi *et al.* 2009) and in Japan (Hishikawa *et al.* 2002; Nishio *et al.* 2007, 2010) and about 440 patients during scanned carbon ion treatment at GSI (Enghardt *et al.* 2004a). At the HIT facility, a PET/CT scanner went into clinical operation (Bauer *et al.* 2012), and a patient study with a planned number of 240 patients to be monitored by means of this device after scanned IBT (Combs *et al.* 2012) commenced recently.

Performing the PET measurement at least shortly after the irradiation is mandatory in all cases, since the relevant β^+-emitters decay rapidly. The measurements can be accomplished by several approaches (Shakirin *et al.* 2011). The method of choice is a measurement during the pauses between beam extraction cycles of a pulsed irradiation and some seconds immediately afterwards (Enghardt *et al.* 2004b). This approach is called in-beam PET. The clinical workflow remains almost undisturbed, and highest signal strength might be detectable. However, expensive, dedicated scanner systems are necessary for a direct implementation into the treatment sites. In contrary to the in-beam PET method, it is feasible to performed the measurements after the irradiation at all. These methods are denoted as off-beam PET and can be distinguished into two concepts. A measurement that is performed inside the treatment room with an individual scanner at the treatment site (Nishio *et al.* 2010) or with a conventional diagnostic scanner nearby (Zhu *et al.* 2011), is named in-room PET. The treatment room remains blocked for a certain time, and the patient throughput is reduced. If the patient has to walk or to be transported to a scanner placed in close vicinity to the treatment room, the PET monitoring will be called off-line PET (Hishikawa *et al.* 2002; Parodi *et al.* 2007c). The diagnostic full-ring scanners offer better solid angle coverage and thus reduced reconstruction artefacts, but due to the delayed start of measurement, only a reduced number of β^+-emitters is available to contribute to the signal. Range verification by means of off-line PET requires angular field directions, since for opposing fields the distal β^+-activity fall-off will overlap with the activity plateau in the entrance channel of the other field.

2.4.1 Principle of PET imaging in ion beam therapy

Generation of positron emitters

Nuclear fragmentations between the primary particles and atomic nuclei of the target material had been identified in section 2.1.1 as an obstacle for the delivery of sharp dose contours. However, among the generated fragments there are β^+-emitting nuclides (Tobias *et al.* 1971; Enghardt *et al.* 1992) which offer the possibility for an indirect, qualitative dose monitoring using PET imaging devises. One of the main advantages is that radioactive nuclides are generated as a by-product during treatment. Thus, no additional ionizing radiation needs to be supplied to the patient and the effect is referred to as autoactivation. Nuclei of β^+-emitters bare an excess of protons in comparison to their stable isotopes. Hence, they are mostly created within fragmentation reaction where neutrons are released. The β^+-emitters are created from the nuclei of the tissue (target) as well as from the nuclei of the impinging ions (projectiles) as long as their mass number Z is at least equal to 5 (for the generation of the lightest β^+-emitter ^{8}B) (Firestone and Shirley 1996). Within peripheral interactions, only a small part of the projectile momentum is transferred to the target atoms. Therefore, the target fragments stay at rest while fragmented projectiles move on with almost the same velocity and only marginal changes in direction. Due to the range scaling (2.6), the projectile fragments will be stopped slightly before or behind the Bragg peak position of the initial projectiles, but they may also undergo secondary fragmentation reactions along their track. If the ion beam consists of light ($Z < 5$) particles like protons or helium ions, no β^+-emitting projectile fragments will be produced, and the induced β^+-activity in the tissue is only formed by the target fragments. These occur along the whole track of the incident ions except for the last section where the projectiles have slowed down and the remaining kinetic energy is below the threshold energy for nuclear reactions. However, it is feasible to exploit only the created plateau of β^+-activity of the target fragments for range verification after IBT with protons as it was firstly demonstrated by Parodi *et al.* (2007b) with phantoms and in a small patient study (Parodi *et al.* 2007c).

From a biochemical point of view, the tissue in the human body constists of water, fat, proteins and carbohydrates. The elemental content of a reference man is dominated by oxygen

Table 2.2: Typical β^+-emitters generated within PMMA during the irradiation with ^{12}C ions of 295 AMeV. The given half-lives $T_{1/2}$ are taken from Firestone and Shirley (1996), the mass and charge numbers (A and Z) define according to (2.6) the relative range in comparison to the initial ^{12}C projectiles ($R/R_{^{12}\mathrm{C}}$). Values printed in grey are hypothetical values, since these β^+-emitters occur as target fragments only while the others are found to be target and projectile fragments as well. The percentage contributions of the nuclides to the projectil and target fragments and the to total number of β^+-mitters are stated as it was simulated with POSGEN (Pönisch *et al.* 2004; Hasch 1996).

					Percentage contribution to		
Nuclide	$T_{1/2}$	A	Z	$R/R_{^{12}\mathrm{C}}$[1]	Target fragm.	Projectile fragm.	All β^+-emitters
^{15}O	122.24 s	15	8	0.70	25.69	0.00	23.16
^{14}O	70.606 s	14	8	0.66	0.78	0.00	0.70
^{13}O	8.58 ms	13	8	0.61	0.02	0.00	0.02
^{13}N	9.965 min	13	7	0.80	2.26	0.00	2.04
^{12}N	11 ms	12	7	0.73	6.57	9.67	6.87
^{11}C	20.39 min	11	6	0.92	59.19	77.45	60.99
^{10}C	19.255 s	10	6	0.83	3.96	8.26	4.39
^{9}C	126.5 ms	9	6	0.75	0.38	2.38	0.57
^{8}B	770 ms	8	5	0.96	1.16	2.24	1.26

(61 wt%), carbon (23 wt%) and hydrogen (10 wt%), followed by nitrogen (2.6 wt%), calcium (1.4 wt%) and phosphorus (1.1 wt%) and other minerals (ICRP 1975). The relevant β^+-emitters originate from the most frequent elements in the body. Due to its low price, good machinability and in particular its composition of carbon, hydrogen and oxygen, PMMA $(\mathrm{C_5H_8O_2})_\mathrm{n}$ is in first approximation considered as tissue equivalent material for IBT and it is therefore often used for experimental investigations. Typical β^+-emitting nuclides created during the irradiation of PMMA with ^{12}C ions are summarized in table 2.2. The amount of induced nuclides per incident ion depends on the cross sections for the reaction channels generating these β^+-emitters and on the exact composition of the tissue. The different half-lives of the β^+-emitters indicate clearly that the relative amount of a certain nuclide will vary strongly with time, even during the irradiation which normally takes up to a few minutes. In biological systems, the additional effect of washout disturbs the original distribution of β^+-emitters (Mizuno *et al.* 2003; Fiedler *et al.* 2008), i.e. the β^+-emitters are transported away from their point of origin by means of blood flow, lymphatic circulation and other metabolic processes, or they diffuse in a random direction. With elapsing time after the irradiation, the number of β^+-emitters decreases considerably and the influence of washout increases (Parodi *et al.* 2008; Knopf *et al.* 2009).

Decay of positron emitters

Except the described mechanism for generating a mixture of β^+-emitters within the irradiated volume, the following processes are the same as in diagnostic PET imaging. The unstable

---

[1] Theoretical values of extremal range deviation relative to the primary, incident ^{12}C ions. These values can only be achieved if β^+emitters are created immediately at the target surface.

β^+-emitters with charge number Z and mass number A change into a more stable state. They decay according to their half-life by converting a proton into a neutron and emitting a positron e^+ and an electron neutrino ν_e

$$^{A}_{Z}X \longrightarrow {}^{A}_{Z-1}Y + e^+ + \nu_e. \tag{2.14}$$

Typically, the neutrino leaves the body without any interaction. The conservation of energy for a three-body decay does not define fixed energies for the particles. Hence, there is an energy spectrum of the emitted positron with a maximum energy of a few MeV or below depending on the Q-value of the β^+-emitter. The positron is slowed down in the body within a distance of some micro- to a few millimetres by releasing its kinetic energy when undergoing several interactions with the surrounding matter, similar as it is known for electrons (Beringer *et al.* 2012). The total stopping power of the positron consist mainly of two parts:

- The radiative stopping power is related to the radiation loss by means of the emission of bremsstrahlung within the Coulomb field of the nuclei or the atomic shell. It is the dominant interaction for high energetic (several tens of MeV) positrons.
- The collision stopping power is the relevant part at the low energy range of the emitted positrons. The theory of Bethe can be applied with well defined mean excitation energy, density effect and shell correction. The transferred energy of the positrons leads to excitation and ionization of the atoms.

Stopping powers of positrons are further discussed and tabulated by the ICRU (1984), and their collision stopping power was e.g. investigated and described in detail by Seltzer and Berger (1982, 1984). Recently, Tufan *et al.* (2013) published an analytical description for the calculation of stopping powers of positrons in human tissue and provided also the data for PMMA shown in figure 2.6.

The slowed down positron forms with a nearby electron a positronium configuration of short life time and annihilates almost instantaneously with the electron. Normally, two

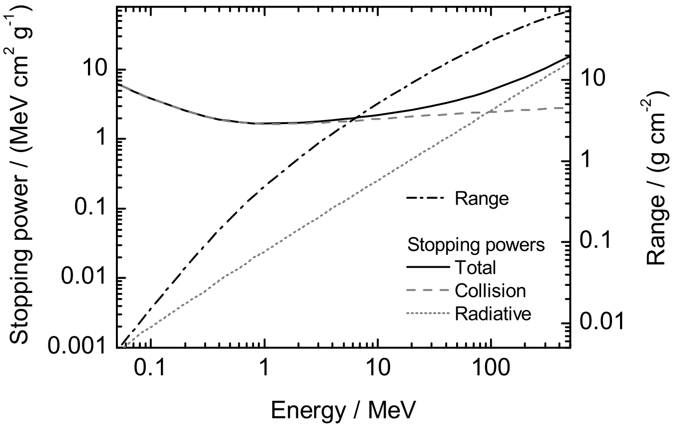

Figure 2.6: Stopping power and range in continuous slowing down approximation of positrons in PMMA calculated by M. Ç. Tufan according to Tufan *et al.* (2013) and with properties of PMMA as specified by Berger *et al.* (2005) (with courtesy of M. Ç. Tufan).

annihilation photons of 511 keV are emitted in opposite direction as determined by the conservation of energy and momentum. Deviations in emittance angle and photon energy will be found for annihilation events that occur when the positron has still a residual kinetic energy. Annihilation events with the emission of 3 photons occurs rarely and shall be neglected here.

The annihilation photons may interact with the surrounding matter along their path when propagating through the patient body and thus will be attenuated. Mainly the incoherent (Compton) scattering contributes to the energy loss and changes in the direction of the photon. The cross section for the photoeffect scales strongly with the effective charge of the material ($\sim Z^{3.8}$) and is of minor importance but also relevant in biological systems. Pair production is not feasible with a photon energy of 511 keV.

Detection of annihilation photons

The detection of both annihilation photons originating from one decay event allows to draw some conclusions about the coordinates where the annihilation and approximately the decay of the β^+-emitter took place. The coincident registration of two photons in different detector segments defines a line of response (LOR) (or more accurately: a volume of response) that connects the two front surfaces of the segments and at which the annihilation must have occurred under ideal circumstances. For a valid LOR, the two detector segments are located within a valid acceptance angle in a full-ring scanner or at different detector heads in a double-head PET scanner. A timing window of typically some nanoseconds specifies whether two detected events are considered as a coincidence. If more than two photons are registered within this timing window and defining a multiple coincidence, the event will be refused. As illustrated in figure 2.7, three possible scenarios can fulfill the timing requirement of a prompt coincidence.

- A true coincidence occurs when both photons of an annihilation event are detected within a valid LOR and none of them is scattered before reaching the detector.
- A scattered coincidence occurs when at least one of the annihilation photons is scattered

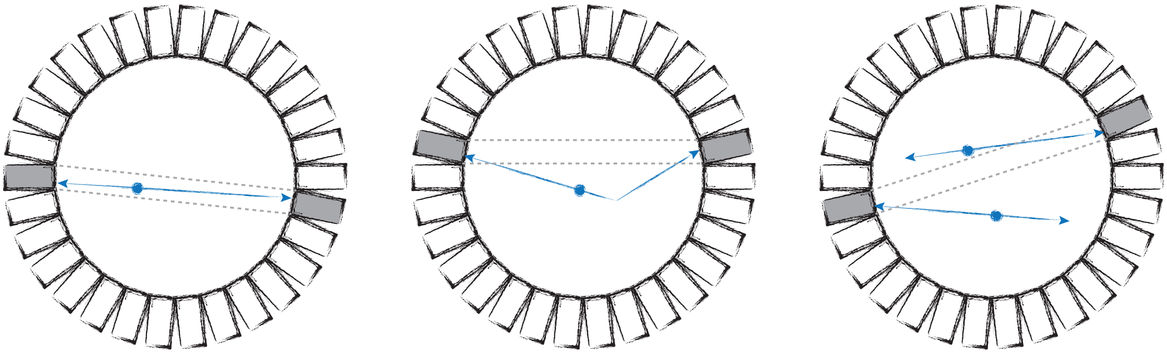

Figure 2.7: Schematic illustration of the three different types of prompt coincidences with indicated detector segments (grey) defining the LORs (dashed) in a full-ring scanner. The annihilation photons of a true coincidence (left) are created (blue spot) within the same LOR as they are detected. The point of annihilation of a scattered coincidence is outside of the defined LOR (middle). Two photons belonging to different annihilation events specify the LOR of a random coincidence (right).

and both photons are detected in a valid LOR. This LOR does not include the point of annihilation. The misplaced LOR will reduce the spatial resolution and the contrast of the reconstructed β^{+}-activity image.

- A random coincidence is detected when two positrons annihilate and one photon of each annihilation hits the detector while the others are absorbed or emitted in an solid angle that is not covered by the PET scanner.

To reduce the influence of scattered coincidences, an energy window is applied and photons with energy below a certain threshold are rejected. Several methods for further scatter and attenuation correction are available (Zaidi 2001). Random coincidences occurring outside the beam extraction cycles are distributed uniformly in time, and just a fraction of them is counted as prompt coincidence, i.e. is included in the prompt timing window. Thus, the number of prompt random events can e.g. be estimated by sampling the random events for each LOR within a delayed timing window (delayed coincidence) and subtracting them from the measured prompt events prior the reconstruction.

Besides the timing and energy resolution, a suitable PET detector needs a high spatial resolution in terms of identifying a small partial volume where the photon interaction occurred. The conventional and widely used detector type is based on scintillation crystals coupled to photomultiplier tubes (PMTs). The scintillator material has a high linear attenuation coefficient due to its high density and high effective charge number and thus is suited to absorb photons. However, the crystal thickness of several millimetres or few centimetres enhance the risk of parallax errors for non-perpendicular impinging annihilation photons. To compensate for parallax errors, the depth of interaction (DOI) in the crystal needs to be determined. Several approaches for DOI measurement and other developments in PET detector technology enabling e.g. time-of-flight (TOF)-PET measurements are presented by Lewellen (2008).

Challenges in image reconstruction and rating the result

Ideally, the reconstruction of the β^{+}-activity should generate an artefact- and noise-free β^{+}-activity distribution with a high contrast ratio. This is hardly achievable, because IBT-PET data processing has to get along with additional challenges compared to the diagnostic PET imaging. A major problem is the deficiency in counting statistics. It is limited by the dose given to the patient and the cross sections for nuclear fragmentation reactions generating the β^{+}-emitters in the body. Furthermore, it is diminished by the limited solid angle coverage if a double-head PET scanner is used. LORs in certain directions are not available, i.e. an important piece of information about the location and dimension of the irradiated volume is lost and reconstruction artefacts are inevitable (Crespo *et al.* 2006).

The reconstructed β^{+}-activity changes strongly with time and location in the body. A mixture of β^{+}-emitting nuclides is created during the course of beam delivery giving rise to a characteristic activity build-up. Concurrently, the decay of the nuclides starts immediately after their generation and takes place according to the different half-lives. Due to the time dependence of the activity and because different physical processes generate the dose or the

β^+-activity, it is obvious that the activity can only be a qualitative measure for the applied dose distribution. Anyway, since the β^+-activity is solely created within the irradiated volume, at least the distal fall-off of the β^+-activity is, depending on the applied ions, somehow correlated to the ion beam range, which is the most important property to be verified. A workflow for a qualitative dose monitoring by means of IBT-PET is described in the next section.

2.4.2 In-beam PET at GSI

About 440 patients have been treated with ^{12}C ions at GSI within a pilot project carried out by DKFZ, UKL-HD, GSI and FZR (now HZDR) between 1997 and 2008. Well fixated tumour entities mainly located in the head and neck region (Schulz-Ertner *et al.* 2007) but also in the pelvis were irradiated typically within 20 fractions (1 fraction per day). Radiation induced β^+-activities were acquired for each fraction by a dedicated PET scanner (BASTEI) and were normally evaluated for the first treatment field per fraction.

Double-head PET scanner BASTEI

Figure 2.8 shows the the installed PET scanner BASTEI (Pawelke *et al.* 1996; Enghardt *et al.* 2004a) at GSI. It consists of two detector heads to allow for variable angular positioning of the patient couch relative to the fixed horizontal beam line. In total, 64 conventional bismuth germanate (BGO) scintillator block detectors as used in the ECAT EXACT PET scanner (CTI PET Systems Inc., Knoxville, TN) are arranged at two spheroid segments of 4 × 8 blocks and cover a solid angel of about 9%. The BGO scintillation crystals (54 mm × 54 mm × 20 mm) of the detector blocks are notched to create an 8 × 8 matrix of crystal elements with a front surface area of 6.75 mm × 6.75 mm. Four PMTs are attached to each BGO crystal block.

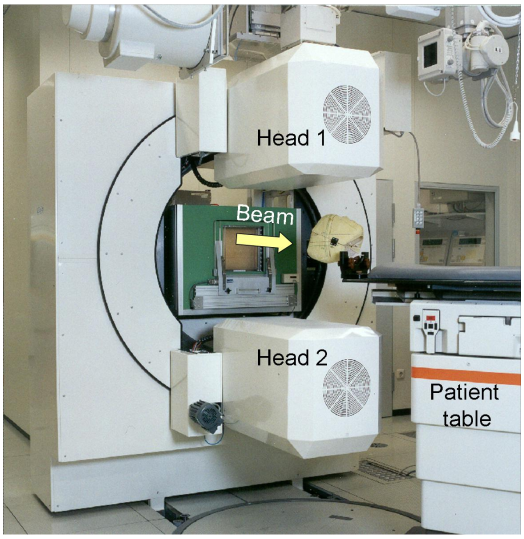

Figure 2.8: Former medical treatment site at GSI with integrated double-head PET scanner BASTEI. The scanner geometry allows for a variable positioning of the patient table relative to the fixed beam window.

Amplitude analyses of the PMT signals define one of the 2048 crystal elements per detector head. Two photons have to be detected at different detector heads to be considered as coincidence. Furthermore, an energy window of 250-850 keV is applied and the prompt as well as the 128 ns delayed timing window have a width of 12 ns. The electronic read-out hardware subdivides each of the two detector heads into 4 buckets consisting of 2 × 4 BGO block detectors. The buckets, their 8 blocks and the crystal elements are numbered internally in a well-defined order.

Listmode data format

The data acquisition of the in-beam PET scanner BASTEI at GSI is performed in listmode format. That means, registered coincidences are stored in their chronological order as single datawords. As depicted in figure 2.9, each of the 32-bit data words includes the information about the fired crystals and contains among others one bit that indicates the beam status at the time when the event was detected, i.e. whether it took place during the beam extraction phase (called spill) or in-between the spills. Time stamps written approximately every 10 ms into the data stream enable the reconstruction of all events measured during an arbitrary time interval. Although some of the bits in the data words don't contain any information, the existing hardware prohibits a direct implementation of additional information from other data acquisition tools into the data words. A retrospective temporal correlation of the listmode data with e.g. a motion acquisition system is only feasible if the system tapes the spill signals which can be assigned to the beam status information given in the PET data.

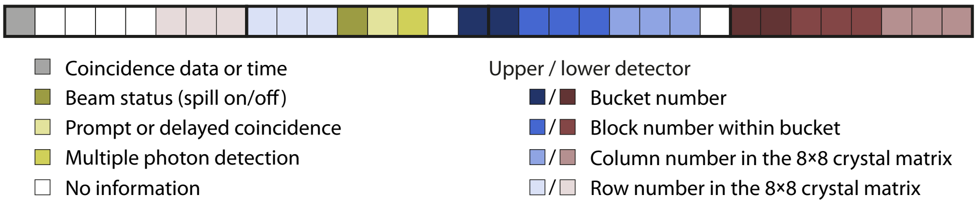

Figure 2.9: Structure of a 32-bit listmode data word of the BASTEI PET scanner. Each square stands for one bit with the possible status 0 or 1. The first bit (grey) defines the data type. If this bit is set (equal to 1), the data word will be a time stamp encoding within the following 31 bits the time elapsed since the start of the measurement. Otherwise the illustrated pattern applies. The bucket, block, row and column numbers (blue and red) define exactly the two crystals that belong to the measured coincidence. Information given by the bits for beam status, delayed and multiple coincidences might be used during the image reconstruction to correct for random coincidences and those coincidences related to prompt γ-rays during the beam extraction.

Workflow of dose monitoring

As stated previously, the β^+-activity is correlated to the applied dose distribution, but the exact dose is not accessible by a β^+-activity measurement. A simple comparison of acquired β^+-activity distributions from different fractions is performed at the National Cancer Center in Kashiwa (Nishio *et al.* 2010) to identify relevant changes in tumour and body shape during fractionated therapy. A more complex monitoring workflow that allows for an early

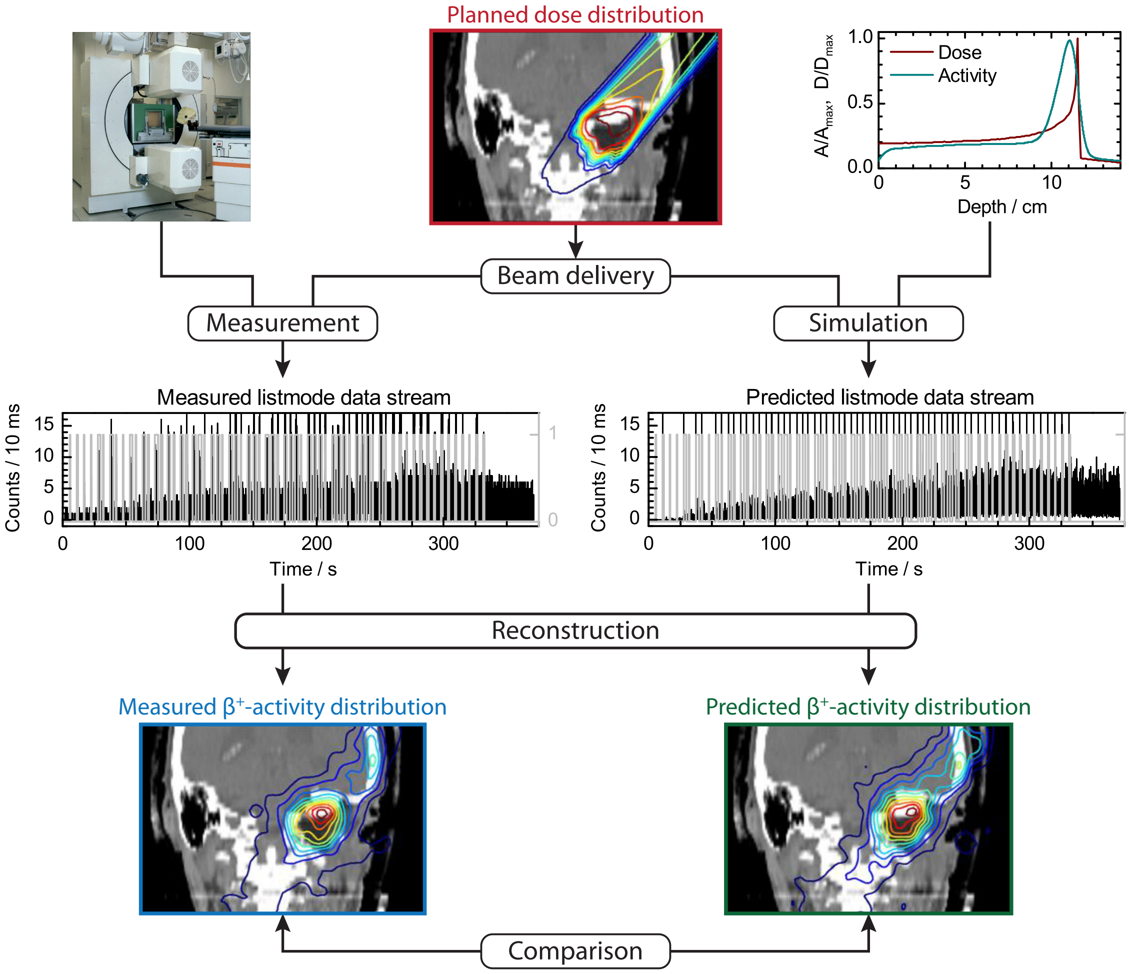

Figure 2.10: Illustration of the workflow performed for each fraction for patients treated within the pilot project at GSI, exemplarily shown for a patient suffering from a tumour at the skull base. A PET listmode data stream (count rate shown in black and beam status in grey) is measured during the delivery of the planned dose and reconstructed afterwards. The information about the exact time structure of the irradiation progress and the relation between dose and activity are taken into account during the simulation of an equivalent listmode data set. The reconstructed predictive β^+-activity distribution is compared to the result from the measurement and deviations are reported to the physicians. Dose and the β^+-activity distributions are shown as coloured contour lines superimposed to the planning CT image.

intervention (already after the first fraction) has been established for the pilot project at GSI and is outlined in figure 2.10. It is based on a comparison of the acquired β^+-activity with an expected one that needs to be simulated for each fraction.

A planned treatment field is delivered to the patient, and an instantaneous acquisition of the annihilation photons is performed by means of BASTEI. To avoid a prolongation of the total treatment time and to sustain an acceptable patient throughput, the PET measurement was only prolonged for 40 s after the beam delivery. Typically less than 10^5 true coincidences had been acquired during the measurement time and where used for reconstruction. An implemented maximum likelihood expectation maximization (MLEM) algorithm (Lauckner 1999; Hinz 2000; Pönisch *et al.* 2003) was applied for the β^+-activity reconstruction. Coincidences acquired during the beam extraction were ignored, since a huge fraction of them are random coincidences related to the prompt γ-ray emission. The iterative reconstruction algorithm is capable to include corrections for photon attenuation and scattering in the tissue on the basis of the planning CT image, for random coincidences as well as for the limited solid angle coverage of the PET scanner and its detection efficiency specified by means of calibration scans. More details about the reconstruction are given in section 3.1.1.

An in-house development of a Monte-Carlo simulation program (Hasch 1996; Pönisch 2003; Pönisch *et al.* 2004) is used for the generation of an expected listmode data set. The time-dependent production and decay of the β^+-emitters within the tissue as well as the emission and detection of the annihilation photons are considered . Since the time structure of the ion beam delivery depends on the daily accelerator parameters and is influenced by possibly occurring interlocks, the predicted listmode data need to be calculated for each applied fraction.

The dose monitoring is completed by a comparison between the measured and the precalculated β^+-activity. Within the pilot project at the GSI the conformity between both β^+-activity distributions was rated and documented by experienced observers. First approaches for an automatisation has recently been obtained (Helmbrecht *et al.* 2012; Kuess *et al.* 2012). If predicted and measured β^+-activity distributions match each other, it can be concluded that the administered dose distribution also matches the planned dose distribution. If not, the reason for the mismatch can be investigated by modifying the planning CT image and recalculating the predicted β^+-activity distribution until it corresponds to the measured one (Enghardt *et al.* 2004b). Relevant deviations indicating changes in the patient's anatomy or its positioning are reported to the physicians who decide about an intervention during the therapy. Although no instantaneous reaction is possible during the beam application by means of IBT-PET, corrective interventions are feasible before the next fraction is applied.

IBT-PET for moving targets

Tumours subject to physiological motion pose an even more urgent demand for *in vivo* treatment verification than static ones. The inherent challenges for a conformal dose application in intra-fractionally moving tumours, especially by the state-of-the-art active beam delivery, increase the risk for an insufficient dose homogeneity and location. To apply the described workflow for IBT-PET, additional information has to be included and handled correctly. These are e.g. the 4D planning CT images, the motion surrogate signal and detailed information about the motion mitigated beam delivery. The simulation of listmode data and the reconstruction of β^+-activity distributions need to be upgraded to dedicated 4D algorithms to account for the motion dependent displacement of the induced β^+-emitters. Moreover, the simulation program has to be adapted by an additional consideration of the time-dependent relative movement between target volume and scanned beam to simulate the accurate β^+-emitter distribution generated during the irradiation. The topic of 4D reconstruction is covered by chapter 3 and the implemented 4D simulation is presented in chapter 4.

3 Reconstruction of in-beam PET data taken from moving targets

Contents

Reconstruction of IBT-PET data sets acquired from moving objects would result in blurred β^+-activity distributions if no motion information was integrated in the reconstruction process. A time-resolved reconstruction algorithm has been selected and implemented for the double-head PET scanner BASTEI. An in-house motion table had been developed and was brought into operation at the former medical beamline at GSI for dedicated phantom studies. Offline measurements revealed a reasonable functionality of the reconstruction algorithm in terms of reliably reducing motion artefacts. In-beam PET data have been acquired from moving targets irradiated with ^{12}C ion pencil beams and using several motion mitigation techniques. The aim was to demonstrate that characteristic properties are also reliably accessible from the 4D reconstructed β^+-activity distribution, similar as it is known from static target measurements. Further improvements towards clinical application are discussed after the presentation of the experimental results. Some parts of the work presented within this chapter have been published in different manuscripts (Laube *et al.* 2010b, 2011, 2012b; Stützer *et al.* 2013) and were presented at several conferences (Laube *et al.* 2009a, 2010a, 2012d,a,c).

3.1 Reconstruction algorithm

It has been shown in the pilot study at GSI that the in-beam PET listmode data taken during patient treatment can be well evaluated with the maximum likelihood expectation maximization (MLEM) algorithm, at least for static tumour entities. The aim of a PET data reconstruction in general is to find the β^+-activity distribution within the image space from which it is most likely to obtain the measured coincidence data. These projection data, in the following called histogram, contain for each LOR the number of detected coincidences during the whole measurement time. Each number is obviously affected by the amount of β^+-activity within the volume of the LOR but also by the individual detection efficiency of both crystals and the material within the field of view (FOV) leading to photon attenuation and scattering. The latter influences can be effectively corrected by means of a calibration scan of the PET scanner (Lauckner 1999) and the patient CT image used for treatment planning (Pönisch 2003), respectively. Starting with the corrected histogram, each voxel in the selected image space is assigned with a discrete β^+-activity during the reconstruction process. Several 4D reconstruction algorithms exist for diagnostic PET imaging (Nehmeh and Erdi 2008) with commercial full-ring scanner systems. For the unique double-head scanner BASTEI, an individual 4D reconstruction had to be implemented.

3.1.1 3D MLEM reconstruction applied at GSI

The investigation of noise-robust 4D tomographic reconstruction algorithms for moving targets is based on the existing 3D MLEM algorithm, which shall briefly be introduced in this section. In a pre-reconstruction step the measured listmode data of the considered time interval (typically from the beginning of the first beam pulse until 40 seconds after the end of the irradiation) are sorted into a histogram consisting of 2048^2 bins. Thereby, coincidences detected during the spills are neglected because most of these events are coincidental hits of prompt γ-rays. A correction for random coincidences is done in each LOR by subtracting the number of delayed events from the number of the prompt coincidences. The remaining events are corrected for the corresponding individual detector efficiencies of both crystals that were gained from a calibration scan with a quasi-two-dimensional (2D) homogeneous β^+-activity distribution in the midplane of the FOV (Lauckner 1999). Furthermore, the histogram is modified according to the individual attenuation probability of the different LORs. If the annihilation photons cross a larger amount or a denser medium, they will have a lower probability to reach the detectors, and consequently a smaller number of coincidences will be measured in those LORs. The integral attenuation coefficients along the LORs for 511 keV photons are deduced from the planning CT scan, and the histogram is weighted by their inverse values. The new histogram represents the projection data that would have been measured with an ideal detector if the same and still unknown β^+-activity distribution had been placed into vacuum. The final step of the pre-reconstructional analysis is the weighting of each LOR by its length in terms of intersected voxels in the image space which is determined on-the-flight by means of a Monte-Carlo method.

The subsequent reconstruction process seeks the β^+-activity distribution in the FOV that would most likely lead to the modified projection data. The applied MLEM algorithm is an iterative reconstruction method. The β^+-activity distribution of the k^{th} iteration step $X^{(k)}$

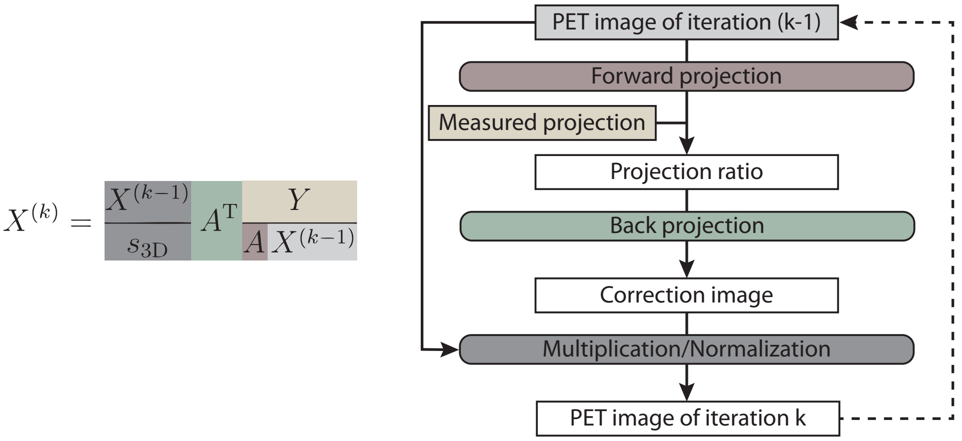

$$X^{(k)} = \frac{X^{(k-1)}}{s_{3\mathrm{D}}} A^{\mathrm{T}} \frac{Y}{A\,X^{(k-1)}}$$

Figure 3.1: Illustration of the calculation rules for one iteration cycle of the 3D MLEM algorithm as given by the iteration formula (3.1). Coloured processes and input parameters in the flowchart (right) correspond to the terms highlighted in the equation (left).

consisting of M voxels is calculated from the image of the $(k-1)^{\mathrm{th}}$ iteration $X^{(k-1)}$ by the formula

$$X^{(k)} = \frac{X^{(k-1)}}{s_{3\mathrm{D}}} A^{\mathrm{T}} \frac{Y}{A\,X^{(k-1)}}, \tag{3.1}$$

where Y is the measured histogram modified according to detector efficiency, attenuation and scatter influence, $s_{3\mathrm{D}}$ a normalization and A the system matrix. The elements a_{ij} ($i = 0 \ldots L$, $j = 0 \ldots M$) of the system matrix denote the probability for measuring a coincidence in a certain LOR i when an annihilation event takes place at a specific voxel j. And the transposed system matrix A^{T} denotes the probability that an annihilation event took place at a specific voxel when a coincidence is measured in a certain LOR. Elements of the (transposed) system matrix will be zero if the LOR does not intersect the corresponding voxel. A is also called projection operator, because the application of A to a β^{+}-activity distribution X, $(A\,X)$, generates a histogram, i.e. the activity in the FOV is projected onto the LORs by a forward projection. And vice versa, if the transposed matrix is applied to a histogram, the information in the LORs will be transformed back into the image space. This operation is called back projection. Without TOF information it is assumed that all voxels within the volume of a LOR have the same probability to contain the point of annihilation for an event measured in this LOR.

In the first iteration cycle, when there is no result from a former iteration, it is commonly accepted to use a homogeneous β^{+}-activity distribution in the image space as a start solution $X^{(0)}$. As shown in figure 3.1, the first step in each iteration cycle is the calculation of a forward projection from the result of the previous cycle. This generates a histogram that would have been measured most likely if $X^{(k-1)}$ had been the real distribution. The result of the forward projection is compared to the modified measured histogram Y by calculating the quotient $Y/(A\,X^{(k-1)})$ for each LOR. Ideally, the histogram of projection ratios will converge to 1 in each LORs with increasing number of iteration cycles. This would indicate that the reconstructed β^+-activity distribution approximates the wanted β^+-activity distribution quite well. For further improvement, a correction image for the result of the last iteration cycle is generated by means of a back projection of the projection ratio histogram. The correction image is multiplied voxel by voxel with the β^+-activity distribution $X^{(k-1)}$. The finally applied normalization $s_{3\mathrm{D}}$ includes a scaling, to ensure that the total amount of β^+-activity in the whole image space is kept constant, and a correction for the position dependent solid angle coverage by the PET scanner. The new distribution $X^{(k)}$ serves as input for the next iteration cycle. For reaching acceptable results, only a few (10 to 20) iteration cycles are necessary. Depending on the computational power, the size of the field of view and the number of measured coincidences, the whole calculation lasts less than 10 minutes for a typical clinical data set.

3.1.2 4D in-beam PET reconstruction methods

The most often occurring, radiation induced β^+-emitters in tissue, like ^{11}C, ^{15}O, ^{10}C and ^{13}N (cp. table 2.2), have relatively large half-lives in comparison to the few seconds long duration of a respiration cycle. Consequently, the nuclides generated at specific locations in the body are transported with the moving anatomical structures relative to the fixed coordinate system of the PET scanner. The statistical process of radioactivity, i.e. the unpredictable time span between the generation and decay of a certain β^+-emitter, in combination with the intra-fractional motion allows a wide range of possible decay locations. Even for a gated irradiation, when the beam is applied at one specific motion phase, the decay of a nuclide will take place at an arbitrary, unpredictable motion phase and a correspondingly shifted location. A retrospective, time-resolved evaluation of the IBT-PET data is necessary to consider the different motion states. For commercial full-ring PET scanners, dedicated 4D reconstruction algorithms might be supplied by the vendors. For the unique geometry of BASTEI, there is no pre-assembled 4D reconstruction available. Several algorithms known from diagnostic PET imaging have been examined in more or less detail and rated for its applicability.

Transformation of LORs prior to 3D reconstruction

Gained time-resolved information on the translation and rotation of the examined body in the FOV of the PET scanner might be used to transform the LOR for each coincidence prior to the reconstruction of the listmode PET data set (Menke *et al.* 1996). The advantage is to retain maximal statistics, and thus a low-noise image from the information content of all coincidences could be calculated. The actual 3D reconstruction algorithm remains unchanged; only the input histogram is modified. Each coincidence is weighted according to the attenuation and detection efficiency in the corresponding LOR and then rebinned to the LORs that would have probably been hit if there was no motion. An additional out-of-FOV correction might be applied (Bühler *et al.* 2004). The LOR transformation can be carried out in the image space or directly at the sinogram (Woo *et al.* 2004). However, due to the geometric arrangement of the BGO block detectors in the BASTEI scanner (cp. section 2.4.2)

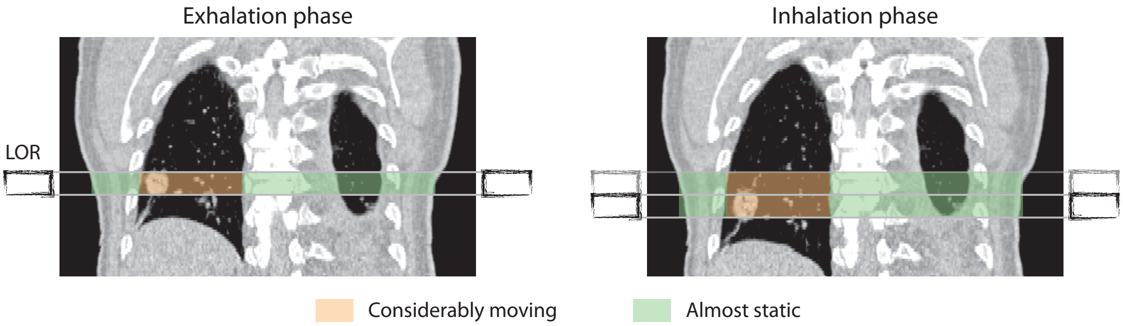

Figure 3.2: Illustration of the impracticability of LOR transformation for lung lesions with the help of a coronal plane from a 4D CT scan at exhalation (left) and inhalation phase (right). A fictitious LOR (not to scale) intersecting the tumour volume in the right lung is marked in both images (black detectors). The coloured areas indicate for this exemplary CT scan sections of almost static structures and considerably moving tissue within the LOR volume, respectively. Without the information at which position along the LOR the annihilation occurred the transformation rule from the inhalation to the exhalation phase is unknown, i.e. whether the LOR has to be transformed (to the upper grey LOR) according to the tumour motion or whether it should remain non-shifted like the ribs.

there are no sinogram data accessible.

The method of LOR transformation works quite well for rigidly moving anatomical structures. Head movement is e.g. easily detected by tracking an attached marker target via an infra-red camera. There is no relative motion between the skeletal parts and the soft tissue inside the skull. As illustrated in figure 3.2, for the thorax and abdomen there may be regions of major or minor pronounced motion impact within a single LOR. Without TOF-PET it is not feasible to locate the actual position of the positron annihilation within the LOR. Therefore, when correcting for the detected motion it is unclear how to transform the coordinates of the LOR. A future application of TOF-PET detectors with a timing resolution better than 200 ps might solve that problem or will at least narrow the region of probable annihilation point coordinates (Crespo *et al.* 2007). Since TOF information has not been available yet, this reconstruction approach for 4D in-beam PET data was not pursued in detail.

Retrospective co-registration of gated reconstructions

For the gated reconstruction algorithm, the listmode PET data are divided into N different subsets according to the registered motion cycle. The poor statistics of IBT-PET data are reduced further for each subset by this gating process. For a sufficiently high number N, the subsets represent events acquired during quasi-static motion phases, and therefore the 3D MLEM algorithm can be applied for each of them. The number of subsets (commonly 8 to 10) as well as the sorting rules should be the same as in the 4D planning CT image to have an appropriate attenuation correction for each motion phase. Traditionally, 4D CT binning is done into isochronous phases between trigger points at exhalation state. This phase sorting will generate subsets of PET data with almost equivalent counting statistics in each phase leading to a similar signal-to-noise ratio (SNR) but with different magnitude of residual motion. First commercially available, retrospective amplitude-binning demonstrated superior

$$X_0^{(k)} = \sum_{t=1}^{N} D_{t\to 0} \left(\frac{X_t^{(k-1)}}{s_{3\mathrm{D}}} A^{\mathrm{T}} \frac{Y_t}{A\, X_t^{(k-1)}} \right)$$

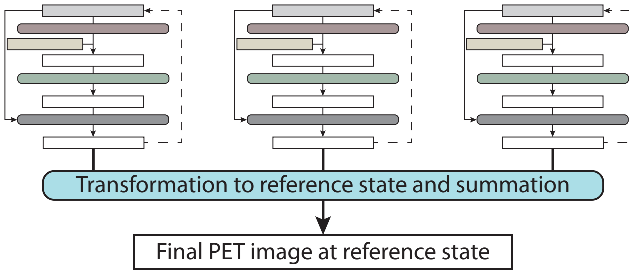

Figure 3.3: Illustration of the calculation rules for the gated reconstruction as given in (3.2). Coloured boxes in the flowchart (right) correspond to the terms highlighted in the equation (left). Small, non-labelled boxes are those shown with same colour in figure 3.1.

performance in terms of reduced CT image artefacts (Li *et al.* 2012) due to comparable motion influence in each subset.

To utilize the full signal acquired during the entire respiration cycles and to improve the inherent low SNR in the individually reconstructed β^+-activity distributions $X_t^{(k)}$, $t = 1 \ldots N$, the images are co-registered as illustrated in figure 3.3 according to

$$X_0^{(k)} = \sum_{t=1}^{N} D_{t\to 0}\, X_t^{(k)} = \sum_{t=1}^{N} D_{t\to 0} \left(\frac{X_t^{(k-1)}}{s_{3\mathrm{D}}} A^{\mathrm{T}} \frac{Y_t}{A\, X_t^{(k-1)}} \right). \tag{3.2}$$

The index 0 indicates the reference state to which all images are registered after k iteration cycles using the individual transformation matrices $D_{t\to 0}$. $X_t^{(k)}$ defines the β^+-activity distribution of a data subset calculated by the 3D MLEM algorithm (3.1) with k iterations from the pre-corrected histogram of the t^{th} motion phase. The transformation matrices have a dimension of $M \times M$, where M stands for the number of voxels in the image space. The elements d_{ij} specify the fraction of voxel j in the distribution of motion phase t that is shifted into voxel i of the reference image. This concept allows to transform rigid or non-rigid objects easily in an arbitrary direction, to rotate them around different axes or to include deformation. For patient treatment, the transformation information has to be deduced for instance from the 4D planning CT image.

Promising results have been demonstrated by the retrospective co-registration in diagnostic PET imaging in terms of contrast improvement and better lesion localisation (Thorndyke *et al.* 2006). For in-beam PET data from phantom experiments, where the β^+-activity distribution was limited to the detector midplane of BASTEI, an equal reconstruction approach has been tested using a fast-performing back projection algorithm instead of the 3D MLEM reconstruction (Parodi *et al.* 2009).

4D MLEM reconstruction

The 4D MLEM reconstruction algorithm (Li *et al.* 2006a; Qiao *et al.* 2006) also assigns each coincidence to a motion phase and corresponding histogram Y_t as explained for the gated reconstruction but processes all coincidences within each iteration cycle to ensure a maximum

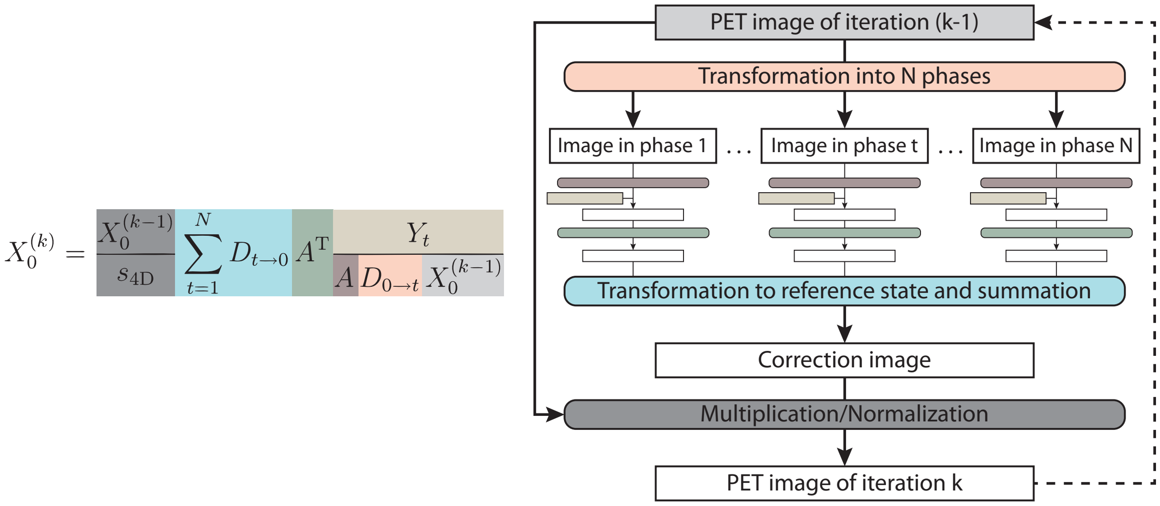

Figure 3.4: Illustration of the 4D MLEM reconstruction algorithm as defined by (3.3). Coloured boxes in the flowchart (right) correspond to the highlighted terms in the equation (left). Small, non-labelled boxes are those shown with same colour in figure 3.1.

of statistics. The β^+-activity distribution after the k^{th} iteration cycle at the reference position $X_0^{(k)}$ is calculated by the iteration formula

$$X_0^{(k)} = \frac{X_0^{(k-1)}}{s_{4\mathrm{D}}} \sum_{t=1}^{N} D_{t\to 0}\, A^{\mathrm{T}} \frac{Y_t}{A\, D_{0\to t}\, X_0^{(k-1)}}. \tag{3.3}$$

As illustrated in figure 3.4, the image $X_0^{(k-1)}$ at reference state is transformed into the different phases by applying the matrices $D_{0\to t}$ (and scaled according to the number of measured coincidences per phase). As in the 3D MLEM, a forward and back projection is calculated in each phase. The resulting correction images are summed up in the reference state under consideration of the limited solid angle coverage of the scanner prior the transformation by the matrices $D_{t\to 0}$. Thus, only the image $X_0^{(k-1)}$ needs to be updated (voxelwise multiplied with the correction image) and normalized by $s_{4\mathrm{D}}$ in each iteration cycle.

3.1.3 Comparison of gated co-registration and 4D MLEM

The reconstruction methods of gated co-registration and 4D MLEM have been implemented for the in-beam PET scanner BASTEI. A comparison of their performance is done by means of a simulation study.

Annihilation point distribution

An annihilation point distribution within a virtual phantom reflecting a geometry similar to a small cylindrical version (Shakirin 2009) of the standard IEC body phantom set$^{\mathrm{TM}}$of the National Electrical Manufacturers Association (NEMA) (cf. figure 3.5) has been created by means of a Monte-Carlo code. Input parameters for this code are the phantom geometry, the total number of annihilation points in the whole phantom, the ratio of annihilation

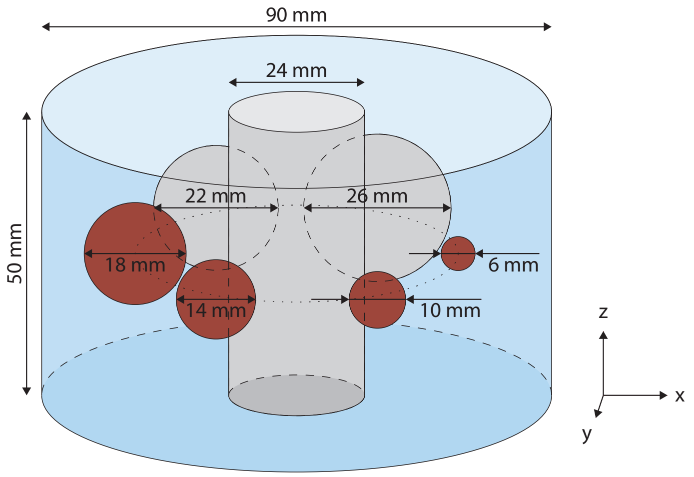

Figure 3.5: Geometry of the NEMA-like phantom. The blue cylinder contains a background annihilation point density. A cylindrical insert is centred in the middle and six spherical inserts are placed with their midpoints at center height at a distance of 28.5 mm from the phantom axis. The four smallest of the six spherical inserts are chosen as hot structures (red), and the cylindrical insert as well as the two biggest spheres are determined as cold inserts (grey).

point densities in cold, background and hot structures and the determination for each insert as hot or cold structure, i.e. to contain a high or low annihilation point density. A cold : background : hot ratio of 0 : 1 : 4 and the filling of the four smallest spheres according to the highest/hot and of all other inserts according to the lowest/cold annihilation point density have been chosen. The resulting numbers of annihilation points in each structure and the annihilation point densities are summarized in table 3.1 for a filling of the phantom with 1.35×10^6 annihilation points. The positions of the randomly chosen annihilation points have been sorted for visualization into a grid of cubic voxels with 1.6875 mm side length. Figure 3.6 shows two cross sections of the generated annihilation point distribution.

Table 3.1: Number and density of simulated annihilation points within the different structures of the NEMA-like phantom for a filling with 1.35×10^6 annihilation points in total and using a cold : background : hot ratio of 0 : 1 : 4.

Structure	Volume / cm^3	Annihilation points	Density / cm^{-3}
Whole phantom	318.09	1 350 000	4244.08
Not insert (background)	275.56	1 256 488	4 559.73
Inner cylinder (cold)	22.62	0	0.00
Sphere 6 mm (hot)	0.11	2 063	18 238.90
Sphere 10 mm (hot)	0.52	9 550	18 238.90
Sphere 14 mm (hot)	1.44	26 205	18 238.90
Sphere 18 mm (hot)	3.05	55 695	18 238.90
Sphere 22 mm (cold)	5.58	0	0.00
Sphere 26 mm (cold)	9.20	0	0.00
Cold	37.40	0	0.00
Background	275.56	1 256 488	4 559.73
Hot	5.13	93 513	18 238.90

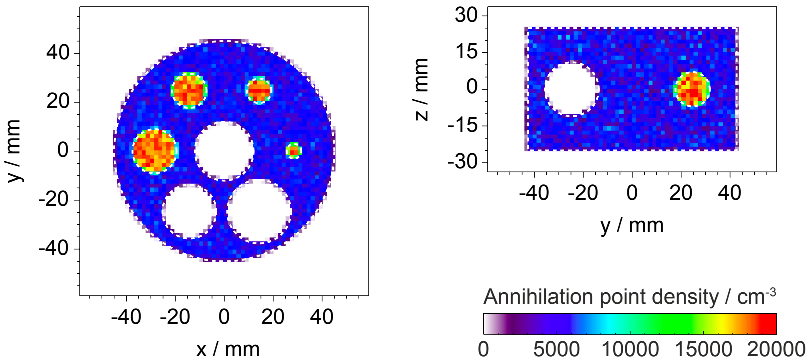

Figure 3.6: Cross sections through the simulated annihilation point distribution for the phantom midplane at $z = 0\,\mathrm{mm}$ (left) and for the plane at $x = -14.3\,\mathrm{mm}$ (right) intersecting the 2 spherical inserts with diameter of 22 mm ($y \approx -25\,\mathrm{mm}$) and 14 mm ($y \approx 25\,\mathrm{mm}$). The shape of the phantom and inserts are outlined by dashed contours.

Simulation of listmode data

The annihilation point distribution has been placed into the field of view of the Bastei scanner with the phantom midpoint at the isocentre and the axis of the cylindrical phantom parallel to the z-axis, which connects the two detector heads. A simulation program has been developed that generates listmode files based on the given annihilation point distribution and a motion of the phantom parallel to the y-axis and according (2.13). A first simulation with an amplitude of 0 mm, i.e. a static phantom, was performed as reference to be reconstructed by the approved 3D MLEM algorithm. A $\cos^2$ motion pattern with a peak-to-peak amplitude of 20 mm and a period of 5 s has been chosen for testing the 4D reconstruction algorithms. The decay times t_d for the different annihilation points are uniformly distributed within the time interval $[0\,\mathrm{s}, 100\,\mathrm{s})$ to ensure a symmetric population of the 9 amplitude-sorted motion phases according to the symmetric motion pattern. For each annihilation point the decay position $\vec{r}_\mathrm{d}$ in the PET-coordinate system of the scanner has been determined by the formula

$$\vec{r}_\mathrm{d} = \vec{r}_\mathrm{stat} + 20\,\mathrm{mm}\left(\cos^2\left(\frac{\pi \cdot t_\mathrm{d}}{5\,\mathrm{s}}\right) - 0.5\right) \cdot \begin{pmatrix} 0 \\ 1 \\ 0 \end{pmatrix}, \qquad (3.4)$$

where $\vec{r}_\mathrm{stat}$ defines the simulated annihilation point coordinate in the static phantom. At positions $\vec{r}_\mathrm{d}$ two annihilation photons are emitted isotropically but in opposite direction. No scattering or attenuation of the photons inside the phantom is considered for that simulation. About 6% of the 1.35×10^6 photon pairs (80 942 for the moving and 81851 for the static phantom) hit the detector crystals of Bastei and are stopped within the crystal depth of 20 mm concerning a linear attenuation coefficient of $0.095\,\mathrm{mm}^{-1}$ for 511 keV photons in BGO. The correlated listmode words (cp. page 31) are saved into the listmode files for the corresponding motion phase.

Reconstruction

Transformation matrices were generated for 9 amplitude-sorted motion phases of the $\cos^2$ phantom motion. All voxels with midpoint coordinate belonging to the cylindrical phantom are considered to be shifted parallel to the y-axis by applying the matrices. Voxels outside the phantom are not transformed by the matrices, neither the voxels next to the phantom in radial direction (distance from phantom axis > 45 mm) nor those above or below the phantom ($|z| > 25$ mm).

The simulated listmode data were reconstructed on an image space comprising $70 \times 70 \times 40$ ($x \times y \times z$) cubic voxels of 1.6875 mm side length. 10 iterations were used for all reconstruction algorithms, the 3D MLEM for the static phantom and the gated co-registration and the 4D MLEM for the moving phantom. Two sections through the resulting β^+-activity distributions are presented in figure 3.7. Similar patterns of activity inside the phantom can be found for all three distributions. This indicates that the 4D algorithms do not perform significantly worse than the 3D MLEM does for the static target. The β^+-activity distribution generated by the gated co-registration discloses slight artefacts in those parts of the image space not belonging to the phantom. Shady patterns are generated next to the phantom in motion direction, and artificially sharp edges are created at the upper and lower phantom layer. A better design of transformation matrices might probably reduce these artefacts. However, with the same transformation matrices, the 4D MLEM seems to have a better performance and to be less

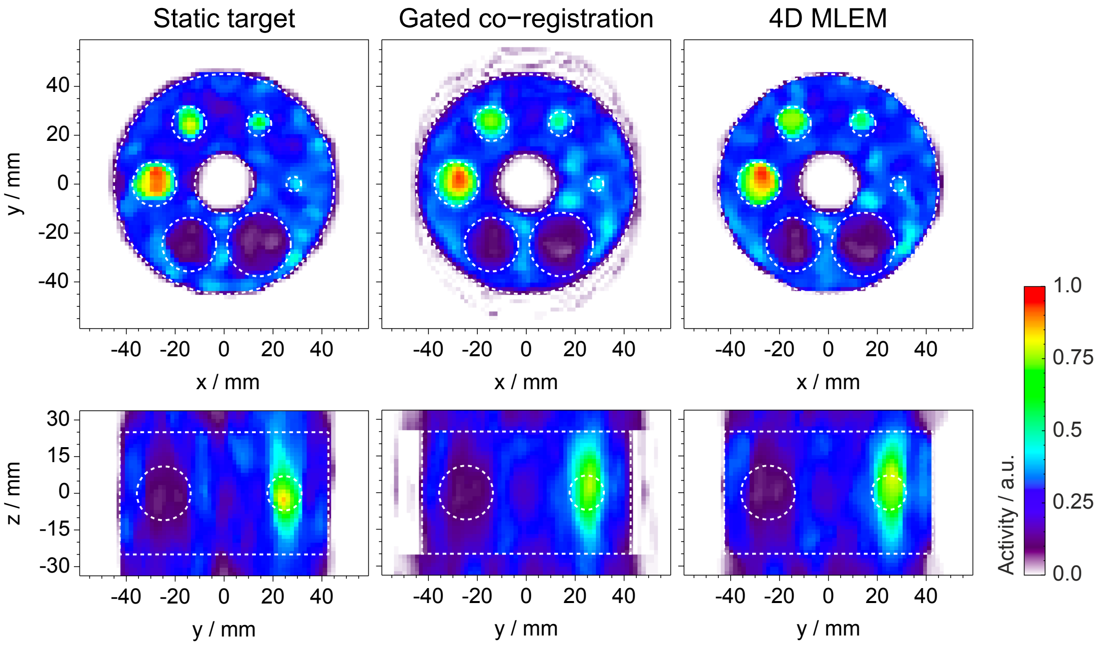

Figure 3.7: Sections through the reconstructed β^+-activity distributions for the static NEMA-like phantom (left) and for the moving one calculated by the gated co-registration (middle) and the 4D MLEM (right). The upper row displays the midplane at $z = 0$ mm and the lower row the plane at $x = -14.3$ mm. The phantom geometry corresponding to the shown sections is outlined by dashed contours. The β^+-activity distributions are scaled to contain the same total amount of activity in the whole image space.

prone to those artefacts. Due to the limited solid angle coverage and the correspondingly missing projections, prolongation artefacts in z-direction are clearly visible in all β^+-activity distributions and the cold and hot spherical inserts are not entirely recovered.

The known phantom geometry allows to quantify the local contrast recovery (LCR) of the reconstruction algorithms, i.e. how clearly the inserts can be resolved within the background activity. For the chosen cold : background : hot ratio of 0 : 1 : 4 the local contrast recovery for the hot inserts ($LCRH$) and for the cold inserts ($LCRC$) have been calculated as defined by Shakirin (2009)

$$LCRH_i = \frac{\widetilde{H}_i - \widetilde{B}_i}{3 \cdot \widetilde{B}_i} \cdot 100\% \qquad\qquad LCRC_i = \frac{\widetilde{B}_i - \widetilde{C}_i}{\widetilde{B}_i} \cdot 100\%. \tag{3.5}$$

$\widetilde{H}_i$, $\widetilde{B}_i$ and $\widetilde{C}_i$ denote for the corresponding insert i the median values of the β^+-activity in the locally considered areas which should contain hot, background and cold activity values, respectively. $\widetilde{H}_i$ and $\widetilde{C}_i$ are determined from all voxels whose midpoint belongs to the corresponding insert. Voxels with a midpoint coordinate that has a maximum distance of 3 mm from the insert (for the cylinder in radial direction only) are taken into account for the $\widetilde{B}_i$ calculation. A $LCRC$ value has also been determined for the phantom boundary for which the voxels with a maximum distance of 3 mm from the boundary have been considered. Those of them located inside the phantom have been used for the calculation of $\widetilde{B}$ and those outside the phantom for the $\widetilde{C}$ calculation, respectively. Results from all three β^+-activity distributions are displayed in figure 3.8. Except for the spherical insert of 22 mm diameter, the LCR values from the 4D MLEM are of same magnitude or exceed those values from the 3D MLEM of the static phantom. LCR of the gated co-registration is inferior for most inserts.

The reconstruction codes have not been optimized for fast performance, yet. The 4D MLEM seems to be a little faster in the current version than the gated co-registration. However, the

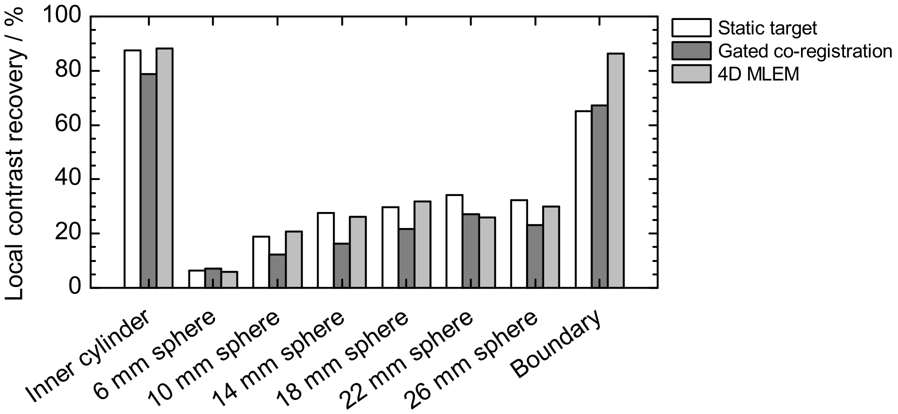

Figure 3.8: Local contrast recovery values for the inserts and the boundary (definition given in the text) of the NEMA-like phantom calculated from the reconstruction results of the static target (white), the gated co-registration (dark grey) and the 4D MLEM (light grey) using (3.5).

better LCR and the avoidance of artefacts related to the image transformation are the main criteria that count in favour to the 4D MLEM. Thus, for following investigations the 4D MLEM algorithm is applied.

3.2 Experiments with moving radioactive sources

The performance of the 4D MLEM has been systematically tested by radioactive source measurements. Therefore, two types of experiments were performed. The first proof-of-principle experiment for testing the correct implementation of the reconstruction workflow with measured data uses a relatively complex 2D motion pattern. In a second experiment campaign, the influence of the motion onto the reconstructed PET images has been investigated systematically for different parameters of the 1D motion pattern and of the reconstruction process.

3.2.1 Rotation of radioactive sources

Experimental setup

As depicted in figure 3.9, the rotating motion table (cf. appendix C.1) from the GSI facility has been positioned in between the two detector heads onto the patient couch. The height was adjusted by the patient couch so that the upper surface of the rotating platform was 1.5 mm below the isocentre height. The horizontal platform is rotated between $-14°$ and $10°$ around the vertical rotation axis which proceeds parallel to the z-axis but shifted by 50 mm in x-direction. The motion period was tuned to a value of about 3.8 s. The motion is monitored indirectly by utilizing a displacement laser sensor (Model OD100-35P840, SICK Vertriebs-GmbH, Düsseldorf, Germany) which is attached to the static part of the motion table and records continuously the distance to the edge of the moving platform.

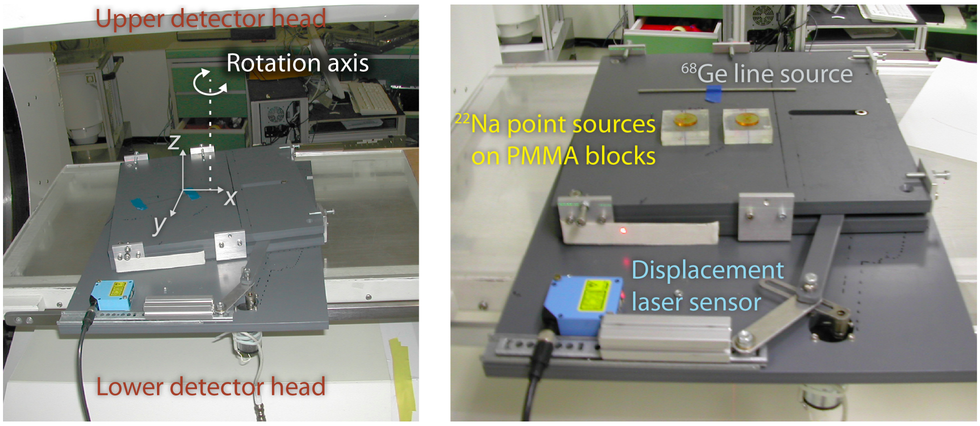

Figure 3.9: Setup for an experiment with the rotating motion table (grey) positioned at the patient couch (transparent) between the two detector heads of the in-beam PET scanner and oriented in the left-handed coordinate system (left). The blue laser sensor mounted at the static part of the motion table measures continuously the distance to the edge (white tape) of the rotating platform. A ^{68}Ge line source and two elevated ^{22}Na point sources are placed off-centred onto the top of the platform (right).

Table 3.2: Isotope, geometry, activity and position of the radioactive β^+-emitting sources.

Source ID	Isotope	Geometry	Activity	z-position	Distance to rotation axis
D8–187	^{68}Ge	line (19 cm)	6.15 MBq	0 mm	≈ 60 mm (min)
MR–137	^{22}Na	point	0.84 MBq	16 mm	≈ 50 mm
MR–138	^{22}Na	point	0.85 MBq	16 mm	≈ 95 mm

Three radioactive β^+-emitting sources with properties as summarized in table 3.2 have been placed onto the rotating platform at different positions. The line source was placed at isocentre height ($z = 0$ mm) parallel to the x-axis and shifted by about -60 mm in the y-direction. The point sources have been placed 50 mm and 95 mm apart from the rotation axis and elevated 16 mm in height by means of two PMMA blocks (cp. figure 3.9). Coincidence data were acquired under rotation and with static motion table as reference.

Data processing

The analogue voltage output signal of the displacement sensor is proportional to the distance to the moving platform but not to the rotation angle. A calibration between the relative amplitude of the laser signal and the rotation angle was done by R. Lüchtenborg from the GSI Biophysics department. The 25 sampling points (equidistant voltage signals) of this calibration and a linear interpolation for steps of 1° is plotted in figure 3.10. The analogue signal of the displacement sensor contains a high frequency noise. To get rid of this noise, a low pass filter has been applied to the signal after a fast Fourier transformation (FFT) (cp. appendix B).

A time correlation between the listmode PET data and the acquired signals from the displacement sensor is feasible by spill-like timing signals logged in both data streams. The coincidences acquired from 16 motion periods were divided into 9 phases spaced by 3° (-14°,

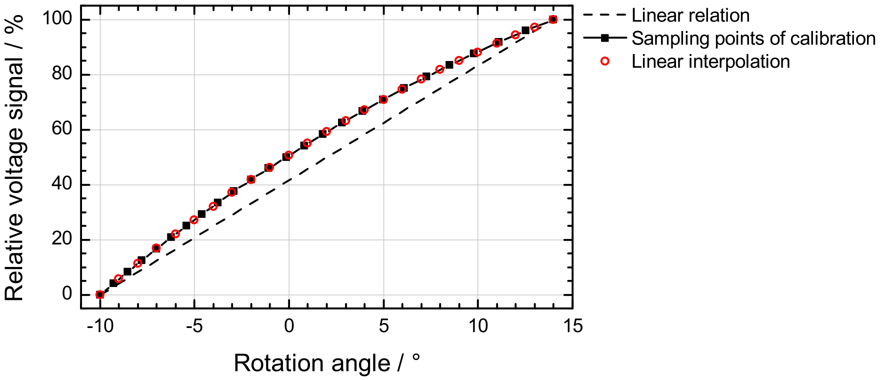

Figure 3.10: Relation between the rotation angle and the relative amplitude of the displacement laser sensor signal. The sampling points of the calibration (black squares) have been interpolated linearly for steps of 1° (red circles). The obtained relation differs obviously from a linear one (dashed line).

-11°, ... 7°, 10°). Corresponding transformation matrices were generated by using a polygon clipping algorithm for the calculation of the intersecting volumes of each rotated voxel with each voxel of the fixed grid in the image space (cp. appendix A.3).

The attenuation correction for the 511 keV annihilation photons is created for each motion phase by approximating the geometry of the motion table with attenuation coefficients μ for the corresponding materials. The internal dimensions of the ball bearing and drive mechanism is unknown. Thus, the attenuation correction considers in z-direction simply

- the 10 mm PMMA ($\mu \approx 0.110\,\mathrm{cm}^{-1}$) of the patient couch,
- 15 mm trovidur ($\mu \approx 0.127\,\mathrm{cm}^{-1}$) for the static part of the motion table,
- a 2 mm air gap to the rotating platform,
- the 38 mm thick rotating platform made of trovidur and including a 135 mm × 269 mm × 8 mm slit at the corner were the coupling from the motor drive enters the platform,
- a screw at the rotation center ($\mu \approx 0.656\,\mathrm{cm}^{-1}$) and
- the 2 PMMA blocks below the point sources, each with a dimension of 50 mm × 50 mm × 16 mm.

Activity reconstruction

The correct sorting of listmode data into motion phases is verified by reconstructing the 9 data subsets separately by the 3D MLEM algorithm. The residual motion of 3° per motion phase is neglected during the reconstruction. The number of coincidences per subset varied between 1.58×10^5 and 4.13×10^5, mainly depending on the residence time of the platform in the corresponding angular interval. The resulting β^+activities in the image space of $140 \times 120 \times 50$ voxels are shown in figure 3.11 for the height of the sources. The line source and the two point sources are well detectable, however with a considerably lower activity density in the ^{68}Ge line source compared to the ^{22}Na sources.

No remarkable blurring within the single images and a clear angular shift between the different phases demonstrate the correct sorting of coincidences into the motion phases. The activity of the point sources in the 2D images of figure 3.11 was fit to a 2D, elliptical Gaussian function

$$F(x,y) = c_0 + c_1 \cdot e^{-U/2}, \qquad U = (x'/g)^2 + (y'/h)^2, \tag{3.6}$$

where c_0 and c_1 are two constant coefficients and $2g$ and $2h$ are the axes lengths of an ellipse which has its centre at (x_c, y_c) and is oriented under an angle ϕ relative to the coordinate axes x and y. Thus, the coordinates of the rotated ellipse x' and y' given in (3.6) are calculated as

$$x' = (x - x_c)\cos\phi - (y - y_c)\sin\phi \qquad y' = (x - x_c)\sin\phi + (y - y_c)\cos\phi. \tag{3.7}$$

The upper part of table 3.3 summarizes the results for all 9 phases. The center coordinates of both sources move as expected. The residual motion per phase of source MR–137 with

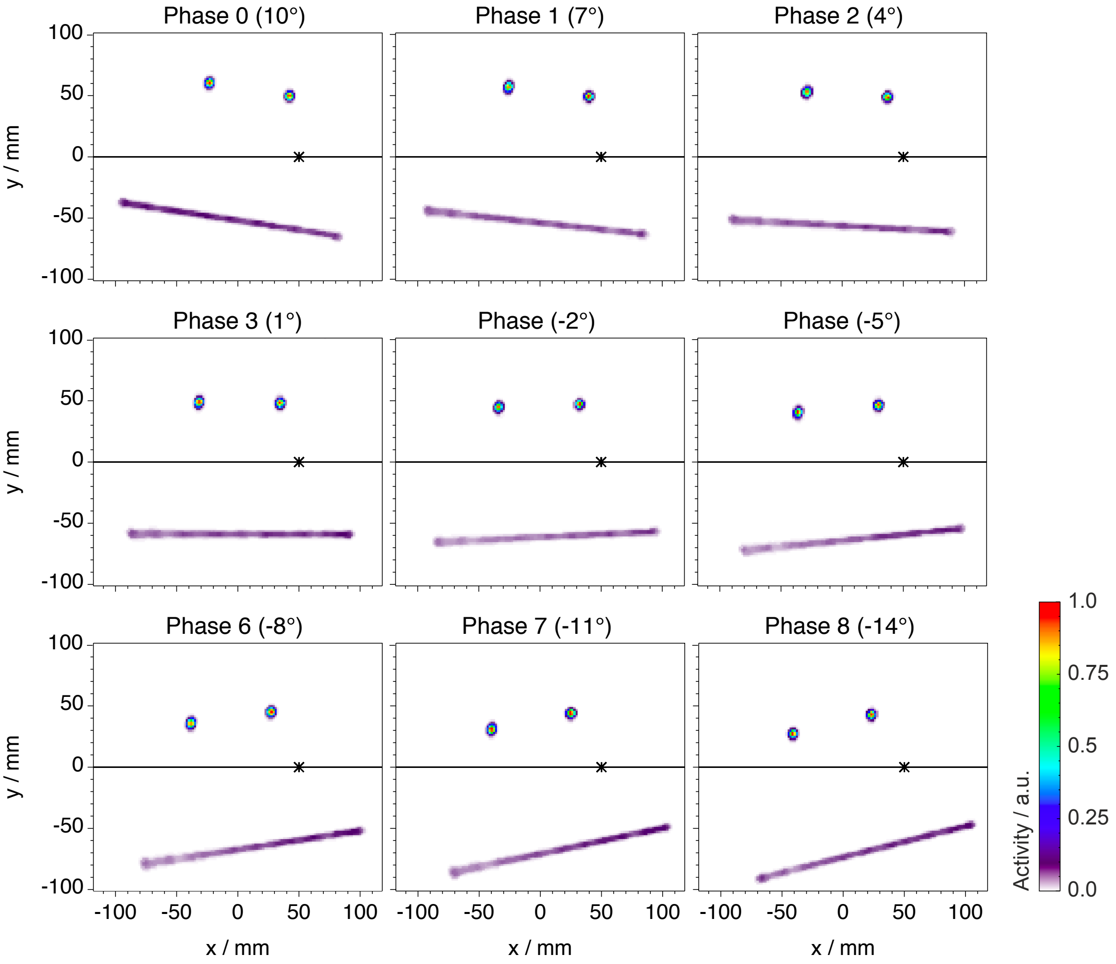

Figure 3.11: 3D MLEM reconstruction results of the phase separated listmode data with rotation angles between 10° (upper left) and $-14°$ (lower right). The upper part of the images ($y > 0$) shows the β^+-activity distribution at a height of $z \approx 16\,\mathrm{mm}$ and the lower part that for isocentre height with $z = 0\,\mathrm{mm}$. The star marks the position of the rotation axis. All images are scaled to their maximum activity.

a distance of about 50 mm to the rotation axis is defined by the arclength of circa 2.6 mm. However, the approximated semi-axes have almost the same size indicating a circular shape of β^+-activity and only inferior motion-related blurring. For source MR–138, there is a larger residual motion per phase defined by the arclength of about 5 mm. Thus, for the majority of the motion phases, there is a slight blurring artefact detectable quantified by the different lengths of the semi-axes g and h.

Figure 3.12 shows the reconstructed β^+-activities from the static reference measurement and from that with rotating platform. The 4D MLEM algorithm with correctly sorted listmode data and dedicated transformation matrices for the 2D motion pattern reproduces the results from the static reference very well. As listed in the lower part of table 3.3, the determined point source positions at (x_c, y_c) and their size is almost identical to those in the static measurement. Only the major-axis for source MR–138 is slightly increased, but stays within the range as for the single motion phases. In contrast to that, a 3D MLEM

Table 3.3: Fit results of point source activities according to (3.6) and (3.7) for images in figure 3.11 and figure 3.12, respectively. For both ^{22}Na point sources the determined center positions at (x_c, y_c) and the two semi-axes g and h are tabulated. The angle ϕ is omitted since it is not very meaningful for the almost circular shapes.

	MR–137				MR–138			
	x_c/mm	y_c/mm	g/mm	h/mm	x_c/mm	y_c/mm	g/mm	h/mm
Phase 0	42.4	49.6	2.1	2.2	−22.8	60.2	2.1	2.2
Phase 1	40.0	49.2	2.1	2.0	−25.6	56.8	2.0	2.4
Phase 2	37.4	48.5	2.1	2.0	−28.6	52.7	2.1	2.4
Phase 3	34.8	47.9	2.1	2.2	−31.3	48.6	2.1	2.3
Phase 4	32.5	47.1	2.0	2.0	−33.7	44.6	2.0	2.3
Phase 5	29.9	46.2	2.0	2.2	−35.9	40.3	2.0	2.2
Phase 6	27.6	44.9	2.2	2.1	−38.0	35.5	2.1	2.4
Phase 7	25.0	43.8	2.1	2.1	−39.8	30.6	2.1	2.3
Phase 8	23.1	42.6	2.0	2.1	−41.1	27.0	2.0	2.0
Static	34.2	47.7	2.1	2.0	−32.0	47.6	2.0	2.0
4D MLEM	34.1	47.7	2.1	2.0	−32.0	47.4	2.1	2.3
3D MLEM	31.0	46.0	9.9	2.1	−33.7	42.8	2.1	17.8

reconstruction without any consideration of the motion shows severe motion artefacts. The size of the β^+-activity spreading is correlated to the distance of the sources to the rotation axis, i.e. to the motion magnitude at the corresponding position in the FOV. Although an approximation of the smeared point source activities by (3.6) and (3.7) is not expedient, the results are included in table 3.3 and confirm at least the clear smearing in one direction.

The examination of the β^+-activities at several z-positions (not shown) reveals that resolving the source positions is at least feasible for the considered spatial region near the midplane between the two detector heads. Prolongation artefacts related to the double-head geometry are still inevitable as already known from static target measurements (Crespo *et al.* 2006).

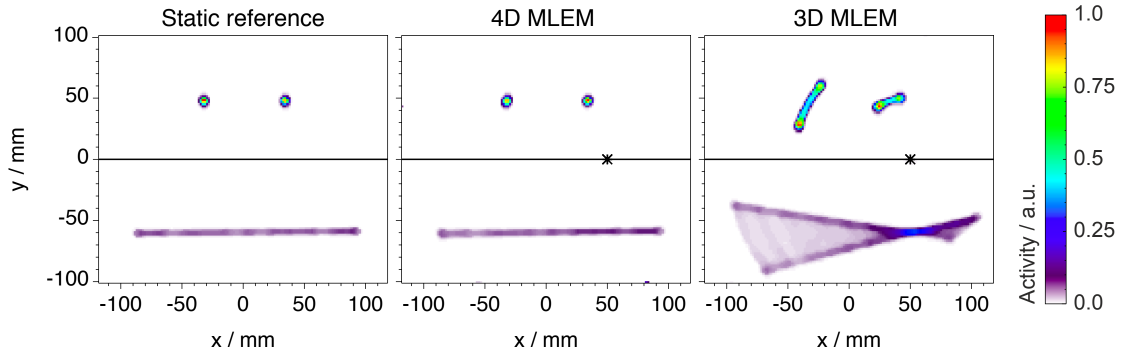

Figure 3.12: Reconstructed β^+-activity distributions from radioactive sources. Images are scaled to their individual maximum. Results are shown for a static reference measurement (left) and for the measurement with platform motion reconstructed with the 4D (middle) and 3D (right) MLEM algorithm. The upper parts of the images ($y > 0$) show the activity at $z \approx 16\,\text{mm}$ and the lower part that at isocentre height ($z = 0\,\text{mm}$). The stars mark the position of the rotation axis, which proceeds perpendicular to the x-y plane.

3.2.2 One-dimensional point source motion

After demonstrating the general functionality of the 4D reconstruction algorithm with a complex motion pattern and correct processing of the listmode data, a more systematic measurement campaign with regular 1D motion patterns has been realised. The aim was to evaluate the reconstruction result as a function of motion parameters and of the listmode data sorting and to find an acceptable setting for the evaluation of subsequent experiments.

Experimental setup

A stack of two ^{22}Na point sources with a total activity of 1.37 MBq was placed at the target holder of the in-house developed motion table (cf. appendix C.2) and positioned in the midplane between the two detector heads ($z = 0$). Motion patterns according to (2.13) have been driven with symmetric maximum elongation in $\pm y$-direction. Different peak-to-peak amplitudes a have been selected: 1 mm, 2 mm, 4 mm, 8 mm, 10 mm, 15 mm, 20 mm, 24 mm, 30 mm, 40 mm, 54 mm and 70 mm. For each value a $\cos^2$- and $\cos^4$-shaped motion was performed, i.e. the exponent $2n$ of the cosine function was adjusted with $n = 1$ and $n = 2$. PET data were acquired during 20 motion periods with a period time $\tau = 6\,\mathrm{s}$.

Data processing

For the PET data reconstruction the listmode data have been divided into 1 to 15 motion phases related to the time-correlated motion signal recorded by the motion table. Both sorting the raw data into motion phases according to the motion amplitude (equal range of residual motion) and sorting the raw data into motion phases according to the phase of the periodic motion (equal length in time) have been tested. The mean residence probability of the point sources inside each motion phase (cp.appendix E) is considered for generating the corresponding transformation matrices.

Final β^+-activity distributions are analysed in the x-y-plane ($z = 0$). β^+-activity profiles parallel (y) and perpendicular (x) to the motion direction have been extracted from the considered 2D images by summing up the pixel values in the corresponding direction. The ratio of the full width at tenth maximum (FWTM) values from both profiles ($\mathrm{FWTM}_y/\mathrm{FWTM}_x$) is calculated as figure of merit for each image. These ratios are studied as a function of the number of considered motion phases N and the mean residual motion in all phases $\overline{\Delta y}$. The mean residual motion for a periodic motion function $y(t)$ is calculated within one cycle as

$$\overline{\Delta y} = \frac{1}{N} \sum_{i=0}^{N-1} \left[\max y(t) - \min y(t)\right]_{t_i \leq t < t_{i+1}} , \tag{3.8}$$

where t_i denotes the times when the target enters a new motion phase. These times can be expressed as $t_i = i \cdot \tau / N$ for time-sorted motion phases. For amlitude sorting, (3.8) can even be reduced to $\overline{\Delta y} = \left(\max y(t) - \min y(t)\right)/N$.

Reconstructed β^+activities

The β^+-activity distributions of the moving point sources were reconstructed on an image space of $100 \times 100 \times 20$ cubic voxels with a side length of 1.6875 mm, which is one-fourth of the BGO crystal segment width of 6.75 mm. 10 iteration steps were used for the 3D MLEM (1 motion phase) and the 4D MLEM (2 to 15 motion phases) reconstructions. The calculated β^+-activity distributions in the midplane using the 3D MLEM algorithm (and neglecting the motion at all) is shown in figure 3.13 for the $\cos^4$-shaped motion ($n = 2$) and the different investigated peak-to-peak amplitudes a. Regions with pronounced activity indicate positions

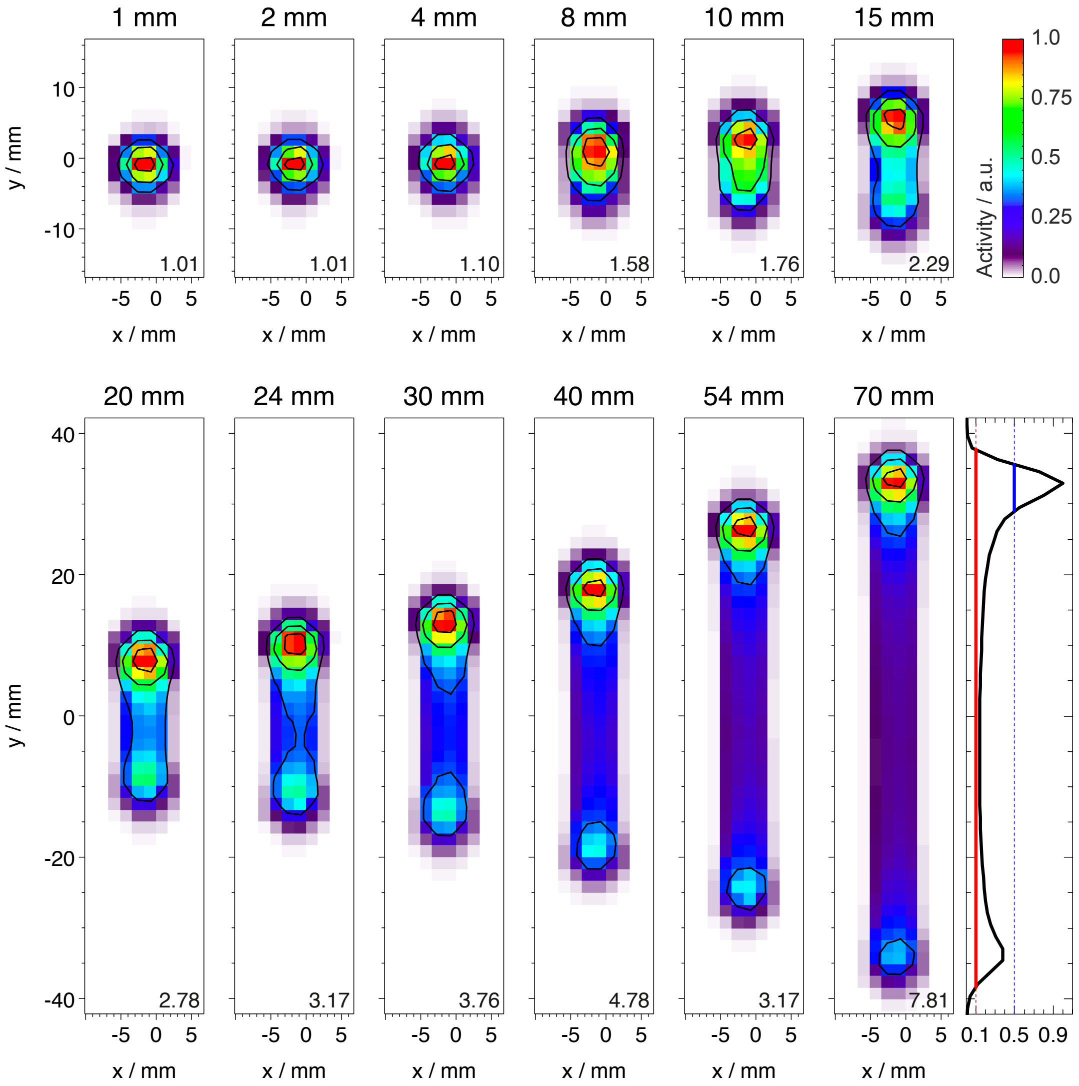

Figure 3.13: Colour-coded β^+-activity distributions reconstructed with the 3D MLEM algorithm from $\cos^4$-shaped ($n = 2$) point source motion with peak-to-peak amplitudes between 1 mm and 70 mm. Each image depicts the activity in the detector midplane and is scaled to its maximum value. Included contour lines are equally spaced. The determined ratio of the FWTM values is written in the lower right corner of each plot. The exemplary profile (black) parallel to the motion direction for 70 mm peak-to-peak amplitude clarifies the necessity to examine the FWTM values (red) instead of the more common FWHM values (blue).

of longer residence times. With increasing amplitude, these positions emerge clearly at the reversal points. Unequal intensities between positive and negative y-coordinates are related to the asymmetric motion pattern of the $\cos^4$ motion. Motion artefacts (prolongation in y-direction) appear already for relatively small motion ranges of approximately 4 mm. This is reflected by the increased values of the FWTM ratio. Instead of the commonly accepted FWHM evaluation, the FWTM values have to be examined to consider the whole range of the activity smearing. By visual investigation, a maximum FWTM ratio of 1.1 and a minimum ratio of 0.9 were defined as the limits for regarding a distribution as undisturbed. This means that the deviation between the two FWTM values is less than 10% and the distribution has almost the circular shape as it is expected from a static point source.

The listmode data have also been reconstructed using the 4D MLEM algorithm with several motion phases which have been determined according to the amplitude or time. For the $\cos^2$ and $\cos^4$ motion with a peak-to-peak amplitude of 30 mm, figure 3.14 shows exemplarily the resulting β^+-activity distributions that have been reconstructed with 1 to 8 motion phases. The FWTM ratio decreases rapidly with rising number of motion phases. However, sorting the listmode data according to the amplitude requires only 5 phases for both motion patterns to reach a FWTM ratio below 1.1. The FWTM ratios for time sorting will fall below that value only if at least 10 ($\cos^2$) or 13 ($\cos^4$) motion phases are considered, which is approximately twice the number as for sorting by amplitude. Additionally, for a small number of motion phases in the time sorting regime (and especially for the asymmetric $\cos^4$ motion) some weird β^+-activity patterns are formed, since there is a considerably large residual motion range within each or some of the motion phases.

FWTM ratios have been determined for both types of motion patterns ($\cos^2$ and $\cos^4$) with various amplitude values, both sorting techniques (by amplitude and time) and for up to 15 motion phases. Results are given in figure 3.15 as a function of the number of motion phases N and the mean residual motion $\overline{\Delta y}$ as defined in (3.8). As already demonstrated for the 30 mm peak-to-peak amplitude in figure 3.14 the remaining motion influence onto the reconstructed β^+-activity distribution is increased for a lower number of motion phases. For the same (small) number of motion phases the FWTM ratio increases with increasing peak-to-peak amplitude. If possible, sorting by amplitude should obviously be preferred, since in comparison to sorting by time, less motion artefacts are produced for the same number of motion phases and the same motion amplitude. It seems that a larger number of phases is required for compensating the artefacts arising from the asymmetric $\cos^4$ motion if listmode data are sorted by time. If FWTM ratios are plotted as a function of the mean residual motion (right column in figure 3.15), then there is no longer a dependence on the peak-to-peak amplitude. Also the dependence on the listmode sorting regime decreases. Results from the asymmetric $\cos^4$ motion are quite similar but show a steeper slope for sorting by time.

From both motion patterns and motion phase sorting regimes, it can be concluded that the spatial resolution of the motion acquisition system should be about half the size of a PET crystal element ($0.5 \cdot 6.75$ mm) to keep the corresponding uncertainty below the mean residual motion where the FWTM ratios are definitely below 1.1. Furthermore, it is indicated

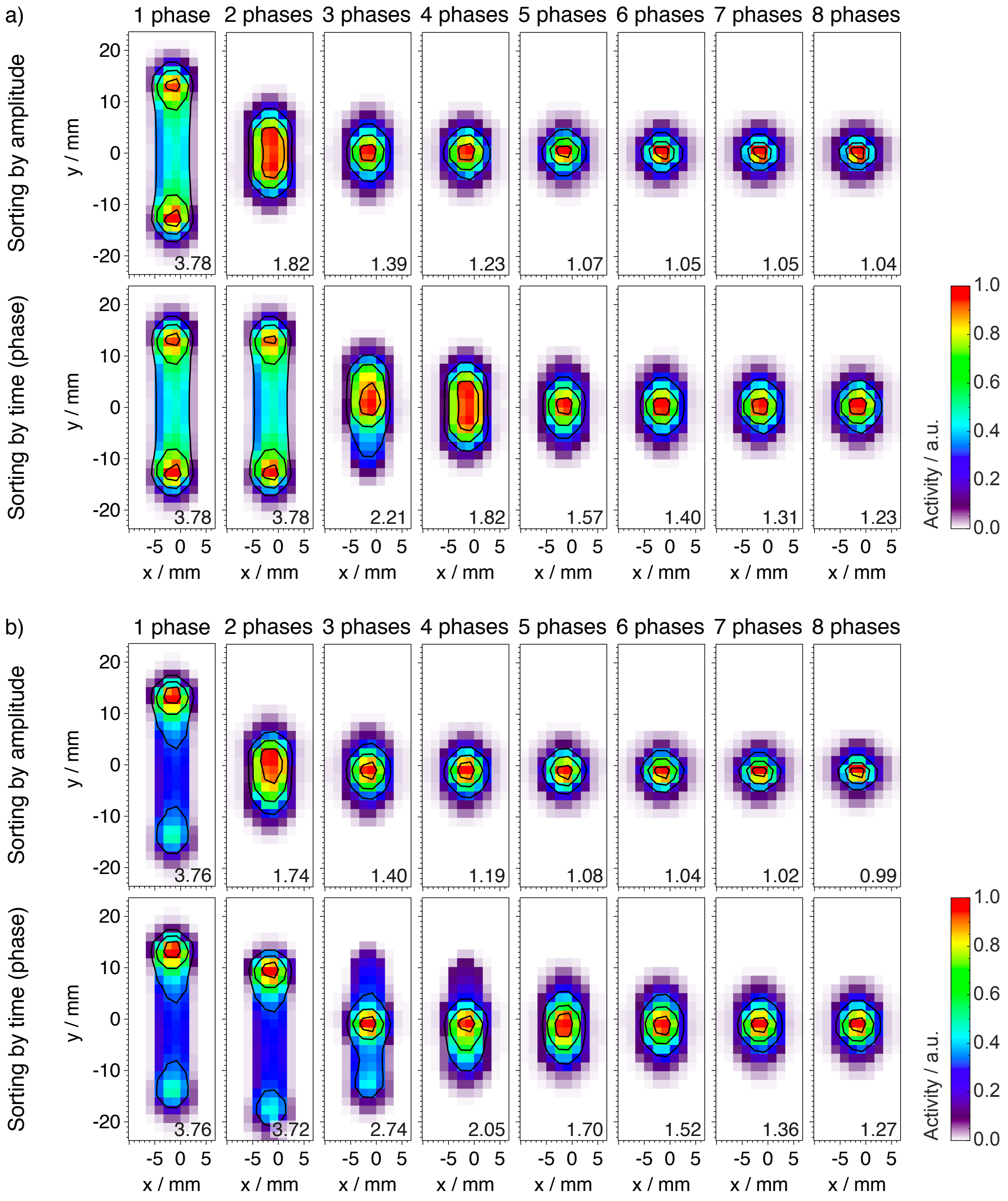

Figure 3.14: Reconstructed β^+-activity distributions and FWTM ratios (in the lower right corner) with increasing number of utilized motion phases defined for (a) $\cos^2$ and (b) $\cos^4$ motion, each with a peak-to-peak amplitude of 30 mm. The upper rows show the results for motion phase sorting by amplitude and the lower ones those for sorting by time.

by the systematic investigation that intra-fractional motion artefacts are reliably diminished by means of the 4D MLEM algorithm, at least for the clinically relevant peak-to-peak amplitudes of maximal 20 mm to 30 mm and utilizing motion phase sorting as specified by the corresponding 4D planning CT image, which consists typically of 8 to 10 motion phases. For further investigations with peak-to-peak amplitudes of 20 mm, a reasonable agreement is to perform listmode data reconstruction with 9 amplitude-sorted motion phases.

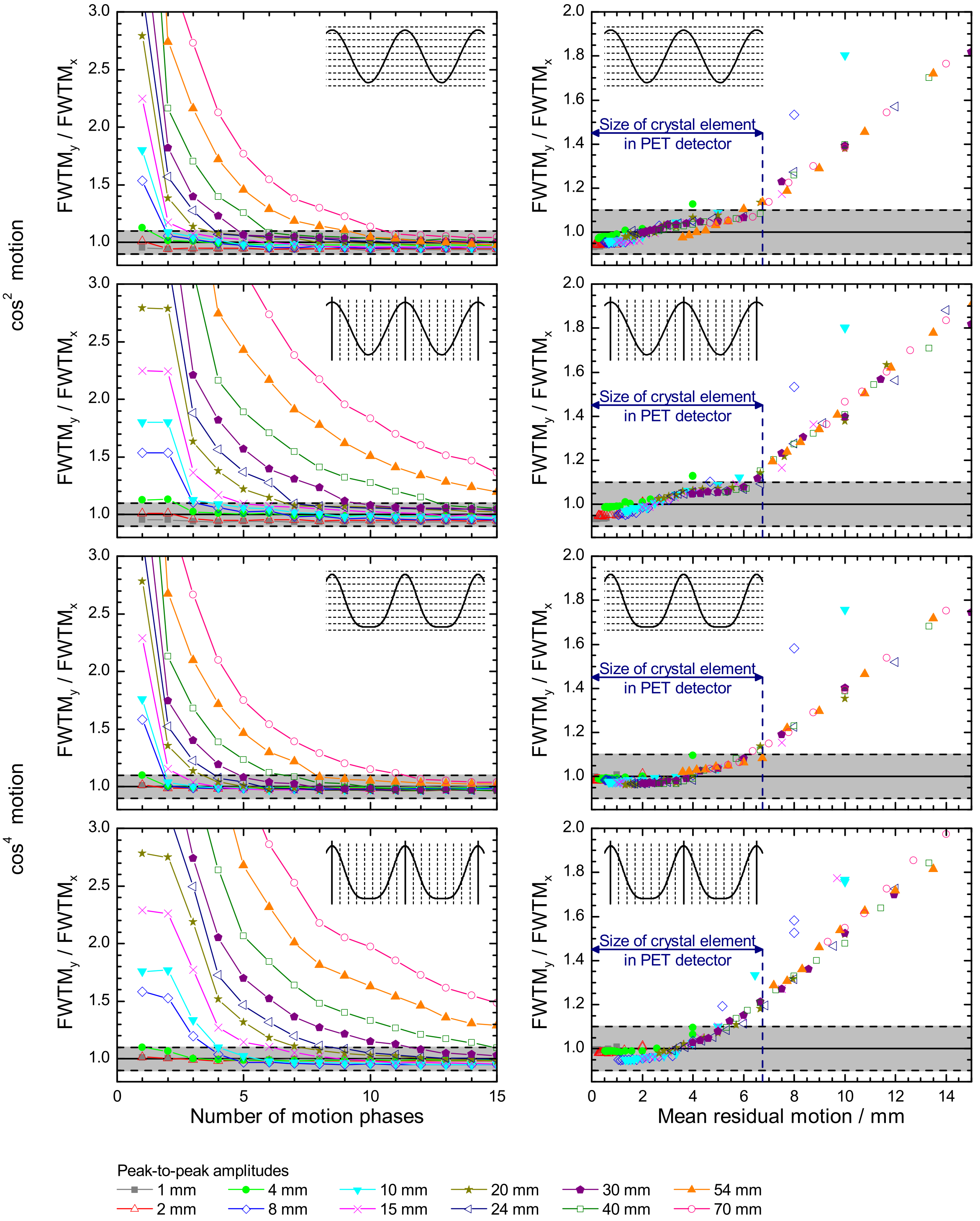

Figure 3.15: Ratio of the FWTM values of the β^+-activity profiles parallel and perpendicular to the motion direction as a function of the used number of motion phases (left) and the mean residual motion amplitude within the motion phases (right) for twelve investigated peak-to-peak amplitudes of a moving point source. Using one motion phase corresponds to a 3D reconstruction. The range of 10% deviation between both FWTM values is highlighted in grey. The first two rows are the results for cos^2-shaped motion ($n = 1$) and the last two rows for cos^4-shaped motion ($n = 2$), both for sorting by amplitude (first and third row) and sorting by time (second and fourth row).

3.3 In-beam PET measurements with moving targets

To test the 4D MLEM algorithm under more realistic conditions, dedicated phantom irradiations combined with in-beam PET measurements have been performed. Two types of experiments had been designed to verify the two major issues that have to be monitored by an *in vivo* dosimetry system in particle therapy: the range of the incident particles within the target material and the lateral field position. Both properties can be well assessed by in-beam PET measurements for static target volumes. It should be demonstrated here that under intra-fractional target motion the β^+-activity distribution ican be well represented in the static reference frame of the target by the 4D MLEM reconstruction algorithm. This would allow for a similar analysis as for static β^+-activity distributions as introduced on page 31. Therefore, static measurements serve as reference for a comparison with the 4D MLEM results.

3.3.1 Verification of lateral field position and gradients

Experiment design

Homogeneous $100\,\mathrm{mm} \times 100\,\mathrm{mm} \times 30\,\mathrm{mm}$ ($x \times y \times z$) PMMA blocks have been manufactured to serve as targets for investigating the conservation of lateral field position and gradients under target motion and different motion mitigated beam deliveries. By means of the stepping motor driven motion table (cf. appendix C.2) a target has been positioned symmetrically between the double-head PET scanner and performed a periodic $\cos^2$- or $\cos^4$-shaped motion according to (2.13) with a peak-to-peak amplitude of 20 mm. The motion proceeded perpendicular to the beam direction. A quasi-mono-energetic ^{12}C ion beam impinged almost parallel to the x-axis on the target front surface and was stopped at a depth of about 60 mm in the target. The maximum of the induced β^+-activity distribution, which is correlated to the Bragg peak region, appears approximately at isocentre depth ($x = 0$).

Due to the selection of two energies with a small difference of 1.1 AMeV (forming a tiny SOBP) and the usage of a 3 mm ripple filter (Weber and Kraft 1999), the region of the β^+-activity maximum is slightly broadened in depth and shifted in upbeam direction. The lateral target displacement was compensated by instantaneous target tracking, gated irradiation with a 30% or a 50% exhalation gating window[1] or by a simple rescanning plan. In the lateral direction, the pencil beam was scanned along a horizontal line encompassing 51 raster point coordinates on a grid with 1 mm spacing. The length of 50 mm was enlarged by adding some rasterpoints as margins for gated and rescanned beam delivery. A total margin length of 6 mm has been added for a gating window of 30%, 10 mm for a gating window of 50% and 20 mm for rescanning. For each planned beam direction, a total number (distributed over the two energies) of 7.6×10^7 ^{12}C ions has been requested to induce a high number of positron

---

[1] Within this thesis the gating window definition is related to the amplitude as follows: The given percentage defines the valid fraction of the peak-to-peak amplitude of the motion (Δa). An exhalation gating window comprises all target positions in the interval $[y_{\min},\, y_{\min} + \Delta a]$ and an inhalation gating window those positions included by the interval $[y_{\max} - \Delta a,\, y_{\max}]$, where $y_{\min}$ and $y_{\max}$ denote the minimum and maximum target elongation.

emitters for these basic experiments. To ensure a homogeneous β^+-activity distribution along the whole field width, all plans consisted of 60 rescans which had been delivered within 2–3 minutes. This is approximately the same time span needed for the delivery of a treatment field under therapeutic conditions. A motion period of $\tau = 6\,\mathrm{s}$ was selected to avoid a beat frequency with the accelerator cycle time which was about 4.5 s (2.3 s beam on, 2.2 s beam off) for target tracking and rescanning and about 8 s (5.8 s beam on - if target inside gating window, 2.2 s beam off) for gated irradiation, respectively.

In-beam PET measurements of the induced β^+-activity distributions were performed during the irradiation and additional 40 s afterwards with ongoing target motion. Thereafter, the motion was stopped and the target positioned at mid elongation. The remaining β^+-activity was assessed in a static follow-up measurement which started 355 s after the irradiation had been finished and lasted 380 s.

Data processing

For the in-beam PET measurements with moving targets, a 4D MLEM reconstruction with 9 amplitude-sorted motion phases and a conventional 3D MLEM reconstruction with neglected target motion have been performed, each within an image space of $90 \times 100 \times 30$ ($x \times y \times z$) voxels. For each motion phase, an attenuation correction has been generated by means of an artificial CT image with the target and motion table platform at mean residence elongation inside the motion phase. For the 3D MLEM reconstruction of the moving and static target, the attenuation correction considers the target at mid elongation position.

All following evaluations are presented for the listmode data with the total number of measured coincidences as well as for a thinned data set which emulates more therapy relevant counting statistics. Therefore, approximately 87.5% of the measured coincidences have been rejected randomly from the in-beam PET data in each motion phase. Events considered for the 3D MLEM reconstruction in the static follow-up measurement have been decreased by limiting the considered time interval for reconstruction to 30 s. Table 3.4 summarizes the approximate number of coincidences gained from the different experiments before and after thinning. The larger the planned target volume (increased margins) the higher is the induced β^+-activity in the target, and this is roughly reflected by the number of detected coincidences.

The main focus of attention was on the lateral β^+-activity fall-off regions. These are investigated by means of (lateral) activity profiles parallel to the motion direction and intersecting the high-activity region correlated to the Bragg peak. Deviations between the 4D MLEM profile and those from the the 3D MLEM or static follow-up are globally quantified by the normalized root mean square error (NRMSE):

$$NRMSE = \frac{1}{\max A^{\mathrm{4D}} - \min A^{\mathrm{4D}}} \sqrt{\frac{1}{m} \sum_{i=1}^{m} \left(A_i - A_i^{\mathrm{4D}}\right)^2}, \tag{3.9}$$

where m specifies the number of data points in the profiles, A_i specifies the activity values in the profile to be compared and A_i^{4D} represents those in the profile from the 4D MLEM

Table 3.4: Approximate number of coincidences contributing to the reconstruction results of the different experiments for the examination of lateral field properties.

	Entire data sets		Thinned data sets	
Experiment	In-beam	Follow-up	In-beam	Follow-up
Tracking – $\cos^2$	5.9×10^5	7.5×10^5	7.4×10^4	7.0×10^4
Tracking – $\cos^4$	5.7×10^5	7.3×10^5	7.1×10^4	6.8×10^4
Gating 30% – $\cos^2$	7.0×10^5	7.9×10^5	8.7×10^4	7.3×10^4
Gating 30% – $\cos^4$	6.3×10^5	7.7×10^5	7.8×10^4	7.2×10^4
Gating 50% – $\cos^2$	6.7×10^5	8.0×10^5	8.4×10^4	7.4×10^4
Gating 50% – $\cos^4$	5.9×10^5	8.0×10^5	7.4×10^4	7.5×10^4
Rescanning – $\cos^2$	8.1×10^5	9.2×10^5	1.0×10^5	8.5×10^4
Rescanning – $\cos^4$	8.0×10^5	9.1×10^5	1.0×10^5	8.5×10^4

reconstruction. More detailed analysis of the motion influence onto the lateral activity gradients and their conservation by means of the 4D MLEM is done by calculating the penumbra widths (between 20% and 80% of the maximum value) at the BEV left (pen_{-y}) and right (pen_{+y}) slopes of the profiles. Furthermore, the centres of mass of the activity profiles y_{COM} are examined by

$$y_{\mathrm{COM}} = \frac{\sum\limits_{i=1}^{m} y_i \cdot A_i}{\sum\limits_{i=1}^{m} A_i} \tag{3.10}$$

to quantify additional differences between 3D and 4D MLEM reconstruction results.

Evaluation of reconstructed β^+-activity distributions

The reconstructed β^+-activity distributions from high and low counting statistics for the $\cos^2$-shaped motion pattern combined with tracking, gating and rescanned beam delivery are shown in figure 3.16. Images from the reduced counting statistics have a clearly enhanced noise level but still reflect the major properties. All images show activity only inside the marked target volume with a characteristic maximum (laterally extended peak) and a sharp distal edge at isocentre depth. In lateral direction, the activity broadens with increasing treatment field size and distributions from the 3D MLEM reconstructions are laterally smeared according to the uncorrected target motion. For all cases the target size was big enough to cover the full width of the β^+-activity distribution. In comparison to the in-beam PET, the static follow-up measurements exhibit a decreased activity in the proximal plateau region relative to the peak activity. This is related to the nuclides mainly contributing to the different parts (cf. table 2.2). The peak activity is predominantly generated by projectile fragments, primarily consisting of ^{11}C with a half-life of 20.39 min. Most target fragments in the plateau region have shorter half-lives like e.g. 122.24 s for ^{15}O, and these are already mostly decayed when starting the follow-up measurement. Therefore, a comparison between the different

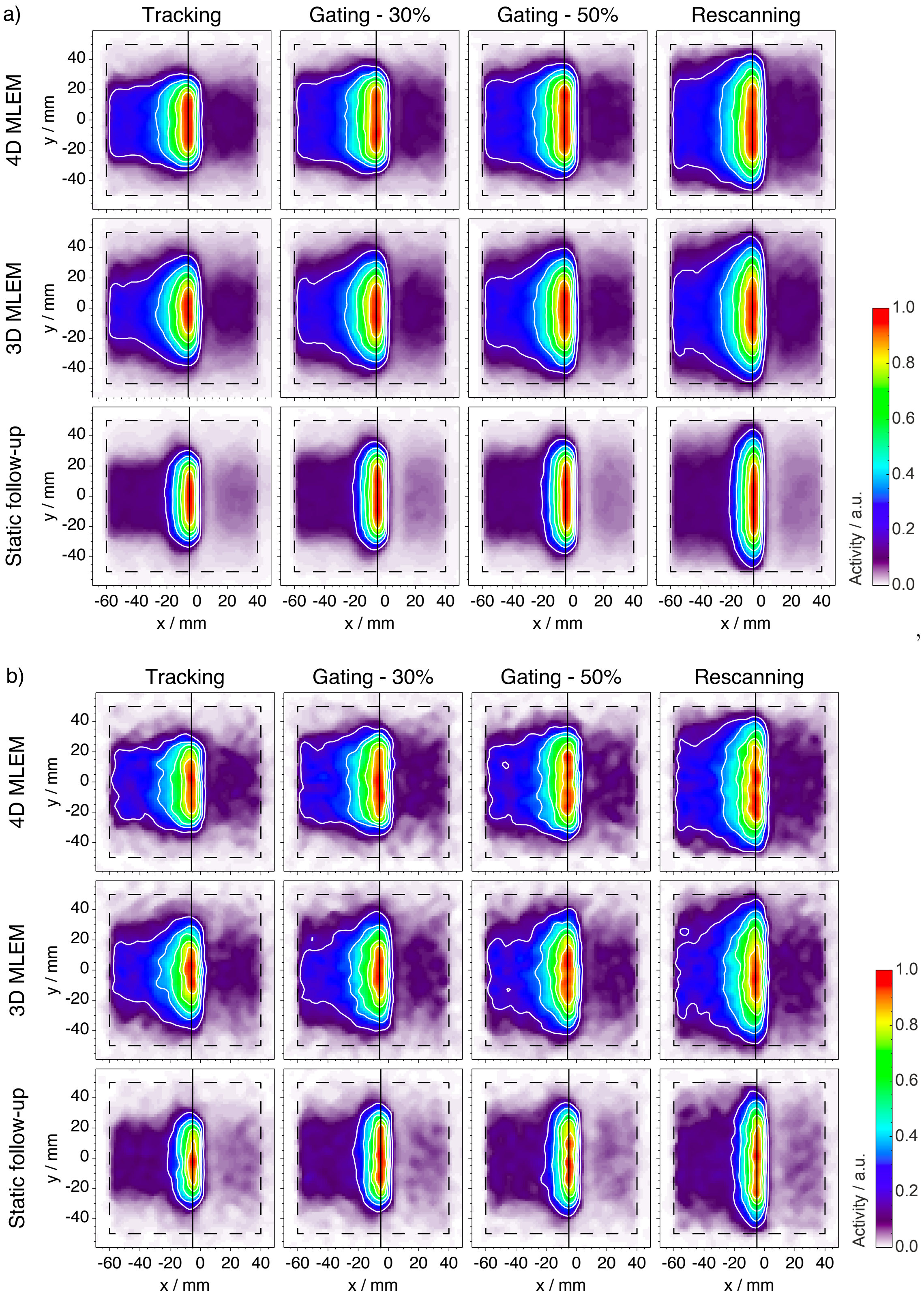

Figure 3.16: Reconstructed β^+-activity distributions summed up over the target height of 3 cm from total (a) and reduced (b) counting statistics. The beam impinged from the left on the target (dashed line). The $\cos^2$-shaped motion in y-direction was compensated by one of the four motion mitigation techniques. Results from in-beam PET data are shown for 4D (1st row) and 3D MLEM (2nd row) reconstruction in comparison to those from the static follow-up measurement (3rd row). Vertical lines indicate the position of evaluated profils.

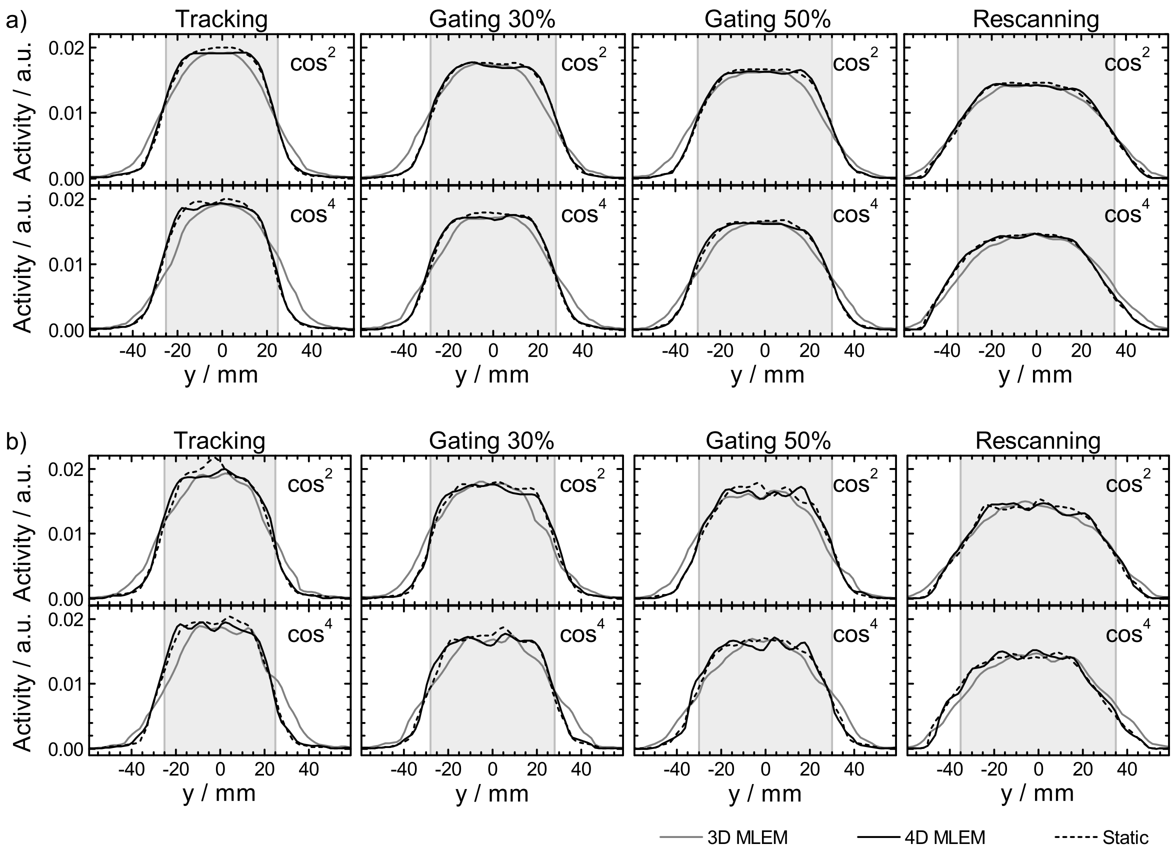

Figure 3.17: Profiles parallel to the motion direction and intersecting the high activity region (as indicated for the $\cos^2$ motion in figure 3.16) calculated from all detected coincidences (a) and from the thinned data sets (b). For each investigated motion-compensated beam delivery (tracking, gating, rescanning) profiles are shown for $\cos^2$-shaped (upper row) and $\cos^4$-shaped (lower row) motion pattern and different reconstruction methods. Solid lines stand for in-beam PET measurements with the moving target reconstructed without (grey) and with (black) consideration of the motion. The dotted line is related to the static follow-up measurement. All profiles are normalized to enclose the same area under the curve. The light grey areas indicate the widths of the treatment plans for the different motion compensation techniques.

distributions is only done in the peak region by extracting activity profiles parallel to the motion direction.

Figure 3.17 presents an overview of the profiles from the different experiments for reconstruction with high statistics (figure 3.17a) as well as for the thinned data sets (figure 3.17b). According to the better SNR in the images gained from high statistics, these profiles show a very smooth curve progression. Although profiles from the thinned data sets contain a higher noise level, the broadening according to the applied motion-compensated beam delivery technique and the related size of the added safety margins is quite well visible. In all diagrams (independent from the motion pattern, the beam delivery and counting statistics) the results from 4D MLEM reconstruction match quite well to those from the static follow-up measurement. This means that the implemented 4D MLEM reconstruction has the potential to disclose deviations from an expected β^+-activity distribution, similar as it is known from the 3D MLEM reconstruction applied for static target analysis.

Results from 3D MLEM reconstructions reach the same maximum values but have shallower lateral slopes. This blurring results in missing activity in the centred target region and additional activity in the more lateral parts. By calculating the centre of mass y_{COM} according to (3.10), it is found that for $\cos^4$ motion the 3D MLEM profiles are shifted to the right side due to the longer residence time of the target at positive elongation. From table 3.5 it

Table 3.5: Statistics of profiles shown in figure 3.17. For each profile the centre of mass y_{COM}, the NRMSE relative to the profile from the 4D MLEM reconstruction and the penumbra values for the left (pen_{-y}) and right (pen_{+y}) slope of the profile between 20% and 80% of the maximum value are tabulated.

	Profiles of figure 3.17a (all data)				Profiles of figure 3.17b (thinned data)			
	y_{COM}	NRMSE	pen_{-y}	pen_{+y}	y_{COM}	NRMSE	pen_{-y}	pen_{+y}
Tracking – $\cos^2$								
3D MLEM	−1.8 mm	7.1%	17.8 mm	18.0 mm	−1.9 mm	7.1%	19.2 mm	17.5 mm
4D MLEM	−1.7 mm	—	10.7 mm	10.0 mm	−1.8 mm	—	10.0 mm	11.5 mm
Static follow-up	−1.7 mm	2.1%	12.0 mm	11.1 mm	−1.7 mm	4.1%	13.4 mm	14.1 mm
Tracking – $\cos^4$								
3D MLEM	0.7 mm	10.1%	17.5 mm	17.5 mm	0.6 mm	10.8%	18.0 mm	17.8 mm
4D MLEM	−1.8 mm	—	9.9 mm	9.7 mm	−2.1 mm	—	9.8 mm	9.5 mm
Static follow-up	−1.8 mm	2.2%	11.1 mm	10.5 mm	−1.8 mm	3.3%	11.6 mm	12.0 mm
Gating 30% – $\cos^2$								
3D MLEM	−1.6 mm	7.9%	17.8 mm	19.1 mm	−1.6 mm	8.8%	18.2 mm	19.2 mm
4D MLEM	0.1 mm		10.9 mm	11.2 mm	0.2 mm	—	9.4 mm	10.8 mm
Static follow-up	0.1 mm	1.7%	11.7 mm	11.9 mm	0.3 mm	3.2%	11.5 mm	12.2 mm
Gating 30% – $\cos^4$								
3D MLEM	−0.1 mm	7.3%	19.4 mm	18.7 mm	0.2 mm	9.0%	20.4 mm	20.3 mm
4D MLEM	−0.7 mm	—	11.0 mm	11.5 mm	−0.5 mm	—	10.2 mm	10.3 mm
Static follow-up	−0.6 mm	2.2%	11.6 mm	11.2 mm	−0.4 mm	4.1%	13.2 mm	11.3 mm
Gating 50% – $\cos^2$								
3D MLEM	−2.0 mm	7.5%	18.1 mm	18.1 mm	−2.2 mm	7.8%	17.1 mm	19.6 mm
4D MLEM	−0.3 mm	—	12.6 mm	12.2 mm	−0.5 mm	—	14.1 mm	13.3 mm
Static follow-up	−0.2 mm	1.9%	12.9 mm	12.3 mm	−0.6 mm	4.5%	15.8 mm	11.9 mm
Gating 50% – $\cos^4$								
3D MLEM	−0.8 mm	7.4%	19.8 mm	21.0 mm	−0.6 mm	9.3%	23.0 mm	21.7 mm
4D MLEM	−1.4 mm	—	11.2 mm	13.0 mm	−1.5 mm	—	11.1 mm	13.2 mm
Static follow-up	−1.2 mm	2.1%	12.8 mm	13.2 mm	−1.1 mm	4.2%	12.9 mm	14.1 mm
Rescanning – $\cos^2$								
3D MLEM	−1.3 mm	4.9%	20.3 mm	21.9 mm	−1.5 mm	5.8%	22.6 mm	25.5 mm
4D MLEM	−1.4 mm	—	16.7 mm	17.0 mm	−1.5 mm	—	17.8 mm	16.9 mm
Static follow-up	−1.4 mm	2.5%	17.5 mm	19.1 mm	−1.5 mm	3.4%	17.0 mm	17.8 mm
Rescanning – $\cos^4$								
3D MLEM	−1.2 mm	7.0%	22.5 mm	23.3 mm	−0.9 mm	7.8%	22.0 mm	23.6 mm
4D MLEM	−3.5 mm	—	16.4 mm	19.1 mm	−3.5 mm	—	15.9 mm	19.9 mm
Static follow-up	−3.7 mm	1.8%	18.3 mm	19.0 mm	−4.0 mm	3.9%	17.9 mm	20.7 mm

can be extracted that the center of mass is shifted by about 2.5 mm if the target tracking or rescanning approach is applied. For gated irradiation, the shift is diminished to circa 0.6 mm, because the gating window has been chosen at exhalation phase. Therefore, the longer residence at exhalation often overlaps with beam-on periods when all coincidences are rejected for reconstruction due to the high number of random coincidences originating from the prompt γ-ray emission. On the contrary, for gated irradiation with symmetric $\cos^2$ motion the center of mass is shifted by about -1.8 mm due to the same practice of coincidence rejection during beam delivery. Thus, irrespective of the smeared slopes, if target motion is disregarded during the in-beam PET data reconstruction, a wrong lateral field position within the target might be identified depending on the interdependency of the beam delivery technique and motion pattern.

Furthermore, table 3.5 summarizes the results of calculated NRMSE and penumbra values for all experiments with high as well as thinned statistics. A general consistency between values from high and thinned statistics is found. However, NRMSE values from thinned data tend to be slightly increased and the penumbra values show a larger variability. The quite good matching between all 4D MLEM and static follow-up measurements is represented by a small NRMSE of $(2.1 \pm 0.3)\%$ for high statistics and $(3.8 \pm 0.5)\%$ for thinned data. Also the penumbra values of 4D MLEM and static profiles are in the same range for all measurements. For rescanning (which is no active motion compensation), the penumbras are considerably increased to values above 15 mm. Even this high value is clearly exceeded for all experiments by the penumbras of 3D MLEM profiles. The distinct difference between 3D and 4D MLEM profiles is quantified by a mean NRMSE and its standard deviation of $(7.4 \pm 1.4)\%$ for high statistics and $(8.3 \pm 1.5)\%$ for thinned data. The quite large standard deviation is related to the different behaviour in several experiments: Profiles differ a lot (NRMSE $> 10\%$) if gradients are large in the 4D profiles (tracking) and the centre of mass is additionally shifted in the 3D profiles ($\cos^4$ motion). If gradients are small in 4D profiles (rescanning) and the 3D centre of mass remains unshifted ($\cos^2$ motion), a relatively high conformity (NRMSE $< 6\%$) can be found between 3D and 4D reconstructed images.

3.3.2 Verification of particle range

Experiment design

To test the reconstruction algorithm with respect to correct range reproduction, a defined modulation of the particle range in the moving target is necessary. Ideally, this requires different particle energies if delivered to homogeneous targets and the exact motion mitigation for each energy. An alternative are targets consisting of different materials, but the density to range calibration and exact positioning might be error-prone. A third, fail-safe possibility has been conceived for testing the range verification under motion by means of in-beam PET. A defined range modulation of the incident ^{12}C ions has been ensured by a special target geometry which is shown in figure 3.18. PMMA blocks of 135 mm × 200 mm × 90 mm ($x \times y \times z$) are furnished at the proximal face surface with three cuboid structures of 10 mm width (y)

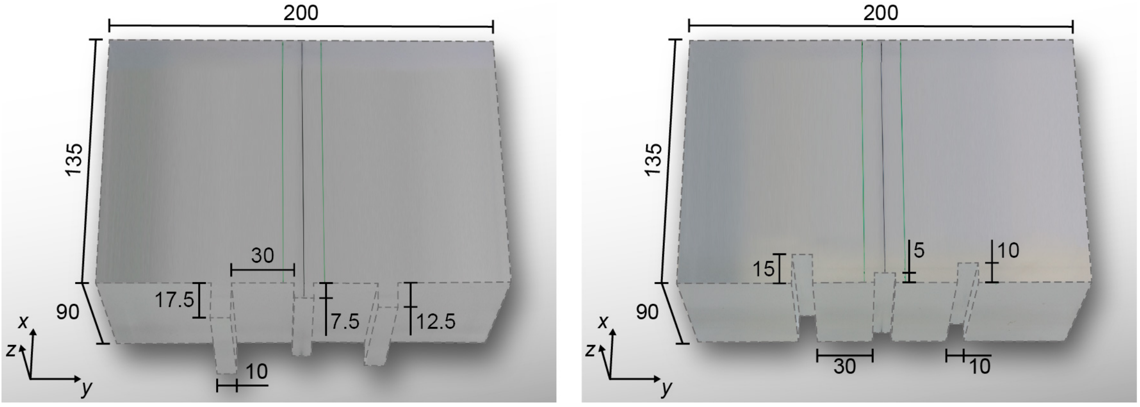

Figure 3.18: PMMA targets for the generation of defined under-ranges of 17.5 mm, 7.5 mm and 12.5 mm (left) and over-ranges of 15 mm, 5 mm and 10 mm (right) and their orientation in the coordinate system of the PET scanner (beam parallel to x, motion parallel to y and detector heads above and below in z-direction). Dimensions are given in mm. The maximum elongation of ±10 mm in y-direction is indicated for the target mid (black line) by the green lines.

and different depths (x). These cuboids are separated by 30 mm and thus form a fence-shaped structure. Cuboid thicknesses of 17.5 mm, 12.5 mm and 7.5 mm have been chosen for realizing defined under-ranges of the ions in the target. For generating over-ranges, the pattern is inversely carved into the PMMA block with depths of 15 mm, 10 mm and 5 mm. Irrespective of the exact motion pattern and motion mitigated beam delivery technique, the distal edge of a treatment field composed of quasi-mono-energetic pencil beams retraces the fence structure at an energy-dependent depth in the target.

The treatment plan and measurement regimes were similar to those for the experiments in section 3.3.1. The treatment plan consisted of 2 energies with a difference of 1.1 AMeV and contained for both energies 141 raster scan coordinates (on a virtual grid with 1 mm spacing) arranged at a horizontal line. The plan with a total number of 10.8×10^9 ^{12}C ions is delivered by means of 60 rescans between the minimum (-70 mm, BEV left) and maximum (70 mm, BEV right) coordinate within approximately 5.3 min. The PET listmode data have been acquired during this time plus additional 40 s and within a static reference measurements taken from the same targets 355 s past irradiation and lasting for 380 s. For two selected measurements, the target motion was compensated by means of lateral tracking. Using the stepping motor driven motion table (cf. appendix C.2), the target with under-range geometry performed a $\cos^2$ motion and the over-range target a $\cos^4$ motion, both according to (2.13), with a peak-to-peak amplitude a of 20 mm and a period τ of 6 s.

Data processing

The data from in-beam PET and static follow-up measurements have been reconstructed on an image space of $100 \times 130 \times 60$ ($x \times y \times z$) voxels and under consideration of the corresponding attenuation corrections. In-beam PET data have been reconstructed by the 4D MLEM with 9 amplitude-sorted motion phases and by the 3D MLEM algorithm, both using the high

Table 3.6: Approximate number of coincidences contributing to the reconstruction results from the entire and thinned data sets for both fence-shaped target geometries.

	Entire data sets		Thinned data sets	
Experiment	In-beam	Follow-up	In-beam	Follow-up
Under-range – $\cos^2$	12.8×10^5	10.2×10^5	7.7×10^4	7.9×10^4
Over-range – $\cos^4$	12.9×10^5	10.2×10^5	7.7×10^4	7.9×10^4

statistics of the entire data sets or a more clinically relevant counting statistics gained by a random rejection of 94% of the initial data in each motion phase. To meet similar statistics in the static follow-up data, the time interval considered for reconstruction was shortened to 25 s. The approximate number of the examined coincidences are summarized in table 3.6 for the original and thinned data sets and both targets. The number of coincidences is similar for the under- and over-range target, since the treatment plan and the motion mitigation technique were the same for both experiments.

Reconstructed β^+-activity distributions are evaluated with respect to a correct reproduction of the distal edge position relative to the static reference by means of an automated range comparison (Helmbrecht *et al.* 2012). Since ^{12}C ion beams have been used, the distal β^+-activity peak is dominated by the projectile fragment ^{11}C which has a reasonably long half-life of 20.39 min. This allows for a good identification of the distal edge position even in the static follow-up measurements. The comparison algorithm operates on 1D profiles in the longitudinal direction (parallel to the beam) and compares for each pixel of the BEV the distal fall-off between a reference profile and a profile from the β^+-activity distribution to be evaluated. Reference profiles are normally obtained from the reconstruction of a simulated data set, but for these experiments, they are extracted from the static follow-up measurement. Profiles to be compared are scaled to their own maximum value. Only the distal interval where the β^+-activity profile decreases from 0.8 to 0.2 is considered for examination. This part is shifted against the reference profile until the area which is enclosed between both profile segments has reached its minimum. The required shift is considered as the range deviation between both distributions at the corresponding position.

Evaluation of reconstructed β^+-activity distributions

Reconstructed β^+-activity distributions in the midplane between both detector heads are represented for the initially high statistics in the upper part of figure 3.19a. From a visual investigation, it is found that the high-activity region inside the target retraces the pattern of the proximal target surface after the 4D MLEM reconstruction and in the static follow-up measurement. This means that the straight line of highest activity proceeds parallel to the y-direction and is disrupted due to the segments corresponding to the convex or concave structures at the target surface which protrude into proximal and distal direction, respectively.

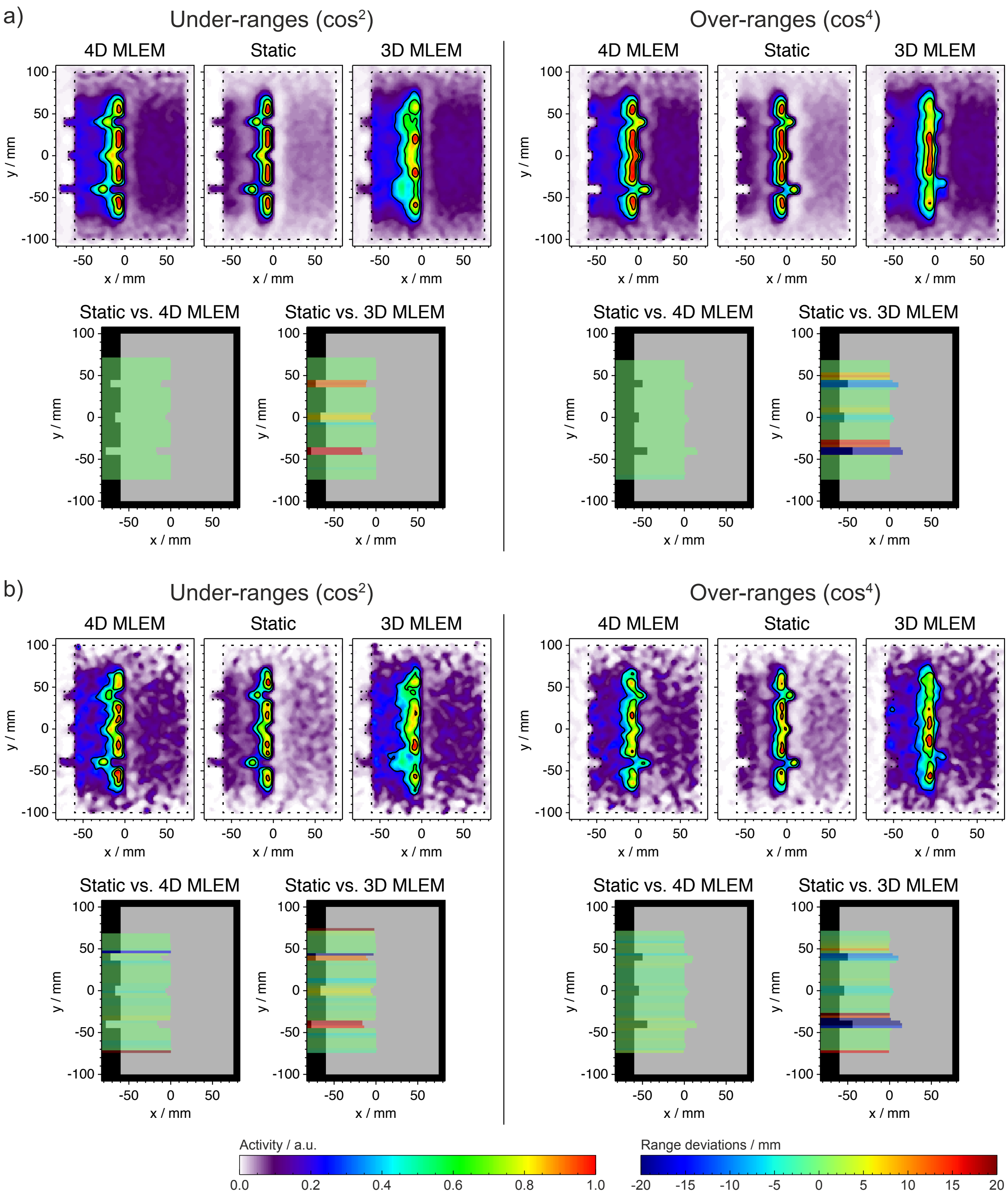

Figure 3.19: Reconstructed β^+-activity distributions in the targets with under-range (left) and over-range (right) geometry for the entire data sets (a) and thinned data sets (b) and the corresponding results from automated range comparison. The respective target is indicated by its dotted boundary in the β^+-activity distributions and as grey scale CT image superimposed to the range differences. β^+-activity images are scaled to their maximum value. Range deviations are indicated in red for detected over-ranges and in blue for detected under-ranges. Same ranges are represented in green.

Contrary to that, the reconstructed β^+-activity distribution using the conventional 3D MLEM algorithm illustrates clearly the malfunctioning of the reconstruction if the target motion is neglected. Besides the broadening of the activity distribution in lateral direction as already shown by the experiments in section 3.3.1, a distinctly and visibly disturbed shape of the distal edge is found. Due to the target motion, β^+-emitters can decay several millimetres apart from the location where they have been created. And since the peak-to-peak motion amplitude is larger than the 10 mm wide target structures, the distal edge seems to form an almost continuous vertical line in the images. This means that approximately the same range would be approved for each 1D profile extracted parallel to the beam direction. Solely, the slight prolongations of the high-activity region into the proximal direction for the under-range target and into the distal direction for the over-range target give an idea of the actually induced shape of the β^+-activity distribution formed by the target geometry. The positions of these prolongations in lateral direction depend directly on the motion pattern. For the symmetric $\cos^2$ motion, a symmetric blurring is formed around the target structures at mid elongation. If the target undergoes the $\cos^4$ motion, the prolongations emphasize the mean residence position in the motion cycle. Thus, the prolongations are shifted to larger y-coordinates relative to the positions of the target structures at mid elongation.

The results of the automated range verification for reconstructions with all measured data are shown in the lower part of figure 3.19a. Range deviations for the 4D and 3D MLEM reconstruction results relative to those for the static measurement are represented as colour-coded bars superimposed to the CT image with the target at mid elongation. The length of a bar illustrates the reference range (where the activity of the static target decreases to the value 0.2) at the corresponding lateral position and its colour the detected deviation. For the over-range as well as the under-range target, the algorithm identifies at all lateral positions the same range for the 4D MLEM reconstruction as that in the static reference. For the 3D MLEM reconstruction, serious range deviations have been found at the positions of the planned range modulations. In the under-range target, these deviations correspond to the disappeared gaps in the pattern of the distal edge, and the detected over-range values coincide with the depth of the convex target structures. A concave structure in the over-range target generates in comparison to the static reference a regions of over-range and a regions of under-range as well. This has to be rated under the consideration of the asymmetric $\cos^4$ motion with a longer residence time at larger y-coordinates. Due to that main residence position, the planned over-ranges are found next to the real target structures which is indicated by the warm colour spectrum (yellow, orange and red). In return, at the actual positions of the planned over-ranges, the distal edge is found at more proximal positions than expected. These deviations are interpreted as under-ranges and are shown in different shades of blue which correspond approximately to the depth of the three target structures.

The upper part of figure 3.19b shows the equivalent reconstruction results for the thinned data sets as for the high statistics in figure 3.19a. The SNR is obviously decreased, but the characteristic patterns of the distal edges are quite well reproduced by the 4D MLEM reconstruction and in the static follow-up measurements. Consequently, the related images for range deviation in the lower part of figure 3.19b consist mainly of bars in different shades of green representing the similar range in both distributions. Only at two profiles in the under-range target, the algorithm was not able to find the correct range which is indicated by one red and one blue bar. Irrespective of these two bars, the maximal absolute range deviation was below 3.5 mm. In the β^+-activity distributions of the 3D MLEM reconstruction, the specific pattern of the distal edge disappears in the same way as seen in figure 3.19a. Images representing the detected range deviations for 3D MLEM reconstructions are quite similar to those extracted for the data sets with high statistics. This includes on the one hand the detected over-ranges in the profiles which intersect the convex structures in the under-range target. On the other hand, in the over-range target the characteristic regions are found with a similar intensity of over- and under-range, except for the smallest structure depth in the middle of the target. No over-range is detected there due to the reduced image quality.

From the experiments with fence-shaped target geometry, it can be concluded that the 4D MLEM algorithm is able to reproduce the exact shape of the distal fall-off region in the reference frame of the target, also for the known low counting statistics in clinical in-beam PET measurements. Thus, irrespective of the applied motion pattern, the information about the correct dose deposition in longitudinal direction can be extracted and over- as well as under-ranges are detectable in a reliable way. This would not be possible if target motion is neglected during the reconstruction process.

3.4 Summary and discussion

Reconstructed β^+-activity distributions from IBT-PET measurements of static and well fixated tumour entities are suitable for monitoring the accurate localization of the dose distribution and particle ranges in the patient. For intra-fractionally moving targets, the image quality suffers from blurring artefacts independent of the applied measurement regime, either in-beam, in-room or off-line. Dedicated time-resolved reconstruction algorithms have to be applied to obtain realistic β^+-activity distributions. Normally, these algorithms are commercially provided for diagnostic imaging with conventional full-ring scanners and can be directly applied for the in-room and off-line PET data reconstruction. In-house developments of IBT-PET scanners which are implemented into the treatment site for in-beam PET measurements have unique detector arrangements (Enghardt *et al.* 2004a; Yamaya *et al.* 2008; Nishio *et al.* 2010) and thus require adapted 4D reconstruction algorithms. In this context, a 4D MLEM algorithm was implemented for the unique in-beam PET scanner Bastei at GSI and was verified by dedicated experiments. Although this scanner is not used for patient monitoring anymore, meaningful information can be acquired for similar future installations.

In comparison to the approved 3D MLEM reconstruction for static targets, a 4D MLEM calculation requires additional operating expense. Several input data have to be handled correctly for a successful image reconstruction:

- Instead of a single 3D CT volumetric image, a whole set is necessary for a time-dependent attenuation and scatter correction.

- Transformation matrices between the different 4D CT image phases have to be created. This is quite simple for the presented phantom experiments with well-defined rigid motion patterns. For real 4D patient CT images, dedicated software has to be utilized to extract the motion information including non-rigid tissue deformation. However, by means of the transformation matrices, any motion can be considered in the 4D MLEM algorithm as it was demonstrated for 1D motion and for the rotating radioactive sources.
- The surrogate motion signal has to be recorded during the whole measurement time and it has to be correlated to the CT phases as well as synchronized with the listmode PET data stream.
- On the basis of the detected motion signal, the listmode PET data have to be divided into the different motion phases, ideally in the same way as given by the 4D CT image. For commercial systems, the user might have no influence on CT and PET data sorting. Traditionally, 4D CT binning is done by phase but first commercially available retrospective amplitude-binning demonstrated superior performance in terms of reduced image artefacts (Li *et al.* 2012). By means of the comprehensive off-beam PET measurements with moving point sources (cp. section 3.2.2), the same finding were obtained for the PET data sorting. Therefore, the evaluation of in-beam PET phantom measurements in section 3.3 was done by amplitude-sorted motion phases, although similar results would be achievable by time sorting using a larger number of motion phases.

Although an instantaneous intervention during the beam application is not possible by means of IBT-PET, a fast evaluation of the a fractionated dose distribution is desired before delivering the next fraction. Therefore, as many as possible steps in the PET reconstruction workflow should be automatized. For instance, in clinical application it is necessary to automatize at least the synchronization of the listmode PET data stream with the motion signal to speed up the data preparation. With the 4 byte long listmode datawords (cp. figure 2.9) of the in-beam PET scanner BASTEI and the existing hardware, it is not feasible to implement the motion information directly into the PET data stream. Thus, the time consuming synchronization was done manually by means of logged accelerator signals in both data streams (cf. appendix D).

Anatomical changes, mispositioning or even treatment errors are mainly reflected by blurred lateral β^+-activity gradients and shifted distal edge positions. The phantom experiments verified that the 4D MLEM algorithm allows for an exact reproduction of both quantities in comparison to static reference measurements. Since the double-head PET scanner has a limited solid angle coverage and the number of induced β^+-emitters in patients is comparably small relative to diagnostic PET imaging, attention was also paid to clinically relevant counting statistics when examining the information content of the images. A reduced SNR decreases the image quality for lowered counting statistics, but the considerable difference between a 4D and a 3D MLEM reconstruction of the same data set remains clearly accessible.

The correct reproduction of the distal edge progression has been approved for range modifications $\geq 5\,\mathrm{mm}$. One might claim that these modifications are quite large and that smaller range variations should also be detectable under the target motion. However, compact lung tumours are often totally embedded in the less dense lung tissue as shown in the CT image in figure 3.2. Changes of the soft tissue geometry (e.g. due to tumour shrinkage during therapy) and/or the dense rib tissue (e.g. due to patient mispositioning) might cause larger range deviations of up to some centimetres in the lung tissue because of the large density differences of the penetrated tissues. These deviations are well detectable at the correct positions after a 4D MLEM reconstruction.

4 Simulation of phase-sorted in-beam PET data for moving targets

Contents

The reconstruction of the induced β^+-activity distribution without motion artefacts in the quasi-static reference frame of a moving target (chapter 3) is only one of the major prerequisites for a successful *in vivo* dose monitoring by means of IBT-PET. Since the dose distribution cannot be extracted directly, the validation of the deposited dose distribution is done by means of a comparison between the β^+-activity distributions reconstructed from the measured and from simulated data, as it is illustrated in figure 2.10. Thus, the simulation software for generating predicted PET data is also an essential part of the whole dose verification routine and needed to be upgraded for intra-fractionally moving target volumes. A first 4D simulation program for listmode data expected to be taken from irradiated moving targets was elaborated together with Dr. Stefan Menkel within the framework of his master's thesis (Menkel 2011). A revised version of the program was published in Physics in Medicine and Biology (Laube *et al.* 2013) and presented at the 4th 4D treatment planning workshop (Laube *et al.* 2012e).

4.1 Upgrading the IBT-PET simulation from 3D to 4D

The new 4D simulation program is widely based on the 3D program which had been developed at FZR and was proven by its application within the cancer treatment pilot project at GSI for the in-beam PET data simulation of about 440 patients with static tumour entities. Details about the 3D simulation code can be found in the literature (Hasch 1996; Pönisch

2003; Pönisch *et al.* 2004). The most relevant parts are briefly outlined together with the description of the new 4D simulation program.

4.1.1 General and motion-related simulation demands

In general, for each incident ion of the therapeutic beam the program has to

- simulate the generation of certain nuclides at distinct positions inside the tissue and at defined time points,
- simulate the decay of the nuclides at a certain time after their generation including all subsequent interaction processes of slowing down the positron until its annihilation,
- simulate the propagation and the interactions of the annihilation photons in the patient specific tissue,
- determine whether the annihilation photons are registered in the PET detectors for creating a true coincidence,
- save these valid events as a listmode data stream which can be processed by the reconstruction program like a measured one.

For the intra-fractional motion the existing 3D IBT-PET data simulation had to be upgraded by using time-resolved (4D) algorithms to consider the relative movement between the target volume and the ion beam. The time-dependent anatomical changes in the patient are relevant to simulate the accurate positron emitter distribution generated during the irradiation. Moreover, the simulation has to account correctly for the motion-dependent displacement of the generated β^+-emitters which are transported together with the moving structures until they decay. The decay positions depend on the random decay times and they usually differ from the positions where the nuclides had been created.

The complexity of the simulation does not only depend on the target motion, but also on the selected motion mitigation technique used during beam delivery. Table 4.1 summarizes for

Table 4.1: Required changes relative to the planned treatment which are instantaneously performed during the different motion mitigated beam deliveries for active pencil beam scanning. The 4D simulation has to consider the actually applied raster scan coordinates and the delivered number of ions with their energy.

Motion mitigated beam delivery	Changes in treatment plan during irradiation
Rescanning	None
Gating	None, only timing of beam delivery is adapted
Lateral tracking	Changed raster point coordinates
Depth-compensated tracking	Energy of ions passively changed before entering the patient (done instantaneously during lateral tracking)
Dose compensation[1]	Number of ions per raster point instantaneously recalculated during depth-compensated tracking

---

[1] Dose compensation defines a sophisticated technique that tries to homogenize the dose distribution in the proximal energy layers taking into account the previous dose allocation from already irradiated more distal energy layers (Lüchtenborg *et al.* 2011).

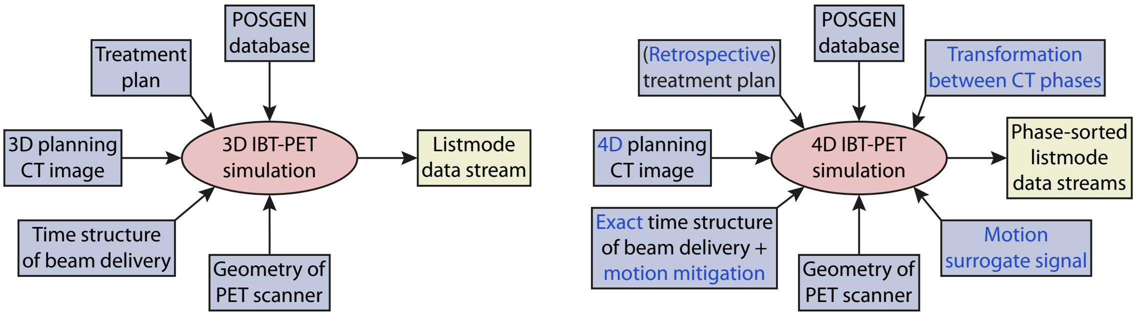

Figure 4.1: Comparison of the required input parameters and information (blue boxes) for the simulation of a IBT-PET listmode data streams that are expected to be measured during the treatment of a static (left) and of an intra-fractionally moving target volume (right). Additional parameters for the 4D simulation program are highlighted.

the different motion mitigation techniques the changes relative to the scheduled treatment plan which are required during irradiation. These changes are not predictable prior the treatment, since they depend on the individual progress of the dose deposition and motion states. To gain simulated listmode data which are comparable to the measured ones, the actual beam directions as well as the real energy and number of ions delivered to these raster coordinates have to be taken into account by the 4D simulation software. Therefore, several input parameters and additional information are required as shown in figure 4.1. These are shortly explained in the following section.

4.1.2 Input parameters for the 4D simulation program

POSGEN database The simulation of the induced positron emitter distributions by ^{12}C ion pencil beams utilizes a database created by the Monte Carlo simulation program POSGEN (Hasch 1996; Pönisch *et al.* 2004). This program is based on the energy-dependent cross sections for nuclear interactions occurring during the irradiation of PMMA with ^{12}C ions (Sihver *et al.* 1996; Sihver and Mancusi 2009). For each of the 252 available ^{12}C ion energies between 80 AMeV and 430 AMeV that can be delivered for therapeutic application by the heavy ion synchrotron at GSI, there exists one database file. These files contain the coordinates of the different β^+-emitting nuclides that are most likely generated inside a PMMA phantom which has been hit by a pencil beam of 10^5 ions with the corresponding energy. A short section of one of the database files is illustrated in figure 4.2. For each possible β^+-emitting nuclide, the half-life and the maximal positron energy can be extracted from an additional look-up table (LUT).

4D planning CT image The simulation of the β^+-emitter distribution in the patient is based on the planning CT. Coordinates of the induced β^+-emitters taken from the POSGEN database are transferred into the CT images under consideration of the breathing cycle and the related CT phases and using a calibration between the HUs that are extracted from the corresponding phase of the 4D planning CT image and the WEPL (Rietzel *et al.* 2007). Fur-

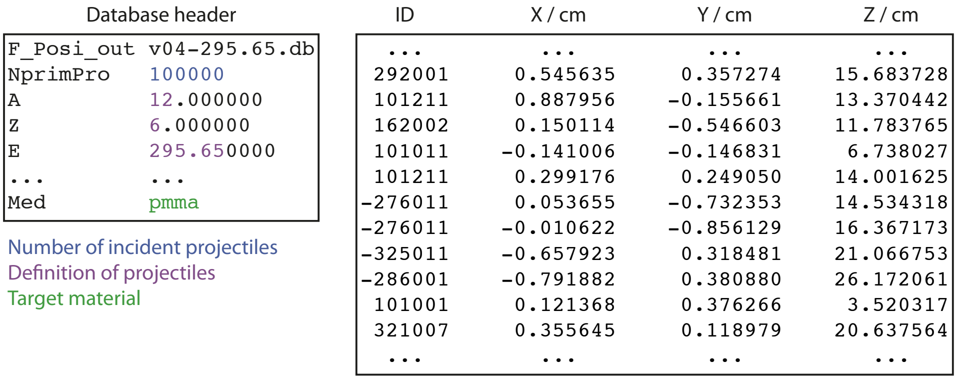

Database header

```
F_Posi_out v04-295.65.db
NprimPro   100000
A          12.000000
Z          6.000000
E          295.650000
...        ...
Med        pmma
```

Number of incident projectiles
Definition of projectiles
Target material

```
   ID         X / cm       Y / cm       Z / cm
   ...         ...          ...          ...
 292001      0.545635     0.357274    15.683728
 101211      0.887956    -0.155661    13.370442
 162002      0.150114    -0.546603    11.783765
 101011     -0.141006    -0.146831     6.738027
 101211      0.299176     0.249050    14.001625
-276011      0.053655    -0.732353    14.534318
-276011     -0.010622    -0.856129    16.367173
-325011     -0.657923     0.318481    21.066753
-286001     -0.791882     0.380880    26.172061
 101001      0.121368     0.376266     3.520317
 321007      0.355645     0.118979    20.637564
   ...         ...          ...          ...
```

Figure 4.2: Exemplary short section of a POSGEN database file (right) with its header (left) for 10^5 ${}^{12}_{6}$C projectiles impinging on PMMA with an energy of 295.65 AMeV. The ID of each generated β^+-emitter allows to identify the specific isotope with its corresponding half-life. The given coordinates of the β^+-emitters in the PMMA target refer to the propagating beam along the Z-axis and the target front surface positioned at $Z = 0$.

thermore, the different CT images are used to simulate the interaction processes of emerging positrons and annihilation photons within the patient tissue

Transformation between CT phases The transportation of the positron emitters with the moving target structures from their position of creation to the decay point is obtained from the transformation between the corresponding motion phases. By means of dedicated software the transformation matrices between the several CT phases can be extracted automatically from the 4D planning CT image. The matrices contain for each voxel in the CT image of the start phase an average 3D vector for its translation to the destination phase. To reduce the number of the required memory-consuming transformation matrices two sets of matrices are used. The first set describes the transformation from each phase to a defined reference phase and the second one the transformation from that reference phase into the different motion phases. In summary the number of required matrices is only twice the number of motion phases in the 4D CT image.

Motion surrogate signal Each point in time during the beam application and thePET measurement can ideally be correlated to one of the 4D CT phases by means of the a dedicated motion surrogate signal. This ensures to position a β^+-emitter from the POSGEN database into the correct CT phase and to determine the CT phase related to its decay time.

(Retrospective) treatment plan The treatment plan for active pencil beam scanning (cp. section 2.2.1) consists of two parts. A so-called plan file defines the target point[2], the couch angle and the gantry angle. Thereby, the beam incidence and the beam direction in the 4D CT image can be calculated. The raster-scan file contains for each required energy slice the beam parameters energy, focus size and intensity as well as the single raster point coordinates

---

[2] The target point is the coordinate in the planning CT image that matches with the fixed isocentre in the treatment room after the patient has been positioned on the treatment couch

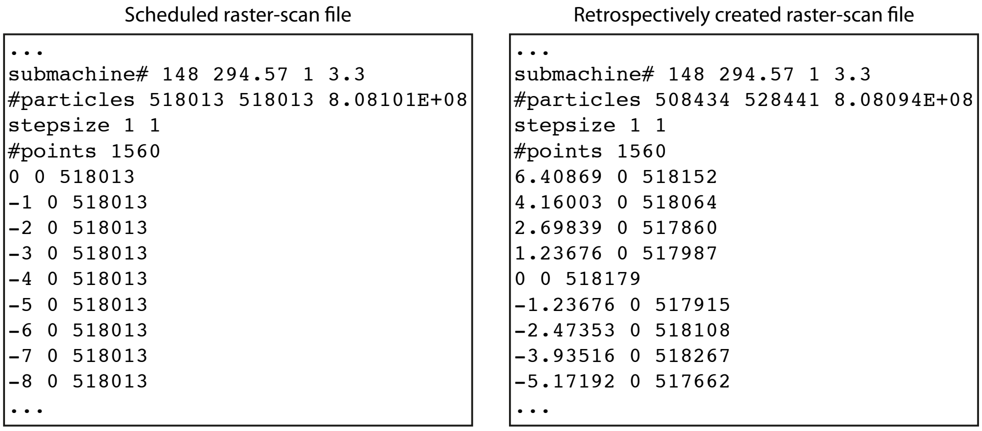

Scheduled raster-scan file

```
...
submachine# 148 294.57 1 3.3
#particles 518013 518013 8.08101E+08
stepsize 1 1
#points 1560
0 0 518013
-1 0 518013
-2 0 518013
-3 0 518013
-4 0 518013
-5 0 518013
-6 0 518013
-7 0 518013
-8 0 518013
...
```

Retrospectively created raster-scan file

```
...
submachine# 148 294.57 1 3.3
#particles 508434 528441 8.08094E+08
stepsize 1 1
#points 1560
6.40869 0 518152
4.16003 0 518064
2.69839 0 517860
1.23676 0 517987
0 0 518179
-1.23676 0 517915
-2.47353 0 518108
-3.93516 0 518267
-5.17192 0 517662
...
```

Figure 4.3: Exemplary, short section of a retrospectively created treatment plan (right) using the information from the multi-wire and ionisation chamber recorded during the irradiation of a moving phantom using the lateral tracking technique. The initially scheduled plan (left) intended a horizontal scanning of the pencil beam from 0 mm to −8 mm with an equal number of ions delivered at each raster point. Since the beam has followed the target motion, actual raster scan coordinates from 6.4 mm to −5.2 mm were detected.

in BEV with the optimized number of ions to be delivered to each point (Krämer *et al.* 2000; Krämer and Scholz 2000). As shown in table 4.1, the planned number of ions is delivered to the planned direction during gated or rescanned beam delivery and the initially scheduled treatment plan can be used for simulation. For more sophisticated motion mitigation by means of tracking or dose compensation, the beam direction and potentially also the number of particles are adjusted during the irradiation according to the current target position. The actual beam direction and the number of delivered ions are monitored during the beam application by MWPCs and ICs mounted at the beam nozzle (cp. section 2.2.2). Thus, a retrospective treatment plan is created that contains for each scheduled raster point the actual beam direction and delivered number of ions with their initial energy. A short example for a retrospective raster-scan file in comparison to the scheduled one is given in figure 4.3.

Exact time structure of the beam delivery and motion mitigation In the 3D simulation program, the irradiation time of the raster points was roughly estimated from the recorded begin and duration of the beam extraction periods of the synchrotron. Within each energy slice, the raster points with their planned number of particles were proportionally divided within the spills of the related energy and the irradiation time of the raster points was simply set to the begin of the corresponding spill. In contrast to that, for the 4D simulation the exact delivery time for each raster point has to be known due to the changing CT image states. The time structure of the beam delivery is documented by the recorded nextpoint signals which are generated when the prescribed amount of ions has been delivered to a raster point (cp. section 2.2.2).

Before the ions enter the target material, their energy might have to be adapted if depth compensated tracking is performed. Due to a possibly relative movement between the target volume and the surrounding tissue the ions could pass other anatomical structures than planned. A wedge system for ion range modification is available for experiments at GSI (Weber *et al.* 2000; Grözinger *et al.* 2006). It increases or reduces the amount of absorbing PMMA material between beam exit window and phantom surface in an extremely fast way (shift of 5 mm WEPL within 16 ms (Saito et al 2009)). The related additional WEPL has to be considered for the ion range determination of the corresponding raster point when positioning the β^+-emitters into the CT images.

Finally, by combining the information from the nextpoint signals, the changing wedge thickness as well as the surrogate motion signal, a LUT is created. In combination with the retrospective treatment plan, the following data are provided for each raster point: the number of delivered ions, the raster scan coordinates, the initial beam energy and its related WEPL, the additional WEPL of the range-compensating wedge system and the CT image phase (extracted from the next point signal in combination with the motion surrogate signal).

Geometry of the PET scanner The final detection of valid coincidences depends directly on the detector geometry. A simulation for a full-ring PET scanner will result in a higher count rate than for a double-head scanner due to the different solid angle coverage. Currently, only the BASTEI scanner geometry (cp. section 2.4.2) with the coordinates of all 4096 BGO crystal elements is implemented. The detection efficiency is simulated using the mean free pathlength of the detector material. Additionally, the format of the listmode data output is related to the considered PET scanner with its valid LORs.

4.1.3 Workflow of the 4D simulation program

A flowchart of the 4D IBT-PET simulation program is shown in figure 4.4. The simulation program processes sequentially the single raster points given by the treatment plan. For each of them the simulation can be divided into the parts of the β^+-emitter generation and the β^+-emitter decay with the subsequent detection of annihilation photons.

Generation of β^+-emitters

For the planned number of ions delivered to one raster point, a related number of β^+-emitters with their coordinates in PMMA is sampled from the POSGEN database. The mixture of β^+-emitters created in a patient differs from that given in the database due to the specific tissue composition in comparison to PMMA. This is basically corrected for by introducing an oxygen enhancement factor that induces an isotope-specific sampling from the POSGEN database. The occurrence of β^+-emitting oxygen isotopes is enhanced relative to other β^+-emitters. The coordinates of the sampled β^+-emitters in PMMA are transformed into WEPL. The information provided by the nextpoint and the motion surrogate signal determines the current CT image phase to be considered. The transversal coordinates are related to the CT image under the consideration of the couch angle and the point of beam incidence. The real depth of the β^+-emitters in the patient measured along the beam direction (given by the retrospective treatment plan) is calculated from the CT image using a HU to WEPL

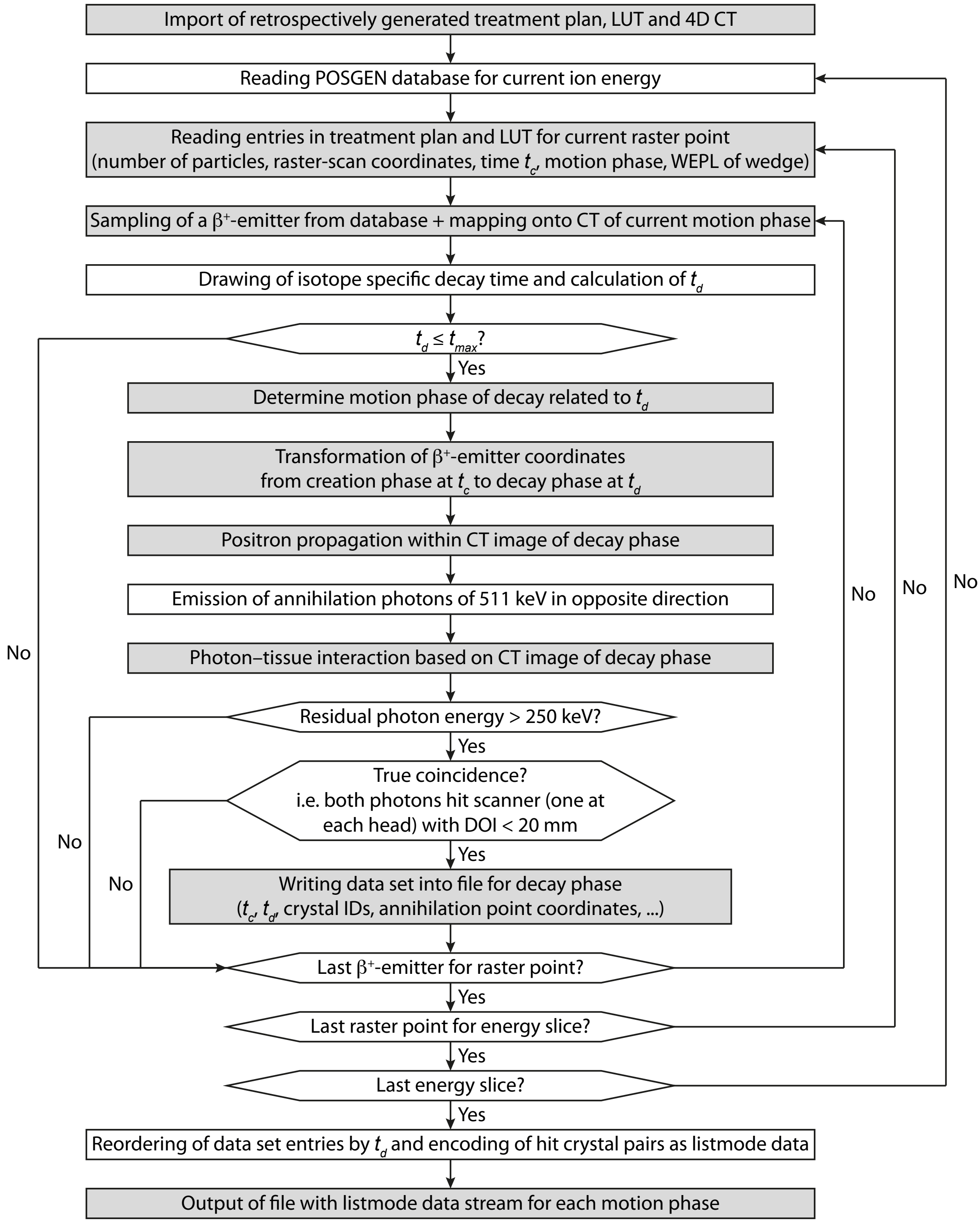

Figure 4.4: Flowchart of the 4D IBT-PET simulation program for generating motion phase sorted listmode files for the geometry of the Bastei PET scanner on the basis of the temporal structure and progress of a real irradiation. Boxes highlighted in grey indicate the new or changed algorithms or sections where e.g. attention has to be paid to the correct handling of the 4D CT image phases.

calibration and the current water-equivalent thickness of the wedge system. All β^+-emitters from one raster point are assigned to one creation time t_c which is equal to the time of the corresponding nextpoint signal.

Decay of β^+emitters

After positioning the β^+-emitters related to the irradiation of one raster point into the CT image the decay is simulated individually for each single β^+-emitter. This includes the positron propagation and positron-electron annihilation as well as the photon propagation, interaction and detection.

A decay time t_d of a nuclide is determined by drawing a random time t from the exponential distribution with the corresponding decay constant and adding it to the creation time t_c of the nuclide ($t_d = t_c + t$). Further simulations are only done for β^+-emitters if their decay time t_d is less than the last time point t_{max} that has been recorded in the data set of the measurement. For β^+-emitters fulfilling this criterion, the CT image phase associated with the time point t_d is extracted. The coordinate of the β^+-emitter is changed from the CT phase of its creation to the CT phase where the decay takes place according to the tissue deformation between the two phases by applying the transformation matrices.

The following simulation steps are done in the same way as in the 3D simulation but with the new coordinates in the CT image phase of the decay. A positron is emitted in an arbitrary direction with an energy randomly chosen from the nuclide-specific β^+spectrum. The ranges of the positrons are taken from the stopping power and range table for electrons (ESTAR) of the National Institute of Standards and Technology (Berger et al. 1999). These are converted into the range in tissue by means of the CT image. The resulting final destination of the positron is considered as the point of annihilation. There, two photons of 511 keV are emitted in arbitrary but opposite directions. Interactions of the photons within the tissue are implemented as a probable incoherent scattering and photon absorption. Photon detection is simulated for the geometry and material of the BASTEI PET scanner.

Creation of listmode data streams

Information about the valid coincidences in each decay phase (like creation time t_c, decay time t_d and coordinates of the positron-electron annihilation as well as the crystal IDs of the LOR) is collected during the simulation progress. Due to the program structure, the data set entries are gathered with ascending creation time t_c of the nuclides related to the currently considered raster point. Therefore, after the simulation of the β^+-emitter decay has been completed for all raster points in all energy slices, the data set entries for the detected coincidences are reordered in each motion phase according to the decay times t_d. Generated listmode data words encode the crystal IDs and the beam status (cp. figure 2.9). The data words of each motion phase are stored as a listmode data stream including time stamps every 10 ms. This allows the same processing by the reconstruction program as for measured listmode files. Different to measured listmode files, random coincidences during the beam extraction periods are omitted, since the physical processes leading to the emission of prompt γ-rays are not included in the simulation software, and neither delayed nor multiple coincidences are simulated.

4.2 Verification of the 4D simulation code by means of a preclinical phantom study

The developed 4D simulation program has been verified by means of a series of test simulations for a 2D moving β^+-emitting source, for artificially simplified and for the real irradiation of moving phantoms (Menkel 2011). An exemplary experiment with one-dimensional sinusoidal target motion has been selected to demonstrate the full potential of the 4D simulation code, namely the simulation of a performed experiment with motion compensated beam delivery by means of depth-compensated target tracking (Saito *et al.* 2009; Bert *et al.* 2010).

4.2.1 Experiment design

Phantom geometry A $100\,\mathrm{mm} \times 100\,\mathrm{mm} \times 30\,\mathrm{mm}$ $(x \times y \times z)$ PMMA block was positioned relative to the isocentre and centre in the FOV of the double-head PET scanner. In the beam direction (x-axis) the isocentre was located 60 mm behind the proximal target surface, and in the y-z plane it was centred in the target. The phantom performed a 1D sinusoidal motion in y-direction with an amplitude of $\pm 10\,\mathrm{mm}$ and a period of about 3.5 s. A fixed PMMA bolus of 7 mm depth was placed proximal to the moving phantom at $y > 0\,\mathrm{mm}$. This means that in BEV one half of the phantom was covered by the bolus and ions passing the bolus require a higher energy to deposit their dose at the same depth in the phantom. This geometry illustrates a simplified model for irradiating a target volume behind tissue of different density, like treating a compact moving lung tumour behind the almost static ribcage with its bony ribs and the less dense intercostal spaces. A sketch of the target setup is shown in figure 4.5.

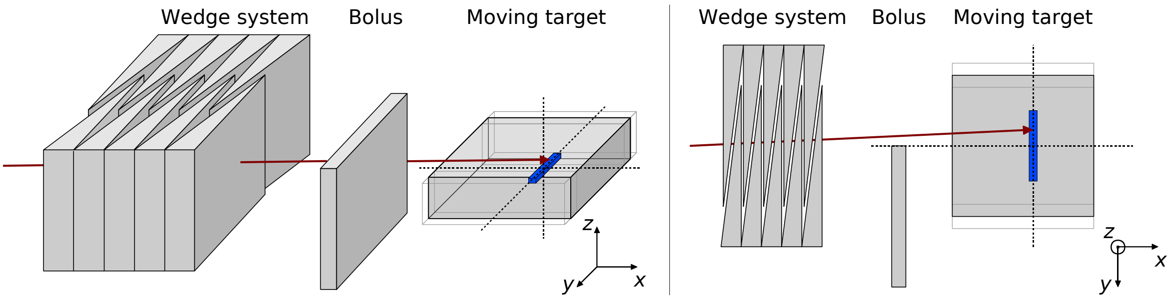

Figure 4.5: Sketch (not to scale) of the experimental setup in oblique projection (left) and bird's eye view (right) with range compensating wedge system, static bolus and the target moving perpendicular to the beam (red) direction. The blue region indicates the position of the planned target volume. Dashed lines mark the coordinate system with the isocentre at the origin. By means of an artificial 4D CT image only the bolus and the target are placed in the FOV of the PET scanner.

Scheduled treatment plan To achieve a constant ion range in the phantom, two levels of ^{12}C ion energies have been used in the treatment plan. The lower level with 294.6 AMeV and 295.7 AMeV was used for raster points with negative y-coordinates and the higher level with 303.1 AMeV and 304.2 AMeV for those with positive y-coordinates. The Bragg peaks are additionally slightly broadened by the 3 mm ripple filter in the beamline (Weber and Kraft 1999). For simplicity and demonstrating basic features, the treatment field created for the static target consists of only 51 different raster scan coordinates located at isocentre height ($z = 0$) on a line segment which proceeds parallel to the y-axis and motion direction ($-25\,\mathrm{mm} \leq y \leq 25\,\mathrm{mm}$). During 60 rescans in each half ($y \leq 0\,\mathrm{mm}$ and $y > 0\,\mathrm{mm}$) a total number of about 3.96×10^9 particles is delivered to the phantom leading to the creation of a high number of β^+-emitters. Thus, the detection of the emerging annihilation photons during the spill pauses results in a clear PET signal which is convenient for such fundamental experiments. For orientation, an estimated mean dose of about 35 Gy is deposited within a total target and bolus volume of about $34\,\mathrm{cm}^3$.

Beam delivery and motion mitigation The whole treatment plan is delivered within 24 spills of a nominal duration of 2 s within a 5 s long synchrotron cycle time. To guaranty an accurate dose deposition in the moving target, the depth-compensating tracking system at GSI has been used. The lateral target tracking is done by the magnets of the raster scanner and the required range compensation due to the static bolus geometry by means of the wedge system. Without range adaptation, the wedges provide a medium water-equivalent thickness of 92.5 mm. If raster points have been planned with the lower energy level but the beam passes the bolus due to the lateral tracking, the wedges will be opened to provide a reduced WEPL of about 84 mm. On the contrary, if raster points have been planned with the higher energy level but the beam misses the bolus during the irradiation, the wedges will be closed to provide an increased WEPL of about 101 mm.

4.2.2 4D in-beam PET data simulation

Preparation of input parameters

An artificial 4D CT image has been created with 9 amplitude-sorted motion phases, and the corresponding transformation information for each voxel was calculated directly from the well-known geometry and rigid phantom motion. A LUT with entries for all 6120 scheduled raster scan points has been generated from the recorded motion and nextpoint signals, the actual beam directions and the changed wedge thickness. A segment of the assembled LUT is shown in figure 4.6. The information about the current motion phase over time is given for the 106 s of the motion compensated beam delivery and for additional 5 min afterwards to allow for a simulation of an in-beam and a subsequent decay measurement.

Simulation of 4D listmode data

The described irradiation with depth-compensated target tracking has been simulated. A section of the resulting count rates of coincidences within the 9 amplitude-sorted listmode PET data files is shown in figure 4.7. It verifies the correct sorting of coincidences into the 9 motion phase sorted data streams. Only if the target resides in a certain motion phase, a count

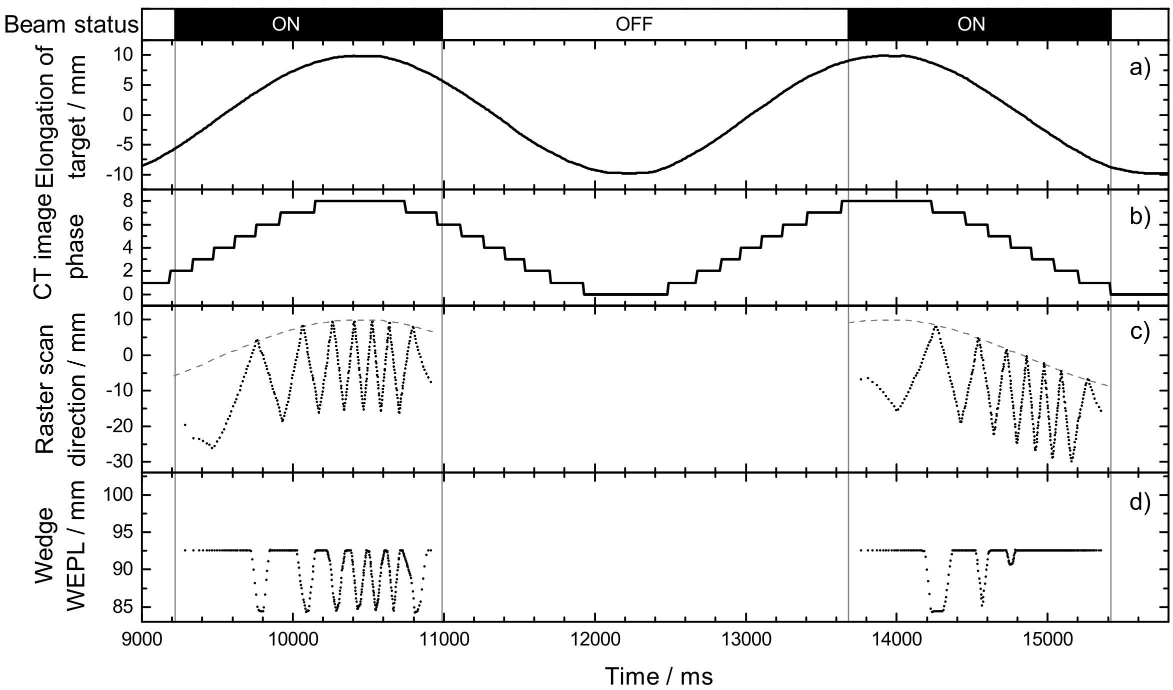

Figure 4.6: Section of the assembled LUT related to the motion surrogate signal for the sinusoidal motion (a). The 9 CT image phases (b) are assigned to time throughout the whole measurement according to the detected target amplitude. The acquired beam directions (c) for the shown 718 raster points irradiated with 294.57 AMeV during two spills differ from the planned coordinates ($0\,\text{mm} \leq y \leq -25\,\text{mm}$) due to the lateral tracking of the target motion (dashed line). Almost 28 rescans of the line-shaped treatment plan are represented by the zigzag pattern. To perform a range compensation, the water-equivalent thickness of the wedges (d) is reduced if the beam (partly) passes the bolus ($y > 0\,\text{mm}$).

rate larger than 0 will be found in the corresponding listmode file. During the irradiation time the count rate rises up to an average value of about 120 coincidences per 10 ms (which is the same order of magnitude as for the measured data) and decreases, as expected, continuously until the end of the simulated measurement time due to the exponential decay of the created positron emitters.

Regardless of the spill signal, a total amount of 2.9×10^6 valid coincidences occurred during the simulated time span. However, coincidences detected during the spills have to be rejected during the reconstruction process for a better comparability between measured and simulated β^+-activity distributions. The reason for that is that measured listmode data contain a huge number of random coincidences due to the prompt γ-ray emission during the beam extraction. These random events do not contain valid PET information but exceed the number of true events by several times. Therefore they are ignored during the reconstruction. Since processes leading to the emission of prompt γ-rays are not included in the simulation program, mainly the coincidences emerging from the short living β^+-emitters ^{13}O, ^{12}N, ^{9}C and ^{8}B are affected by the omission of the coincidences detected during spills. The remaining number of coincidences per motion phase is primarily related to the residence time of the target within this phase, but it might happen that a motion phase overlaps more often with

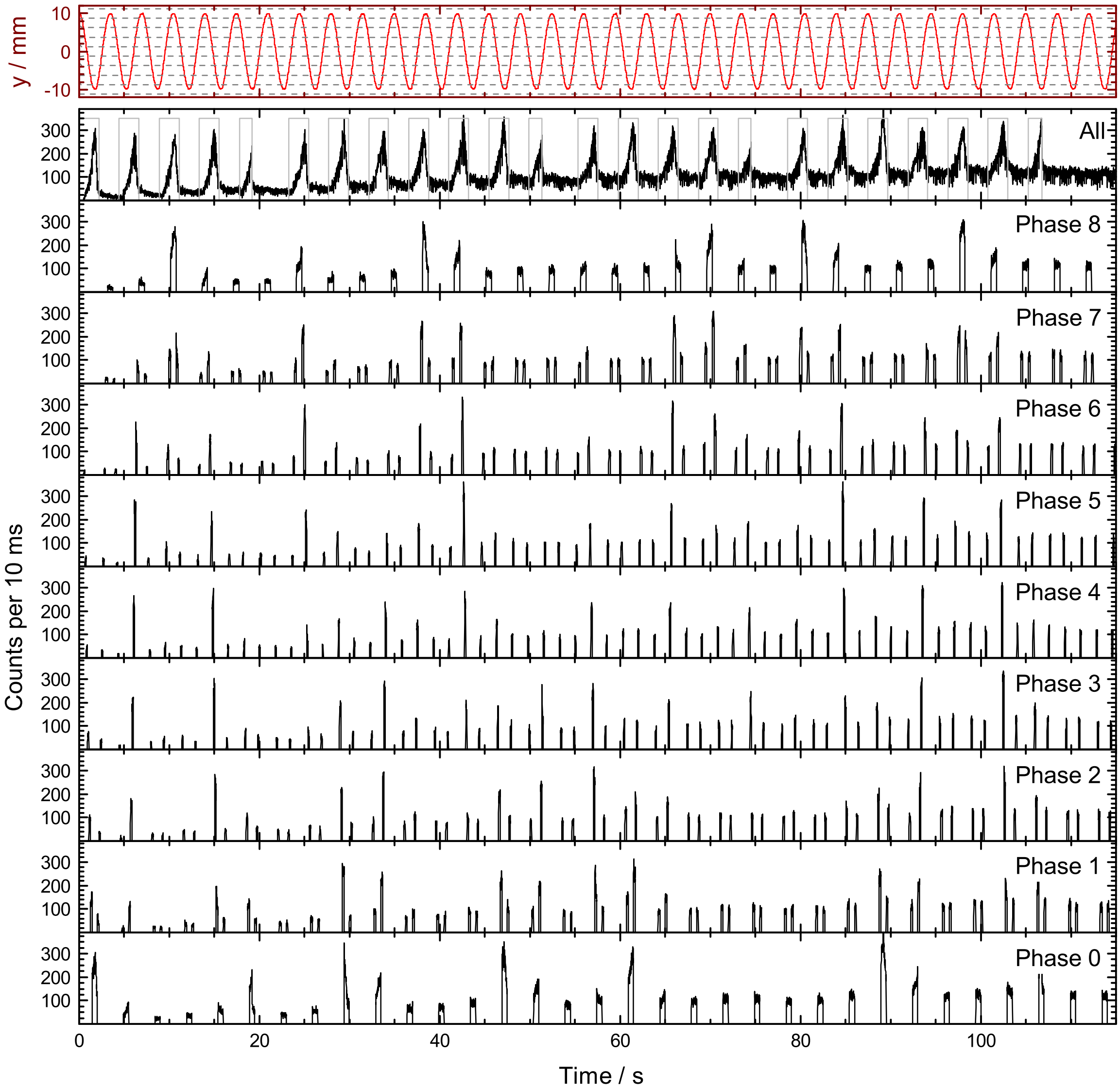

Figure 4.7: Simulated count rates of coincidences in the 9 listmode PET data files (3rd-11th row) detected by the double-head PET scanner during the irradiation and shortly afterwards. The motion signal (1st row, red) was used for the identification of the related amplitude-sorted (grey dashed lines) CT image phase at decay time. The summation of coincidences from all motion phases (2nd row) shows the target activation during the irradiation with 24 spills (grey). Increased count rates during the spills correspond to the fast decay of β^+-emitters with short half-lives ($< 1\,\mathrm{s}$), namely ^{13}O, ^{12}N, ^{9}C and ^{8}B (cp. table 2.2).

spill signals than other phases, and thus a larger fraction of coincidences will be rejected. Additionally, the amount of coincidences per phase is affected by the interdependency between the position of the β^+-activity within the FOV and the spatially variable solid angle coverage by the PET scanner. The partitioning of simulated coincidences to the motion phases is summarized in table 4.2.

Table 4.2: Amplitude intervals of motion phases, number of simulated coincidences per phase (4th column), number of coincidences considered for reconstruction (5th column) and the relative amount of rejected coincidences which occurred during the spill signals (6th column).

Phase	Amplitude / mm min	max	All coincidences	Coincidences out of spill	Rejection rate of coincidences
0	−11.25	−8.75	511 065	383 172	25.2 %
1	−8.75	−6.25	322 773	244 326	24.3 %
2	−6.25	−3.75	256 776	193 255	24.7 %
3	−3.75	−1.25	229 039	170 377	25.6 %
4	−1.25	1.25	225 709	168 736	25.2 %
5	1.25	3.75	238 758	178 461	25.3 %
6	3.75	6.25	261 463	194 388	25.7 %
7	6.25	8.75	349 707	259 960	25.7 %
8	8.75	11.25	487 520	359 769	26.2 %
All	−11.25	11.25	2 882 810	2 151 444	25.4 %

Reconstruction of phase-sorted listmode data and rating the results

It has to be verified that the coincidences are correctly assigned to the 9 motion phases and that from each phase-sorted listmode data stream an equivalent information about the induced β^+-activity in the target can be deduced. Therefore, the listmode data streams have been simply reconstructed phase by phase with the 3D MLEM algorithm (cp. section 3.1.1). For each of the 9 reconstructions an image space of $110 \times 80 \times 40$ cubic voxels with a side length of 1.6875 mm was used. Figure 4.8 depicts the central plane (located symmetrically between the two detector heads at $z = 0$) of the β^+-activity distributions. It is clearly visible that the activity appears only in the phantom and the static bolus but not in air-filled space in between them. The average phantom position is shifted in the y-direction (perpendicular to the beam direction) from phase to phase as given by the 4D planning CT image. The generated β^+-activity distribution in the middle of the phantom is displaced in the same way and the steep lateral activity gradients in motion direction are preserved in all phases. This proves that the lateral target tracking is processed correctly by the simulation code. Furthermore, the β^+-activity maximum in the beam direction (x) is located at the same depth ($x \approx 0$) for all y-coordinates, and thus forms a vertical line in all phases. Since the range is not affected by the 7 mm thick bolus under target motion, the program processes the information from the wedge system for the range compensation of ions with heterogeneous energy levels correctly as well.

Profiles parallel to the motion direction (y) and intersecting the high activity region ($x = 0$, $z = 0$) have been extracted from each phase for a more detailed evaluation. The profiles are shown in figure 4.9. Despite the homogeneous dose deposition, the β^+-activity is higher for smaller y-coordinates than at the side with the static bolus in front of the target. This is simply caused by the fact that the irradiation was started with the beam delivery to the negative y-coordinates (no bolus) during the first 12 spills. Thus, the measuring time for

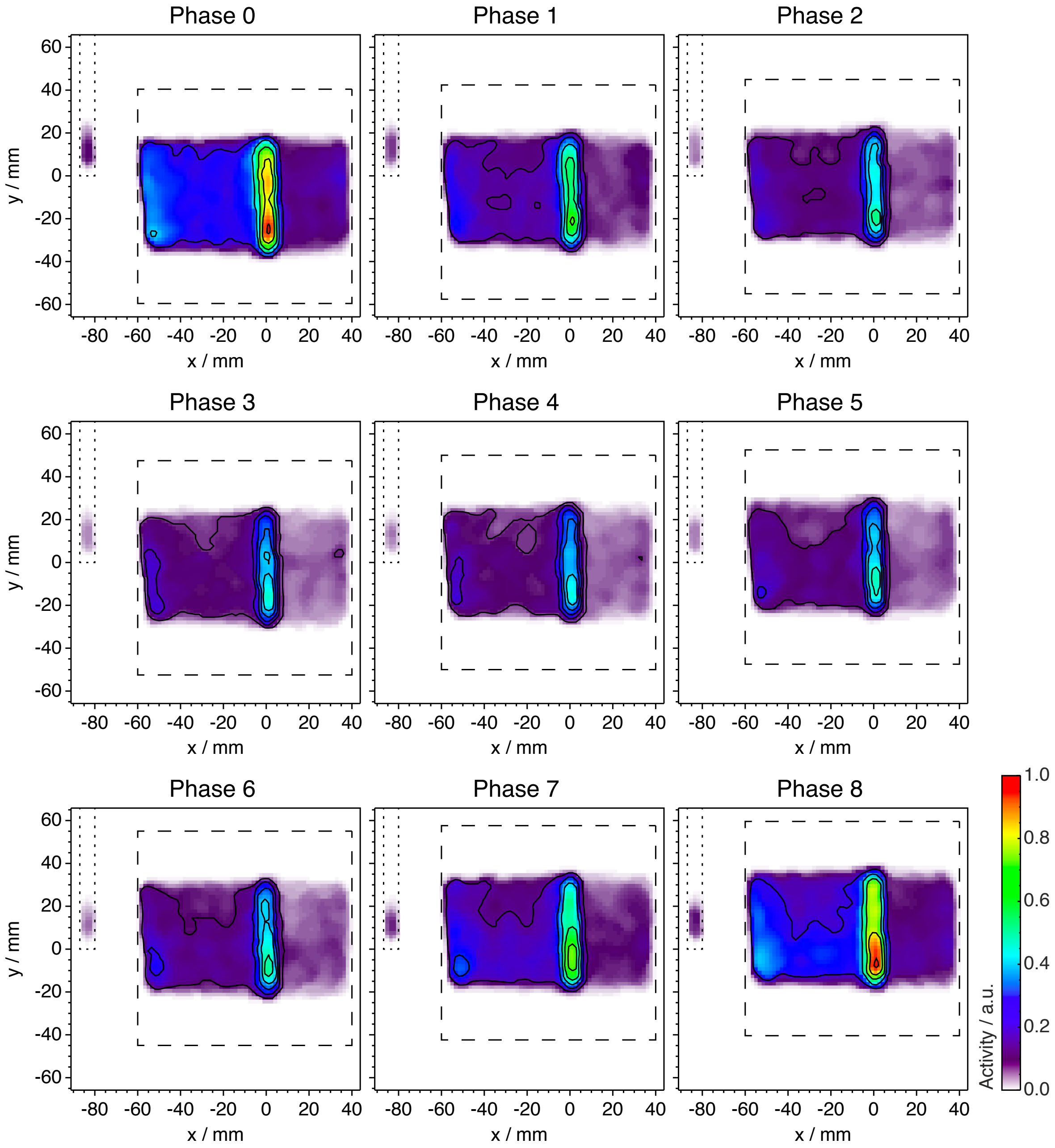

Figure 4.8: Coloured contour plots of the phase by phase reconstructed β^+-activity distributions for the central plane in the image space (summation over 2 voxel slices near $z = 0$). The ^{12}C ion beam impinged on the moving phantom (dashed square changing position in y-direction from phase to phase) from the left side after it had eventually passed the 7 mm thick bolus (dotted rectangle at $y > 0$), and it was stopped in the target at isocentre depth ($x = 0$). While the 5 contour lines are equally spaced between the minimum and maximum value in each phase, the colour coding is normalized to the global maximum value of all phases.

annihilation photons emerging from this side of the target is longer than for the other side where the β^+-emitters were generated during the second half of the irradiation. Besides their asymmetric progression, the profiles show clearly a similar shape for all phases and they are shifted according to the motion by about $2 - 3$ mm from phase to phase. A mean FWHM

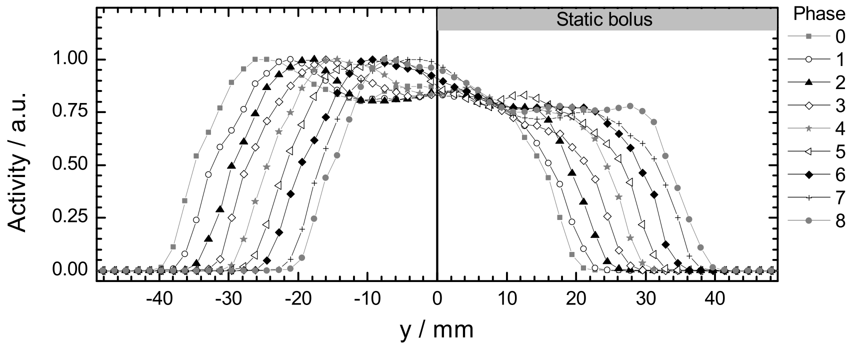

Figure 4.9: β^+-activity profiles extracted parallel to the motion direction in the phantom at Bragg peak depth ($x = 0$) from images in figure 4.8. All profiles are normalized to their own maximum value. According to the target motion from phase to phase the profiles are shifted in BEV from left (phase 0) to right (phase 8). For orientation, the position of the static bolus is indicated by the grey box.

value of 48.7 mm with a rather small standard deviation of 0.5 mm has been determined from the 9 profiles. Additionally, the conservation of the lateral activity gradients becomes manifested when considering the penumbra values and their standard deviations. Due to the skewness of the profiles, these values have been calculated between 20% and 80% for the left ($y < 0$) and between 60% and 10% of the profile maximum at the right slopes ($y > 0$). Mean penumbra values with small standard deviation of (6.9 ± 0.6) mm ($y < 0$) and (6.2 ± 0.6) mm ($y > 0$) were found, respectively.

4.2.3 Comparison with 3D simulation

Beam delivery by means of correct depth-compensated target tracking generates the same dose distribution in the target as it can be expected from a static target irradiation. Related β^+-activity distribution are assumed to be almost similar in both cases. To draw final conclusions about the correct operation of the 4D simulation program, it needs to be verified that the obtained results are of similar quality as the results from the 3D simulation program for static targets and that the high computational effort of using 4D CT images, LUT and transformation rules is mandatory.

Look-up tables for comparative simulations

Since it has been proven for the 4D simulation in section 4.2.2 that the reconstructed β^+-activity distributions from different motion phases contain similar information, only one (the 4^{th}) of the 9 phases has been selected for the comparison study. For a better comparability, the 4D simulation has been repeated with the same LUT as in section 4.2.2 but higher statistics to obtain a similar number of coincidences in the 4^{th} motion phase as in the data to which it is compared to. This is on the one hand an exact β^+-activity distribution which was calculated by applying the static treatment plan to a fixed and non-elongated target with a wedge system providing the medium WEPL of 92.5 mm. On the other hand, a simulation

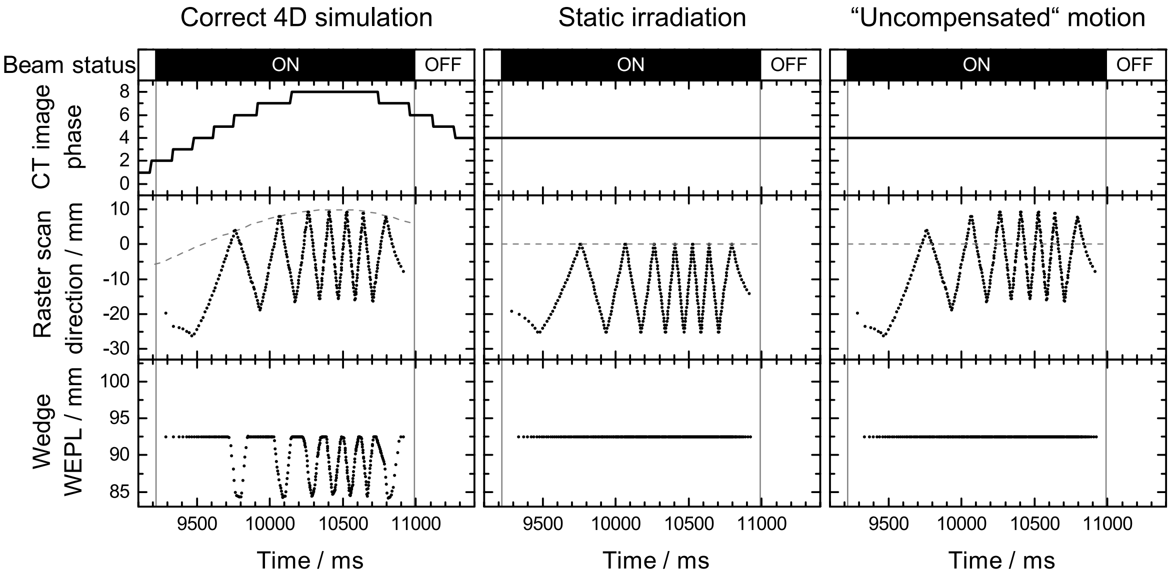

Figure 4.10: Sections of the assembled LUTs for comparative simulations. During correct 4D simulation (left) the target motion is correctly addressed to the different CT image phases, the raster scanner follows the lateral target motion and the wedge system performs the correspondingly required depth compensation. For a static irradiation (middle) the phantom resides in the non-elongated CT image phase and the scheduled raster point coordinates are delivered without required depth compensation. For an uncompensated-like simulation (right) the relative motion between pencil beam and target is introduced by considering the recorded raster points of lateral beam tracking to be applied to a static target. Thus, a relative motion between pencil beam and static bolus is simulated, and without changes in the wedge thickness, no depth compensation is performed.

is performed which shows that neglecting the relative motion between the pencil beam and the target as well as ignoring the necessary range compensation causes a clear deterioration of image quality. To induce the relative motion between the phantom and the beam, the retrospectively generated treatment file with the measured raster point coordinates from target tracking has been applied to a fixed and non-elongated target. The LUT contains only that single CT phase, i.e. no 4D CT image has been considered. Therefore, no transformation of the β^+-emitter coordinates needs to be done. Additionally, the logged changes in the wedge status have been ignored in the LUT to demonstrate the impact of a missing range compensation on the resulting β^+-activity distribution. Sections of the 3 assembled LUTs are shown in figure 4.10.

Comparison of simulation results

The reconstruction results from the simulated listmode data for the mid elongation phase of the correct 4D simulation, for the 3D static reference simulation and for the simulation without compensation of the ion range and of the relative motion between beam and phantom are shown in figure 4.11. From a visual survey, it is found that the 4D simulation generates a distribution of equal shape as the static reference. The width of the distribution in the motion direction (y) and the width of the high-activity region (x) are conserved. Slight deviations of absolute values are only visible in the plateau region and in the middle of the high-activity

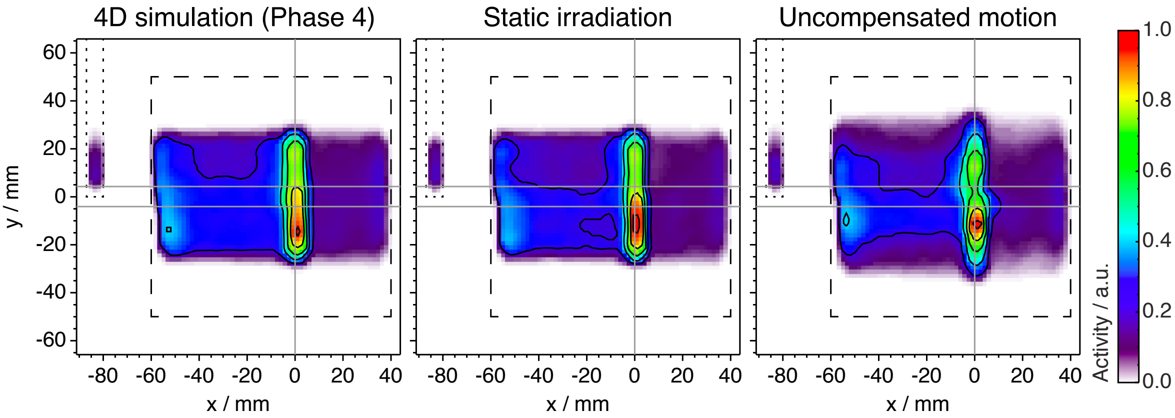

Figure 4.11: Reconstructed β^+-activity distributions in the midplane of the image space and target. Results have been obtained from the correct depth-compensated target tracking by the 4D simulation program in the non-elongated 4th phase similar to that in figure 4.8 but with 2.27×10^6 coincidences (left), from the simulation of a static target irradiation with 2.30×10^6 obtained coincidences (middle) and an irradiation without range and motion compensation containing 2.27×10^6 coincidences (right). Images are normalized to their own maximum value. The grey lines indicate the position of the extracted profiles shown in figure 4.12.

region. The result of the uncompensated simulation depicts a clear lateral broadening of the β^+-activity distribution, since there was a relative motion between the pencil beam and the phantom. The β^+-activity at Bragg peak depth ($x = 0$) in the middle of the target ($y \approx 0$) protrudes slightly to the distal (for $y < 0$) as well as proximal (for $y > 0$) direction due to the missing range compensation.

These findings are also well illustrated by profiles which intersect the target volume longitudinally, parallel to the beam direction and those proceeding parallel to the motion direction at Bragg peak depth. Figure 4.12 shows the profiles from each of the three distributions. Longitudinal profiles for voxels with coordinates of $y \approx -4.2\,\text{mm}$ and $y \approx 4.2\,\text{mm}$ match quite well for intervals proximal and distal to the region of the β^+-activity peak. Profiles from uncompensated motion bare a considerably reduced height of the activity peak. An obvious loss of the steep gradients at the proximal or distal edge of the peak appears without depth compensation, since the beam of higher energy partially misses the bolus and the beam with the lower energy level might pass the bolus before entering the target. The lateral profiles for the three simulations do not bare large differences in FWHM values of 49.2 mm, 49.3 mm and 47.2 mm (static reference, 4D simulation and uncompensated motion). However, the blurring of the lateral activity fall-off for the uncompensated motion simulation is well reflected by the penumbra values which are increased by more than a factor of two. For the left slope the penumbra between 20% and 80% of the maximum is raised from 7.1 mm and 6.8 mm (4D simulation and static reference) to 15.0 mm. Similarly, the penumbra value for the right slope between 60% and 10% rises from 6.2 mm and 6.9 mm (4D simulation and static reference) to 15.9 mm.

The comparably larger drop in the middle of the lateral profile from the uncompensated motion can only be rated under the consideration of the β^+-activity smearing in the longitudinal

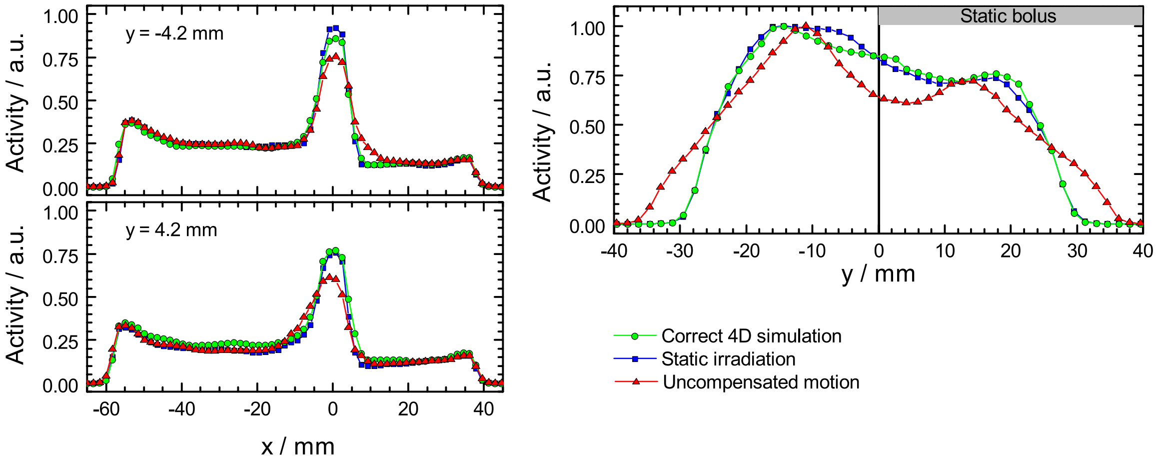

Figure 4.12: β^+-activity profiles extracted from figure 4.11 which intersect the phantom parallel to the beam direction for voxels with y-coordinates equal to -4.2 mm and 4.2 mm (left) and parallel to the motion direction at the Bragg peak depth (right). Profiles from the 4D simulation show only slight deviations from the static reference simulation. For the uncompensated motion simulation distinct deviations are found at the distal (upper left) and proximal (lower left) edges of the peak region as well as in the middle and the fall-off regions of the lateral profile (right).

direction. Therefore, activity difference images have been calculated. Both the 4D simulated β^+-activity distribution and that from the uncompensated motion simulation are compared to the static reference distribution by calculating the differences pixel by pixel. Resulting images are presented in figure 4.13. Difference values for the 4D simulation range between -0.08 and 0.11, but the image does not show a pronounced pattern. In contrast to that, the difference image for the uncompensated motion simulation contains values between -0.22 and 0.29 and bares an obvious structure. The dark blue area in the middle ($x = 0$, $y = 0$) which corresponds to the drop in the lateral profile in figure 4.12 as well as the proximal and distal red spots illustrate the dislocation of the high-activity region due to the influence of missing range compensation for the bolus when doing lateral tracking. Red and blue stripes at the

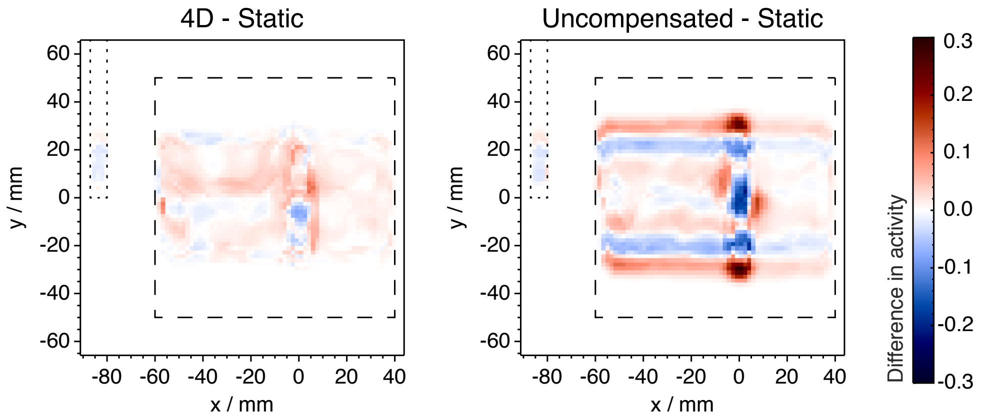

Figure 4.13: Difference images between the β^+-activity distributions depicted in figure 4.11. The images show the absolute deviation for each voxel in the midplane of the 4D simulation result (left) and the uncompensated motion simulation (right) from the static reference simulation.

lateral regions are related to the blurred gradients due to the relative motion between pencil beam and target. The remaining deviations between the reference and 4D simulation might be ascribed to different origins. First of all, only limited time sections of the whole measurement time are assigned to the 4^{th} phase. These cannot represent the exact development of the count rate and the β^+-activity distribution in time and space, respectively. Secondly, there are also analogue influences as for the uncompensated simulation, since there is a small residual motion within the 4D CT image phase. These 2.5 mm (cf. table 4.2) are below the spatial resolution in the midplane of the PET scanner system which is about 5 mm due to the large detector crystals and the double-head geometry (Lauckner 1999). Anyway, the residual motion might slightly influence the 4D PET images. And thirdly, the observed differences between the presented β^+-activity distributions appear primarily in the target region which is affected by the rapid transition between bolus and air. This could indicate that the response time of the wedge system is too long for that density gradient. Fortunately, such sharp edges occur rarely in patient tissue.

4.3 Summary and discussion

Similar as for IBT-PET dose monitoring in static target volumes, a measured and reconstructed β^+-activity distribution from an intra-fractionally moving target can only be interpreted correctly by the comparison to an expected, simulated distribution. The first simulation program for the generation of predicted IBT-PET listmode data under the exact consideration of intra-fractional motion and motion-compensated dose delivery by scanned ion beams has been developed. Among others, its performance was also validated within the presented preclinical phantom study including one of the most complex motion mitigated beam delivery techniques that allows to test the total functionality. Depth-compensated tracking requires the most complex simulation input. Since the verification can only be done by analysing the afterwards reconstructed β^+-activity distribution high counting statistics were emulated to reduce additional reconstruction artefacts. To limit the inevitable influence of the limited solid angle coverage in the reconstructed images, the target volume was positioned in the midplane of the detector heads. Although the line-shaped geometry of the target volume is clinically irrelevant, it allowed together with the clear 1D sinusoidal motion for an explicit assessment of both lateral and distal discrepancies in the β^+-activity.

It was clearly demonstrated that the 4D simulation program satisfies the demands of considering the target motion and motion mitigation. Therefore, in comparison to the clinically approved 3D IBT-PET simulation program, the presented 4D upgrade requires an additional set of input data and the handling of the given information. On the one hand, it has been validated by the comparison to a static reference simulation that this management offers sufficient accuracy. On the other hand, it was shown by a comparison to a simulation for uncompensated motion that the additional effort is mandatory. Otherwise a correct dose monitoring would not be feasible. Besides the 4D planning CT image and the corresponding transformation specifications between the single phases, the centrepiece of the input parameters is an individually generated LUT. Its content depends on the applied motion mitigation technique. In any case the nextpoint signal from each raster point is mandatory and needs to be synchronized with the motion signal and the CT image phase. For simple rescanning or for gated irradiation, the treatment plan is delivered without changing the raster scan coordinates and no further data are required in the LUT. For lateral target tracking, a retrospectively generated treatment plan provides the actually applied raster scan coordinates. Potentially changed numbers of ions delivered to these raster points are also given in this retrospective plan and can be used for simulating real-time dose compensation. If range compensated tracking is performed by means of a fast moving absorber, the LUT will be extended by the water-equivalent absorber thickness in the beam path.

The 4D IBT-PET simulation program in its current version is feasible or can easily be upgraded to simulate motion phase sorted listmode data streams from intra-fractionally moving targets including arbitrary motion patterns, motion-compensated beam delivery with actively scanned pencil beams of a certain ion species provided by synchrotron or cyclotron accelerators and considering different PET scanners and IBT-PET modalities:

- It is expected that deformations related to the complex 3D motion patterns found in patients and including transversal, longitudinal, rotational and deformable motion should in principle be manageable by means of the transformation matrices (cp. appendix A).
- The POSGEN database for the spatial β^+-emitter distribution is currently available for ^{12}C ion beams only. Databases are required for each ion species used for IBT to apply the 4D simulation program with its current workflow. Since most of the existing ion beam therapy facilities make use of proton beams (PTCOG 2012), there is an urgent need for the creation of a proton beam database. Furthermore, databases for larger pencil-beam widths should be available for gated irradiation to produce simulation results equivalent to the measured distributions. An artificial beam broadening has been suggested for that motion mitigation method to generate a larger overlap between adjacent raster spots and thus to minimize the interplay patterns due to the residual target motion in the gating window and the beam scanning motion (Bert *et al.* 2009).
- The implemented usage of the nextpoint signals for the definition of the irradiation time of each raster point, instead of the spill signals from the synchrotron, makes the simulation program also applicable for the continuous wave beam delivery by cyclotrons. These accelerators are much more often in therapeutic use, especially for proton beam therapy, because of their reliability, relative simplicity, the lower investment costs and operational expenses.
- According to the used PET scanner, the detector material and the crystal coordinates defining the valid LORs have to be modified, and the output format of the listmode data needs to be changed. Up to now, only the double-head in-beam PET scanner geometry from BASTEI at GSI has been considered by the 4D simulation program, but the implementation of other, mainly full-ring, geometries might be easily possible.

- The simulation of the different IBT-PET modalities (in-beam, in-room, off-line) is possible by setting an appropriate maximum value of allowed decay time t_{max} and selecting the correct time interval for the data reconstruction. If the patient needs to be moved prior to an off-line or in-room PET measurement and therefore the motion acquisition system might be disconnected, it has to be ensured to assemble the total LUT with an exact temporal relation between the last next point signal, the begin of the motion acquisition in the PET measurement position and the PET data stream.

A future testing of the simulation program with real patient data is desired. Unfortunately, until now there are no data available from which a complete LUT could have been created.

5 Interpretation of 4D IBT-PET data with respect to deficient motion mitigation or data processing

Contents

An increased risk for spatial dose misses is expected for the treatment of intra-fractionally moving tumour volumes because of the continuous density changes in the irradiated tissue affecting the ion range and because of the more complex beam delivery due to sophisticated motion mitigation techniques. For static target volumes, the IBT-PET imaging has been used to detect a potential misdosage by a more or less objective comparison between the simulated and measured β^+-activity distributions (cp. figure 2.10). If deviations are found, they can normally be addressed to unexpected changes in the anatomical patient geometry or to positioning uncertainties. In the rare case of serious treatment errors not being excluded by the therapy control system, IBT-PET for static target volumes will detect an inaccurate induced β^+-activity distribution. Although high standards of quality assurance are available in clinical environment when applying gated or tracked ion beams to patients, some special focus was put on the detectability of an imaginable failure of the motion mitigated beam delivery (Laube *et al.* 2009a,b). As explained in section 5.1, the interpretation of resulting β^+-activity distributions might become difficult with the conventional comparison of the results from simulation and measurement. Additionally, a correct correlation between the motion detection and the listmode PET data stream has to be assured. The impact of a mismatch between both data streams is shown in section 5.2.

5.1 Detectability of failed motion mitigation

For a safe beam delivery, failures during dose application need to be detected reliably in real time, especially for the active beam delivery by means of pencil beam scanning. The beam monitoring with MWPCs has the potential to generate an immediate interrupt of the treatment if a planned raster point position was missed by the pencil beam. However, for lateral target tracking another and potentially more complex interlock system is desired, since the scheduled raster point positions are adapted in real time due to the target motion.

Consequently, the beam will miss the positions given in the treatment plan if tracking is performed exactly. Currently, the actually applied beam directions (and the number of delivered ions) can be monitored but only evaluated retrospectively. For gated irradiation, the pencil beam positions can be monitored by the MWPCs as it is done for static targets. As long as there is no real-time correlation between the MWPC signals and the motion acquisition, an additional system is required that would cause an interlock if a breakdown of the gating system occurs. An investigation of the detectability of a failed motion mitigation in the IBT-PET data is presented in the following sections by means of basic experiments.

5.1.1 Failure in gated beam delivery

Experiment description

An experiment with a target geometry (100 mm × 100 mm × 30 mm PMMA), motion direction and motion amplitude as described in section 3.3.1 was carried out. The target performed of a $\cos^2$ motion with a maximal elongation of ±10 mm perpendicular to the incident beam direction. Motion compensation was planned to be performed by means of gated beam delivery using a 10% inhalation gating window. The treatment plan includes ions of two similar energies to be delivered to a line segment with raster point coordinates between (0 mm, −17 mm) and (0 mm, 35 mm). 60 rescans along that interval have been scheduled for each energy resulting in 3180 raster points per energy. Considering the mean target elongation within the gating window the ions are deposited in the middle of the target. According to the recommendations by Bert *et al.* (2009) the width of the pencil beam was enlarged for the gated beam delivery to a FWHM of about 10 mm. Acquired in-beam PET data comprise the time of irradiation and a 5 min decay measurement with ongoing target motion.

The progress of the irradiation is documented by the logged motion, gating and spill signals which are illustrated in figure 5.1. Motion mitigated beam delivery was performed correctly

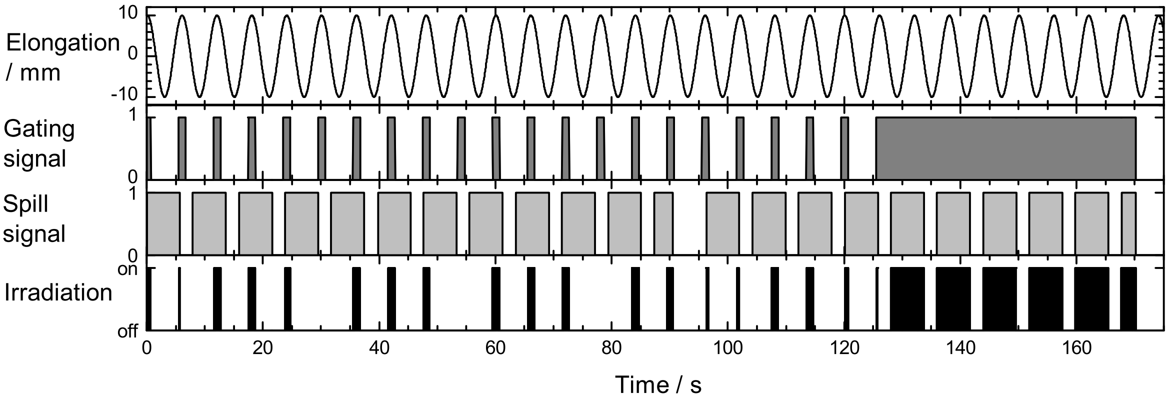

Figure 5.1: Documentation of the gated irradiation by means of the gating signals related to the target elongation and the spill signals. The beam is delivered when spill and gating signal overlap. Since there was a hang-up of the gating sensor after approximately 125 s (16 spills) the irradiation proceeded irrespective of the motion signal.

for the first energy slice (spill 1 to 12), i.e. the target was just then irradiated when both gating and spill signal overlapped. Due to the fact that the gating sensor went out of operation after circa 650 raster points in the second energy slice, the remaining ions have been delivered irrespective of the actual target position.

Comparison between measured and simulated β^+-activity distribution

Actually, deviations from the planned dose distribution should be assessable by a comparison between measured and simulated β^+-activity distribution (cp. figure 2.10). Thus, a LUT for the 4D simulation program was generated from the logged motion signal, raster scan coordinates and nextpoint signals and it was used for the calculation of predicted PET data. Both measured and simulated listmode data streams have been reconstructed by the 4D MLEM algorithm using 9 amplitude-sorted motion phases. To illustrate the expected shape of the initially planned β^+-activity distribution for correct motion mitigation, a second listmode data stream was simulated. The scheduled raster points with the logged nextpoint signals and a static target with elongation according to the gating window have been assumed for generating the corresponding LUT. Data have been reconstructed by a 3D MLEM algorithm, and the resulting β^+-activity distribution was transformed into the reference position with target at mid elongation.

A comparison between the measured and the two simulated β^+-activity distributions reconstructed for an arbitrary time interval in the decay measurement (100–300 s after the end of the irradiation) is presented in figure 5.2. The smaller peak-plateau activity ratio in the simulated distributions should be neglected here. Too many ^{10}C and ^{11}C target fragments are simulated in the entrance channel. This is an inherent characteristic of the utilized POSGEN database which has already been verified by Priegnitz (2012). However, the distal peak position, relevant for range verification, matches exactly between simulated and measured

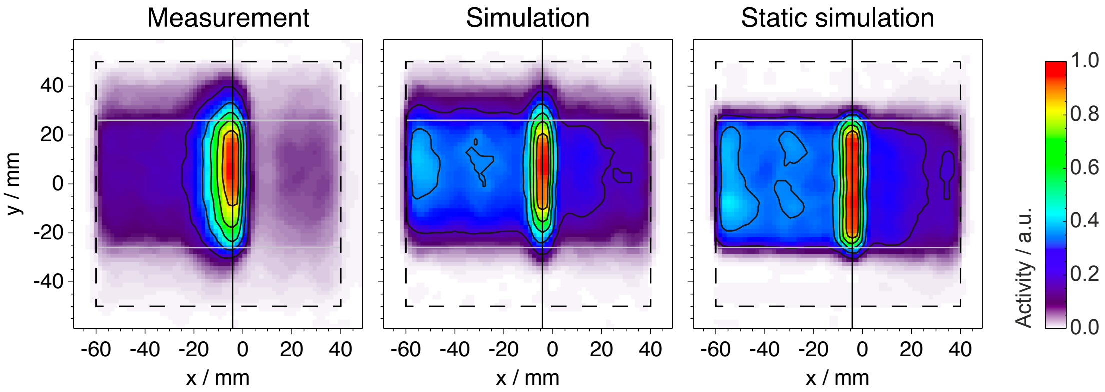

Figure 5.2: Measured (left) and simulated (middle) β^+-activity distribution with approximately the same lateral width and position in the target for the inaccurate gated beam delivery (incident particles from the left). A simulated static target where the incident beam matches the scheduled lateral positions for all raster points results in a more confined β^+-activity distribution and a better homogeneity in the peak region (right). Horizontal grey lines indicate the planned lateral field width and help to guide the eye. Vertical black lines mark the extracted profiles shown in figure 5.3.

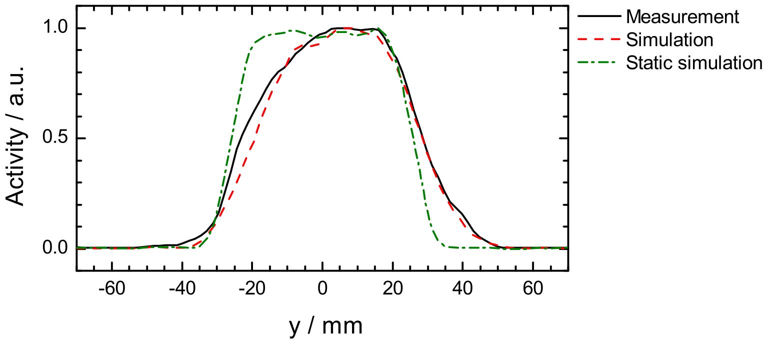

Figure 5.3: Lateral profiles parallel to the motion direction and intersecting the peak region as indicated in the β^+-activity distributions in figure 5.2. Results from measurement (black) and simulation (red) with failed gating show similar shifted position and skewness while the profile from the static simulation (green) is almost centred in the target and has symmetric, steep gradients. Profiles are normalized to their maximum value.

β^+-activities. The β^+-activity distributions from the inaccurately gated treatment exhibit a pronounced blurring in motion direction, particularly at positive y-coordinates. Blurring seems to be of similar amount in measured and simulated results, especially when taking the different pencil beam widths into account. Solely for the static simulation, the β^+-activity is confined to the planned target region and the homogeneity in the peak area is considerably improved. These findings are also clearly validated by the extracted profiles shown in figure 5.3. The expected symmetric box shape with steep gradients is reproduced by the static simulation. The two profiles from the inaccurate gating are modified in the same way. Their skewness can be understood as a superposition of a box-shaped profile from the fraction delivered with correct gating and the symmetric blurring from the $\cos^2$ motion with shifted centre of mass from the second fraction with failed gating.

Conclusion

The presented experiment demonstrates that treatment errors related to deficient motion mitigation cannot reliably be discovered by IBT-PET using the hitherto existing workflow. A comparison between a measured and simulated β^+-activity distribution is insufficient for such cases since the information about the actual beam delivery serves directly as input for the LUT used in the 4D simulation. Thus, treatment errors are also reproduced by the simulation. Remedy could be provided by means of an additional simulation where the scheduled treatment plan is delivered to the static target volume under consideration of the real time structure given by the nextpoint signals.

5.1.2 Failure in lateral target tracking

Systematic experiments have been carried out to investigate the detectability of a failed lateral target tracking. Two different types of failures have been imitated:

- a breakdown of the tracking system leading to an uncompensated beam delivery and

- a worst case scenario of a phase-shifted tracking, i.e. the pencil beam is (according to a sign error) compensated to the opposite direction than the target is elongated.

To potentially confirm the failed motion compensation, the measured β^+-activity distributions are compared to a static reference measurement within this experiment campaign.

Target geometries and treatment plans

Different to the experiment presented in the previous section for the failed gating, special target geometries have been designed to allow for an immediate visualization of potential failures in the tracking process for the 20 mm peak-to-peak $\cos^2$ motion. The main difference is the reduced lateral target size. The line-shaped treatment plans were adapted to fit almost exactly into the target under consideration of the finite pencil beam width. Due to the omitted lateral target margins, the beam will partly miss the phantom if lateral tracking is performed inaccurately. A second phantom of suitable size is positioned in the FOV of the PET scanner and is utilized to absorb the ions which miss the target. A related β^+-activity distribution is then generated in this second phantom.

In a first experiment setup a moving PMMA target of 80 mm × 50 mm × 47 mm was planned to be irradiated with a laterally tracked ^{12}C pencil beam. The treatment plan includes 60 rescans along a line segment between the lateral coordinates of −22 mm and 22 mm. A second PMMA block (called stopper in this experiments) of 100 mm × 100 mm × 30 mm was positioned distal to the target and remained in its static position. An image of the motion table enabling the relative motion between the two phantoms and showing their positioning is given in figure C.5 (page 119). This setup is a rough approximation to anatomical characteristics when compact NSCLCs move inside the lungs which are simply replaced by air in this experiment. A mismatch between tumour position and ion beam should lead to a considerable overshoot in the less dense surrounding lung tissue and to the generation of β^+-emitters in the distal thoracic wall.

To include the imitation of the adjacent and also moving but less dense lung tissue a second phantom geometry was designed which is shown in figure 5.4. The target consists of a graphite cuboid of 92 mm × 40 mm × 30 mm where the carbon ion beam of about 313 AMeV

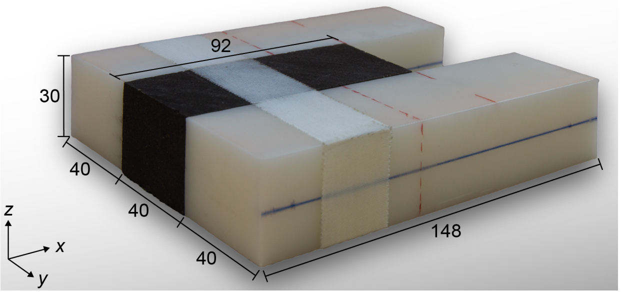

Figure 5.4: Inhomogeneous phantom composed of a graphite target (black) and laterally attached PE stoppers (white). Dimensions are given in mm. The phantom is moved parallel to the y-direction while the pencil beam impinges parallel to the x-axis.

is stopped after having passed the 80 mm thick PMMA wedges for a potential distal tracking. According to the target width of 40 mm, the treatment plan includes only lateral raster scan coordinates between −17 mm and 17 mm which have been scheduled to be rescanned 60 times. Ions missing the graphite target are stopped in the laterally attached and also moving polyethylene (PE) phantoms of 148 mm × 40 mm × 30 mm. The related β^+-activity peak is formed at a larger depth than in the graphite target due to the lower density of PE.

Interpretation of reconstructed β^+-activity distributions

For both target geometries 4 different experiments have been performed. The treatment plan was once delivered to the static phantoms. A measurement with correct tracking demonstrates that similar confined β^+-activity distributions can be generated under target motion. Failures in the tracking system have been emulated by omitting the tracking at all and by performing a phase-shifted tracking with an offset of 180°. Images were reconstructed by the 4D MLEM algorithm with 9 amplitude-sorted motion phases and using IBT-PET data acquired during the irradiation and within the next 300 s with ongoing target motion.

Relative motion of homogeneous PMMA phantoms Results for the PMMA targets are summarized in figure 5.5. The β^+-activity is mainly concentrated in the small (moving) proximal PMMA phantom. For the irradiation with static target and for the correct tracking,

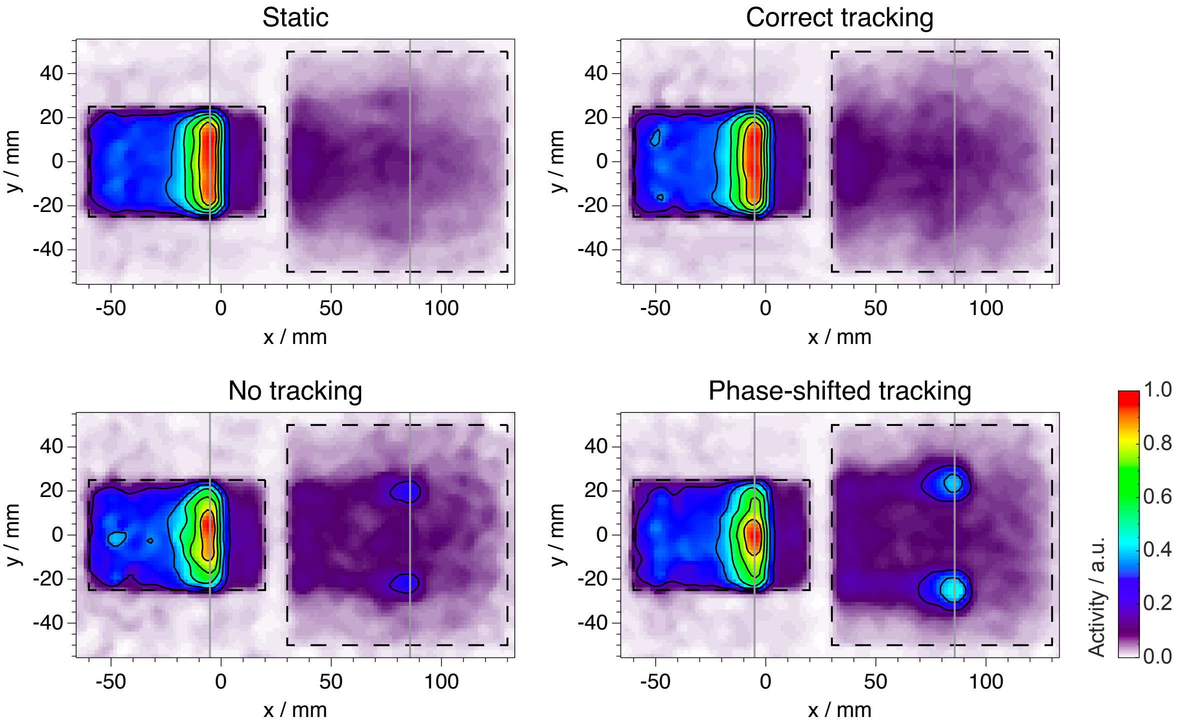

v

Figure 5.5: Reconstructed β^+-activity distributions in the PMMA target (left dashed contour) and the PMMA stopper (right dashed contour) for the different irradiation scenarios. Images are summed over 10 voxels in z-direction and scaled to their individual maximum. Profiles extracted parallel to the motion direction (y-axis) and shown in figure 5.6 are indicated by vertical grey lines.

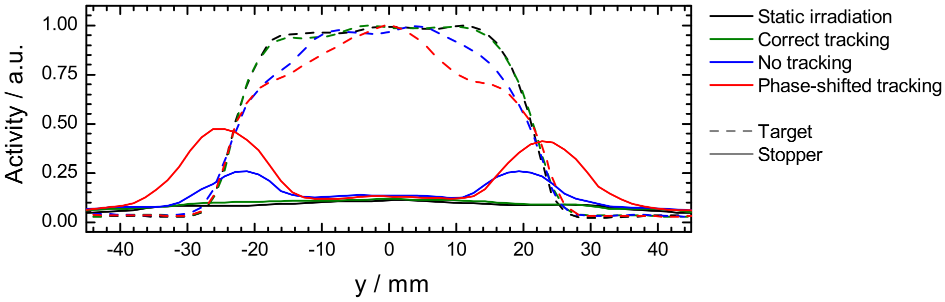

Figure 5.6: β^+-activity profiles intersecting the PMMA target (dashed) and PMMA stopper (solid) parallel to the motion direction extracted from the distributions shown in figure 5.5. Profiles have been calculated as a summation over 8 voxels in x- and 10 voxels in z-direction and are scaled to the maximum value in the target.

there appears only a small amount of background β^+-activity in the stopper generated by light projectile fragments that may escape the phantom. Without lateral tracking, a certain amount of the delivered ions misses the moving phantom and penetrates the stopper at the more lateral segments which are temporarily not covered by the moving phantom. In this case, the β^+-activity is formed in the stopper just directly behind the target. In the worst case of phase-shifted tracking, the β^+-activity spots in the stopper are also spread to positions lateral to the mid-elongated target. Their lateral size as well as their relative activity values are almost doubled in comparison to the experiment without any tracking. With increasing amount of β^+-activity in the stopper, the lateral gradients of the β^+-activity in the target phantom are getting smaller. Profiles proceeding parallel to the motion direction and intersecting the high activity regions near the Bragg peak in the target and stopper are plotted in figure 5.6 and illustrate the discussed characteristics. The presented β^+-activity distributions can also be differentiated on a more quantitative scale by e.g. comparing several properties of the profiles as given in table 5.1. Especially the NRMSE values of the stopper profiles are extremely large for the deficient tracking scenarios and the width of the profile in the target is considerably reduced.

Table 5.1: Comparison of several properties of the profiles shown in figure 5.6. The NRMSEs relative to the profiles of the static reference were calculated according to (3.9). Width$_{80\%}$ denotes the full width of the target profiles at 80% of their maximum value and Max the maximum value of the stopper profile relative to the maximum of the corresponding target profile.

	Target		Stopper	
	NRMSE	Width$_{80\%}$	NRMSE	Max
Static	—	37.8 mm	—	0.11
Correct tracking	1.3%	37.8 mm	8.6%	0.12
No tracking	5.9%	30.1 mm	60.3%	0.26
Phase-shifted tracking	9.5%	21.0 mm	134.6%	0.47

Graphite-PE phantom Similar clear results have been obtained from the experiments utilizing the graphite-PE phantom. Figure 5.7 displays the reconstructed β^+-activity distributions in the phantom for the different irradiation scenarios. Measurements from the static reference and the correct tracking match again quite well. The β^+-activity is limited to the graphite target. Without tracking the lateral activity gradients are decreased in the graphite phantom and an additional small amount of β^+-activity is found in the adjacent PE stoppers. For phase-shifted tracking, the induced activity region in the whole phantom is almost doubled in lateral size in comparison to the static reference. Related to the peak-to-peak motion amplitude, a considerable amount of β^+-activity is induced in the PE stoppers on a lateral scale of up to 20 mm. Profiles intersecting the high β^+-activity regions near the Bragg peak position in the target and stoppers have been extracted from the four measurements and are shown in figure 5.8. Some selected properties of these profiles are summarized in table 5.2. Like for the PMMA stopper in the previous experiment, the NRMSEs in the PE stoppers are a clear indicator for the deficient motion compensation. The maximum value in a stopper profile relative to the corresponding one in the target has only a limited significance when

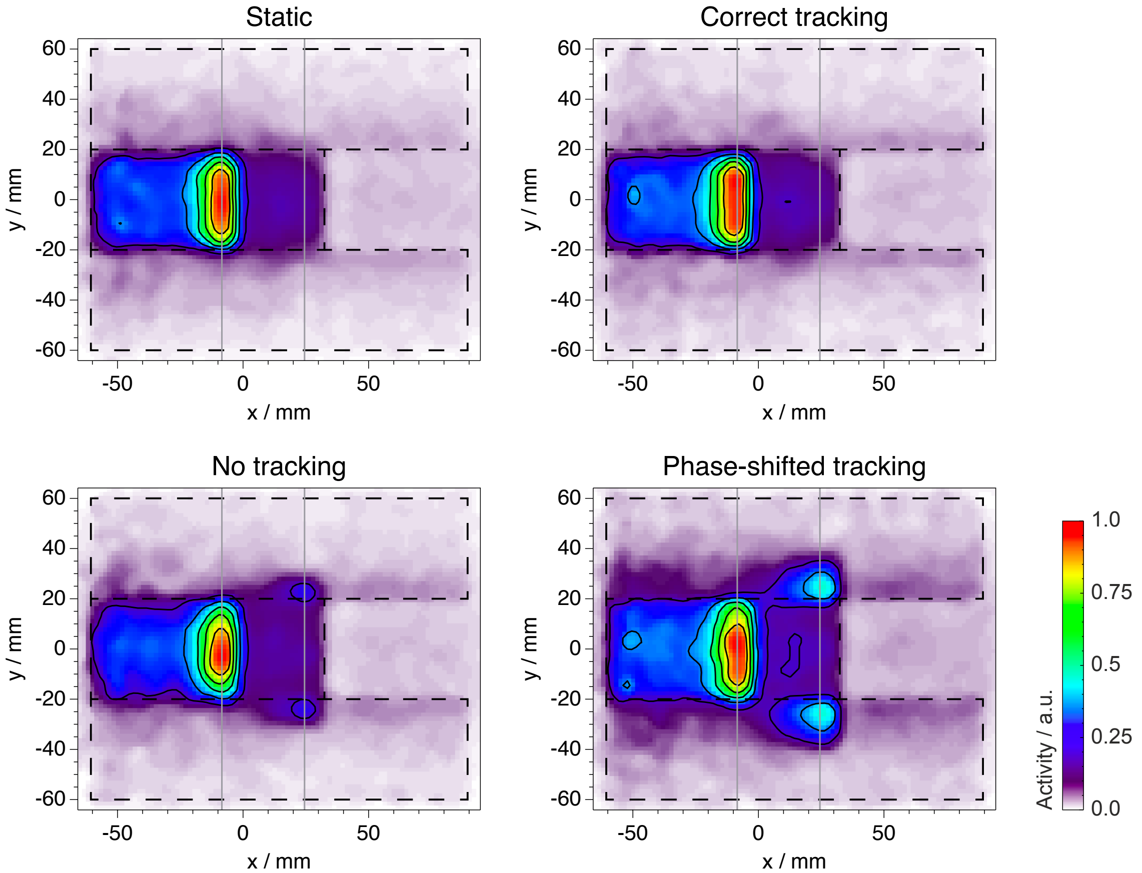

Figure 5.7: Measured β^+-activity distributions in the graphite target (dashed mid rectangle) and the adjacent PE stoppers (upper and lower dashed rectangles). Images are formed by the summation over 10 voxels slices in z-direction and are scaled to their individual maximum value. Extracted profiles shown in figure 5.8 are indicated by vertical grey lines intersecting the high activity regions in the graphit target and PE stoppers.

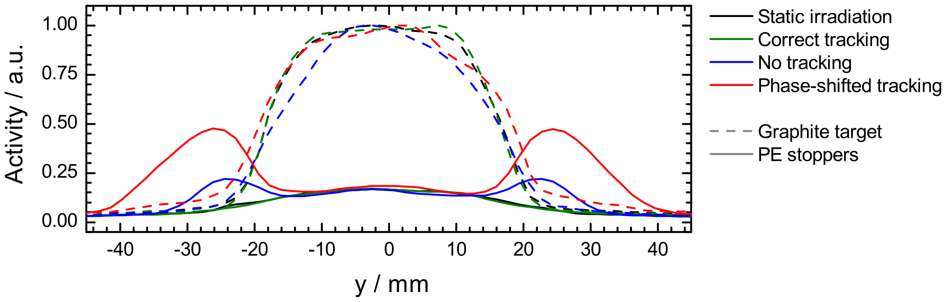

Figure 5.8: β^+-activity profiles extracted from the four distributions shown in figure 5.7. The profiles intersect the graphite phantom (dashed) or the PE stoppers (solid) parallel to the motion direction and have been calculated as summation of 8 voxels in x- and 10 voxels in z-direction. The target and the stopper profile of one measurement are scaled to their common maximum value.

Table 5.2: Comparison of some properties of the profiles shown in figure 5.8. The NRMSEs relative to the profiles of the static reference were calculated according to (3.9). Width$_{80\%}$ denotes the full width of the target profiles at 80% of their maximum value and Max the maximum value of the stopper profile relative to the activity maximum in the corresponding target profile.

	Target		Stopper	
	NRMSE	Width$_{80\%}$	NRMSE	Max
Static	—	27.1 mm	—	0.17
Correct tracking	1.4%	27.9 mm	2.3%	0.17
No tracking	4.6%	20.8 mm	27.9%	0.22
Phase-shifted tracking	11.6%	26.0 mm	94.4%	0.47

interpreting the results related to the failed tracking scenarios, since β^+-emitter yields are unequal in the different materials (Priegnitz *et al.* 2012).

Discussion

Similar as presented for the failure in the gated beam delivery, the deficient tracking is only reliably detectable if the resulting β^+-activity distribution is compared to a static reference. For real patient treatments, the static reference distribution needs to be created by means of a simulation as it was shown in section 5.1.1. Due to the steep density gradients in the thorax region, particle ranges might be strongly affected if deviations from the planned conditions occure. Thus, an incorrect dose delivery is expected to be discovered when the measured β^+-activity distribution is compared to the simulated static reference.

Although the differences in the β^+-activity distributions of the performed experiments are obvious to the observer, the (semi-) automatic range comparison algorithm by Helmbrecht *et al.* (2012) fails to detect them. The reason for that is plausible. For the additional lateral activity related to a failed lateral target tracking, there is no relevant amount of activity at the same position in the reference distribution to which the measured one could be compared to. The same holds true for each comparison between a confined β^+-activity distribution with steep gradients and a laterally smeared β^+-activity distribution, which might be related to an incorrect motion mitigation or a deficient data handling prior the reconstruction process. In all cases, the algorithm would not raise any alarm, but this is highly appreciated. Similarly, the amount of activity found in the PMMA stopper directly behind the target might be too low in comparison to the target activity to be considered for the definition of the distal β^+-activity fall-off within the individual profiles. Furthermore, even if the deviations would have been identified by a certain algorithm, it might become difficult to assign them to their actual origin, because there are more degrees of freedom when motion is taken into account. For instance, a β^+-activity located distal to (behind) the planned target volume could arise from the failed lateral tracking as illustrated by the PMMA target and stopper geometry, but a tumour shrinkage might also lead to a relevant amount of β^+-activity distal to the planned target volume.

The presented experiments without tracking have also clearly demonstrated the drawback of solely using the rescanning technique for motion mitigation under active beam delivery. Additional safety margins are required in the treatment plan, and a misplaced dose at the outer parts of the treatment field has to be accepted when trying to homogenize the dose inside the target volume.

5.2 Deficient correlation between motion and PET data

The occurrence of blurred β^+-activity distributions is not solely an indication for an inaccurate motion mitigation. Physiological processes like the biological washout that might be another possible origin for an additional smearing of the β^+-activity should also be neglected in the following examination. An incorrect consideration of the intra-fractional target motion might also have a strong influence on the blurring in the reconstructed image. There are two main tasks to be fulfilled prior to the actual 4D IBT-PET data reconstruction to realize a successful motion handling:

- the extraction of the real, complex motion patterns and the related creation of the corresponding transformation matrices and attenuation corrections from the 4D planning CT image and
- the assignment of the PET listmode data to the correct motion phases by means of a suitable surrogate signal.

For the first task there exist several commercial and open source software packages which enable a suitable handling of 4D patient CT images. The second task demands a time correlation between both data streams. At the experimental in-beam PET facility at GSI, there does not exist any dedicated hardware module for the combination of both data streams. Instead, the synchronisation had to be done manually as described in appendix D. As shown below, a slight delay in one signal branch, which might also occur at a commercial system, can seriously influence the image quality.

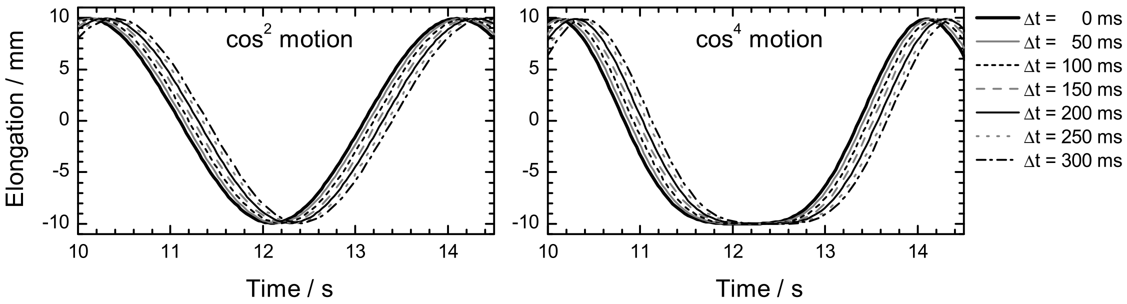

Figure 5.9: Section of the $\cos^2$ (left) and $\cos^4$ (right) motion signal of the moving point source and its shifting Δt by up to 300 ms in time to induce a slightly incorrect correlation with the listmode PET data.

Systematic point source experiment

The consequences of a deficient correlation between the motion information and the listmode PET data stream was systematically analysed by means of a moving ^{22}Na point source of 945 kBq. Its 1D motion pattern was either of $\cos^2$ and $\cos^4$ shape with a peak-to-peak amplitude of 20 mm and a period time of 4 s. The listmode PET data and the motion information had been recorded simultaneously by the different data acquisition systems and both data streams were synchronized afterwards. The motion information was artificially shifted by multiples of 50 ms to induce a delay Δt relative to the original data stream as it is illustrated in figure 5.9. The PET listmode data have been divided into 9 amplitude-sorted and time-sorted motion phases, each according to the time-shifted motion information and were reconstructed by the 4D MLEM algorithm. The results from the amplitude-sorted listmode data are visualized in figure 5.10. The blurring of the β^+-activity distributions parallel to the motion direction increases with rising time delay Δt while delays with up to 100 ms seem to be tolerable. The specific influence of the asymmetric $\cos^4$ motion becomes already visible in the reconstructed β^+-activity distribution for $\Delta t \geq 250$ ms which corresponds to a period fraction of 6.25%. The blurring effect is quantified in table 5.3 by the ratio of the FWTM values, similar as it was introduced in section 3.2.2. For measurements including the asymmetric $\cos^4$ motion with the larger gradients in the motion curve, the β^+-activity distributions are more affected by the incorrect correlation than those from the $\cos^2$ motion. If time-sorted motion phases are used, an incorrect correlation between the motion and the PET data by about 100 ms (2.5% of the motion period) will already lead to a FWTM ratio above 1.1, since there remains even for the correct correlation an increased motion influence after the reconstruction in comparison to the amplitude-sorted motion phases (cp. figure 3.14 and 3.15).

Discussion

For the temporal correlation between the motion and PET data, it is not reasonable to state a tolerable inaccuracy in terms of an absolute time offset. The influence of an deficient correlation onto the final β^+-activity distribution depends on several motion parameters

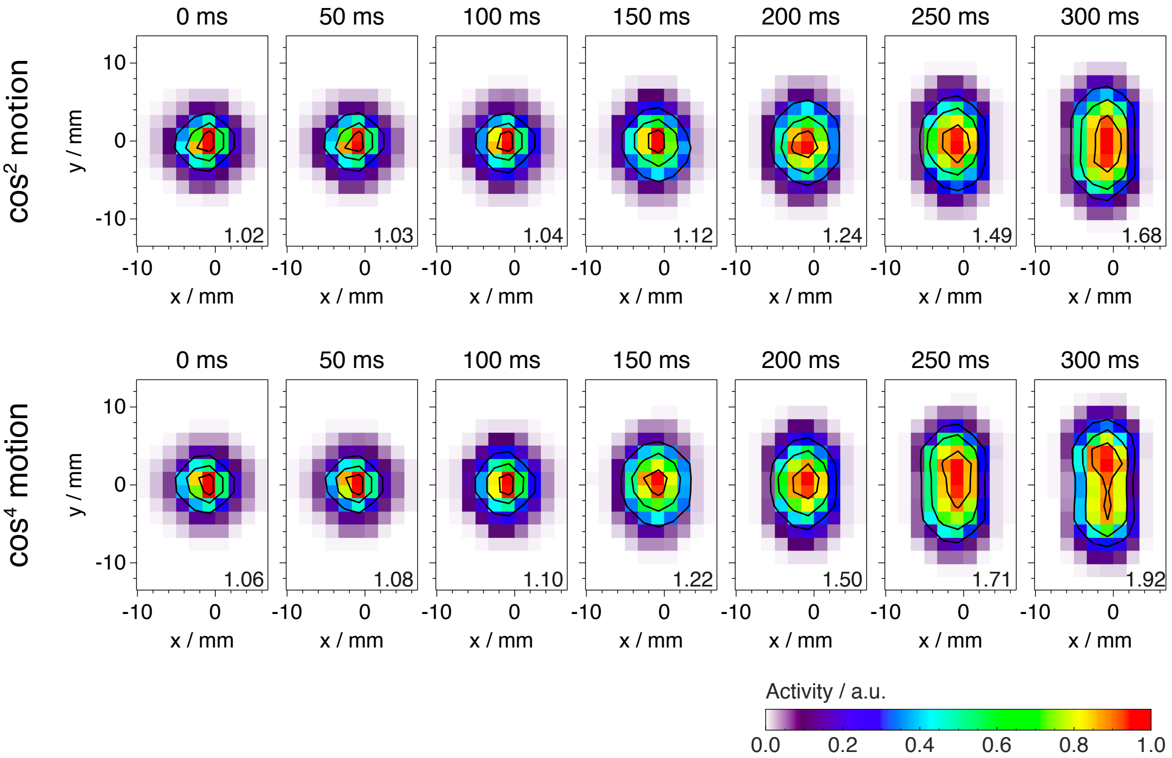

Figure 5.10: Reconstructed β^+-activity distributions of the ^{22}Na point source performing a $\cos^2$- (top) or $\cos^4$-shaped (bottom) motion. An increasing (from left to right) time offset of 0 ms to 300 ms was added to the corresponding motion signal before sorting the listmode data into the 9 amplitude-sorted motion phases. The according blurring in the motion direction (y) is quantified by the ratio of the FWTM values of the distribution ($\mathrm{FWTM}_y/\mathrm{FWTM}_x$) which is given in the lower right corner.

like the peak-to-peak amplitude, the period time and the exact motion pattern with all irregularities. These parameters determine the gradients in the motion curve and thus the absolute deviation in elongation for a certain time delay. The amount of coincidences that is sorted into wrong motion phases and the absolute difference in the transformation vectors for the correct and wrong motion phase determine the blurring in the final image. Also the

Table 5.3: FWTM ratios ($\mathrm{FWTM}_y/\mathrm{FWTM}_x$) for β^+-activity distributions of the point source that have been reconstructed with 9 amplitude- or time-sorted motion phases. Listmode PET data were assigned to these phases according to the $\cos^2$- or $\cos^4$-shaped motion signal which was delayed relative to the exact synchronized motion signal by Δt.

Δt:	0 ms	50 ms	100 ms	150 ms	200 ms	250 ms	300 ms
	9 amplitude-sorted motion phases						
$\cos^2$ motion:	1.02	1.03	1.04	1.12	1.24	1.49	1.68
$\cos^4$ motion:	1.06	1.08	1.10	1.22	1.50	1.71	1.92
	9 time-sorted motion phases						
$\cos^2$ motion:	1.05	1.06	1.11	1.17	1.29	1.41	1.62
$\cos^4$ motion:	1.07	1.08	1.12	1.25	1.36	1.54	1.79

inaccurate attenuation correction for coincidences that are sorted into a wrong motion phase influence the result but should be of minor importance.

The examined tolerance for a wrong temporal correlation between the PET and motion data of more than 50 ms seems to be fairly high. However, the limited accuracy for real-time tumour motion detection and the related unavoidable mis-sorting of coincidences into motion phases strengthen clearly the aim to aspire the best achievable accuracy in signal correlation. The verification of the correct correlation is desired when evaluating 4D IBT-PET data of patients. A quite simple and effective method would be the attachment of a point source with low β^+-activity to the moving body surface. The source activity can only be reproduced as a circular-shaped β^+-activity in the reconstructed image if there is a correct motion correlation. Otherwise, a data reconstruction in small intervals of a few ten milliseconds and the subsequent fit of the source position could be used to extract the immanent motion signal. However, such a usage of a radioactive source is debatable due to the additional radiation exposure to the patient. The correct correlation between the PET and motion acquisition systems should at least be verified with the presented point source method as one part of the daily routine checks.

5.3 Recommendations for the 4D IBT-PET workflow

A suitable workflow based on the comparison between a measured and an expected, simulated β^+-activity distribution (cp. figure 2.10) had been developed and was successfully applied under clinical conditions for the examination of IBT-PET data taken from static and well fixated target volumes (Enghardt *et al.* 2004a). An ingenious algorithm (Helmbrecht *et al.* 2012) allows to semi-automatically identify and quantify local deviations between the two distributions by comparing their 1D profiles parallel to the beam direction. Mismatches between the two distributions are typically related to anatomical changes during the fractionated therapy. Such a hypothesis can be verified by an according CT image modification and recalculation of the β^+-activity distribution (Parodi and Enghardt 2002; Parodi 2004).

The same workflow but with adapted an 4D reconstruction algorithm (cp. section 3) and a 4D simulation program (cp. section 4) is intended to be applied for intra-fractionally moving targets. However, within the previous sections it was demonstrated by dedicated experiments that special circumstances could result in a misleading interpretation of the 4D IBT-PET data.

- A similar shape may appear in the measured and simulated β^+-activity distribution although a crucial error occurred within the motion mitigation (cp. section 5.1.1). A potential failure in the dose delivery is reproduced by the simulation software due to the direct incorporation of the beam monitoring information in the simulation input parameters.
- Deviations between the two β^+-activity distributions may occur like e.g. shown in section 5.1.2, but they are not detectable by the comparison algorithm planned to be used

for semi-automatic evaluation. This would always be the case if one of the distributions is prolonged in a direction perpendicular to the incident beam. Since the predominant motion direction in the thoracic and abdominal region is in cranio-caudal direction, a blurring perpendicular to the incident beam direction is more likely than in parallel direction and might be caused by a deficient motion compensation or insufficient reconstruction accuracy.

- Blurred β^+-activity distributions might be generated from the measured 4D IBT-PET data after a deficient motion correlation (cp. section 5.2). The simulation would not reproduce such a blurring as long as the motion mitigation worked well and the nextpoint data are correlated correctly with the motion information. Consequently, the attempt to explain this detectable deviation between the two distributions by unexpected anatomical changes and related CT image modifications will fail.

The following briefly summarized suggestions and recommendations may prevent the observer from a mis-interpretation of the 4D IBT-PET data.

1. Perform a consistency check of the input parameters under consideration of the applied motion mitigation technique when creating the LUT for the simulation program. For a gated beam delivery this could e.g. be an examination whether the nextpoint signals have only been acquired at certain motion states of the target.
2. Perform an additional simulation of the beam delivery with original rasterpoint coordinates delivered to the static target (i.e. to the CT image phase that belongs to the treatment plan) under consideration of the the actual time structure of the treatment progress given by the recorded nextpoint signals. This results in a β^+-activity distribution with intended ranges and lateral dimension.
3. Compare the measured β^+-activity distribution not only to the simulated distributions but also to those acquired from previous fractions. It is unlikely that the same motion mitigation errors are reproduced twice in a similar way.
4. The results of the comparison algorithm should be rated critically. A declaration of no objection might also be related to the fact that certain activity is only found in one of the two distributions. Make also use of more intuitive comparison algorithms like the calculation of difference images (as shown in figure 4.13) from the simulated and measured β^+-activity distribution to ensure a more reliable statement for the comparison of the field edges.
5. If possible, apply the range verification algorithm to 1D profiles which are almost parallel to the predominant motion direction.
6. Evaluate other comparison algorithms, like that from Kuess *et al.* (2012), with respect to their applicability to 4D IBT-PET data, i.e. whether they can detect the differences between the measured and simulated distributions which are not accessible by the algorithm of Helmbrecht *et al.* (2012).
7. Ensure a correct correlation between the listmode PET data and the motion data by at least daily routine checks. The benefit from the inclusion of an immanent motion

signal into the PET data by means of a point source of low β^+-activity attached to the patient surface should be tested if the additional radiation exposure is justifiable.

8. By means of dedicated hardware changes in accordance with the Medical Devices Act the motion information could directly be included into the listmode data stream. A certain free bit in the listmode words could be used to switch between encoding coincidences or motion information, similar as it is done for the timewords (cp. figure 2.9).

6 Summary and outlook

IBT is a promising treatment option for radio-resistant tumours and those in close vicinity to OARs. The inverse depth-dose profiles of ion beams with the tunable Bragg peak position in the tissue allow for tumour conformal dose distributions. This enables a potential dose escalation in the tumour volume under simultaneous sparing of the surrounding normal tissue. Often occurring cancer types with high fatality rates like NSCLC or hepatocellular carcinoma could most effectively benefit from the potential dose escalation. Such target volumes in the thorax and upper abdominal region undergo intra-fractional motion, mainly related to respiration. Since the particle range in the patient depends strongly on the composition and density of the penetrated tissue and this tissue might undergo continuous density changes during a breathing cycle, IBT becomes prone to misdosage when treating intra-fractionally moving targets. Thus, an exact dose delivery demands high standards for quality assurance. These include reliable motion monitoring and mitigation techniques, but also a non-invasive dose monitoring system is highly desired.

The positron emission tomography, which can be performed as in-beam, in-room or offline measurement, is the only non-invasive, *in vivo* and *in situ* method for an indirect dose monitoring that has been applied under clinical conditions so far. For static tumour entities treated at the former medical beamline at GSI, a suitable IBT-PET workflow was developed which is mainly based on the comparison between the measured, radiation induced β^+-activity distribution in the patient and another one that is predicted by a Monte-Carlo simulation. Within this thesis, an upgrade of both the reconstruction of the 3D β^+-activity distribution and the simulation of the adequate PET listmode data stream was realized for intra-fractionally moving targets. The performance of the newly implemented 4D reconstruction and simulation algorithms was evaluated in detail by means of extensive measurement campaigns with moving radioactive sources and irradiated phantoms as well as accompanying simulation studies.

For the reconstruction of IBT-PET data taken from moving target structures, a 4D MLEM and a gated co-registration algorithm have been implemented taking into account the special geometry of the double-head PET scanner Bastei. With analogue computing time and under similar operation expense, i.e. the generation of motion phase sorted listmode data, related attenuation and scatter corrections and transformation matrices, it was shown in a simulation study that the 4D MLEM outperforms the gated co-registration method in terms of generating better local contrast recoveries. The general applicability of the algorithm for different motion patterns was demonstrated by the successful reduction and disappearance of the motion influence in the reconstructed β^+-activity distributions from moving radioactive sources. For 1D $\cos^2$ and $\cos^4$ motion with certain peak-to-peak amplitudes, it was clearly illustrated by systematic point source measurements that the motion influence can be more effectively reduced with the same number of motion phases if amplitude-sorted phases are applied. Additionally, it was revealed that the reduction of motion related activity blurring is mainly dependent on the mean residual motion, which is a quantity that combines the dependence on the peak-to-peak amplitude, the asymmetry of the real motion pattern, the number of applied motion phases and the method of motion phase sorting. Choosing parameters to obtain a mean residual motion of about half of a PET crystal size was found to be a worthwhile thumb rule to achieve acceptable results. Furthermore and most importantly, it has been demonstrated from measurements with moving PMMA targets of dedicated geometries and which had been irradiated using several motion mitigation techniques that relevant characteristics of the induced β^+-activity distributions are reproduced correctly after a 4D MLEM reconstruction. These are in particular the lateral field position and gradients as well as the particle range. They can also be deduced with a sufficient accuracy if only a reduced and clinically relevant counting statistic is available.

Within a second part of the thesis, the first simulation algorithm for the calculation of motion phase sorted listmode PET data has been implemented. By means of the correct processing of a variety of additional input information in comparison to the program for static targets, it is capable to simulate all available motion mitigation techniques, the creation and decay of β^+-emitters at motion-dependent positions and finally the scanner-specific listmode data streams. The proper functionality of the 4D simulation software was verified in a detailed phantom study including the sophisticated motion mitigation by depth-compensated tracking.

In summary, this thesis contributes on a large scale to a potential future application of the IBT-PET dose monitoring for intra-fractionally moving targets by providing the required algorithms for the β^+-activity reconstruction and simulation. Both algorithms are mandatory to apply afterwards the approved comparison method for the interpretation of the 4D IBT-PET data. However, selected and well-designed experiments were presented which demonstrated impressively that under certain circumstances the comparison might result in wrong or at least misleading conclusions. Appropriate recommendations for an adapted evaluation procedure were given in the thesis.

Except for one experiment with rotational movement, the investigated motion patterns in this thesis were restricted to 1D $\cos^2$ and $\cos^4$ functions without any irregularity. Systematic examinations of the achievable accuracy in the reconstructed β^+-activity distributions from more realistic, multi-directional motion patterns including several irregularities should be one of the next objectives for improving the 4D IBT-PET dose monitoring. Especially, the quantification of the influence of an imprecise motion detection on the reconstruction and simulation results is of high priority, since the assessment of the exact tumour motion in real time, its matching with the 4D planning CT image and the performance of a correct motion compensation will be one of the main challenges in the future when delivering ion beams to moving targets. Finally, 4D IBT-PET investigations incorporating real treatment plans, 4D patient CT images and breathing curves are desired to rate the expectable benefit from a 4D IBT-PET dose monitoring.

7 Appendix

Contents

A Transformation matrices

A.1 Composition of transformation matrices

In general, β^{+}-activity images comprising $N_x \times N_y \times N_z$ voxels are handled as 1D vectors with N_{vox} elements when calculating the transformed images. Voxels with static set-up components remain at their position under transformation and those belonging to a movable part are partitioned into the different voxels that intersect the transformed voxel volume. The element d_{ij} of an $N_{\mathrm{vox}} \times N_{\mathrm{vox}}$ transformation matrix denotes the fraction of voxel j that is transformed into voxel i.

The following examples illustrate the composition of transformation matrices in a fictitious 2D image space consisting of 9 voxels (pixels) of which the 2 coloured ones belong to a moving structure that undergoes a rigid transformation indicated by the coloured arrows.

- Static image space:

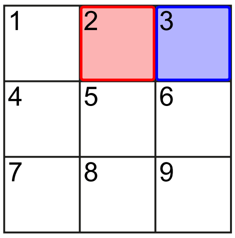

$$\Rightarrow \begin{pmatrix} 1&0&0&0&0&0&0&0&0\\ 0&1&0&0&0&0&0&0&0\\ 0&0&1&0&0&0&0&0&0\\ 0&0&0&1&0&0&0&0&0\\ 0&0&0&0&1&0&0&0&0\\ 0&0&0&0&0&1&0&0&0\\ 0&0&0&0&0&0&1&0&0\\ 0&0&0&0&0&0&0&1&0\\ 0&0&0&0&0&0&0&0&1 \end{pmatrix}$$

- Shifting by an integer number of voxels parallel to axis:

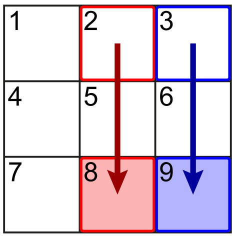

$$\Rightarrow \begin{pmatrix} 1 & 0 & 0 & 0 & 0 & 0 & 0 & 0 & 0 \\ 0 & 0 & 0 & 0 & 0 & 0 & 0 & 0 & 0 \\ 0 & 0 & 0 & 0 & 0 & 0 & 0 & 0 & 0 \\ 0 & 0 & 0 & 1 & 0 & 0 & 0 & 0 & 0 \\ 0 & 0 & 0 & 0 & 1 & 0 & 0 & 0 & 0 \\ 0 & 0 & 0 & 0 & 0 & 1 & 0 & 0 & 0 \\ 0 & 0 & 0 & 0 & 0 & 0 & 1 & 0 & 0 \\ 0 & 1 & 0 & 0 & 0 & 0 & 0 & 1 & 0 \\ 0 & 0 & 1 & 0 & 0 & 0 & 0 & 0 & 1 \end{pmatrix}$$

- Shifting by an arbitrary number of voxels parallel to axis:

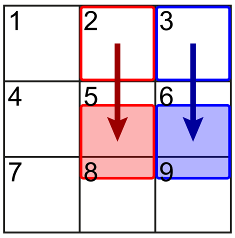

$$\Rightarrow \begin{pmatrix} 1 & 0 & 0 & 0 & 0 & 0 & 0 & 0 & 0 \\ 0 & 0 & 0 & 0 & 0 & 0 & 0 & 0 & 0 \\ 0 & 0 & 0 & 0 & 0 & 0 & 0 & 0 & 0 \\ 0 & 0 & 0 & 1 & 0 & 0 & 0 & 0 & 0 \\ 0 & 0.7 & 0 & 0 & 1 & 0 & 0 & 0 & 0 \\ 0 & 0 & 0.7 & 0 & 0 & 1 & 0 & 0 & 0 \\ 0 & 0 & 0 & 0 & 0 & 0 & 1 & 0 & 0 \\ 0 & 0.3 & 0 & 0 & 0 & 0 & 0 & 1 & 0 \\ 0 & 0 & 0.3 & 0 & 0 & 0 & 0 & 0 & 1 \end{pmatrix}$$

- Shifting by an arbitrary number of voxels in an arbitrary direction:

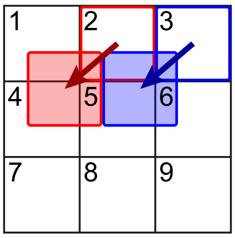

$$\Rightarrow \begin{pmatrix} 1 & 0.28 & 0 & 0 & 0 & 0 & 0 & 0 & 0 \\ 0 & 0.12 & 0.28 & 0 & 0 & 0 & 0 & 0 & 0 \\ 0 & 0 & 0.12 & 0 & 0 & 0 & 0 & 0 & 0 \\ 0 & 0.42 & 0 & 1 & 0 & 0 & 0 & 0 & 0 \\ 0 & 0.18 & 0.48 & 0 & 1 & 0 & 0 & 0 & 0 \\ 0 & 0 & 0.18 & 0 & 0 & 1 & 0 & 0 & 0 \\ 0 & 0 & 0 & 0 & 0 & 0 & 1 & 0 & 0 \\ 0 & 0 & 0 & 0 & 0 & 0 & 0 & 1 & 0 \\ 0 & 0 & 0 & 0 & 0 & 0 & 0 & 0 & 1 \end{pmatrix}$$

By this geometrical approach of overlapping volumes, even arbitrary non-rigid transformations are feasible. The third case (shifting by an arbitrary number of voxels parallel to axis) is relevant for the investigated experimental setups with 1D motion patterns where the targets move parallel to the y-direction.

Basically, for voxels filled with air no reason exists to shift them. They shouldn't contain a considerable amount of β^+-activity. However, they might do in regions close to volumes with a high β^+-activity because of the partial volume effect due to limited spatial resolution. To conserve the lateral gradients of the β^+-activity in the phantoms, it has been decided to shift all voxels in the image space positioned laterally to the moving targets. This is feasible for the performed experiments, since there is nothing else than air and the motion platform which is transformed anyway. For a potential application of the 4D MLEM algorithm to patient data, one has to look carefully at the transformation matrices and transition maps created from 4D CT scans. The consequences for shifting also the adjacent voxels by the transformation matrix for the fictitious 2D image space are shown below:

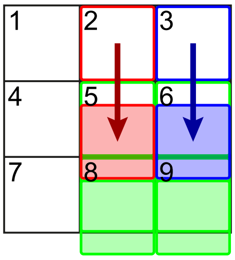

$$\Rightarrow \begin{pmatrix} 1 & 0 & 0 & 0 & 0 & 0 & 0 & 0 & 0 \\ 0 & 0 & 0 & 0 & 0 & 0 & 0 & 0 & 0 \\ 0 & 0 & 0 & 0 & 0 & 0 & 0 & 0 & 0 \\ 0 & 0 & 0 & 1 & 0 & 0 & 0 & 0 & 0 \\ 0 & 0.7 & 0 & 0 & 0 & 0 & 0 & 0 & 0 \\ 0 & 0 & 0.7 & 0 & 0 & 0 & 0 & 0 & 0 \\ 0 & 0 & 0 & 0 & 0 & 0 & 1 & 0 & 0 \\ 0 & 0.3 & 0 & 0 & 0.7 & 0 & 0 & 0 & 0 \\ 0 & 0 & 0.3 & 0 & 0 & 0.7 & 0 & 0 & 0 \end{pmatrix}$$

Whole voxels (8^{th} and 9^{th}) or parts of them (5^{th} and 6^{th}) are positioned outside of the field of view while other voxels are empty after transformation (2^{nd} and 3^{rd}). These voxels are located at the peripheral areas of the image space. One has to make sure that the image space is large enough to keep those voxels far away from the regions of high β^+-activity. The empty voxels might additionally be compensated by out-of-FOV corrections (Langner *et al.* 2008).

A.2 Storage of transformation matrices

The size of the transformation matrix is defined by the image space consisting of $N_{\text{vox}} = N_x \times N_y \times N_z$ voxels. Each voxel has the possibility to be (partly) transformed into one of these voxels. This results in transformation matrices with a dimension of $N_{\text{vox}} \times N_{\text{vox}}$. Most of the matrix values are equal to zero, since a single voxel can only be split up into a limited number of voxels. For rigid translation where the voxel shape and volume is conserved under transformation a maximum number of 8 matrix elements per column have a non-zero value.

There exist many methods for storing those large-scale sparse matrices (Barrett *et al.* 1994). Computer memory is effectively used by storing non-zero matrix elements only. The simplest way is saving the matrix in triplet form. A non-zero matrix element is described by its value, its row index and its column index. Other elements are equal to zero. The exemplary matrix at the end of appendix A.1 for shifting the two moving and laterally adjoined voxels 2 and 3 by 1.7 voxel lengths parallel to a coordinate axis would contain following triplets (counting indices from 0 to 8):

Value:	1	1	0.7	0.7	1	0.3	0.7	0.3	0.7
Row index:	0	3	4	5	6	7	7	8	8
Column index:	0	3	1	2	6	1	4	2	5

Triplets have been stored in NetCDF format. The exact image space dimensions (number of voxels in each direction and the size of the voxels) have been added for testing whether the matrix can be applied to a certain image and will generate valuable transformation results. During the 4D reconstruction the handling and processing of transformation matrices is done by means of the fast performing *CSparse* package (Davis 2006) which is used for reading the triplet form, calculating normalization and compressing the matrices to a more dense (Compressed Column Storage) format. Further routines allow for a comfortable application of the matrices to the PET images by matrix-vector multiplication.

A.3 Transformation matrices for rotation

For pure translational rigid motion the intersection volumes of 2 voxels are always rectangular cuboids whose volume can easily be calculated. For rotational motion the intersection volume has in general the shape of an irregular polyhedron. In the performed experiments the rotation axis is parallel to one coordinate axis (z-axis). The intersection volume is then determined as prism volume, $V = b \cdot h$, with height h equal to the voxel height and a polygonal base area b. Consequently, the calculation of the volume can be broken down to a 2D consideration (in the x-y plane). One has to specify the intersecting areas of two arbitrarily oriented squares (which are a special type of polygons). The area b of the resulting polygon can be calculated with the Gaussian trapezoidal function

$$2 \cdot b = \sum_{i=1}^{n} (y_i + y_{i+1}) \cdot (x_i - x_{i+1}), \tag{7.1}$$

where x_i and y_i are the counter-clockwise labelled coordinates of the n polygon vertices and the index $n + 1$ is equal to the index 1 in a closed polygon. The calculation of the vertices of the polygon can be done by so-called polygon clipping algorithms, e.g. by the Sutherland-Hodgman algorithm (Sutherland and Hodgman 1974). Smith (2012) provides a code that clips a polygon given by its vertices to a unit pixel grid and calculates the intersection areas with each pixel in the grid. This code was slightly adapted and integrated into a routine for the creation of the transformation matrices. For proof-of-principle experiments the whole image space was rotated by a certain angle. The following example demonstrates the population of matrix elements for an image space consisting of one voxel slice only and that is rotated by 30° around an axis intersecting the image plane in the perpendicular direction at the common vertex of voxel 5, 6, 8 and 9. Two voxels are highlighted for better understanding.

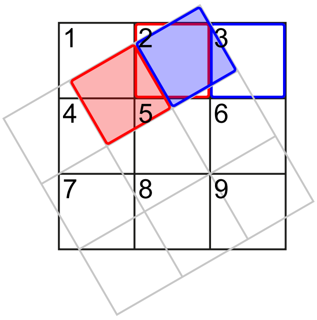

$$\Rightarrow \begin{pmatrix}
0.15 & {\color{red}0.40} & 0 & 0 & 0 & 0 & 0 & 0 & 0 \\
0 & {\color{red}0.15} & {\color{blue}0.76} & 0 & 0 & 0.02 & 0 & 0 & 0 \\
0 & 0 & {\color{blue}0.15} & 0 & 0 & 0.13 & 0 & 0 & 0 \\
0.40 & {\color{red}0.31} & 0 & 0.15 & 0.13 & 0 & 0 & 0 & 0 \\
0 & {\color{red}0.13} & {\color{blue}0.02} & 0 & 0.58 & 0.27 & 0 & 0 & 0 \\
0 & 0 & 0 & 0 & 0 & 0.58 & 0 & 0 & 0.27 \\
0 & 0 & 0 & 0.76 & 0.02 & 0 & 0.15 & 0 & 0 \\
0 & 0 & 0 & 0.02 & 0.27 & 0 & 0.13 & 0.58 & 0 \\
0 & 0 & 0 & 0 & 0 & 0 & 0 & 0.27 & 0.58
\end{pmatrix}$$

B Noise reduction in analogue signals by FFT-based filtering

The analogue signal of the displacement sensor contains high frequency noise. This may cause misassignment of listmode date to the motion phases. For well-defined and analytically prescribed regular motion patterns the signal can be smoothed quite well by a corresponding fitting function. Otherwise a low pass filtering in the frequency domain can be applied after a FFT-based filtering to eliminate the high frequency noise. The filter function w for the signal frequencies f of the utilized parabolic low pass filter is described in the frequency space by

$$w(f) = \begin{cases} 1 - \frac{f^2}{f_c^2} & \text{for } f \leq f_c, \\ 0 & \text{for } f > f_c, \end{cases} \tag{7.2}$$

where f_c stands for a selectable cutoff frequency. This cutoff frequency is adjusted by the integer parameter m in the formula

$$f_c = \frac{1}{m \cdot \Delta t}, \quad m \geq 2. \tag{7.3}$$

Δt denotes here the time interval between two data points belonging to the noisy signal.

For experiments with the rotating motion table, data were sampled at a frequency of 100 Hz. A cutoff frequency with a value of approximately 50 times of the motion frequency (1/3.8 Hz ≈ 0.26 Hz) was chosen. This results in a value of 8 for the parameter m. FFT filters with higher f_c values tend to retrace the noise in the signal. Lower cutoff frequencies do not approximate very well the curvature and extrema of the periodic signal. Figure B.1 shows a section of the analogue voltage signal from the displacement sensor and the influence of the chosen cutoff frequency onto the FFT filtered signal for 3 exemplary values of f_c.

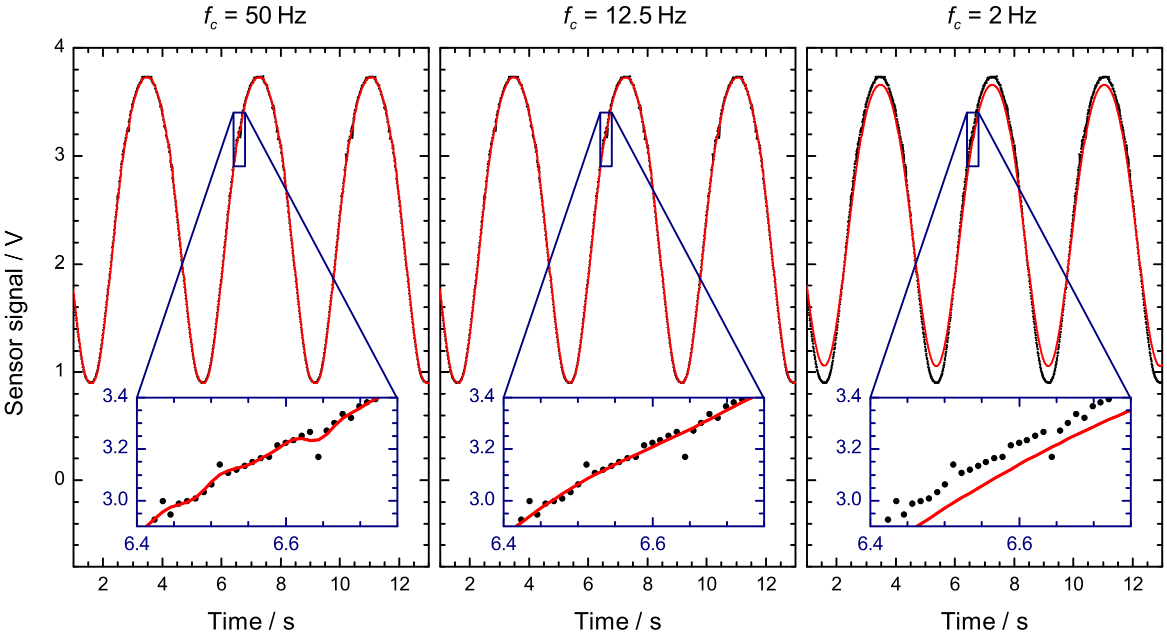

Figure B.1: Results of parabolic FFT-based filtering (red) of the acquired motion signal (black) for 3 cutoff frequencies. A cutoff frequency of 50 Hz (left) is too high, since the filtered function graph retraces the signal fluctuations as shown in the inset diagram. For too low values (right), relevant frequencies are rejected and the measured signal is not well approximated.

C Motion tables and corresponding motion patterns

C.1 Rotational motion

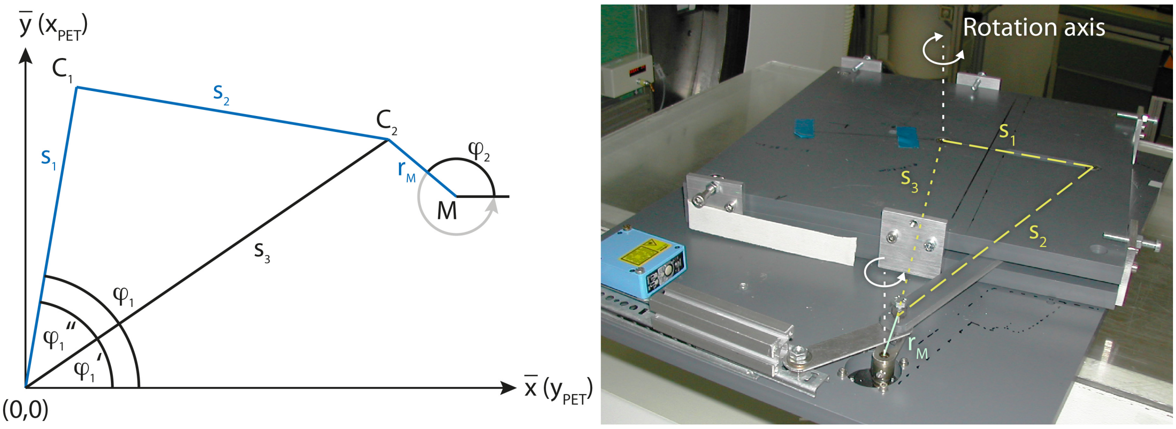

Figure C.2: Sketch of the coupling (blue) between the motor drive (rotation axis at $\vec{M}$) with rotation angle φ_2 and the rotation of the platform (rotation axis at coordinate (0,0) and rotation angle φ_1) in a right handed coordinate system (left). The connection rod of length s_2 transmits the motion between the coupling points C_1 and C_2 at the distances s_1 and r_M from the respective rotation axes. An image of the motion table is overlain by the two rotation axes and the considered distances (right).

The motion table for rotational motion used for experiments in section 3.2.1 is driven by an electric motor. By means of its supply voltage, the motion period is freely adjustable. The coupling between the motor and the platform is outlined in figure C.2 within the right-handed coordinate system $(\bar{x}, \bar{y})$. The angle φ_1 of the platform is a function of the rotation angle φ_2 of the motor. The lengths of the con-rods s_1, s_2 and r_M can be set by screws in elongated mounting hole and are fixed during an experiment. The length of s_3 changes continuously by the position of the coupling point C_2 related to the angle φ_2. The coordinates of the coupling point C_1 follow immediately from that.

The coordinates of the coupling point C_2 are given by the formula

$$\vec{C}_2 = \vec{M} + r_M \cdot \begin{pmatrix} \cos\varphi_2 \\ \sin\varphi_2 \end{pmatrix} . \tag{7.4}$$

With that, the length s_3 can be deduced from the relation

$$s_3^2 = C_{2\bar{x}}^2 + C_{2\bar{y}}^2 = \left(M_{\bar{x}} + r_M \cdot \cos\varphi_2\right)^2 + \left(M_{\bar{y}} + r_M \cdot \sin\varphi_2\right)^2 , \tag{7.5}$$

and the angle φ_1' from

$$\tan\varphi_1' = \frac{C_{2\bar{y}}}{C_{2\bar{x}}} = \frac{M_{\bar{y}} + r_M \cdot \sin\varphi_2}{M_{\bar{x}} + r_M \cdot \cos\varphi_2} . \tag{7.6}$$

With equation (7.5) and the law of cosines adapted for the triangle with the sides s_1, s_2 and

s_3 the angle φ_1'' is given in the formula

$$\cos\varphi_1'' = \frac{s_1^2 - s_2^2 + s_3^2}{2\cdot s_1 s_3} = \frac{s_1^2 - s_2^2 + (M_{\bar{x}} + r_M\cdot\cos\varphi_2)^2 + (M_{\bar{y}} + r_M\cdot\sin\varphi_2)^2}{2\cdot s_1\sqrt{(M_{\bar{x}} + r_M\cdot\cos\varphi_2)^2 + (M_{\bar{y}} + r_M\cdot\sin\varphi_2)^2}}. \tag{7.7}$$

Finally, the rotation angle φ_1 of the motion platform in dependence of φ_2 can be calculated by using equations (7.6) and (7.7)

$$\begin{aligned}\varphi_1 &= \varphi_1' + \varphi_1'' \\ &= \arctan\frac{M_{\bar{y}} + r_M\cdot\sin\varphi_2}{M_{\bar{x}} + r_M\cdot\cos\varphi_2} + \arccos\frac{s_1^2 - s_2^2 + (M_{\bar{x}} + r_M\cdot\cos\varphi_2)^2 + (M_{\bar{y}} + r_M\cdot\sin\varphi_2)^2}{2\cdot s_1\sqrt{(M_{\bar{x}} + r_M\cdot\cos\varphi_2)^2 + (M_{\bar{y}} + r_M\cdot\sin\varphi_2)^2}}.\end{aligned} \tag{7.8}$$

It has to be noted that the angle φ_1 in equation (7.8) is not the rotation angle α of the platform which is used in the transformation matrices. The angle α is defined in the left-handed coordinate system of the PET scanner which is here indicated with the subscript. Following relations hold true: $\alpha = 0$ for $y_{\mathrm{PET}} = \bar{x} = 0$ and $\alpha = \frac{\pi}{2}$ for $x_{\mathrm{PET}} = \bar{y} = 0$. That means $|\alpha| = |\varphi_1 - \frac{\pi}{2}|$.

C.2 Motion table with stepping motor for precise 1D motion patterns

A motion table has been developed to emulate motion patterns as given by (2.13). This in-house made motion table is shown in figure C.3. A stepping motor drives a dedicated target holder made up of PMMA along a linear axis. The protruding target support of 6 mm thickness allows for well-defined attenuation correction. It is the only part of the whole system that is placed in the FOV when the motion table has been adjusted to perform a target mo-

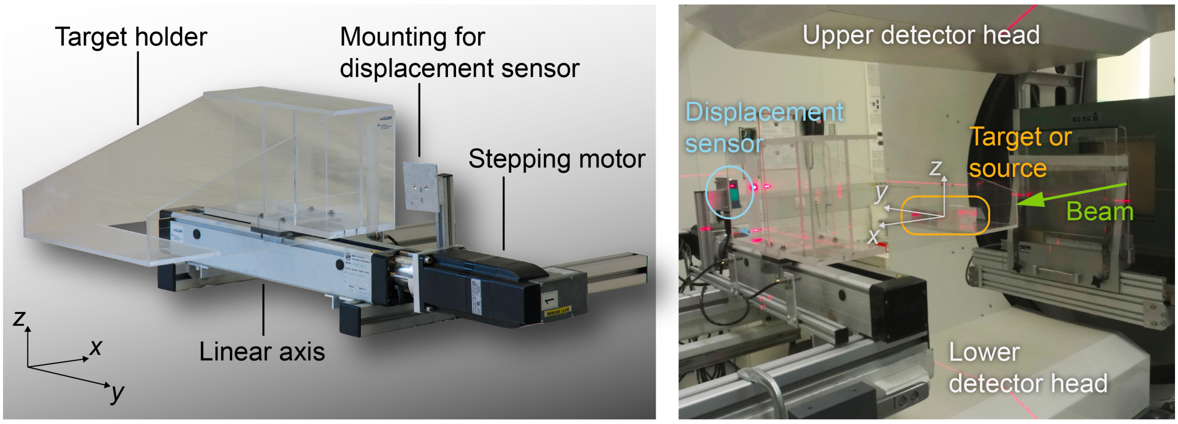

Figure C.3: Motion table for 1D motion patterns driven by a stepping motor along a linear axis. Components are labelled in the left figure. The right image shows the motion table with displacement sensor operating at the treatment site including the double-head PET scanner. The marked (left-handed) coordinate systems allow for better understanding of the motion table orientation in between the two detector heads. Motion proceeds parallel to the y-axis.

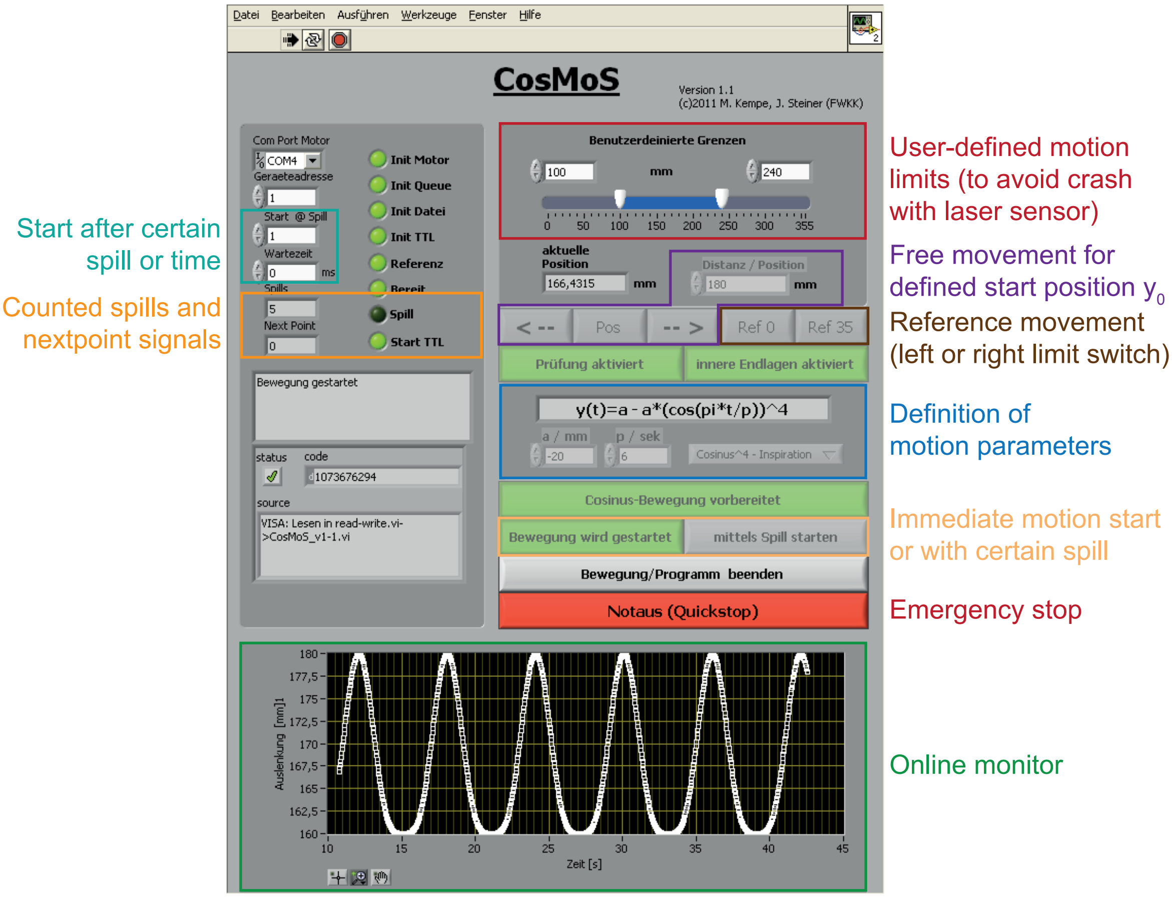

Version 1.1
(c)2011 M. Kempe, J. Steiner (FWKK)

Com Port Motor: COM4
Geraeteadresse: 1
Start @ Spill: 1
Wartezeit: 0 ms
Spills: 5
Next Point: 0

Bewegung gestartet

status: ✓ code: 1073676294
source: VISA: Lesen in read-write.vi->CosMoS_v1-1.vi

Benutzerdeinierte Grenzen: 100 mm 240
aktuelle Position: 166,4315 mm
Distanz / Position: 180 mm

y(t)=a - a*(cos(pi*t/p))^4
a / mm: -20
p / sek: 6
Cosinus^4 - Inspiration

Start after certain spill or time

Counted spills and nextpoint signals

User-defined motion limits (to avoid crash with laser sensor)

Free movement for defined start position y_0

Reference movement (left or right limit switch)

Definition of motion parameters

Immediate motion start or with certain spill

Emergency stop

Online monitor

Figure C.4: Screenshot of the graphical user interface of CosMoS in an early version 1.1 with some highlighted functionalities.

tion in the left-right direction in BEV at the fixed horizontal beamline at GSI. This motion along the y-axis in the left-handed coordinate system of the PET scanner would correspond to a cranio-caudal motion within a patient treated in conventional supine position. An attached laser displacement sensor (Model OD100-35P840, SICK Vertriebs-GmbH, Düsseldorf, Germany) records the actual elongation of the target holder and generates a surrogate signal which controls the motion mitigated beam delivery by means of gating or tracking.

The developed LabVIEW control software CosMoS (which stands for COSinusartige MOtorSteuerung) for the stepping motor records the motion and other signals like the nextpoint signals, the trigger signals for a predefined gating window and the beam status from the accelerator. The latter one allows an optional triggering of the motion start at exhalation ($\Phi_0 = \pi/2$) or inhalation ($\Phi_0 = 0$) with the begin of the first spill. Arbitrary values can be chosen for the start position y_0, the peak-to-peak amplitude a and the period time τ, both for n equal to 1 or 2. A screenshot of the graphical user interface of CosMoS version 1.1 is shown in figure C.4. The motion table is equipped with several safety measures. Besides an emergency stop, inner limit switches can be set by the user to avoid an accidental crash with the mounted displacement laser sensor or other equipment nearby. These switches can be turned off for reference movement when the platform is driven to one of the limit switches at the end of the linear axis. An online motion monitor gives a visual feedback to the user who operates the motion table from the control room, i.e. outside of the experiment bunker.

The functionality of the motion table has been considerably increased in the recent past. In the current version 2.0, an analytically described variation of amplitude, frequency and baseline has been incorporated. The related investigations are beyond the scope of this thesis. This thesis does only refer to experiments with regular motion patterns described by (2.13).

C.3 Motion table enabling relative target movement

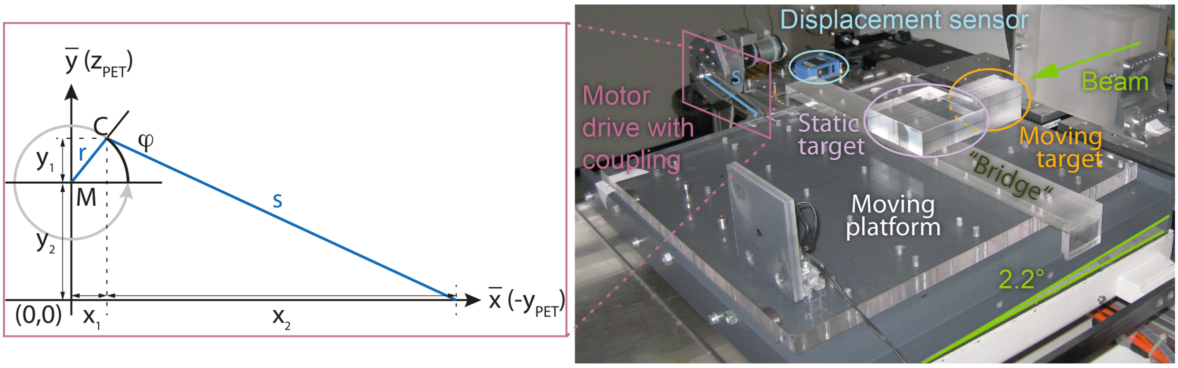

Figure C.5: Motion table for relative motion between two targets. Components are labelled in the right image which shows the setup for one of the presented experiments in section 5.1.2. A bridge device spans the moving platform and carries a static target (here made of 100 mm×100 mm×30 mm PMMA). Another one (labelled in orange and consisting of 80 mm × 50 mm × 47 mm PMMA) is positioned on the platform in front of the static target. A laser displacement sensor measures continuously the distance to the platform which is driven by an electric motor. A draft (not to scale) on the left shows the coupling between the motor drive with rotation centre at M and the motion platform by means of the connection rod of length s.

For performing experiments with targets moving relative to each other (where one is at rest), a motion table from GSI, also dedicated for 1D motion patterns, has been used. As shown in figure C.5, it consists of a moving platform which is slightly tilted against the treatment couch by about 2.2° to move exactly parallel to the incident beam. This angle is neglected within all other experiments. An additional bridging device allows to position phantoms at arbitrary fixed positions in the field of view of the camera directly next to moving targets. The motion of the platform is provided by a coupling to an electric motor. A sketch of that coupling is also shown in figure C.5 with a right-handed coordinate system $(\bar{x}, \bar{y})$. The location of the coupling point C of the connection rod with length s is described by the radial distance r from the centre of the rotation axis M and the continuously changing rotation angle φ. The distance of the moving platform x_p from the origin of the coordinate system $(\bar{x}, \bar{y})$ is described as

$$\begin{aligned} x_p &= x_1 + x_2 \\ &= r\cos\varphi + \sqrt{s^2 - (y_1 + y_2)^2} \\ &= r\cos\varphi + \sqrt{s^2 - (r\sin\varphi + y_2)^2}, \end{aligned} \tag{7.9}$$

where y_2 and s are fixed quantities of about 25 mm and 155 mm and r can be adjusted on a limited scale. For emulating a peak-to-peak amplitude of 20 mm during experiments a radial distance r of 10 mm was chosen. The exact motion calculation according to (7.9) results in a peak-to-peak amplitude of the moving platform of 20.27 mm. Considering the manufacturing accuracy of the motion table and the accuracy for length determination of s and y_2 a peak-to-peak amplitude of 20 mm has been assumed for data evaluation when interpreting the voltage signal of the laser displacement sensor.

D Synchronisation of PET, motion and beam monitoring data

A reliable synchronisation between the listmode PET data stream and the logged motion signal is essential for an accurate sorting of acquired coincidences into the corresponding motion phases leading to reconstructed images without motion artefacts (section 3). The creation of the LUT serving as input for the 4D simulation program (section 4) requires additionally a correct synchronization of data acquired from the beam monitoring and motion compensation systems. In all cases, synchronization was achieved manually by means of the spill signals provided from the accelerator side as TTL pulses which are tapped by the different data streams. The so-called signal 46 and signal 51 indicate the start and the end of a (potential) beam extraction cycle, respectively. These signals are one part provided by the MEFI bus (Machine, Energy, Focus, Intensity) and can be gathered at different crates in the therapy control room and in the treatment room.

Figure D.6 shows an example of the different data streams with their corresponding spill signals which have been acquired from the gated irradiation presented in section 5.1.1. Since the motion was driven and recorded by the motion table with stepping motor (cp. appendix C.2), the data acquisition was started with the begin of the motion that coincided with the beginning of the first particle-containing spill. Motion monitoring can also be performed by the laser displacement sensor. In those cases, the motion data acquisition is started prior the first empty spill. A potential energy adaptation by the wedge system for depth-compensated tracking was logged on the same time scale. For off-beam source measurements (cp. section 3.2), artificial timing signals 46 and 51 were provided from the main control room. These signals have been logged by the PET and motion acquisition system and were used for synchronization as usual.

Since timing signals in the PET or motion logging are sometimes acquired with a delay of some tens of milliseconds, a reliable synchronization is not feasible by simply calculating the offset for a certain single signal. The time offsets between the different data streams were defined as the mean time difference for all available signals 46 and 51, exclusive the delayed ones. This manually performed synchronization is extremely time-consuming and prolongs unnecessarily the whole 4D IBT-PET workflow. For a future clinical application, a universal interface that allows the parallel recording of the different signals by a single system should be aspired. Commonly, new commercially available particle treatment facilities offer at least

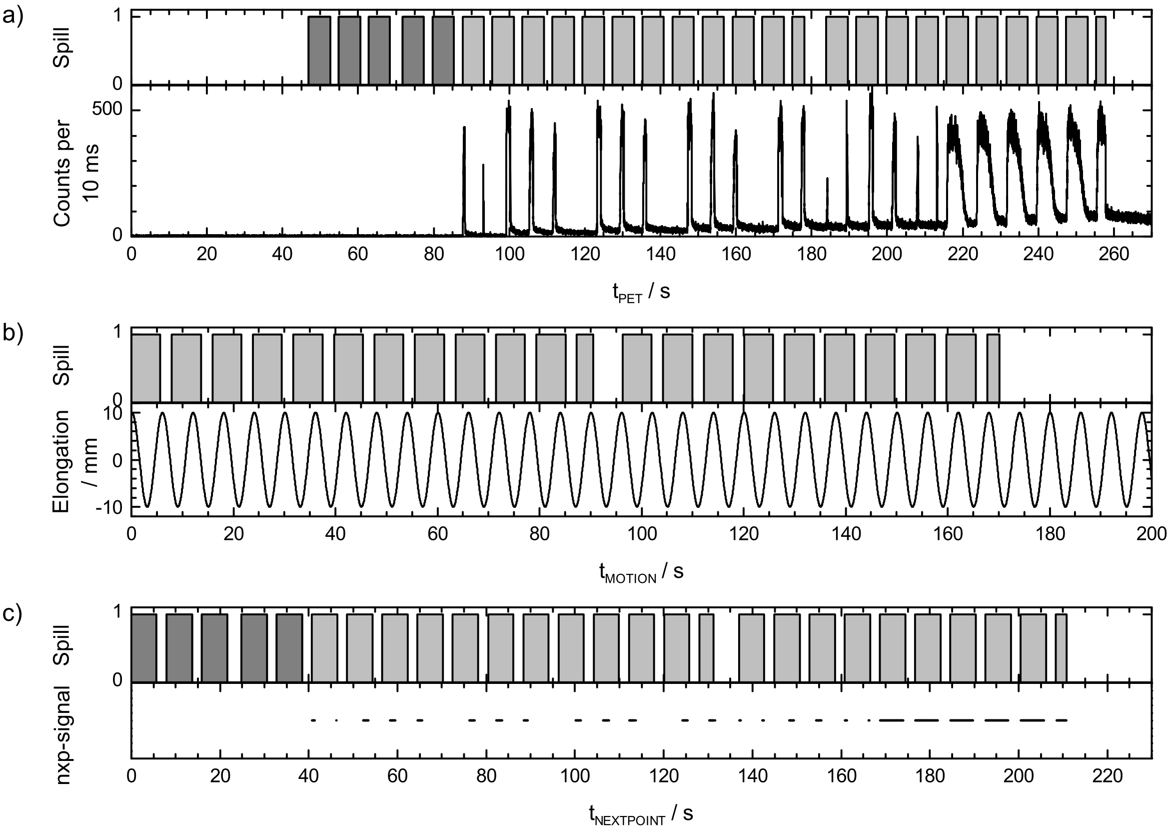

Figure D.6: Illustration of the different data streams belonging to the measurement with failed gating presented in section 5.1.1. The PET listmode data acquisition (a) was started about 46 s before the irradiation began with 5 initial empty spills (dark grey). Motion (b) was started with the first spill delivering particles. Thus, the 5 empty spills are not logged by the motion table. The acquisition of SAM (Steuerung und Auslese Modul) data starts with the first empty spill and includes the recording of nextpoint signals (c). As it is clearly visible in the listmode and nextpoint data, the gated irradiation performed as expected for 16 spills and broke down with the begin of the 17th spill. From that moment on, particles have been delivered throughout the whole spills irrespective of the motion state. Two spills (12th and 22nd of those marked in light grey) are shortened due to the interrupt by the end-of-plane signal which indicats that all raster points of one energy have been delivered.

a coupling between the gating equipment and the beam control system. These universal beam triggering systems could be used for a simultaneous acquisition of the signals from the accelerator, motion acquisition, beam monitoring and potential range compensation. Thus, only a single data stream needs to be correlated to the in-beam or in-room PET signals or to the motion and PET data from an off-line PET measurement.

E Sorting PET data by time or amplitude and calculating corresponding mean offsets

After synchronizing the PET listmode data stream with the motion signal, the datawords can be sorted into different motion phases. Two potential methods are available. Their influence has been investigated in more detail in section 3.2.2.

The conventional way of sorting is referred to as sorting by time or sorting by phase and is based on the proportional division of each motion cycle into a user-defined number N of intervals with equal length in time. To define the length of a motion cycle, the trigger times indicating its start and end have to be extracted. These triggers are typically set at the reversal points of the motion with maximum elongation as shown in figure E.7. In a next step, the times t_i are defined when a new motion phase i starts and the listmode data stream can be directly split into several files according to the embedded time stamps. The start of the first phase t_1 is equal to the trigger time for the begin of the motion cycle and the N^{th} phase stops with the next trigger time. Sorting by time has the advantage to accumulate similar statistics in all motion phases but several phases might comprise a rather large residual motion amplitude.

For sorting by amplitude, the global minimum and maximum value of the voltage or position signal (depending on used motion table) were defined. By convention, the phase definition is performed in that way that the extremal elongations correspond to the mid of the encompassed amplitude interval of the related phase (cf. figure E.7). Thus, the peak-to-peak amplitude is divided by $N-1$ to define the constant amplitude interval per phase. With that knowledge the minimal and maximal amplitude value belonging to a certain phase can easily be calculated. Taking the motion information into account, it is possible to identify the times t_i when the new motion phases will start and thus to assign the single listmode data to a certain phase. The reduced mean residual motion within the motion phases in comparison to the sorting by time leads to a better reduction of motion artefacts when same parameters had been used for reconstruction. However, as obviously visible in the lower right graph

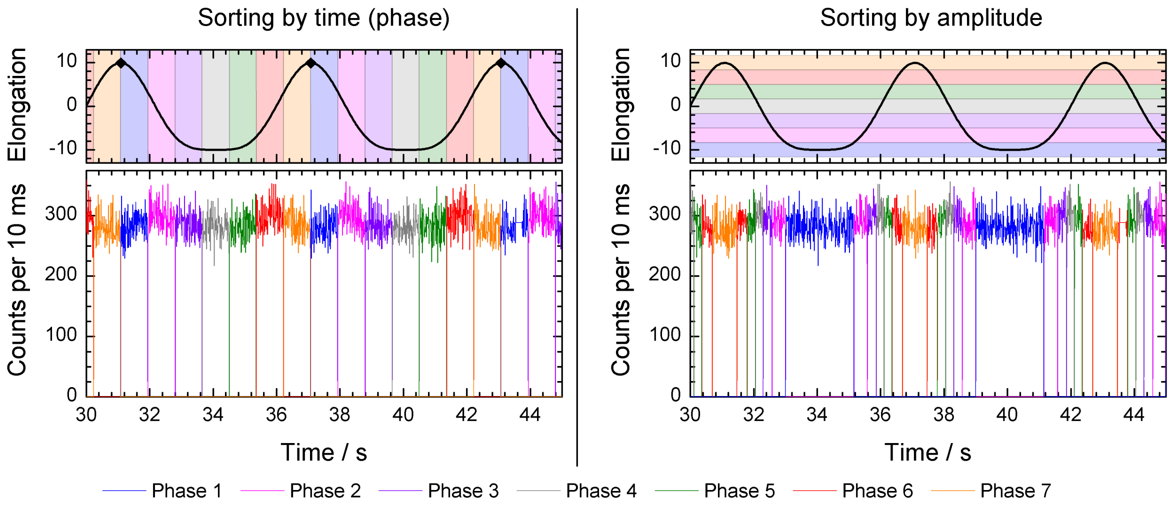

Figure E.7: Illustration of sorting a listmode data stream into 7 motion phases according to the time (left) or amplitude (right) for a $\cos^4$ motion with 20 mm peak-to-peak amplitude (top). Black diamonds in the upper left graph indicate the extracted trigger times for the start of new motion cycles. Amplitude intervals have always been chosen in that way that reversal points are placed in the middle of the minimum and maximum amplitude interval (upper right).

of figure E.7, different numbers of coincidences are assigned to the different motion phases due to the shorter and longer residence times of the target volume within certain amplitude intervals. Especially those phases including the reversal points of the motion contain larger parts of the original listmode data stream. This imbalance is considered by a reasonable scaling during the 4D MLEM reconstruction.

Ideally, the same way of PET data sorting is applied as for the 4D planning CT image which provides the phase-specific attenuation and scatter correction for the β^+-activity reconstruction. Furthermore, the transformation matrices need to be extracted from the 4D CT image. Irrespective of the concrete 3D motion pattern of the real patient breathing curve, the target volume will always be represented at its mean residence position in the corresponding CT image. This fact was also taken into account for the investigated 1D $\cos^2$ and $\cos^4$ motion patterns when positioning the targets into the different motion phases for calculating the artificial 4D CT images, attenuation corrections and transformation matrices. For a 1D motion described by the function $f(t)$ the mean residence position in phase i is given as

$$\overline{y_i} = \frac{1}{t_{i+1} - t_i} \cdot \int_{t_i}^{t_{i+1}} f(t)\, dt, \tag{7.10}$$

where t_i and t_{i+1} are the times when the target enters and leaves the i^{th} motion phase, respectively. For motion patterns according (2.13) the integration can be performed analytically by following expressions:

$$f(t) = \cos^2(t): \qquad \overline{y_i} = \frac{1}{2} + \frac{\sin(2t_{i+1}) - \sin(2t_i)}{4 \cdot (t_{i+1} - t_i)} \tag{7.11}$$

$$f(t) = \cos^4(t): \qquad \overline{y_i} = \frac{3}{8} + \frac{\sin(2t_{i+1}) - \sin(2t_i)}{4 \cdot (t_{i+1} - t_i)} + \frac{\sin(4t_{i+1}) - \sin(4t_i)}{32 \cdot (t_{i+1} - t_i)}. \tag{7.12}$$

An example for the mean residence positions calculated according to these equations is summarized in table E.1 for 9 motion phases of the $\cos^2$- and $\cos^4$-shaped motion pattern with maximal elongation of ±10 mm.

Table E.1: Mean residence positions for targets performing 1D $\cos^2$ and $\cos^4$ motion patterns with maximal elongation of ±10 mm and considering 9 motion phases. These offset vectors are necessary for the creation of the corresponding attenuation corrections and transformation matrices.

	Mean offsets for $\cos^2$ motion		Mean offsets for $\cos^4$ motion	
Phase	Time-sorted	Amplitude-sorted	Time-sorted	Amplitude-sorted
1	9.207 mm	−9.580 mm	8.471 mm	−9.736 mm
2	4.899 mm	−7.597 mm	1.248 mm	−7.639 mm
3	−1.701 mm	−5.036 mm	−6.364 mm	−5.053 mm
4	−7.506 mm	−2.514 mm	−9.606 mm	−2.525 mm
5	−9.798 mm	0.000 mm	−9.996 mm	−0.008 mm
6	−7.506 mm	2.514 mm	−9.606 mm	2.508 mm
7	−1.701 mm	5.036 mm	−6.364 mm	5.031 mm
8	4.899 mm	7.597 mm	1.248 mm	7.593 mm
9	9.207 mm	9.580 mm	8.471 mm	9.579 mm

Bibliography

Ando K, Kase Y (2009) Biological characteristics of carbon-ion therapy. *Int J Radiat Biol* 85(9):715–728.

Badura E, Brand H, Essel HG, Haberer T, Hardel H, Hoffmann J, Kurz N, Liebold P, Ott W, Poppensieker K, Richter M (2000) Control System for Cancer Therapy with a Heavy Ion Beam at GSI. *IEEE Trans Nucl Sci* 47(2):170–173.

Badura E, Eickhoff H, Essel H, Haberer T, Hoffmann J, Krause U, Ott W, Poppensieker K, Richter M, Schardt D, Steiner R, Voss B (1997) Safety and control system for the GSI Therapy Project. In: *ICALEPCS*. Beijing.

Barrett R, Berry M, Chan TF, Demmel J, Donato J, Dongarra J, Eijkhout V, Pozo R, Romine C, der Vorst HV (1994) *Templates for the Solution of Linear Systems: Building Blocks for Iterative Methods, 2nd Edition*. SIAM, Philadelphia, PA. 4.3.1 Survey of Sparse Matrix Storage Formats.

Bauer J, Unholtz D, Sommerer F, Kurz C, Haberer T, Combs SE, Welzel T, Herfarth K, Debus J, Parodi K (2012) First clinical experience with offline PET/CT-based in-vivo verification of scanned carbon ion irradiation. *Radiother Oncol* 103(Supplement 1):S323.

Berger MJ, Coursey JS, Zucker MA, Chang J (2005) ESTAR, PSTAR, and ASTAR: Computer Programs for Calculating Stopping-Power and Range Tables for Electrons, Protons, and Helium Ions (version1.2.3). National Institute of Standards and Technology. [accessed: 25 January 2013]. URL: `http://physics.nist.gov/Star`.

Beringer J, Arguin JF, Barnett RM, Copic K, Dahl O, Groom DE, Lin CJ, Lys J, Murayama H, Wohl CG, Yao WM, Zyla PA, Amsler C, Antonelli M, Asner DM, Baer H, Band HR, Basaglia T, Bauer CW, Beatty JJ, Belousov VI, Bergren E, Bernardi G, Bertl W, Bethke S, Bichsel H, Biebel O, Blucher E, Blusk S, Brooijmans G, Buchmueller O, Cahn RN, Carena M, Ceccucci A, Chakraborty D, Chen MC, Chivukula RS, Cowan G, D'Ambrosio G, Damour T, de Florian D, de Gouvêa A, DeGrand T, de Jong P, Dissertori G, Dobrescu B, Doser M, Drees M, Edwards DA, Eidelman S, Erler J, Ezhela VV, Fetscher W, Fields BD, Foster B, Gaisser TK, Garren L, Gerber HJ, Gerbier G, Gherghetta T, Golwala S, Goodman M, Grab C, Gritsan AV, Grivaz JF, Grünewald M, Gurtu A, Gutsche T, Haber HE, Hagiwara K, Hagmann C, Hanhart C, Hashimoto S, Hayes KG, Heffner M, Heltsley B, Hernández-Rey JJ, Hikasa K, Höcker A, Holder J, Holtkamp A, Huston J, Jackson JD, Johnson KF, Junk T, Karlen D, Kirkby D, Klein SR, Klempt E, Kowalewski RV, Krauss F, Kreps M, Krusche B, Kuyanov YV, Kwon Y, Lahav O, Laiho J, Langacker P, Liddle A, Ligeti Z, Liss TM, Littenberg L, Lugovsky KS, Lugovsky SB, Mannel T, Manohar AV, Marciano WJ, Martin AD, Masoni A, Matthews J, Milstead D, Miquel R, Mönig K, Moortgat F, Nakamura K, Narain M, Nason P, Navas S, Neubert M, Nevski P, Nir Y, Olive KA, Pape L, Parsons J, Patrignani C, Peacock JA, Petcov ST, Piepke A, Pomarol A, Punzi G, Quadt A, Raby S, Raffelt G, Ratcliff BN, Richardson P, Roesler S, Rolli S, Romaniouk A, Rosenberg LJ, Rosner JL, Sachrajda CT, Sakai Y, Salam GP, Sarkar S, Sauli F, Schneider O, Scholberg K, Scott D, Seligman WG, Shaevitz MH, Sharpe SR, Silari M, Sjöstrand T, Skands P, Smith JG, Smoot GF, Spanier S, Spieler H, Stahl A, Stanev T, Stone SL, Sumiyoshi T, Syphers MJ, Takahashi F, Tanabashi M, Terning J, Titov M, Tkachenko NP, Törnqvist NA, Tovey D, Valencia G, van Bibber K, Venanzoni G, Vincter MG, Vogel P, Vogt A, Walkowiak W, Walter CW, Ward DR, Watari T, Weiglein G, Weinberg EJ, Wiencke LR, Wolfenstein L, Womersley J, Woody CL, Workman RL, Yamamoto A, Zeller GP, Zenin OV, Zhang J, Zhu RY, Harper G, Lugovsky VS, Schaffner P (2012) Review of Particle Physics. *Phys Rev D* 86:010001.

Bert C, Durante M (2011) Motion in radiotherapy: particle therapy. *Phys Med Biol* 56(16):R113–R144.

Bert C, Gemmel A, Saito N, Chaudhri N, Schardt D, Durante M, Kraft G, Rietzel E (2010) Dosimetric precision of an ion beam tracking system. *Radiat Oncol* 5(61).

Bert C, Gemmel A, Saito N, Rietzel E (2009) Gated Irradiation with Scanned Particle Beams. *Int J Radiat Oncol Biol Phys* 73(4):1270–1275.

Bert C, Grözinger SO, Rietzel E (2008) Quantification of interplay effects of scanned particle beams and moving targets. *Phys Med Biol* 53(9):2253–2265.

Bert C, Rietzel E (2007) 4D treatment planning for scanned ion beams. *Radiat Oncol* 2:24.

Bert C, Saito N, Schmidt A, Chaudhri N, Schardt D, Rietzel E (2007) Target motion tracking with a scanned particle beam. *Med Phys* 34(12):4768–4771.

Bethe H (1930) Zur Theorie des Durchgangs schneller Kopuskularstrahlen durch Materie. *Annalen der Physik* 397(3):325–400.

Blattmann H (1992) Beam delivery systems for charged particles. *Radiat Environ Biophys* 31(3):219–231.

Brand H, Essel HG, Hardel H, Hoffmann J, Kurz N, Ott W, Richter M (1998) Therapy Slow Control System, Data Analysis and Online Monitoring. In: Grundinger U (Ed.) *GSI Scientific Report 1997*. pp. 146–148.

Brandner ED, Wu A, Chen H, Heron D, Kalnicki S, Komanduri K, Gerszten K, Burton S, Ahmed I, Shou Z (2006) Abdominal organ motion measured using 4D CT. *Int J Radiat Oncol Biol Phys* 65(2):554–560.

Bray F, Jemal A, Grey N, Ferlay J, Forman D (2012) Global cancer transitions according to the Human Development Index (2008–2030): a population-based study. *Lancet Oncol* 13(8):790–801.

Britton KR, Starkschall G, Tucker SL, Pan T, Nelson C, Chang JY, Cox JD, Mohan R, Komaki R (2007) Assessment of Gross Tumor Volume Regression and Motion Changes During Radiotherapy for Non–Small-Cell Lung Cancer as Measured by Four-Dimensional Computed Tomography. *Int J Radiat Oncol Biol Phys* 68(4):1036–1046.

Bühler P, Just U, Will E, Kotzerke J, van den Hoff J (2004) An Accurate Method for Correction of Head Movement in PET. *IEEE Trans Med Imaging* 23(9):1176–1185.

Bush DA, Slater JD, Shin BB, Cheek G, Miller DW, Slater JM (2004) Hypofractionated Proton Beam Radiotherapy for Stage I Lung Cancer. *Chest* 126(4):1198–1203.

Cao W, Lim GJ, Lee A, Li Y, Liu W, Ronald Zhu X, Zhang X (2012) Uncertainty incorporated beam angle optimization for IMPT treatment planning. *Med Phys* 39(8):5248–5256.

Chaudhri N, Saito N, Bert C, Franczak B, Steidl P, Durante M, Rietzel E, Schardt D (2010) Ion-optical studies for a range adaptation method in ion beam therapy using a static wedge degrader combined with magnetic beam deflection. *Phys Med Biol* 55(12):3499–3513.

Chiba T, Tokuuye K, Matsuzaki Y, Sugahara S, Chuganji Y, Kagei K, Shoda J, Hata M, Abei M, Igaki H, Tanaka N, Akine Y (2005) Proton Beam Therapy for Hepatocellular Carcinoma: A Retrospective Review of 162 Patients. *Clin Cancer Res* 11(10):3799–3805.

Chu WT, Ludewigt BA, Renner TR (1993) Instrumentation for treatment of cancer using proton and light-ion beams. *Rev Sci Instrum* 64(8):2055–2122.

Combs SE, Bauer J, Unholtz D, Kurz C, Welzel T, Habermehl D, Haberer T, Debus J, Parodi K (2012) Monitoring of patients treated with particle therapy using positron-emission-tomography (PET): the MIRANDA study. *BMC Cancer* 12:133.

Combs SE, Nikoghosyan A, Jäkel O, Karger CP, Haberer T, Münter MW, Huber PE, Debus J, Schulz-Ertner D (2009) Carbon ion radiotherapy for pediatric patients and young adults treated for tumors of the skull base. *Cancer* 115(6):1348–1355.

Crespo P, Shakirin G, Enghardt W (2006) On the detector arrangement for in-beam PET for hadron therapy monitoring. *Phys Med Biol* 51(9):2143–2163.

Crespo P, Shakirin G, Fiedler F, Enghardt W, Wagner A (2007) Direct time-of-flight for quantitative, real-time in-beam PET: a concept and feasibility study. *Phys Med Biol* 52(23):6795–6811.

Davis TA (2006) *Direct Methods for Sparse Linear Systems.* SIAM, Philadelphia, PA. Part of the SIAM Book Series on the Fundamentals of Algorithms.

Eickhoff H, Haberer T, Kraft G, Krause U, Richter M, Steiner R, Debus J (2009) The GSI Cancer Therapy Project. *Strahlenther Onkol* 175(2 Supplement):21–24.

Endo M, Koyama-Ito H, Minohara S, Miyahara N, Tomura H, Kanai T, Kawachi K, Tsujii H, Morita K (1996) HIPLAN - a heavy ion treatment planning system at HIMAC. *J Jpn Soc Ther Radiol Oncol* 8(3):231–238.

Engelsman M, Rietzel E, Kooy HM (2006) Four-dimensional proton treatment planning for lung tumors. *Int J Radiat Oncol Biol Phys* 64(5):1589–1595.

Enghardt W, Crespo P, Fiedler F, Hinz R, Parodi K, Pawelke J, Pönisch F (2004a) Charged hadron tumour therapy monitoring by means of PET. *Nucl Instrum Methods Phys Res A* 525:284–288.

Enghardt W, Fromm WD, Geissel H, Keller H, Kraft G, Magel A, Manfraß P, Münzenberg G, Nickel F, Pawelke J, Schardt D, Scheidenberger C, Sobiella M (1992) The spatial distribution of positron-emitting nuclei generated by relativistic light ion beams in organic matter. *Phys Med Biol* 37(11):2127–2131.

Enghardt W, Parodi K, Crespo P, Fiedler F, Pawelke J, Pönisch F (2004b) Dose Quantification from In-Beam Positron Emission Tomography. *Radiother Oncol* 73(Supplement 2):S96–S98.

Ferlay J, Shin HR, Bray F, Forman D, Mathers C, Parkin DM (2010a) Estimates of worldwide burden of cancer in 2008: GLOBOCAN 2008. *Int J Cancer* 127(12):2893–2917.

Ferlay J, Shin HR, Bray F, Forman D, Mathers C, Parkin DM (2010b) GLOBOCAN 2008 v2.0, Cancer Incidence and Mortality Worldwide: IARC CancerBase No. 10 (Online). International Agency for Research on Cancer. [accessed: 26 November 2012]. URL: `http://globocan.iarc.fr`.

Fiedler F, Priegnitz M, Jülich R, Pawelke J, Crespo P, Parodi K, Pönisch F, Enghardt W (2008) In-beam PET measurements of biological half-lives of ^{12}C irradiation induced β^+-activity. *Acta Oncol* 47(6):1077–1086.

Firestone RB, Shirley VS (1996) *Table of Isotopes.* 8th ed. John Wiley & Sons Inc, New York.

Fox J, Ford E, Redmond K, Zhou J, Wong J, Song DY (2009) Quantification of Tumor Volume Changes During Radiotherapy for Non-Small-Cell Lung Cancer. *Int J Radiat Oncol Biol Phys* 74(2):341–348.

Furukawa T, Inaniwa T, Sato S, Shirai T, Mori S, Takeshita E, Mizushima K, Himukai T, Noda K (2010a) Moving target irradiation with fast rescanning and gating in particle therapy. *Med Phys* 37(9):4874–4879.

Furukawa T, Inaniwa T, Sato S, Shirai T, Takei Y, Takeshita E, Mizushima K, Iwata Y, Himukai T, Mori S, Fukuda S, Minohara S, Takada E, Murakami T, Noda K (2010b) Performance of the NIRS fast scanning system for heavy-ion radiotherapy. *Med Phys* 37(11):5672–5682.

Gaimard JJ, Schmidt KH (1991) A reexamination of the abrasion-ablation model for the description of the nuclear fragmentation reaction. *Nucl Phys A* 531(3-4):709–745.

Gemmel A, Hasch B, Ellerbrock M, Weyrather WK, Krämer M (2008) Biological dose optimization with multiple ion fields. *Phys Med Biol* 53(23):6991–7012.

Gensheimer MF, Yock TI, Liebsch NJ, Sharp GC, Paganetti H, Madan N, Grant PE, Bortfeld T (2010) In vivo Proton Beam Range Verification using Spine MRI Changes. *Int J Radiat Oncol Biol Phys* 78(1):268–275.

Gierga DP, Brewer J, Sharp GC, Betke M, Willett CG, Chen GTY (2005) The correlation between internal and external markers for abdominal tumors: Implications for respiratory gating. *Int J Radiat Oncol Biol Phys* 61(5):1551–1558.

Goodhead DT, Belli M, Mill AJ, Bance DA, Allens AL, Hall CS, Ianzani F, Simone G, Stevens LD, Stretch A, Tabocchini AM, Wilkinson RE (1992) Direct comparison between protons and alpha-particles of the same LET: I. Irradiation methods and inactivation of asynchronous V79, HeLa and C3H 10T$\frac{1}{2}$ Cells. *Int J Radiat Biol* 61(5):611–624.

Grözinger SO, Bert C, Haberer T, Kraft G, Rietzel E (2008) Motion compensation with a scanned ion beam: a technical feasibility study. *Radiat Oncol* 3:34.

Grözinger SO, Rietzel E, Li Q, Bert C, Haberer T, Kraft G (2006) Simulations to design an online motion compensation system for scanned particle beams. *Phys Med Biol* 51(14):3517–3531.

Haberer T, Becher W, Schardt D, Kraft G (1993) Magnetic scanning system for heavy ion therapy. *Nucl Instrum Methods Phys Res A* 330(1-2):296–305.

Harris EJ, Miller NR, Bamber JC, Symonds-Tayler JRN, Evans PM (2010) Speckle tracking in a phantom and feature-based tracking in liver in the presence of respiratory motion using 4D ultrasound. *Phys Med Biol* 55(12):3363–3380.

Hasch BG (1996) *Die physikalischen Grundlagen einer Verifikation des Bestrahlungsplanes in der Schwerionen-Tumortherapie mit der Positronen-Emissions-Tomographie*. Dissertation, Technische Universität Dresden.

Heeg P, Eickhoff H, Haberer T (2004) Die Konzeption der Heidelberger Ionentherapieanlage HICAT. *Z Med Phys* 14:17–24.

Helmbrecht S, Santiago A, Enghardt W, Kuess P, Fiedler F (2012) On the feasibility of automatic detection of range deviations from in-beam PET data. *Phys Med Biol* 57(5):1387–1397.

Herrmann T, Baumann M, Dörr W (2006) *Klinische Strahlenbiologie - kurz und bündig.* 4th ed. Elsevier, Urban & Fischer, Munich.

Hinz R (2000) *Beiträge zur Einführung der Positronen-Emissions-Tomographie bei der Schwerionen-Tumortherapie.* Dissertation, Technische Universität Dresden. Wissenschaftlich-Technische Berichte FZR-286, ISSN 1437-322X.

Hishikawa Y, Kagawa K, Murakami M, Sakai H, Akagi T, Abe M (2002) Usefulness of Positron-Emission Tomographic Images after Proton Therapy. *Int J Radiat Oncol Biol Phys* 53(5):1388–1391.

Hoinkis C, Tillner F (2013) Depth-dose distributions in water of 6 MV and 15 MV photons provided by an Siemens Artiste accelerator with a field size of 100 mm × 100 mm and measured with a source-to-surface distance of 900 mm and a source-to-axis distance of 1000 mm. University Hospital Carl Gustav Carus Dresden, Clinic of Radiotherapy and Radiooncology. Personal communication.

Hoisak JDP, Sixel KE, Tirona R, Cheung PCF, Pignol JP (2004) Correlation of lung tumor motion with external surrogate indicators of respiration. *Int J Radiat Oncol Biol Phys* 60(4):1298–1306.

Hsi WC, Indelicato DJ, Vargas C, Duvvuri S, Li Z, Palta J (2009) In vivo verification of proton beam path by using post-treatment PET/CT imaging. *Med Phys* 36(9):4136–4146.

Hüfner J (1985) Heavy fragments produced in proton-nucleus and nucleus-nucleus collisions at relativistic energies. *Phys Rep* 125(4):129–185.

Hughes S, McClelland J, Tarte S, Lawrence D, Ahmad S, Hawkes D, Landau D (2009) Assessment of two novel ventilatory surrogates for use in the delivery of gated/tracked radiotherapy for non-small cell lung cancer. *Radiother Oncol* 91(3):336–341.

Hui Z, Zhang X, Starkschall G, Li Y, Mohan R, Komaki R, Cox JD, Chang JY (2008) Effects of Interfractional Motion and Anatomic Changes on Proton Therapy Dose Distribution in Lung Cancer. *Int J Radiat Oncol Biol Phys* 72(5):1385–1395.

IAEA (2000) Absorbed Dose Determination in External Beam Radiotherapy: An International Code of Practice for Dosimetry Based on Standards of Absorbed Dose to Water. International Atomic Energy Agency, Vienna Technical Report Series no. 398 (Tech. Rep.).

IAEA (2008) Relative Biological Effectiveness in Ion Beam Therapy. International Atomic Energy Agency, Vienna Technical Report Series no. 461 (Tech. Rep.).

ICRP (1975) Report of the Task Group on Reference Man. *Ann ICRP* 23, chapter 2 gross and elemental content of reference man.

ICRU (1984) ICRU Report 37 - Stopping Powers for Electrons and Positrons. International Commission on Radiation Units and Measurements (Tech. Rep.).

ICRU (1993a) ICRU Report 49 - Stopping Powers and Ranges for Protons and Alpha Particles. International Commission on Radiation Units and Measurements (Tech. Rep.).

ICRU (1993b) ICRU Report 50 - Prescribing, Recording, and Reporting Photon Beam Therapy. International Commission on Radiation Units and Measurements (Tech. Rep.).

ICRU (1999) ICRU Report 62 - Prescribing, Recording, and Reporting Photon Beam Therapy, Supplement to ICRU report 50. International Commission on Radiation Units and Measurements (Tech. Rep.).

ICRU (2007) ICRU Report 78 - Prescribing, Recording, and Reporting Proton-Beam Therapy. *Journal of the ICRU* 7(2):1–210.

ICRU (2011) ICRU Report 85 - Fundamental Quantities and Units for Ionizing Radiation (Revised). *Journal of the ICRU* 11(1):1–35.

Iseki Y, Kanai T, Kanazawa M, Kitagawa A, Mizuno H, Tomitani T, Suda M, Urakabe E (2004) Range verification system using positron emitting beams for heavy-ion radiotherapy. *Phys Med Biol* 49(14):3179–3195.

Iwata H, Murakami M, Demizu Y, Miyawaki D, Terashima K, Niwa Y, Mima M, Akagi T, Hishikawa Y, Shibamoto Y (2010) High-dose proton therapy and carbon-ion therapy for stage I nonsmall cell lung cancer. *Cancer* 116(10):2476–2485.

Iwata Y, Noda K, Shirai T, Murakami T, Furukawa T, Mori S, Fujita T, Itano A, Shouda K, Mizushima K, Fujimoto T, Ogitsu T, Obana T, Amemiya N, Orikasa T, Takami S, Takayama S, Watanabe I (2012) Design of a superconducting rotating gantry for heavy-ion therapy. *Phys Rev ST Accel Beams* 15(4):044701.

Jäkel O, Debus J (2000) Selection of beam angles for radiotherapy of skull base tumours using charged particles. *Phys Med Biol* 45(5):1229–1241.

Jäkel O, Hartmann GH, Karger CP, Heeg P (2000) Quality assurance for a treatment planning system in scanned ion beam therapy. *Med Phys* 27(7):1588–1600.

Jäkel O, Jacob C, Schardt D, Karger CP, Hartmann GH (2001) Relation between carbon ion ranges and x-ray CT numbers. *Med Phys* 28(4):701–703.

Jäkel O, Karger CP, Debus J (2008) The future of heavy ion radiotherapy. *Med Phys* 35(12):5653–5663.

Jäkel O, Reiss P (2007) The influence of metal artefacts on the range of ion beams. *Phys Med Biol* 52(3):635–644.

Jensen AD, Münter MW, Debus J (2012) Review of clinical experience with ion beam radiotherapy. *Br J Radiol* 84(Special Issue 1):S35–S47.

Kanai T, Endo M, Minohara S, Miyahara N, Koyama-Ito H, Tomura H, Matsufuji N, Futami Y, Fukumura A, Hiraoka T, Furusawa Y, Ando K, Suzuki M, Soga F, Kawachi K (1999) Biophysical characteristics of HIMAC clinical irradiation system for heavy-ion radiation therapy. *Int J Radiat Oncol Biol Phys* 44(1):201–210.

Kanai T, Furusawa Y, Fukutsu K, Itsukaichi H, Eguchi-Kasai K, Ohara H (1997) Irradiation of Mixed Beam and Design of Spread-Out Bragg Peak for Heavy-Ion Radiotherapy. *Radiat Res* 147(1):78–85.

Kanematsu N, Matsufuji N, Kohno R, Minohara S, Kanai T (2003) A CT calibration method based on the polybinary tissue model for radiotherapy treatment planning. *Phys Med Biol* 48(8):1053–1064.

Karger CP, Hartmann GH, Jäkel O, Heeg P (2000) Quality management of medical physics issues at the German heavy ion therapy project. *Med Phys* 27(4):725–736.

Kato H, Tsujii H, Miyamoto T, Mizoe Je, Kamada T, Tsuji H, Yamada S, Kandatsu S, Yoshikawa K, Obata T, Ezawa H, Morita S, Tomizawa M, Morimoto N, Fujita J, Ohto M (2004) Results of the first prospective study of carbon ion radiotherapy for hepatocellular carcinoma with liver cirrhosis. *Int J Radiat Oncol Biol Phys* 59(5):1468–1476.

Keall PJ, Mageras GS, Balter JM, Emery RS, Forster KM, Jiang SB, Kapatoes JM, Low DA, Murphy MJ, Murray BR, Ramsey CR, Van Herk MB, Vedam SS, Wong JW, Yorke E (2006) The management of respiratory motion in radiation oncology report of AAPM Task Group 76. *Med Phys* 33(10):3874–3900.

Kellerer A, Brenot J (1974) On the statistical evaluation of dose-response functions. *Radiat Environ Biophys* 11:1–13.

Knopf A, Bert C, Heath E, Nill S, Kraus K, Richter D, Hug E, Pedroni E, Safai S, Albertini F, Zenklusen S, Boye D, Söhn M, Soukup M, Sobotta B, Lomax A (2010) Special report: Workshop on 4D-treatment planning in actively scanned particle therapy—Recommendations, technical challenges, and future research directions. *Med Phys* 37(9):4608–4614.

Knopf A, Parodi K, Bortfeld T, Shih HA, Paganetti H (2009) Systematic analysis of biological and physical limitations of proton beam range verification with offline PET/CT scans. *Phys Med Biol* 54(14):4477–4495.

Knopf AC, Hong TS, Lomax A (2011) Scanned proton radiotherapy for mobile targets—the effectiveness of re-scanning in the context of different treatment planning approaches and for different motion characteristics. *Phys Med Biol* 56(22):7257–7271.

Kormoll T, Fiedler F, Schöne S, Wüstemann J, Zuber K, Enghardt W (2011) A Compton imager for in-vivo dosimetry of proton beams—A design study. *Int Nucl Instrum Methods Phys Res A* 626-627:114–119.

Kraft G (2000) Tumor therapy with heavy charged particles. *Prog Part Nucl Phys* 45(Supplement 2):S473–S544.

Krämer M, Jäkel O, Haberer T, Kraft G, Schardt D, Weber U (2000) Treatment planning for heavy-ion radiotherapy: physical beam model and dose optimization. *Phys Med Biol* 45(11):3299–3317.

Krämer M, Scholz M (2000) Treatment planning for heavy-ion radiotherapy: calculation and optimization of biologically effective dose. *Phys Med Biol* 45(11):3319–3330.

Kuess P, Birkfellner W, Enghardt W, Helmbrecht S, Fiedler F, Georg D (2012) Using statistical measures for automated comparison of in-beam PET data. *Med Phys* 39(10):5874.

Kumagai M, Mori S, Hara R, Asakura H, Kishimoto R, Kato H, Yamada S, Kandatsu S (2009) Water-equivalent pathlength reproducibility due to respiratory pattern variation in charged-particle pancreatic radiotherapy. *Radiol Phys Technol* 2(1):112–118.

Kurosawa S, Kubo H, Ueno K, Kabuki S, Iwaki S, Takahashi M, Taniue K, Higashi N, Miuchi K, Tanimori T, Kim D, Kim J (2012) Prompt gamma detection for range verification in proton therapy. *Curr Appl Phys* 12(2):364–368.

Kurz C, Mairani A, Parodi K (2012) First experimental-based characterization of oxygen ion beam depth dose distributions at the Heidelberg Ion-Beam Therapy Center. *Phys Med Biol* 57(15):5017–5034.

Lambert J, Suchowerska N, McKenzie DR, Jackson M (2005) Intrafractional motion during proton beam scanning. *Phys Med Biol* 50(20):4853–4862.

Langen KM, Jones DTL (2001) Organ motion and its management. *Int J Radiat Oncol Biol Phys* 50(1):265–278.

Langner J, Dittrich S, Pötzsch C, Beuthien-Baumann B, van den Hoff J (2008) Reduzierung des Out-of-Field-of-View Einflusses auf die Event-basierte Bewegungskorrektur von Hirnuntersuchungen in der PET. In: *46th Annual DGN Conference, Leipzig.* German Society of Nuclear Medicine.

Laube K, Bert C, Chaudhri N, Fiedler F, Parodi K, Rietzel E, Saito N, Enghardt W (2009a) 4D in-beam PET Datenauswertung für bewegte Phantome bei Bestrahlung mit einem getrackten $^{12}C^{6+}$-Strahl. Presentation at: *DPG Frühjahrstagung*, München.

Laube K, Bert C, Chaudhri N, Fiedler F, Parodi K, Rietzel E, Saito N, Enghardt W (2009b) 4D in-beam PET of moving targets for different irradiation scenarios. In: Große K (Ed.) *GSI Scientific Report 2008*. GSI Helmholtzzentrum für Schwerionenforschung, p. 400.

Laube K, Bert C, Chaudhri N, Fiedler F, Parodi K, Rietzel E, Saito N, Enghardt W (2010a) 4D-in-beam-PET für periodisch bewegte Phantome bei Bestrahlung mit einem mitgeführten ^{12}C-Strahl. E-poster at: *16. Jahreskongress der Deutschen Gesellschaft für Radioonkologie*, Magdeburg.

Laube K, Bert C, Chaudhri N, Fiedler F, Parodi K, Rietzel E, Saito N, Enghardt W (2010b) On the difference of 3D and 4D in-beam PET for a periodically moving target. In: Große K (Ed.) *GSI Scientific Report 2009*. GSI Helmholtzzentrum für Schwerionenforschung, p. 503.

Laube K, Bert C, Fiedler F, Helmbrecht S, Parodi K, Priegnitz M, Saito N, Enghardt W (2012a) Time resolved (4D) reconstruction of in-beam PET data for the dose monitoring of intra-fractionally moving target volumes in ion beam therapy. Presentation at: *Tomography, data processing and image reconstruction for medicine and engineering*, Dresden.

Laube K, Bert C, Fiedler F, Helmbrecht S, Priegnitz M, Saito N, Enghardt W (2012b) Verification of ion range in moving targets. In: Große K (Ed.) *GSI Scientific Report 2011*. GSI Helmholtzzentrum für Schwerionenforschung, p. 534.

Laube K, Bert C, Fiedler F, Helmbrecht S, Priegnitz M, Saito N, Enghardt W (2012c) Zeitaufgelöste (4D) Rekonstruktion von in-beam PET Daten für das Dosismonitoring bei der Bestrahlung von bewegten Zielvolumina in der Ionentherapie. In: *Abstractband der 43. Jahrestagung der Deutschen Gesellschaft für Medizinische Physik*. pp. 90–92.

Laube K, Fiedler F, Bert C, Saito N, Enghardt W (2012d) Reconstruction of 4D in-beam PET data for quality control of moving target irradiation in ion beam therapy. *Radiother Oncol* 102(S1):S43–S44.

Laube K, Fiedler F, Schöne S, Bert C, Enghardt W (2011) Influence of point source motion in PET images and its compensation. In: Große K (Ed.) *GSI Scientific Report 2010*. GSI Helmholtzzentrum für Schwerionenforschung, p. 470.

Laube K, Menkel S, Bert C, Enghardt W, Helmbrecht S, Saito N, Fiedler F (2013) 4D particle therapy PET simulation for moving targets irradiated with scanned ion beams. *Phys Med Biol* 58(3):513–533.

Laube K, Menkel S, Fiedler F, Bert C, Saito N, Enghardt W (2012e) 4D PT-PET simulation for dose monitoring in moving targets treated with scanned ion beams. Presentation at: *4th 4D treatment planning workshop*, Erlangen.

Lauckner K (1999) *Entwicklung eines iterativen 3D Rekonstruktionsverfahrens für die Kontrolle der Tumorbehandlung mit Schwerionen mittels der Positronen-Emissions-Tomographie.* Dissertation, Technische Universität Dresden. Wissenschaftlich-Technische Berichte FZR-264, ISSN 1437-322X.

Lewellen TK (2008) Recent developments in PET detector technology. *Phys Med Biol* 53(17):R287–R317.

Li H, Noel C, Garcia-Ramirez J, Low D, Bradley J, Robinson C, Mutic S, Parikh P (2012) Clinical evaluations of an amplitude-based binning algorithm for 4DCT reconstruction in radiation therapy. *Med Phys* 39(2):922–932.

Li T, Thorndyke B, Schreibmann E, Yang Y, Xing L (2006a) Model-based image reconstruction for four-dimensional PET. *Med Phys* 33(5):1288–1298.

Li XA, Stepaniak C, Gore E (2006b) Technical and dosimetric aspects of respiratory gating using a pressure-sensor motion monitoring system. *Med Phys* 33(1):145–154.

Liu HH, Balter P, Tutt T, Choi B, Zhang J, Wang C, Chi M, Luo D, Pan T, Hunjan S, Starkschall G, Rosen I, Prado K, Liao Z, Chang J, Komaki R, Cox JD, Mohan R, Dong L (2007) Assessing Respiration-Induced Tumor Motion and Internal Target Volume Using Four-Dimensional Computed Tomography for Radiotherapy of Lung Cancer. *Int J Radiat Oncol Biol Phys* 68(2):531–540.

Llacer J, Chatterjee A, Jackson HC, Lin JC, Zunzunegui MV (1979) An Imaging Instrument for Positron Emitting Heavy Ion Beam Injection. *IEEE Trans Nucl Sci* 26(1):634–647.

Lodge M, Pijls-Johannesma M, Stirk L, Munro AJ, De Ruysscher D, Jefferson T (2007) A systematic literature review of the clinical and cost-effectiveness of hadron therapy in cancer. *Radiother Oncol* 83(2):110–122.

Lomax A (1999) Intensity modulation methods for proton radiotherapy. *Phys Med Biol* 44(1):185–205.

Lomax AJ (2008) Intensity modulated proton therapy and its sensitivity to treatment uncertainties 2: the potential effects of inter-fraction and inter-field motions. *Phys Med Biol* 53(4):1043–1056.

Lu HM, Brett R, Sharp G, Safai S, Jiang S, Flanz J, Kooy H (2007) A respiratory-gated treatment system for proton therapy. *Med Phys* 34(8):3273–3278.

Lüchtenborg R, Saito N, Durante M, Bert C (2011) Experimental verification of a real-time compensation functionality for dose changes due to target motion in scanned particle therapy. *Med Phys* 38(10):5448–5458.

Lujan AE, Larsen EW, Balter JM, Ten Haken RK (1999) A method for incorporating organ motion due to breathing into 3D dose calculations. *Med Phys* 26(5):715–720.

Mah D, Hanley J, Rosenzweig KE, Yorke E, Braban L, Ling CC, Leibel SA, Mageras G (2000) Technical aspects of the deep inspiration breath-hold technique in the treatment of thoracic cancer. *Int J Radiat Oncol Biol Phys* 48(4):1175–1185.

MedicalPhysicsWeb (2012) Treatments begin on HIT's heavy ion gantry [accessed: 05 February 2013] URL: `http://medicalphysicsweb.org/cws/article/research/50584`.

Menke M, Atkins MS, Buckley KR (1996) Compensation methods for head motion detected during PET imaging. *IEEE Trans Nucl Sci* 43(1):310–317.

Menkel S (2011) *Simulation von In-beam-PET-Datensätzen bei der Bestrahlung bewegter Zielvolumina mit* ^{12}*C-Ionen*. Master's thesis, Technische Universität Dresden.

Minohara S, Endo M, Kanai T, Kato H, Tsujii H (2003) Estimating uncertainties of the geometrical range of particle radiotherapy during respiration. *Int J Radiat Oncol Biol Phys* 56(1):121–125.

Minohara S, Kanai T, Endo M, Noda K, Kanazawa M (2000) Respiratory gated irradiation system for heavy-ion radiotherapy. *Int J Radiat Oncol Biol Phys* 47(4):1097–1103.

Miyamoto T, Baba M, Sugane T, Nakajima M, Kagei K, Tomoyasu Y, Hirasawa N, Sugawara T, Yamamoto N, Koto M, Ezawa H, Kadono K, Tsujii H, Mizoe Je, Yoshikawa K, Kandatsu S, Fujisawa T (2007) Carbon Ion Radiotherapy for Stage I Non-small Cell Lung Cancer Using a Regimen of Four Fractions during 1 Week. *J Thorac Oncol* 2(10):916–926.

Miyamoto T, Yamamoto N, Nishimura H, Koto M, Tsujii H, Mizoe Je, Kamada T, Kato H, Yamada S, Morita S, Yoshikawa K, Kandatsu S, Fujisawa T (2003) Carbon ion radiotherapy for stage I non-small cell lung cancer. *Radiother Oncol* 66(2):127–140.

Mizuno H, Tomitani T, Kanazawa M, Kitagawa A, Pawelke J, Iseki Y, Urakabe E, Suda M, Kawano A, Iritani R, Matsushita S, Inaniwa T, Nishio T, Furukawa S, Ando K, Nakamura YK, Kanai T, Ishii K (2003) Washout measurement of radioisotope implanted by radioactive beams in the rabbit. *Phys Med Biol* 48(15):2269–2281.

Mori S, Chen GTY, Endo M (2007) Effects of Intrafractional Motion on Water Equivalent Pathlength in Respiratory-Gated Heavy Charged Particle Beam Radiotherapy. *Int J Radiat Oncol Biol Phys* 69(1):308–317.

Mori S, Wolfgang J, Lu HM, Schneider R, Choi NC, Chen GTY (2008) Quantitative Assessment of Range Fluctuations in Charged Particle Lung Irradiation. *Int J Radiat Oncol Biol Phys* 70(1):253–261.

Nehmeh SA, Erdi YE (2008) Respiratory Motion in Positron Emission Tomography/Computed Tomography: A Review. *Semin Nucl Med* 38(3):167–176.

Nihei K, Ogino T, Ishikura S, Nishimura H (2006) High-dose proton beam therapy for Stage I non–small-cell lung cancer. *Int J Radiat Oncol Biol Phys* 65(1):107–111.

Nishio T, Miyatake A, Inoue K, Gomi-Miyagishi T, Kohno R, Kameoka S, Nakagawa K, Ogino T (2007) Experimental verification of proton beam monitoring in a human body by use of activity image of positron-emitting nuclei generated by nuclear fragmentation reaction. *Radiol Phys Technol* 1(1):44–54.

Nishio T, Miyatake A, Ogino T, Nakagawa K, Saijo N, Esumi H (2010) The Development and Clinical Use of a Beam On-Line PET System Mounted on a Rotating Gantry Port in Proton Therapy. *Int J Radiat Oncol Biol Phys* 76(1):277–286.

Ogino T (2012) Clinical evidence of particle beam therapy (proton). *Int J Clin Oncol* 17(2):79–84.

Paganetti H, Jiang H, Parodi K, Slopsema R, Engelsman M (2008) Clinical implementation of full Monte Carlo dose calculation in proton beam therapy. *Phys Med Biol* 53(17):4825–4853.

Paganetti H, Niemierko A, Ancukiewicz M, Gerweck LE, Goitein M, Loeffler JS, Suit HD (2002) Relative biological effectiveness (RBE) values for proton beam therapy. *Int J Radiat Oncol Biol Phys* 53(2):407–421.

Parodi K (2004) *On the feasibility of dose quantification with in-beam PET data in radiotherapy with* ^{12}C *and proton beams.* Dissertation, Technische Universität Dresden. Wissenschaftlich-Technische Berichte FZR-415, ISSN 1437-322X.

Parodi K, Bortfeld T, Haberer T (2008) Comparison Between In-Beam and Offline Positron Emission Tomography Imaging of Proton and Carbon Ion Therapeutic Irradiation at Synchrotron- and Cyclotron-Based Facilities. *Int J Radiat Oncol Biol Phys* 71(3):945–956.

Parodi K, Enghardt W (2002) An iterative approach for local dose quantification from in-beam PET data. In: Grundinger U (Ed.) *GSI Scientific Report 2001.*

Parodi K, Ferrari A, Sommerer F, Paganetti H (2007a) Clinical CT-based calculations of dose and positron emitter distributions in proton therapy using the FLUKA Monte Carlo code. *Phys Med Biol* 52(12):3369–3387.

Parodi K, Paganetti H, Cascio E, Flanz JB, Bonab AA, Alpert NM, Lohmann K, Bortfeld T (2007b) PET/CT imaging for treatment verification after proton therapy: A study with plastic phantoms and metallic implants. *Med Phys* 34(2):419–435.

Parodi K, Paganetti H, Shih HA, Michaud S, Loeffler JS, DeLaney TF, Liebsch NJ, Munzenrider JE, Fischman AJ, Knopf A, Bortfeld T (2007c) Patient Study of In Vivo Verification of Beam Delivery and Range, Using Positron Emission Tomography and Computed Tomography Imaging After Proton Therapy. *Int J Radiat Oncol Biol Phys* 68(3):920–934.

Parodi K, Saito N, Chaudhri N, Richter C, Durante M, Enghardt W, Rietzel E, Bert C (2009) 4D in-beam positron emission tomography for verification of motion-compensated ion beam therapy. *Med Phys* 36(9):4230–4243.

Partridge M, Ramos M, Sardaro A, Brada M (2011) Dose escalation for non-small cell lung cancer: Analysis and modelling of published literature. *Radiother Oncol* 99(1):6–11.

Paul H, Schinner A (2003) Empirical stopping power tables for ions from ${}_3$Li to ${}_{18}$Ar and from 0.001 to 1000 MeV/nucleon in solids and gases. *At Data Nucl Data Tables* 85:377–452.

Pawelke J, Byars L, Enghardt W, Fromm WD, Geissel H, Hasch BG, Lauckner K, Manfraß P, Schardt D, Sobiella M (1996) The investigation of different cameras for in-beam PET imaging. *Physics in Medicine and Biology* 41(2):279–296.

Pedroni E, Bacher R, Blattmann H, Böhringer T, Coray A, Lomax A, Lin S, Munkel G, Scheib S, Schneider U, Tourovsky A (1995) The 200-MeV proton therapy project at the Paul Scherrer Institute: Conceptual design and practical realization. *Med Phys* 22(1):37–53.

Peeters A, Grutters JPC, Pijls-Johannesma M, Reimoser S, De Ruysscher D, Severens JL, Joore MA, Lambin P (2010) How costly is particle therapy? Cost analysis of external beam radiotherapy with carbon-ions, protons and photons. *Radiother Oncol* 95(1):45–53.

Phillips MH, Pedroni E, Blattmann H, Boehringer T, Coray A, Scheib S (1992) Effects of respiratory motion on dose uniformity with a charged particle scanning method. *Phys Med Biol* 37(1):223–234.

Pijls-Johannesma M, Grutters JPC, Verhaegen F, Lambin P, De Ruysscher D (2010) Do We Have Enough Evidence to Implement Particle Therapy as Standard Treatment in Lung Cancer? A Systematic Literature Review. *Oncologist* 15(1):93–103.

Pijls-Johannesma M, Pommier P, Lievens Y (2008) Cost-effectiveness of particle therapy: Current evidence and future needs. *Radiother Oncol* 89(2):127–134.

Pönisch F (2003) *Optimierung der Positronen-Emissions-Tomographie bei der Schwerionentherapie auf der Basis von Röntgentomogrammen.* Dissertation, Technische Universität Dresden. Wissenschaftlich-Technische Berichte FZR-378, ISSN 1437-322X.

Pönisch F, Enghardt W, Lauckner K (2003) Attenuation and scatter correction for in-beam positron emission tomography monitoring of tumour irradiations with heavy ions. *Phys Med Biol* 48(15):2419–2436.

Pönisch F, Parodi K, Hasch BG, Enghardt W (2004) The modelling of positron emitter production and PET imaging during carbon ion therapy. *Phys Med Biol* 49(23):5217–5232.

Priegnitz M (2012) *Ein neues Konzept zur Modellierung der Positronenemitter-Produktion bei der Partikeltherapie.* Dissertation, Technische Universität Dresden. Wissenschaftlich-Technische Berichte HZDR-029, ISSN 2191-8708.

Priegnitz M, Fiedler F, Kunath D, Laube K, Enghardt W (2012) An Experiment-Based Approach for Predicting Positron Emitter Distributions Produced During Therapeutic Ion Irradiation. *IEEE Trans Nucl Sci* 59(1):77–87.

PTCOG (2012) Particle therapy facilities in operation (incl. patient statistics). [updated: 13 January 2013, accessed: 16 January 2013]. URL: `http://ptcog.web.psi.ch/ptcentres.html`.

Qiao F, Pan T, Clark Jr JW, Mawlawi OR (2006) A motion-incorporated reconstruction method for gated PET studies. *Phys Med Biol* 51(15):3769–3783.

Rietzel E, Bert C (2010) Respiratory motion management in particle therapy. *Med Phys* 37(2):449–460.

Rietzel E, Pan T, Chen GTY (2005) Four-dimensional computed tomography: Image formation and clinical protocol. *Med Phys* 32(4):874–889.

Rietzel E, Schardt D, Haberer T (2007) Range accuracy in carbon ion treatment planning based on CT-calibration with real tissue samples. *Radiat Oncol* 2(1):14.

Rinaldi I, Brons S, Gordon J, Panse R, Voss B, Jäkel O, Parodi K (2013) Experimental characterization of a prototype detector system for carbon ion radiography and tomography. *Phys Med Biol* 58(3):413–427.

Roellinghoff F, Richard MH, Chevallier M, Constanzo J, Dauvergne D, Freud N, Henriquet P, Le Foulher F, Létang JM, Montarou G, Ray C, Testa E, Testa M, Walenta AH (2011) Design of a Compton camera for 3D prompt-γ imaging during ion beam therapy. *Nucl Instrum Methods Phys Res A* 648(Supplement 1):S20–S23.

Rusthoven KE, Kavanagh BD, Cardenes H, Stieber VW, Burri SH, Feigenberg SJ, Chidel MA, Pugh TJ, Franklin W, Kane M, Gaspar LE, Schefter TE (2009) Multi-Institutional Phase I/II Trial of Stereotactic Body Radiation Therapy for Liver Metastases. *J Clin Oncol* 27(10):1572–1578.

Safai S, Bula C, Meer D, Pedroni E (2012) Improving the precision and performance of proton pencil beam scanning. *Transl Cancer Res* 1(3):196–206.

Saito N, Bert C, Chaudhri N, Gemmel A, Schardt D, Durante M, Rietzel E (2009) Speed and accuracy of a beam tracking system for treatment of moving targets with scanned ion beams. *Phys Med Biol* 54(16):4849–4862.

Schaffner B, Pedroni E (1998) The precision of proton range calculations in proton radiotherapy treatment planning: experimental verification of the relation between CT-HU and proton stopping power. *Phys Med Biol* 43(6):1579–2027.

Schall I, Schardt D, Geissel H, Irnich H, Kankeleit E, Kraft G, Magel A, Mohar MF, Münzenberg G, Nickel F, Scheidenberger C, Schwab W (1996) Charge-changing nuclear reactions of relativistic light-ion beams ($5 \leq Z \leq 10$) passing through thick absorbers. *Nucl Instrum Methods Phys Res B* 117(3):221–234.

Schardt D, Elsässer T, Schulz-Ertner D (2010) Heavy-ion tumor therapy: Physical and radiobiological benefits. *Rev Mod Phys* 82:383–425.

Schneider U, Pedroni E, Lomax A (1996) The calibration of CT Hounsfield units for radiotherapy treatment planning. *Phys Med Biol* 41(1):111–124.

Schulz-Ertner D, Nikoghosyan A, Hof H, Didinger B, Combs SE, Jäkel O, Karger CP, Edler L, Debus J (2007) Carbon ion radiotherapy of skull base chondrosarcomas. *Int J Radiat Oncol Biol Phys* 67(1):171–177.

Schulz-Ertner D, Tsujii H (2007) Particle Radiation Therapy Using Proton and Heavier Ion Beams. *J Clin Oncol* 25(8):953–964.

Schwaab J, Sarti C, Kurz C, Zhang X, Bongers A, Parodi K, Jenne J (2012) Calibration of an ultrasound tracking system for moving organs in heavy ion therapy. In: *Abstractband der 43. Jahrestagung der Deutschen Gesellschaft für Medizinische Physik*. pp. 657–661.

Seco J, Robertson D, Trofimov A, Paganetti H (2009) Breathing interplay effects during proton beam scanning: simulation and statistical analysis. *Phys Med Biol* 54(14):N283–N294.

Seltzer SM, Berger MJ (1982) Evaluation of the collision stopping power of elements and compounds for electrons and positrons. *Int J Appl Radiat Isot* 33(11):1189–1218.

Seltzer SM, Berger MJ (1984) Improved procedure for calculating the collision stopping power of elements and compounds for electrons and positrons. *Int J Appl Radiat Isot* 35(7):665–676.

Seppenwoolde Y, Shirato H, Kitamura K, Shimizu S, van Herk M, Lebesque JV, Miyasaka K (2002) Precise and real-time measurement of 3D tumor motion in lung due to breathing and heartbeat, measured during radiotherapy. *Int J Radiat Oncol Biol Phys* 53(4):822–834.

Serber R (1947) Nuclear Reactions at High Energies. *Phys Rev* 72:1114–1115.

Shakirin G (2009) System Solution for In-Beam Positron Emission Tomography Monitoring of Radiation Therapy. In: Poll R, Füssel J (Eds.) *Dresdner Beiträge zur Medizintechnik*, Vol. 8. TUDpress.

Shakirin G, Braess H, Fiedler F, Kunath D, Laube K, Parodi K, Priegnitz M, Enghardt W (2011) Implementation and workflow for PET monitoring of therapeutic ion irradiation: a comparison of in-beam, in-room, and off-line techniques. *Phys Med Biol* 56(5):1281–1298.

Shimizu S, Shirato H, Kagei K, Nishioka T, Bo X, Dosaka-Akita H, Hashimoto S, Aoyama H, Tsuchiya K, Miyasaka K (2000) Impact of respiratory movement on the computed tomographic images of small lung tumors in three-dimensional (3D) radiotherapy. *Int J Radiat Oncol Biol Phys* 46(5):1127–1133.

Shirato H, Harada T, Harabayashi T, Hida K, Endo H, Kitamura K, Onimaru R, Yamazaki K, Kurauchi N, Shimizu T, Shinohara N, Matsushita M, Dosaka-Akita H, Miyasaka K (2003) Feasibility of insertion/implantation of 2.0-mm-diameter gold internal fiducial markers for precise setup and real-time tumor tracking in radiotherapy. *Int J Radiat Oncol Biol Phys* 56(1):240–247.

Shirato H, Seppenwoolde Y, Kitamura K, Onimura R, Shimizu S (2004) Intrafractional tumor motion: lung and liver. *Semin Radiat Oncol* 14(1):10–18.

Sihver L, Mancusi D (2009) Present status and validation of HIBRAC. *Radiat Meas* 44(1):38–46.

Sihver L, Tsao CH, Silberberg R, Barghouty AF, Kanai T (1996) Calculations of depth-dose distributions, cross sections and momentum loss. *Adv Space Res* 17(2):105–108.

Skinner HD, Hong TS, Krishnan S (2011) Charged-Particle Therapy for Hepatocellular Carcinoma. *Semin Radiat Oncol* 21(4):278–286.

Smeets J, Roellinghoff F, Prieels D, Stichelbaut F, Benilov A, Busca P, Fiorini C, Peloso R, Basilavecchia M, Frizzi T, Dehaes JC, Dubus A (2012) Prompt gamma imaging with a slit camera for real-time range control in proton therapy. *Phys Med Biol* 57(11):3371–3405.

Smith JDT (2012) IDL related Offerings. [updated: 27 February 2012, accessed: 23 March 2013]. URL: `http://tir.astro.utoledo.edu/jdsmith/code/idl.php`.

Sternheimer RM, Berger MJ, Seltzer SM (1984) Density effect for the ionization loss of charged particles in various substances. *At Data Nucl Data Tables* 30(2):261–271.

Sternheimer RM, Peierls RF (1971) General Expression for the Density Effect for the Ionization Loss of Charged Particles. *Phys Rev B* 3(11):3681–3692.

Stützer K, Bert C, Enghardt W, Helmbrecht S, Parodi K, Priegnitz M, Saito N, Fiedler F (2013) Experimental verification of a 4D MLEM reconstruction algorithm used for in-beam PET measurements in particle therapy. *Phys Med Biol* 58(15):5085–5111.

Sutherland IE, Hodgman GW (1974) Reentrant Polygon Clipping. *Commun ACM* 17(1):32–42.

Testa E, Bajard M, Chevallier M, Dauvergne D, Le Foulher F, Freud N, Létang JM, Poizat JC, Ray C, Testa M (2009) Dose profile monitoring with carbon ions by means of prompt-gamma measurements. *Nucl Instrum Methods Phys Res B* 267(6):993–996.

Thorndyke B, Schreibmann E, Koong A, Xing L (2006) Reducing respiratory motion artifacts in positron emission tomography through retrospective stacking. *Med Phys* 33(7):2632–2641.

Tobias C, Chatterjee A, Smith A (1971) Radioactive fragmentation of N^{7+} ion beam observed in a beryllium target. *Physics Letters A* 37(2):119–120.

Tobias CA, Fabrikant JI, Benton EV, Holley WR (1980) Projection Radiography and Tomography. In: Pirruccello MC, Tobias CA (Eds.) *Biological and medical research with accelerated heavy ions at the Bevalac, 1977-1980.* California Univ., Berkeley (USA). Lawrence Berkeley Lab., pp. 335–346. URL: `http://www.osti.gov/energycitations/product.biblio.jsp?osti_id=6602047`. Technical Report LBL-11220.

Tsujii H, Kamada T (2012) A Review of Update Clinical Results of Carbon Ion Radiotherapy. *Jpn J Clin Oncol* 42(8):670–685.

Tsunashima Y, Vedam S, Dong L, Umezawa M, Sakae T, Bues M, Balter P, Smith A, Mohan R (2008) Efficiency of respiratory-gated delivery of synchrotron-based pulsed proton irradiation. *Phys Med Biol* 53(7):1947–1959.

Tufan MÇ, Namdar T, Gümüş H (2013) Stopping power and CSDA range calculations for incident electrons and positrons in breast and brain tissues. *Radiat Environ Biophys* 52(2):245–253.

Urakabe E, Kanai T, Kanazawa M, Kitagawa A, Noda K, Tomitani T, Suda M, Iseki Y, Hanawa K, Sato K, Shimbo M, Mizuno H, Hirata Y, Futami Y, Iwashita Y, Noda A (2001) Spot Scanning Using Radioactive ^{11}C Beams for Heavy-Ion Radiotherapy. *Jpn J Appl Phys* 40(Part 1, No. 4A):2540–2548.

Voss B, Junk H, Stelzer H (1998) The Monitoring system of the Therapy Project. In: Grundinger U (Ed.) *GSI Scientific Report 1997.* p. 187.

Wambersie A, Hendry JH, Andreo P, DeLuca PM, Gahbauer R, Menzel H, Whitmore G (2007) The RBE issues in ion-beam therapy: conclusions of a joint IAEA/ICRU working group regarding quantities and units. *Radiat Prot Dosimetry* 122(1-4):463–470.

Weber U, Becher W, Kraft G (2000) Depth scanning for a conformal ion beam treatment of deep seated tumours. *Phys Med Biol* 45(12):3627–3641.

Weber U, Kraft G (1999) Design and construction of a ripple filter for a smoothed depth dose distribution in conformal particle therapy. *Phys Med Biol* 44:2765–2775.

Wilson RR (1946) Radiological Use of Fast Protons. *Radiother Oncol* 47(5):487–491.

Wong JW, Sharpe MB, Jaffray DA, Kini VR, Robertson JM, Stromberg JS, Martinez AA (1999) The use of active breathing control (ABC) to reduce margin for breathing motion. *Int J Radiat Oncol Biol Phys* 44(4):911–919.

Woo SK, Watabe H, Choi Y, Kim KM, Park CC, Bloomfield PM, Iida H (2004) Sinogram-based motion correction of PET images using optical motion tracking system and list-mode data acquisition. *IEEE Trans Nucl Sci* 51(3):782–788.

Yamaya T, Inaniwa T, Minohara S, Yoshida E, Inadama N, Nishikido F, Shibuya K, Lam CF, Murayama H (2008) A proposal of an open PET geometry. *Phys Med Biol* 53(3):757.

Yuan Y, Andronesi OC, Bortfeld TR, Richter C, Wolf R, Guimaraes AR, Hong TS, Seco J (2013) Feasibility study of in vivo MRI based dosimetric verification of proton end-of-range for liver cancer patients. *Radiotherapy and Oncology* 106(3):378–382.

Zaidi H (2001) Scatter modelling and correction strategies in fully 3-D PET. *Nucl Med Commun* 22(11):1181–1184.

Zenklusen SM, Pedroni E, Meer D (2010) A study on repainting strategies for treating moderately moving targets with proton pencil beam scanning at the new Gantry 2 at PSI. *Phys Med Biol* 55(17):5103–5121.

Zhu X, España S, Daartz J, Liebsch N, Ouyang J, Paganetti H, Bortfeld TR, El Fakhri G (2011) Monitoring proton radiation therapy with in-room PET imaging. *Phys Med Biol* 56(13):4041–4057.

Acknowledgements

And time for reflection with colleagues is for me a lifesaver; it is not just a nice thing to do if you have the time. It is the only way you can survive. – Margaret J. Wheatley

I would like to acknowledge all my colleagues in Dresden, Darmstadt and Heidelberg as well as the important people in my life from whom I've received a lot of support during my PhD studies and who generously spent their time for discussions leading finally to the successful completion of this thesis.

First of all I gratefully thank my supervisor Professor Dr. Wolfgang Enghardt for his enthusiasm in ion beam therapy, for allocating this challenging and fascinating topic for me and for introducing me to his impressive organized scientific working style. I always enjoyed the analytic discussions with him and his encouraging words. I appreciated his deep interest in my work and his trust in my abilities when he e.g. delegated me as his substitute to the IBIBAM conference 2010 or assigned me several tasks like the supervision of a master's thesis or the guidance of lab courses.

I thank Prof. Dr. Thomas Cowan for allowing me to use the infrastructure and to perform main parts of my work at the radiation physics department of the HZDR. I warmly thank Dr. Fine Fiedler for her patient introduction to in-beam PET and the PET-specific equipment at GSI, for her attendance and support during all shifts and maintenance periods and for the application and defence of our beam times. Thank you for bearing all my doubts and answering my endless questions during the past years. For his introduction to MLEM reconstruction I thank Dr. Georgy Shakirin, now with Philips. Special thank goes to Dr. Marlen Priegnitz for taking time for our fruitful discussions and for all her helpful suggestions as well as for her support during the experiments. It was a great pleasure to work with you. Similar I can say for Dr. Daniela Kunath who always found time to listen and encouraged me to work on. Furthermore, I thank Sebastian Schöne, Heide Rohling and Stephan Helmbrecht for their support during experiment or maintenance periods in Darmstadt. The latter I also acknowledge for his range comparison tool used for the insets in figure 3.19. I take my hat off to Dr. Stefan Menkel who managed to create a first version of the 4D simulation program during his 5 month master's thesis and I thank him for the good cooperation. I am grateful to got a lot of assistance and help from engineer Manfred Sobiella during several on-site maintenance visits of our PET scanner in Darmstadt. Additionally, I thank his team for the fabrication of various targets and thank him, Robert Schönert and Mathias Kempe for the design, construction and programming as well as the later modification of the stepping motor driven linear motion table. Besides the already mentioned colleagues, I like to thank the members of the Radiation Physics division of the HZDR and the members of the OncoRay groups Medical

Radiation Physics, Laser-Radiooncology and In-vivo Dosimetry for new Types of Radiation that they contributed with their friendly and cooperative nature to a warm and harmonious working atmosphere: Marc Berthel, Dr. Elke Beyreuther, Anne Dreyer, Christian Golnik, Fernando Hueso González, Dr. Mario Helm, Dr. Volker Hietschold, Dr. Cordelia Hoinkis, Dr. Uwe Just, Dr. Leonhard Karsch, Dr. Thomas Kormoll, Lydia Laschinsky, Elisabeth Leßmann, Dr. Steffen Löck, Umar Masood, Andreas Müller, Melanie Oppelt, Dr. Guntram Pausch, Dr. Jörg Pawelke, Dr. Christian Richter, Dr. Michael Schürer, Prasad Thute, Falk Tillner, Yuan Tian and Dr. Wolfgang Wagner.

From the HIT facility in Heidelberg I would like to thank Prof. Dr. Katia Parodi, now with the LMU in Munich, for her initial experiment ideas, her support and overview during the first experiments and introducing me by that to 4D in-beam PET. I thank you for your persisting interest in this work and for our active collaboration within the ENVISION workpackage 4.

During my studies I enjoyed each of the numerous trips to the GSI Helmholtzzentrum in Darmstadt and I am very thankful to have met so many friendly, cooperative and open-hearted people there. There is of course the former head of the motion team Prof. Dr. Christoph Bert, now with the university hospital in Erlangen, who mainly introduced me to the motion mitigation world. Over the years I have learned to love his endearing chaotic but also impressively creative and imaginative working style and his special sarcasm after long night shifts. I would like to specially thank you for your encouraging attitude, taking care for me at several business trips and supporting my 4D PET experiments together with your whole group. I explicitly express my thank to Dr. Nami Saito who reliably kept track of the motion compensation issues in our experiments and figured out a solution for each problem if anyhow possible, Anna Constantinescu who enabled with her work the gated beam delivery at GSI and Dr. Robert Lüchtenborg who supported me e.g. with the rotating motion platform and helped to endure a completely failed beam time. Together with other current and former motion team members like Dr. Naved Chaudhri, Dr. Robert Kaderka, Dr. Christian Graeff, John Eley and Dr. Peter Steidl they were capable at each day or night time to create a friendly and collegial working atmosphere. This holds also true for other members of the biophysics department and I would like to thank exemplarily Dr. Michael Scholz, Dr. Thomas Friedrich, Dr. Chiara La Tessa and Christoph Schuy for their cooperative beam time sharing. I thank Dr. Michael Krämer for the IT support at GSI and Dr. Dieter Schardt for his readily technical support whenever required and possible. I also want to deeply thank the accelerator crew at the heavy ion synchrotron facility for their cooperation and the delivery of ion beams with requested properties. I acknowledge representatively the department heads Petra Schütt and Uwe Scheeler who were always keen to meet all of our special requirements.

Last but not least, I sincerely thank my parents and my husband for their deep love, patience and understanding. It is overwhelming to feel how proud you are. Frank, I thank you thousandfold for your unfailing support and motivation, for proofreading the manuscript, your interest and our long clarifying discussions and that you lit up my life whenever needed. I finally would like to thank my family, family in-law and friends for always lending a willing ear, to let me forget all stresses and strains and to recognize the really important things.

Technische Universität Dresden
Medizinische Fakultät Carl Gustav Carus
Promotionsordnung vom 24. Juli 2011

Erklärungen zur Eröffnung des Promotionsverfahrens

1. Hiermit versichere ich, dass ich die vorliegende Arbeit ohne unzulässige Hilfe Dritter und ohne Benutzung anderer als der angegebenen Hilfsmittel angefertigt habe; die aus fremden Quellen direkt oder indirekt übernommenen Gedanken sind als solche kenntlich gemacht.

2. Bei der Auswahl und Auswertung des Materials sowie bei der Herstellung des Manuskripts habe ich Unterstützungsleistungen von folgenden Personen erhalten: Prof. Dr. W. Enghardt, Dr. Fine Fiedler, Dr. Marlen Priegnitz.

3. Weitere Personen waren an der geistigen Herstellung der vorliegenden Arbeit nicht beteiligt. Insbesondere habe ich nicht die Hilfe eines kommerziellen Promotionsberaters in Anspruch genommen. Dritte haben von mir weder unmittelbar noch mittelbar geldwerte Leistungen für Arbeiten erhalten, die im Zusammenhang mit dem Inhalt der vorgelegten Dissertation stehen.

4. Die Arbeit wurde bisher weder im Inland noch im Ausland in gleicher oder ähnlicher Form einer anderen Prüfungsbehörde vorgelegt.

5. Die Inhalte dieser Dissertation wurden in folgender Form veröffentlicht:
    - Laube K, Bert C, Chaudhri N, Fiedler F, Parodi K, Rietzel E, Saito N, Enghardt W (2009) 4D in-beam PET of moving targets for different irradiation scenarios. In: Große K (Hrg.) *GSI Scientific Report 2008.* GSI Helmholtzzentrum für Schwerionenforschung, S. 400.
    - Laube K, Bert C, Chaudhri N, Fiedler F, Parodi K, Rietzel E, Saito N, Enghardt W (2010) On the difference of 3D and 4D in-beam PET for a periodically moving target. In: Große K (Hrg.) *GSI Scientific Report 2009.* GSI Helmholtzzentrum für Schwerionenforschung, S. 503.
    - Laube K, Fiedler F, Schöne S, Bert C, Enghardt W (2011) Influence of point source motion in PET images and its compensation. In: Große K (Hrg.) *GSI Scientific Report 2010.* GSI Helmholtzzentrum für Schwerionenforschung, S. 470.
    - Laube K, Bert C, Fiedler F, Helmbrecht S, Priegnitz M, Saito N, Enghardt W (2012) Verification of ion range in moving targets. In: Große K (Hrg.) *GSI Scientific Report 2011.* GSI Helmholtzzentrum für Schwerionenforschung, S. 534
    - Laube K, Fiedler F, Bert C, Saito N, Enghardt W (2012) Reconstruction of 4D in-beam PET data for quality control of moving target irradiation in ion beam therapy. *International Conference on Translational Research in Radio-Oncology*

  and Physics for Health in Europe, Geneva. (Abstract veröffentlicht in: *Radiother Onco*l 102(S1):S43–S44.)
  - Laube K, Menkel S, Bert C, Enghardt W, Helmbrecht S, Saito N and Fiedler F (2013) 4D particle therapy PET simulation for moving targets irradiated with scanned ion beams. *Phys Med Biol* 58(3):513–533
  - Stützer K, Bert C, Enghardt W, Helmbrecht S, Parodi K, Priegnitz M, Saito N, Fiedler F (2013) Experimental verification of a 4D MLEM reconstruction algorithm used for in-beam PET measurements in particle therapy. *Phys Med Biol* 58(15):5085-5111

6. Ich bestätige, dass ich die Promotionsordnung der Medizinischen Fakultät Carl Gustav Carus der Technischen Universität Dresden anerkenne.

Dresden, 24. Juni 2013

Hiermit bestätige ich die Einhaltung der folgenden aktuellen gesetzlichen Vorgaben im Rahmen meiner Dissertation (Nicht angekreuzte Punkte sind für meine Dissertation nicht relevant.)

☐ das zustimmende Votum der Ethikkommission bei Klinischen Studien, epidemiologischen Untersuchungen mit Personenbezug oder Sachverhalten, die das Medizinproduktegesetz betreffen

☐ die Einhaltung der Bestimmungen des Tierschutzgesetzes

☐ die Einhaltung des Gentechnikgesetzes

☒ die Einhaltung von Datenschutzbestimmungen der Medizinischen Fakultät und des Universitätsklinikums Carl Gustav Carus.

Dresden, 24. Juni 2013